Factors affecting the performance of a Quadrupole Mass Spectrometer

Thesis submitted in accordance with the requirements of the University of Liverpool for the degree of

Doctor in Philosophy

by

Thomas J. Hogan

Department of Electrical Engineering and Electronics

The University of Liverpool

November 2011

Abstract

A Quadrupole Mass Filter (QMF) is a key component of a Quadrupole Mass Spectrometer (QMS) that provides the mass to charge discrimination required to separate the component species of a sample. A custom software package has been developed that accurately simulates the performance of the QMF. When used in conjunction with a public domain field solver program a powerful software toolbox is created that can accurately predict the performance characteristics of a range of QMF electrode geometries. This software toolbox has been used to investigate the effects of the ratio of circular electrode radius r to electric field radius r_0 for zone 1 ($a \approx 0.237$, $q \approx 0.706$) and zone 3 ($a \approx 3.16$, $q \approx 3.23$) operation. The magnitude and variation of the '*tail*' in the mass spectral peak shapes apparent for zone 1 is much decreased for zone 3 and does not influence QMF resolution.

In collaboration with the Atomic Weapons Establishment (AWE) the requirements for a QMF and Electronic Control Unit for integration into a QMS were investigated. The QMS is be used for the qualitative and quantitative identification of Hydrogen and Helium isotopes. To successfully separate Hydrogen Tritium (HT) from diatomic Deuterium (D_2) a resolution greater than 930 is required. Simulation results demonstrated that this is achievable if hyperbolic profile electrodes are used in conjunction with operation in stability zone 3.

A second investigation undertaken as a collaborative project with the Massachusetts Institute of Technology (MIT) investigated the characteristics of a QMF manufactured using Micro-Electro Mechanical Systems (MEMS) technology. The process technology employed is more suited to the manufacture of square electrodes which produce electric fields that are far from optimum. Results show that this limitation in the electric field can be significantly overcome by operating the QMF in zone 3.

Some of this data together with information provided by users of QMSs was used to develop a specification for an electronic control unit (ECU) for a QMS. An ECU has now been designed and manufactured. The testing and evaluation of the ECU has now commenced.

ACKNOWLEDGEMENTS

"*No man is an island*" although coined by John Donne nearly 400 years ago it is a phrase that I consider to be very pertinent to my own experiences whilst undertaking this project. This project is a culmination of a journey which without the goodwill of others would have been immensely more difficult, if not impossible. Firstly if the opportunity had not arisen the journey would not have been started. For that opportunity I must thank Professor Steve Taylor my supervisor who offered me the opportunity to undertake research work in his research group and has provided on-going support and advice throughout the duration. At the same time I must take the opportunity to thank my second supervisor Dr. Ray Gibson whose work on numerical modelling provided an inspiration for my own attempts at extending his work. Thirdly, I must thank Dr. Gerard Edwards who also reawakened my desire to undertake a project such as this.

Several present and past members of the Mass Spectrometry Group at the University of Liverpool also deserve to be acknowledged and thanked at this time; Dr. Phillip Turner and Dr. Neil France were fellow travellers and provided me with invaluable insight and support in the early days of my time at the University of Liverpool; Dr. Boris Brkić for undertaking CPO simulations and also for his invaluable support and advice; Dr. Jeyan Sreekumar for assisting me by undertaking computer simulations for the AWE project. I would also like to thank Mrs. Farnoush Salarzaei and Mr. Sarfaraz U. Syed for posing interesting questions regarding the usage of the QMS2 software package together with other interesting discussions. So thank you all for your contributions, it was great that our paths crossed.

I would like to also thank the Atomic Weapons Establishment (AWE) for providing funding to undertake some of the work that contributed to my project as a whole and in particular to Dr. Phillip Turner and Mr. Brian Garney of AWE for their assistance and support. Another important opportunity was offered by Dr. Kerry Cheung, Dr. L. F. Velásquez-García and Professor A. I. Akinwande of the Massachusetts Institute of Technology (MIT) who allowed me to assist on one of their projects by undertaking computer simulations for them. So thank you, it is greatly appreciated.

Without the support of my family there would be no purpose. So to my wife Lynda, my daughter Marie and my son Paul, together with their respective spouses Gareth and Catherine and the latest addition to the family, Marie and Gareth's daughter Rosie, many thanks for your love and support which was very and still is important to me. Finally as a tribute to my late parents Patrick and Annie, you are still remembered and very close to my heart.

CONTENTS

FIGURES

TABLES

Chapter 1

1. INTRODUCTION

1.1 Quadrupole mass spectrometer

The mass spectrometer (MS) is the generic name given to instruments used to undertake the analytical technique of mass spectrometry [1]. In mass spectrometry the mass-to-charge ratio (*m/z*) of charged particles (usually positive ions) are measured in order to identify the species present in a sample [2]. The quadrupole mass spectrometer (QMS) is a particular example of a MS. It selectively filters analyte ions on the basis of their mass to charge ratio (*m/z*) enabling the relative abundances of the constituent components to be measured [1].

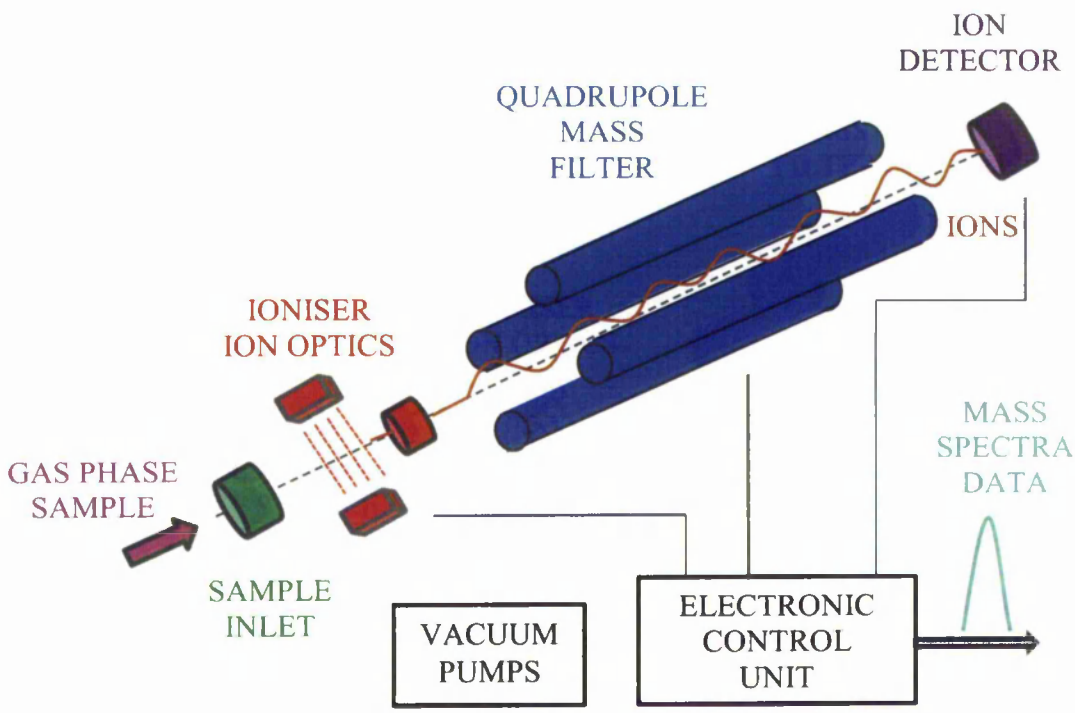

Figure 1.1. Outline representation of a quadrupole mass spectrometer system with the QMF outer casing being omitted for clarity.

Figure 1.1 shows an outline representation of a typical QMS. It is comprised of a number of different sub-systems, each one of which influences its overall performance [1], they are;

a) Sample inlet

The sample inlet provides an interface between the analyte source and the ioniser. For the case of a gas phase analyte, pressure reduction with minimal mass discrimination effects are desirable attributes. Capillary tubes, leak valves, orifices and frits are all common types of sample inlet.

b) Ioniser

This sub system creates atomic and molecular charged particles (ions) from the input sample. A number of different types of ioniser exist and include electron impact (EI), inductively coupled plasma (ICP), electrospray (ESI) and chemical (CI). A suitable arrangement of ion optics is provided between the ioniser output and the input to the QMF to achieve maximum transfer efficiency of the ions.

c) Quadrupole Mass Filter (QMF)

Provides the mass to charge ratio filtering action required to identify and quantify the constituent components of the ionised analyte.

d) Ion detector

Ions that successfully pass through the QMF emerge at the exit and impinge on the ion detector depositing a charge. The Faraday Cup is the simplest and most rugged form of ion detector. Where greater sensitivity is required, various forms of electron multiplier (EM) are used.

e) Electronic control unit (ECU)

The generation of the ioniser, QMF and ion detector control voltages and data acquisition interfaces are provided by the ECU. Mass spectra data can be transferred to a host computer or displayed locally.

f) Vacuum pumps

To achieve the correct operating pressure for the QMS, a vacuum pumping system is required. This usually consists of a combination of two pumps: (i) a low vacuum pump such as diaphragm or rotary, (ii) a high vacuum pump such as a turbomolecular, diffusion or ion.

1.2 Focus of thesis

It is the QMF and ECU that are the main focus of the work contained in this thesis. The emergence of the QMF is largely due to the seminal work carried out by Wolfgang Paul [3]. Originally QMFs employed hyperbolic profile electrodes but for reasons of manufacturing economy, QMFs fitted with circular electrodes soon found widespread acceptance in commercial QMSs [2]. QMFs constructed with circular electrodes provide inferior performance characteristics when compared to QMFs constructed with hyperbolic electrodes [2], [4]. While commercially available QMSs provide an operational specification that satisfies the majority of user applications, for some more specialised applications their performance has been shown to be inadequate [5-6].

For a large proportion of the time the QMF has been in existence computer simulation techniques have been used to investigate its performance characteristics. An early example of such research was by Lever who used a Fortran IV program running on an IBM 7094 computer with off-line curve plotter to investigate ion trajectories for a hyperbolic electrode QMF [7]. Since this time other researchers such as Dawson [8], Batey [9], Gibson, Taylor and Leck [10], Douglas and Konenkov [11], have all used computer simulation techniques to investigate different aspects of QMF performance.

The primary aim of this project was to apply computer simulation techniques to obtain a better understanding of the factors that determine the performance window of a QMF when operated in a manner that is applicable for more specialised applications. A secondary aim was the design of an electronic control unit (ECU) for incorporation into a QMS taking into account information obtained from the computer simulations.

1.3 Thesis organisation

A review of previous research relating to the QMS but more specifically to the QMF, is provided in Chapter 2. Firstly, the early years are briefly visited to provide a historical background to the origins of the Mass Spectrometer. The emerging application of electro-dynamic fields in Mass Spectrometry is identified as a significant milestone in the evolution of the Mass Spectrometer and specifically a

seminal point for the QMS. The QMF is then discussed in terms of hyperbolic and circular electrode profiles and the performance differences that the two types of electrodes provide. Alternative stability zones are then introduced followed on by a review of the impact of fringing fields on QMF performance. The related topics of alternative electrode geometries and miniaturisation are then discussed. Finally the characteristics of non-sinusoidal electrode drive are considered.

In Chapter 3 a brief overview of the physical principles that govern the operation of a QMF both for hyperbolic and circular electrodes is provided. The concepts of field solver methods for obtaining solutions to the electric field generated by a QMF are then explained. The modules of the public domain field solver package used for this work are discussed and the operational flow used in generating a field file for an electrode geometry is explained. The custom software packages developed to calculate the ion trajectories and generate mass spectra are then discussed. Examples of the graphical user interface (GUI) of the programme are provided as an aid to further understanding how the software is controlled and the facilities it provides.

The software previously discussed was then applied to investigating QMF operational performance for stability zone 3 and the results are presented in Chapter 4. To validate the software, previously published results for operation in zone 1 were reproduced for each of the two investigations included in this Chapter. Then an examination of the performance characteristics of a QMF when operating in zone 3 for different electrode geometries was undertaken. Following on from this, the effects of displaced electrodes were considered together with a method of compensation using differential electrode drive.

Chapter 5 extended the investigation work of Chapter 4 with an investigation into two specialised applications. Firstly, a feasibility study was undertaken to consider the issues of separating low mass isotopes of hydrogen and helium. The second was an investigation into a miniaturised QMF consisting of square electrodes and manufactured using a monolithic process technology.

The design of the electronic control unit for a QMS is described in Chapter 6. The philosophy and reasoning behind the particular system design is justified. Each of the individual controllers is then discussed with salient design features highlighted. Each of the controllers is described through a combination of schematics and explanation. The firmware for each of the controllers is also discussed and the concept of firmware reuse explained. The commercial software packages used in the generation

of the circuit schematics, layout of the printed circuit boards and generation of the design files required for manufacturing are also briefly discussed. The firmware and hardware design and development are mentioned together with a brief outline of the design path. The custom application program for controlling the QMS is introduced and an example of the GUI associated with programme shown.

Finally in Chapter 7 the overall conclusions for the project are presented and discussed. Possibilities for future work are also identified.

Chapter 2

2. HISTORICAL REVIEW

2.1 Overview

Wolfgang Paul the German Physicist and co-inventor of the Paul Trap stated in his Nobel Lecture in December 1989 that "*There are many examples in physics showing that higher precision revealed new phenomena, inspired new ideas or confirmed or dethroned well established theories*" [12]. This statement is still applicable today and precision is very pertinent to the operation of a Quadrupole Mass Spectrometer (QMS).

The QMS is one type of mass spectrometer which provides a method of identifying the relative abundances of the constituent components of an analyte by selectively filtering analyte ions. A QMS can be used in a wide range of applications which includes: residual gas analysis of the vacuum systems that are employed in high energy experimental physics, process control in the semiconductor industry, drug testing, pharmaceutical research and assaying. As a consequence of this wide ranging usage they are deployed in very differing environments ranging from the relatively benign situation of a laboratory, the more hostile environment of a process plant, to more extreme situations such as aquatic monitoring and aerospace deployment. Traditionally a QMS used in process applications is known as a Residual Gas Analyser (RGA) and is a more rugged implementation of the QMS found in a laboratory.

Any brief account of scientific history runs the risk of failure to mention key personnel as the process of science is often achieved through the small contributions of a large number of researchers. In these introductory paragraphs a number of researchers have been identified and their contributions outlined but they are not the only players that have contributed to this important sphere of analytical science. In this chapter a brief review of previous research that is pertinent to the remainder of the thesis is presented.

2.2 Early years

An early observer of charged particles was the German scientist Eugen Goldstein (1850-1930) who advanced the understanding of glow discharge tubes naming the observable light emissions as cathode rays [13]. This was followed by his discovery that discharge tubes with a perforated cathode produced a glow in the region of the cathode produced by positively charged ions which he called canal rays. The characteristics of the canal rays or positive ions were dependent on the residual gas(es) within the vacuum tube. A little later Wilhelm Wien identified anode rays as possessing positive charge [14]. He used a piece of apparatus known as a velocity filter, in which the magnetic deflection of positively charged ions is compensated by the superimposed force due to an electrostatic field.

Around the same time, J. J. Thomson discovered the electron and its associated mass to charge ratio (m/z) [15]. He went onto research positive ions and discovered that there are 'different types of positive ions for each element' [16]. This was a seminal moment in the evolutionary path of mass spectrometry. Thomson then went on to identify two isotopes of Neon [1]. This work was further extended by another Cambridge scientist; Francis W. Aston (a student of Thomson) who produced a mass spectrometer with an order of magnitude improvement in resolving power. With this he was able to identify a number of isotopes including three isotopes of Lead [17]. At about the same time, A. J. Dempster of the University of Chicago improved the resolution by employing a sector magnetic analyser and also developed the first electron impact ion source [18]. He is also credited with discovering Uranium 235.

2.3 Electro-dynamic fields

Up until the early 1950s the majority of mass spectrometers used magnetic fields for the focusing or mass discrimination mechanism. These are commonly termed 'static' instruments due to their focusing field remaining largely constant [1].

To achieve rapid identification of a wide range of constituent components in a sample, a different type of instrument was sought. It is at this point that the use of a time varying (dynamic) focusing mechanism emerges, due in part to work in high energy particle accelerators. The development of this class of instrument which uses a *quadrupole electro-dynamic field* to achieve mass filtering action is attributable to

Paul and his co-workers at the University of Bonn [15]. Their significant contribution in this field is signified by the patents they hold for a quadrupole filter [19-20] and the associated paper published in 1958 [3].

An electro-dynamic field provides a mechanism by which charged particles can be separated on the basis of their mass to charge ratio (m/z). Devices that employ this mechanism are generically termed mass filters, but strictly they are mass to charge filters. The physical realisation of this device can and has taken many forms. In the early stages of their development there were (to name a few): the Quadrupole Mass Filter (QMF) [21] a linear device producing a two dimensional field, the Monopole Mass Filter [22] a linear device producing a quarter of the QMF field. A third class of this type of device is the Quadrupole Ion Trap (QIT) [3] which produces a three dimensional field. The first two filters rely on a continuous stream of ions flowing through the filter for the duration of the analytical scan, whereas the QIT stores a sample and then executes an analytical scan in a repeated periodic manner.

An example of a mass spectra for a QMF showing the variation of transmission against m/z and the method for calculating the resolution of the QMF [23] is shown in Figure 2.1.

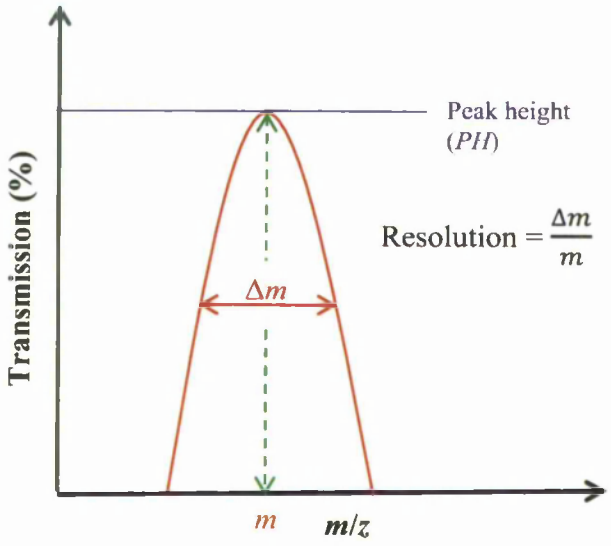

Figure 2.1. Drawing of a mass spectra showing the relationship of m and Δm for calculating the QMF resolution, where Δm is measured at a nominated percentage of the peak height.

The first mass spectra using a linear QMF were obtained in 1954 for the element Rubidium [12], using frequency scanning, since then voltage scanning has been the

preferred choice. In less than ten years from this date exceptionally high resolution was demonstrated by von Zahn with a QMF of length 5.82 m, achieving a resolution of 16,000 [23]. The interest and take up in the technology is reinforced by feasibility studies undertaken by Brubaker for equipment for lunar crust and atmosphere analysis [24], and astronaut breath analysis [25] in the 1960s.

2.4 Quadrupole Mass Spectrometer – A system

Following Dawson [26], a QMS or RGA is a system comprising of a number of individual functional blocks, each contributing to the overall performance. Additionally the characteristics of the interface between each block also impacts on overall system performance. The achievable performance may be limited by: the ion source, mass analyser, length and mechanical tolerances [26]. Just as the QMS comprises a number of different blocks, so has previous research taken a number of different routes in characterising the QMS and the QMF.

2.5 Quadrupole Mass Filter

2.5.1 Overview

The theoretical basis of the operation of a quadrupole QMF relies on the fact that a certain configuration of hyperbolic electrodes, driven by a particular arrangement of voltages, produces a quadrupole voltage distribution in the central area between the electrodes. This results in an electric field that increases linearly with increasing displacement from the central axis and is independent (uncoupled) in the two axes. The relatively simple construction coupled with a straightforward electronic drive requirement and the linear relationship between mass and drive amplitude has destined the QMF for widespread usage.

The equations of motion for the trajectory of ions in the x and y direction for a hyperbolic electrode QMF (see Figure 2.2) can be defined by the Mathieu equation [2] (also see section 3.2.1). Solutions to this equation termed Mathieu functions result in areas of stable and unstable ion trajectories [2], [27]. The Mathieu equation was originally devised by the French mathematician Emile Léonard Mathieu (1835-1890) in 1868 as a result of investigating another practical problem, that of the vibrational modes of a stretched membrane having an elliptical boundary [27]. These

functions and the associated Mathieu Stability Diagram provide an important tool and aid to understanding QMF operation [2].

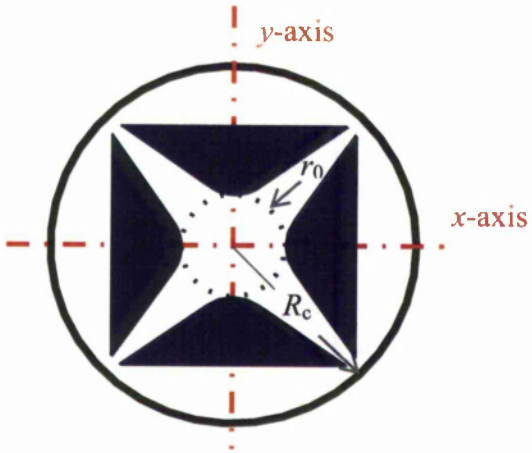

Figure 2.2. Cross section of a hyperbolic electrode QMF with a central field area of radius r_0 and an enclosure of radius R_c.

A convenient method of visualizing these solutions is through the Mathieu Stability Diagram [2], [27]. Figure 2.3 shows the Mathieu Stability Diagram for the x and y direction overlaid. Areas where x stable and y stable overlap are called stability zones and indicate that the ions overall motion will be theoretically stable. In practice the first of these, stability zone 1 ($a \approx 0.237$, $q \approx 0.706$) [2] is the one in most common usage. The next two, zone 2 ($a \approx 0$, $q \approx 7.547$) and zone 3 ($a \approx 3.16$, $q \approx 3.23$) provide characteristics that are beneficial for certain applications [2]. Zone 1 and zone 3 are the two zones that are the focus of the work contained in this thesis. Figure 2.4 provides an illustration of stable and unstable ions within a QMF.

Much early work on the performance characteristics of QMF based mass spectrometers was undertaken by Brubaker in the 1960s. An early paper of Brubaker demonstrated that for a circular electrode QMF, sensitivity is determined by the product of the transmission efficiency and entrance aperture area [28]. The same paper reported that the excitation frequency was the single most important factor that determines the resolving power of the QMF. He also made the point that the analysis

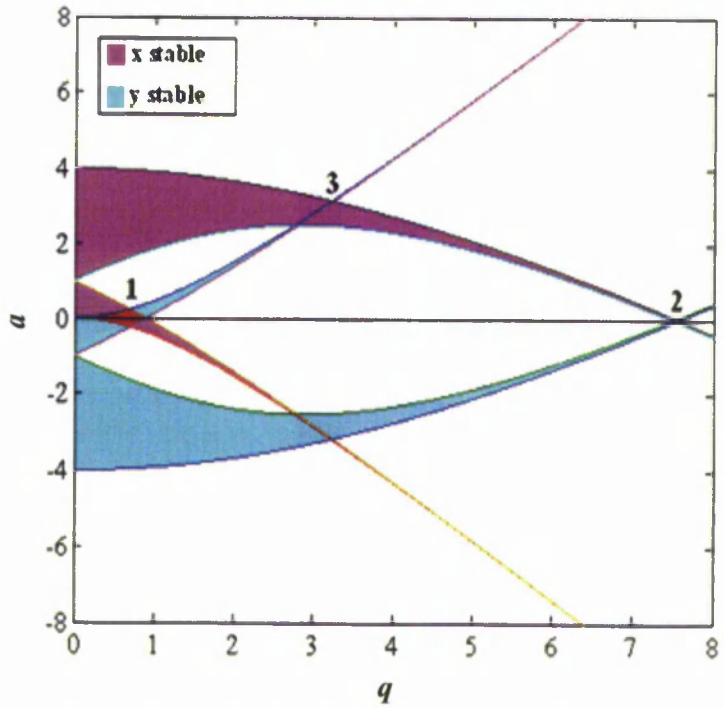

Figure 2.3. Mathieu stability diagram showing the first three stability zones with the coloured areas defining the stable x and y operating conditions.

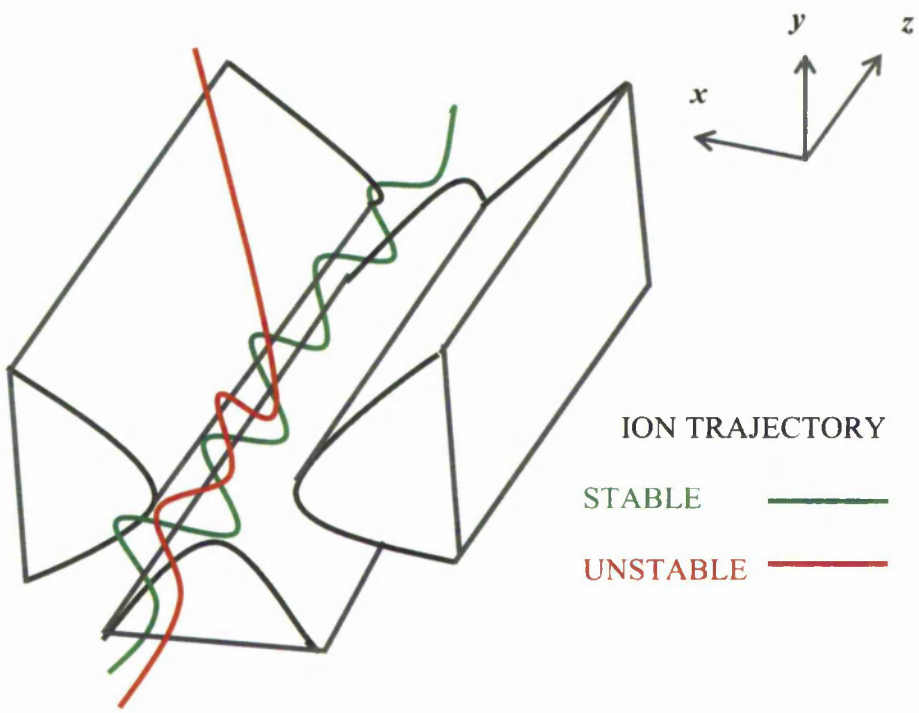

Figure 2.4. Quadrupole mass filter showing stable and unstable ion trajectories (the upper y-electrode has been omitted for clarity).

of the performance of a QMF correlated with the degrees of freedom of the operating conditions, had so far hampered the development of the QMF/QMS. Considerable work was undertaken firstly by Brubaker [24-25], [28-29] and then by Dawson [30-33] since which time the application of computer based simulation techniques has emerged, providing a powerful tool for investigating the numerous performance sensitivities of the QMF.

A multitude of performance operating condition relationships has gradually emerged over the following 40+ years. Although this field of endeavour could be considered to be to some degree mature, the demand for smaller low power devices has opened up other areas of research, that of the methods for miniaturisation and the performance characteristics of more novel electrode geometries.

2.5.2 Hyperbolic electrodes

Batey used numerical integration of the Mathieu equations to demonstrate how the ion trajectories in the x and y axis varied as the mass scan line increased [9]. Ma reported on a turbo-PASCAL program which ran under DOS on a general purpose PC with a VGA monitor [34]. The program used a fourth order Runge-Kutta algorithm to solve the Mathieu equation, allowing the x and y trajectories of ions to be calculated independently. Provision for varying the input position of the ion and its phase relationship to the Radio Frequency (RF) electrode drive was also provided.

Varying the RF phase at the ions point of entry to the QMF produced different effects in the ions x and y trajectories. The distance into the QMF before ions became unstable was dependent on the RF phase at the point of entry, indicating that shorter mass filters may accept ions that are outside the predicted stable zone. Also investigated was the effect of increasing the number of RF cycles which ions experienced during their passage through the QMF. This showed increasing resolution and a small reduction in peak transmission as the number of RF cycles increased up to 200 cycles, above this, no effective improvement was predicted.

Voo applied the same program to investigating the effects of initial ion energy and found that as ion energy increases the percentage of transmitted ions increases [35]. They also found that Nitrogen ions only passed through the QMF when they entered

the QMF with RF phases of 90° and 270°, drawing the conclusion that if the ions could be gated into the QMF, the transmission characteristics of the QMF could be improved. The spatial input conditions of the ions were found to possess some important characteristics: (i) they are symmetrical about the x and y axis, (ii) the percentage transmission of ions decreases as the entry position moves further away from the central axis, (iii) at very small excursions from the central axis with RF phase angles of 90° and 270°, 100% transmission was observed. All of these results were obtained for the normal combination of sinusoidal RF and DC electrode voltages. It was suggested that a square wave RF may be beneficial when driving miniature high frequency QMFs. This may decrease power dissipation and enable digital only RF stages to be implemented. The square wave was approximated by the successive addition of odd harmonics to the fundamental sine wave (Fourier series). The addition of these harmonics resulted in decreasing sensitivity as the number of harmonics was increased. Tunstall compared experimental results with those predicted by the same computer simulation program for the relationship between ΔM (where a minimum value corresponds to a maximum in resolution R_{max}) and transmission for ions exposed to differing numbers of RF cycles (N_c) [36]. Good correlation between the two sets of results were reported and showed that the well known relationship between R_{max} and N_c^2 was approximately correct.

The simulation programs relied on predicting performance based on a relatively small number of ions and therefore only a small proportion of the available initial conditions for ions were represented in any of the results. Gibson extended this previous work with a new program incorporating an enhanced ion source representation [4]. Investigation of the behaviour of a large ensemble of ions ($>10^5$) randomly injected in RF phase at each mass point on the mass scale was now possible. A comparison of experimental and simulated mass peaks for Helium at different instrument resolution settings was presented and good agreement between the two sets of results was obtained. Close examination showed differences in peak structure and shape but this was attributed to the fact that minor changes to the computer model resulted in large changes to peak transmission and shape. The radius of the uniformly illuminated ion source was shown to have a significant impact on transmission and shape, even though the resolution stayed almost identical. Contour maps provided a graphical representation of the spatial entry position of detected ions and how this entry position varied across the mass peak; on the low mass side

ions close to the x axis are successfully detected, gradually progressing to equal x and y axis detection success as the mass peak is approached, then moving increasingly to y axis detection success with increasing progression along the high mass side. When the exit aperture was less than the radius of the QMF, peak structure was in evidence. Similar effects had been observed from experimental data. The results obtained suggested that a dependency between peak structure, amplitude and exit radius size existed.

2.5.3 Circular electrodes

As with other forms of instrumentation there is a continual drive to reduce power consumption, physical size and cost of manufacture. One widely used method of reducing cost was the early adoption of circular electrodes in place of the theoretically optimum hyperbolic [2]. Figure 2.5 shows the cross section of a QMF constructed from circular electrodes. Circular are cheaper to manufacture and easier to mount accurately (no rotational mounting precision required) during manufacture. This also applies to maintenance and repair operations where the instrument is disassembled and reassembled. These operations can introduce alignment errors between the electrodes, the ion source and ion detector [37].

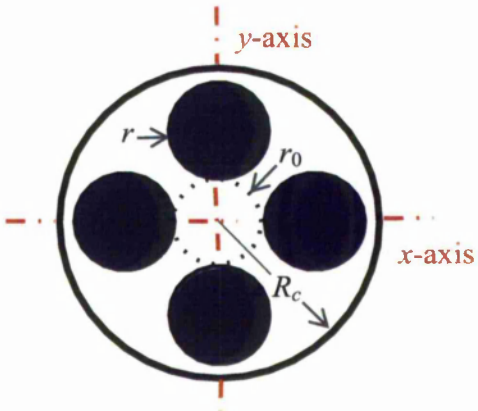

Figure 2.5. Cross section of a QMF constructed from circular electrodes of radius r with a central field area of radius r_0 and enclosure of radius R_c.

Circular electrodes when mounted in the same nominal configuration as hyperbolic electrodes produce a voltage distribution that approximates to the

quadrupole distribution generated by hyperbolic electrodes. Unlike the ideal quadrupole, these alternative electrode geometries result in more complex potential distributions and electric fields, consisting of quadrupole and higher-order components and are termed *multipole* distributions [38]. The relative magnitudes of these terms are defined by A_N where N is the order of the multipole (see section 3.2.2 for a more detailed explanation).

The ratio of electrode radius r to field radius r_0 and known as r/r_0 controls the relative magnitudes of the individual components of the *multipole* field [11]. Early empirical research undertaken by Dayton in the field of Quadrupole Magnets for high energy accelerators identified the ratio of 1.148 [39] as providing a close match to the quadrupole field. Unfortunately this value was erroneously reported as 1.16 in Paul's [3] work and Brubaker [28] also used the incorrect value of 1.16. Previous treatments of this problem assumed that zero potential was at an infinite distance from the electrodes. In a practical QMF the electrodes are enclosed within a conductive circular container to achieve the vacuum necessary for correct QMF operation. Denison employed a computer program to numerically calculate the potential distribution, using the results to obtain the value of r/r_0 where the A_6 term is zero [40]. For the electrode configuration contained within a grounded enclosure of radius $3.54 \times r_0$ a value of $r/r_0 = 1.1468$ was found. The difference from Dayton's value was shown to be due to the presence of an enclosure. The use of an $r/r_0 = 1.16$ was found to be detrimental to the achievable performance and that a value 1.1468 provided superior performance [40].

Ions as they pass through the QMF are exposed to a linear restoring force when hyperbolic electrodes are used; this force is non-linear when circular electrodes are used. It was also shown that hyperbolic electrodes produce twice the resolution at the same sensitivity compared with an equivalent circular electrode QMF [28]. Brubaker also observed that due to circular electrodes closely approximating the ideal field only in the central region, an increase in the field radius of a factor of two is required to achieve a similar performance to the hyperbolic electrode QMF [28]. This has a large impact on the power requirement due to power varying to the fourth power of r_0 [37]. This may be a deciding factor in applications such as space and covert monitoring, where power consumption, physical size and weight may be critical.

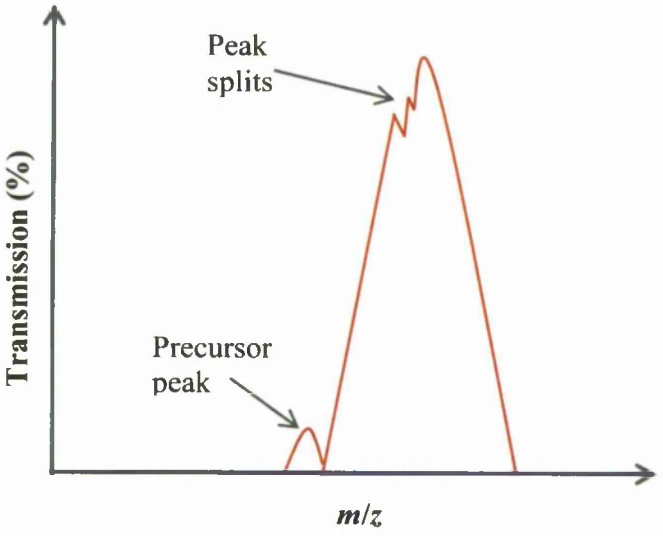

Figure 2.6. Drawing of a mass spectra showing examples of a precursor peak and peak splits.

Precursor (secondary) peaks on the low mass side of the main peak and peak splitting (see Figure 2.6) were frequently observed when operating at high resolution settings [33]. Whetten postulated that these artefacts could be due to the use of circular electrodes and the higher order field terms (A_6 and A_{10}) that they generate [33]. Calculation showed that the much larger A_6 term introduces a resonance line on the low mass side near the peak of the Mathieu stability diagram when operated at high resolution. Resonance lines are points on the stability diagram where distortions in the electric field generated by the QMF produce forces on the ion that reinforces the natural frequency of the ion trajectory. This produces an increase in the ion trajectory amplitude and can result in premature ejection of ions that would normally be stable. Figure 2.7 shows an example of these resonance lines superimposed on the stability diagram for zone 1. However the effect of the A_{10} term was not taken into account which may have impacted on their findings [11]. They suggested that these effects could be avoided by the use of hyperbolic electrodes or compensated by a small bias in the y-direction across the quadrupole. In arriving at this conclusion consideration was not given to the difficulty in avoiding rotational placement errors of hyperbolic electrodes, which may introduce similar artefacts in the peak shape.

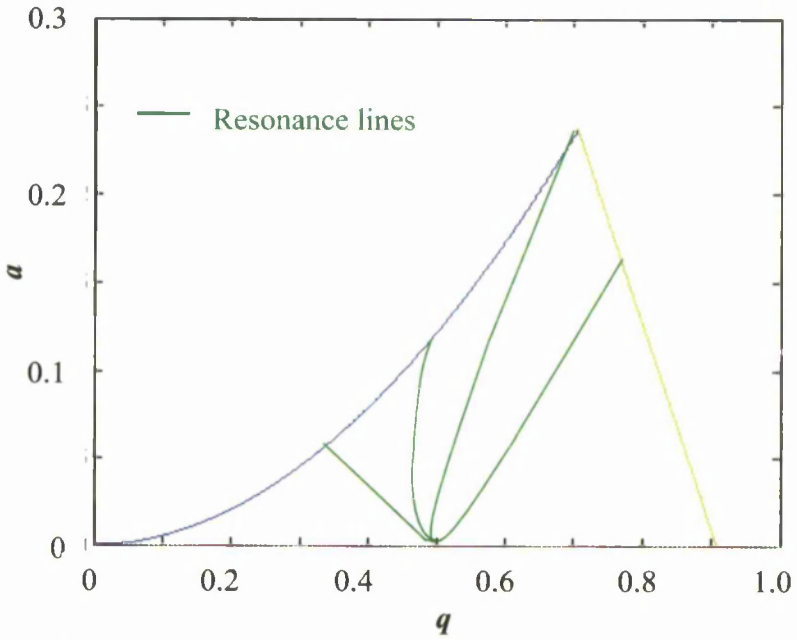

Figure 2.7. QMF zone 1 stability diagram showing an example of resonance instability lines due to field distortions [30].

Peak shape distortions and peak splitting can also be due to spacing errors in hyperbolic electrode assemblies that result in third and fourth order field distortions [30].These field imperfections give rise to resonance lines that pass through or very close to the apex of the Mathieu stability diagram and intersect with the mass scan line. Calculated ion trajectories showed that as the distortion is increased ions that were previously stable go unstable after a decreasing number of RF cycles. Operation at high resolution requires lower distortions than required for operation at low resolution. Only a single ion RF phase entry condition was examined which is not representative of a real QMF where a complete range of RF phases would be experienced, but it was assumed that similar characteristics would be expected [30].

The r/r_0 problem was revisited by Reuban et al [41]. They used a semi-analytic conformal mapping approach to deduce the value of r/r_0 for a quadrupole electrode configuration contained in a grounded enclosure that provided a zero value for the A_6 term [41]. A comparison of an ion trajectory for three cases: a pure quadrupole field, the Denison case, and for the new value were undertaken. The new value, $1.14511 \times r_0$ was found to provide a closer fit to the ion trajectory obtained when using hyperbolic electrodes. Again, only one ion entry phase was considered and it was concluded that if the trajectories of a large number of ions were simulated, peak

shapes could be obtained and compared. A more recent investigation by Schulte proposed making A_6 and A_{10} equal and opposite by suitable selection of r/r_0 [42]. This results in a decrease in non-linear resonance effects and improves the sensitivity of the QMF.

Gibson and Taylor observed that ensuring the A_6 term is zero as a method of identifying the optimum value of r/r_0 was based on an assumption [43]. No proof that this provides optimum QMF performance had been previously demonstrated. Custom designed software was used to solve the electric fields for a range of r/r_0 ratios. The trajectories of a large number of ions were then calculated for ions under varying RF phase and spatial entry conditions. They go on to show that peak shape, transmission and resolution are highly dependent on the value of r/r_0 for the range r/r_0 = 1.12 to 1.16 and that the effects of these variations are more pronounced at high instrument resolution settings. They suggested that an r/r_0 ratio in the range of 1.12 to 1.13 achieves the best performance and that an electrode radius tolerance of 1% should be sought to minimise the performance variability. Also noted were the very small differences in peak shape when changing the enclosure radius from 3.6 × r_0 to 4.2 × r_0.

An alternative approach to understanding the optimum value of r/r_0 was undertaken by Douglas et al who explained the relationship in terms of the A_6 and A_{10} multipoles [11]. It was stated that simply making the A_6 term zero is insufficient as the next higher multipole term A_{10} also has a significant influence on performance. They arrived at approximately the same value ($r/r_0 \approx 1.130$), which minimised to some extent the low mass tailing associated with circular electrodes. This value of r/r_0 is where the A_6 and A_{10} terms are approximately equal and opposite and interact in such a way as to cancel each other out [11].

2.5.4 Comparative performance

A comparison of performance between QMFs constructed from hyperbolic and circular electrodes is very difficult experimentally due to mechanical and system differences that may exist between the different instruments. These difficulties have been circumvented through the use of software simulation techniques. Gibson reported on a custom software package that enabled the performance for both

hyperbolic and circular electrode QMFs to be predicted [43]. The computer simulation model calculated a grid of electric field values for the QMF and then calculated the ion trajectories for a large number of ions entering the QMF under random RF phase and spatial position. For the case of hyperbolic electrodes the electric field was calculated from an analytical expression and for the circular electrodes a simple relaxation process was used to find the potential at each of the grid points. The field gradient was obtained by partial differentiation of the potentials. For the circular electrodes an r/r_0 ratio of 1.148 was used throughout. For the same instrument resolution setting the circular electrodes demonstrated reduced transmission and increased peak width, with increased mass tailing on the low mass side also being observed compared with the hyperbolic QMF. For the case where the ion experiences a low number of RF cycles (20 – 25) the difference between hyperbolic and circular electrodes is small. This difference increases with an increasing number of RF cycles to a value > 2, but exact differences were found to be dependent on the instrument resolution setting [4].

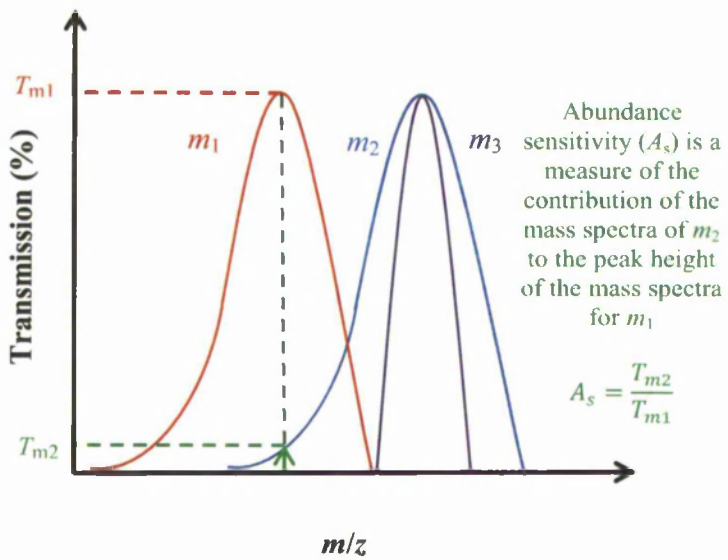

Figure 2.8. Drawing of mass spectra for m_1 and m_2 for a circular electrode QMF showing the effect of the m_2 low mass tail on the abundance sensitivity [44] of m_1. Also shown are the mass spectra (m_3) for a hyperbolic electrode QMF highlighting the absence of a low mass tail and zero abundance sensitivity with respect to m_1.

The presence of a low mass tail which occurs when circular electrodes are used is of importance as it can affect the measurement accuracy for any closely adjacent

mass peak [45] (abundance sensitivity). Figure 2.8 shows an example of this effect with the low mass tail of the mass spectra for m_2 contributing to peak height of mass spectra for m_1.

Austin undertook a large number of detailed experiments into the performance of QMS systems [37]. He found that low mass tails were present in mass spectra and that they can manifest themselves in a number of different forms. The relationship of this tailing to operating effects was investigated by Gibson and Taylor who reproduced using computer simulated mass spectra the presence of these low mass tails (see Figure 2.8) [45]. The general shape and position of the computed peaks were similar (ignoring calibration effects) to those reported by Austin, with the relative position of the secondary peaks with respect to the main peaks being approximately the same. There is however a significant difference in the amplitude of the computed secondary peak compared to the experimental one. Gibson and Taylor reported that the value of r/r_0 affected the shape and amplitude of the low mass tail but that the nature of the changes was the same for all values of r/r_0 investigated.

A number of interrelationships between main peak and the low mass tail were also investigated through computer simulation. Increasing the instrument resolution setting decreased the main peak width, while at the same time a less rapid decrease in the main peak height was observed. Accompanying this, there was a concurrent change in the low mass tail which at low instrument resolution settings merges with the main peak. As the instrument resolution setting is increased the main peak and low mass tail visibly separate, forming two distinct peaks. The amplitude of the low mass tail decreased less slowly than the main peak. In the limit, where no main peak is present, the low mass tail was still present. A well-defined peak shape was obtained when ions experienced approximately 80 RF cycles. The shape of low mass tail continued changing until the ions experienced over 200 RF cycles. The low mass tail was also found to be sensitive to the ion source radius and it was suggested that contributory ions to the low mass tail originate close to the x axis and at a large distance from the central axis [45].

2.5.5 Mechanical imperfections

In general the prediction of the behaviour of QMF performance has assumed perfect electrode geometry and this is nearly always true for published experimental results. A systematic experimental investigation of the effects of mechanical tolerances on the QMF is difficult, due to the variability introduced during the assembly and disassembly cycle. One approach is the manufacture of a range of QMSs, each with one of the imperfections to be investigated. This would be a costly exercise and in all probability only a very limited number of the possible combinations could be economically considered.

One experimentalist, Story did undertake a set of experiments on a QMS to investigate the effects of a misaligned QMF electrode [46]. One electrode of the QMF was mounted on micrometer screws, one at either end. The micrometer screws passed through the vacuum allowing fine adjustment of the position of each end of the electrode without recourse to dismantling of the unit. The alignment of the remaining three electrodes, ion source and ion detector were maintained across the experiments. Some of Story's experimental results are reproduced in Dawson [37]. Dawson investigated the relationship between mechanical or electrical imperfections and the resultant performance limitations [47] and the effects of bent or bowed electrodes [48].

It is known that imperfect construction of a QMF results in degraded performance and if excessive [37], it may not provide performance that is acceptable even for the least demanding of applications. The previously reported computer simulations techniques [4], [43] used a field solving technique that relied on the symmetrical characteristics of the electrode arrangement. When electrodes are misplaced this symmetry is destroyed. Taylor and Gibson [49] used Poisson/Superfish [50-51] a public domain software package to generate the electric fields for QMF electrode assemblies with a displaced electrode. Simulations using previously generated fields and those produced by Poisson/Superfish produced similar results [49]. Single electrode displacements were investigated. For an inward displacement of a single x electrode, the mass peak shifted to a lower mass scale position with a small increase in peak height. No significant change in peak shape was observed. Different

outcomes were observed for a y electrode displacement. For displacements up to $0.001 \times r_0$, the peak position moved to a lower mass scale position with a small reduction in peak height. As the displacement was increased further, a precursor peak emerged. Both the precursor and the main peak moved progressively to a lower mass scale point for increasing displacement. Similar characteristics were reported for outward displacements of the electrodes except that the shift on the mass scale was to a higher mass position. Adjusting the relative drive amplitude to compensate for the electrode displacement which is the subject of a number of patents [52-54] was also evaluated. Simulations generated showed that small errors in radial placement could be compensated satisfactorily for by this method [49].

2.6 Stability Zone3

Certain applications require performance that is outside the realms of that achievable from QMFs constructed within acceptable physical limits and operated in stability zone 1. Although not in common usage, stability zone 3 provides a means of achieving a higher resolution from a conventionally proportioned QMF [6], [56]. Zone 3 is of rhomboidal shape with an unequal aspect ratio (see Figure 2.3). Two operating areas provide high resolution, one close to the upper left hand tip ($a \approx 3.16$, $q \approx 3.23$), and the other close to the lower right hand tip ($a \approx 2.52$, $q \approx 2.82$). The increased a and q values for zone 3 result in higher RF and DC electrode drive voltages, limiting the maximum mass for given available maximum drive voltages. A higher resolution is achievable for ion exposure to a given number of RF cycles [56] compared to zone 1. Some researchers, term this zone as zone 2 [57] while others including the definition adopted in this thesis, refer to it as zone 3 [56].

For a given ion energy the velocity of ions is greater for low mass ions such as those found in thermonuclear experiments [57] and also helium leak detection in hydrogen rich environments [58]. Hiroki reported on a comparison of performance using the same QMS for operation in zone 1 and zone 3 [6]. The electrodes were of hyperbolic profile with a length of 200 mm, an r_0 of 4 mm and a RF frequency of 2.5 MHz were used. Zone 3 provided sharper peak shapes and the tail components produced by adjacent peaks were less than for zone 1 operation, providing improved

abundance sensitivity. Zone 3 sensitivity was about 2% of that obtained for Helium when operating in zone 1.

A common tracer gas is ^{4}He which is used for the detection of small leaks. Deuterium is often found in certain physics experiments and standard QMSs are incapable of discriminating between ^{4}He (4.0026 amu) and D_2 (4.0282) which requires a minimum baseline resolution of ≈ 161. Minimum baseline resolution is determined by the difference between the two masses and the mass of the species the resolution is referenced to. Figure 2.9 provides a graphical illustration of the minimum baseline resolution calculation.

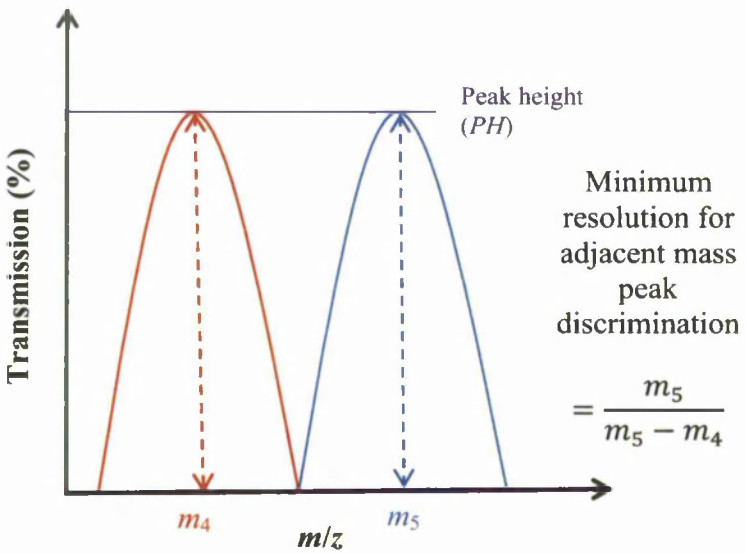

Figure 2.9. Determination of minimum baseline resolution to identify two adjacent species.

Hiroki used the same QMS previously reported [6] to successfully separate ^{4}He and D_2 achieving a resolution of 320 with 18% valley separation [57]. Figure 2.10 provides a graphical illustration of the calculation of valley separation. For ion energies ≥ 20 eV increased peak tailing was apparent with an associated reduction in resolution. A later set of experiments were reported by Hiroki et al. again using a QMF of the same dimensions but operating at 3.58 MHz [58]. A peak ratio of ^{3}He and HD of 0.1 was detected and a justification made that this could be improved with a proposed new controller operating at 7 MHz.

Hiroki et al. also reported that the lower tip of zone 3, and zone 1, exhibit a longer peak tail on the low mass side than on the high mass side [59]. The upper tip of zone 3 has a much shorter peak tail on the low mass side, making it more suitable for detecting ^4He in the presence of a large abundance of D_2 [59]. The increased resolving power of the upper zone 3 tip was quantified showing that a resolution of ≈ 200 is achieved with 23 % of the RF cycles, and 63 % for the lower zone 3 tip, compared to zone 1 operation. The ability to detect ^4He at abundance levels of 10^{-4} of D_2 was also demonstrated.

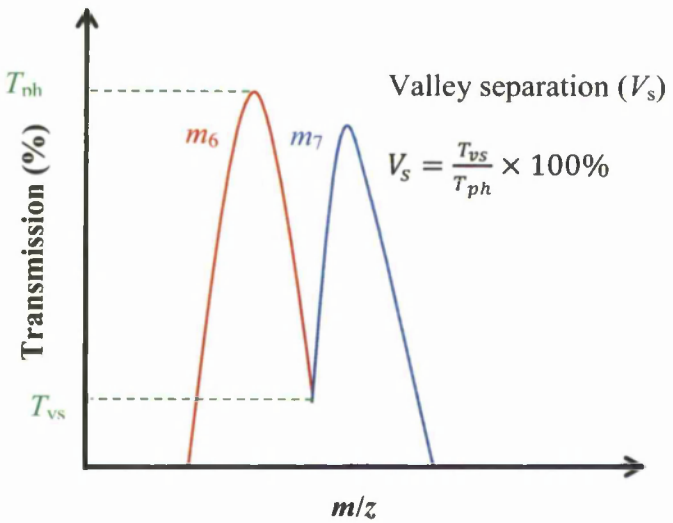

Figure 2.10. Mass spectra of two masses m_6 and m_7 illustrating the valley separation between the two mass peaks.

Du reported on a set Inductively Coupled Plasma – Mass Spectrometry (ICP-MS) experiments with a QMF for Magnesium [56], obtaining resolutions of 1000 and 2000 for the zone 3 lower and upper tips respectively. A limiting resolution of 4000 at 59 amu was obtained but acceptable sensitivity could be obtained for resolutions up to 1000. The upper tip was found to provide generally better performance in terms of resolution and sensitivity than the lower tip.

Pedder used a 200 mm long, 19 mm diameter QMF to investigate the relative performances of zone 1 and zone 3 when resolving ^4He and D_2 [60]. Typical simulated ion trajectories indicated much higher relative amplitudes of the higher harmonic frequencies for both x and y axis when operating in zone 3 compared to zone 1. Figure 2.11 shows a number of phase space acceptance ellipses for a QMF.

The ellipses provide a method of depicting theoretical conditions for an ion to successfully pass through the QMF. The eye in the centre represents a "*sweet spot where if an ion enters within these conditions it will have a theoretical stable trajectory*" [61].

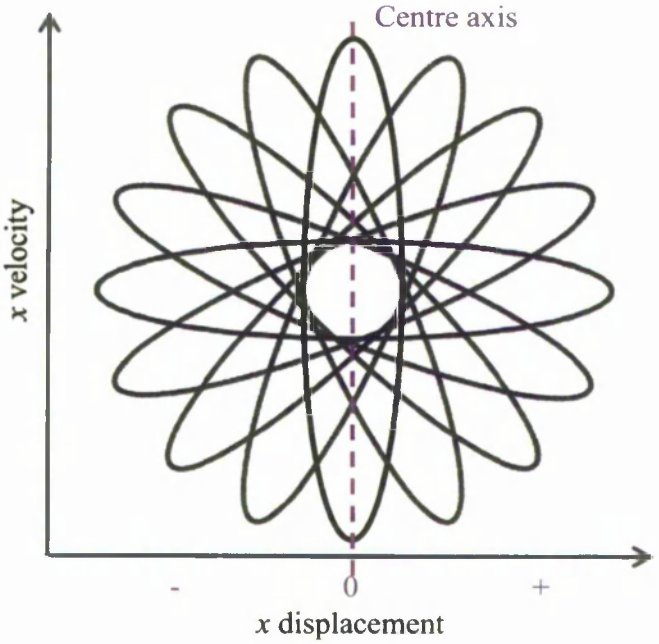

Figure 2.11. Example of a *x*-axis phase space acceptance ellipse for a QMF. A similar ellipse can be produced for the *y*-axis [61].

Pedder compared the phase space acceptance ellipses for zone 1 and zone 3, it was concluded that these predicted superior abundance sensitivity and resolution for zone 3 operation [60]. It was also pointed out that quantitative measurements of closely spaced species of wide dynamic range can be challenging for zone 1 operation. This difficulty was attributed to poorer focusing in the *y* axis. Zone 1 spectra for ^4He and D_2 when shown at high gain were characterised by a high inter-peak valley indicating overlapping of the two peaks therefore reducing the accuracy of abundance measurements. For zone 3 the high gain mass spectra were well separated with only the noise floor of the electronic measurement system visible between the two peaks. The results also showed a distinct precursor present on the low mass side of the D_2 peak. There is also an indication on the low mass side of the ^4He peak that a similar artefact could exist. More recent research has demonstrated

that this class of artefact can be a result of mechanical or drive voltage tolerances [49]. Pedder also makes the point that with zone 3 ultra-high resolution can be achieved but with the disadvantage of reduced transmission [60].

Other zone 3 characteristics that have been noted by Du et al. [62] are the presence of structure on the mass spectral peaks. They stated such features are due to focusing effects arising from the variation in the spatial excursions as the ions progress through the QMF and therefore varying the distance from the axis when they exit the QMF. The effect was more severe at higher ion energies.

2.7 Fringing fields

So far, only the two dimensional aspects of a QMF have been considered. In practice, the ions have to pass from the ionizer into the QMF, and out of the QMF to the detector. These transitions are not abrupt but diffuse. In the near vicinity of the QMF this diffuse zone arises because of fringing fields and gives rise to unwanted behaviour of the ion trajectories, with detrimental mass dependent effects on ion transmission (sensitivity). Brubaker observed that due to the shape of the y-stability zone, the decreasing RF and DC amplitudes with increasing distance from the entrance of the QMF results in the instability of ions [29], which otherwise would be transmitted through the QMF. This effect reduces the number of ions that enter the QMF and are successfully transmitted, or alters their entry conditions in the y axis ensuring rejection later in their passage through the QMF. He also observed that ions of low velocity suffered from significantly reduced effective aperture, producing a mass dependency to the effective aperture. The solution Brubaker identified [37], and which relied on the fact that an RF only field results in stable ions, was the introduction of a *delayed DC ramp*. Immediately in front of the main QMF a set of auxiliary electrodes with RF only excitation was introduced, ensuring that the RF fields increased to their instantaneous maximum amplitude, prior to the DC component of the field being encountered.

As a result of the computer simulations of fringing fields undertaken by Dawson [32] he concluded that short concurrent RF and DC ramps of less than approximately three RF cycles provided superior performance to that obtained from an abrupt (ideal) entrance field. For ramps longer than this value smaller effective apertures

would result. It was suggested that these characteristics may result in unfavourable discrimination against high mass ions due to their lower relative velocity.

Hunter reported on three dimensional computer modelling of the fringing fields [63]. He showed that for a certain range of distances between the aperture entrance plate and the QMF entrance there were marked differences from predictions obtained from a linear approximation. From computed results [63] it was concluded that the acceptance of the QMF was relatively insensitive to the distance between the QMF electrode ends and the aperture entrance plate.

Alternative methods of negating the effects of the fringing field have been reported by Marmet [64] and Fite [65]. Marmet proposed fitting a gridded box immediately in front of the QMF entrance and applying a parameterised time varying voltage to the box to eliminate the fringing field. A different method of achieving separation of the fringe fields by utilising characteristics of non-metallic materials was proposed by Fite. A hollow tube manufactured from a leaky dielectric material was positioned in front of and on-axis with the QMF. A small portion of the hollow tube projected into the QMF with the other end of the tube mounted on a grounded metallic faceplate with the ions focused so they entered the QMF through the hollow tube. The characteristics of this arrangement are such that the RF penetrates the tube, while the DC component is excluded, producing a *delayed DC ramp* [65].

All of the above were based on operation in stability zone 1. The effects of fringing fields for operation in zone 3 have been reported by a few researchers. Konenkov found that the fringing fields increased the QMF acceptance less effectively in zone 3 than zone 1 [66]. Hiroki found that the fringe length sensitivity is stronger for high resolution zone 3 operation than for zone 1 [67]. The resolution increased when both the inlet and outlet fringe field lengths were reduced. The effects of an RF only pre-filter were also investigated experimentally and theoretically by Hiroki [68]. A factor of two increase in Helium peak height was obtained when compared with the no pre-filter case.

2.8 Alternative electrode geometries

Traditionally QMFs have utilised hyperbolic or more usually circular electrodes arranged symmetrically. Other geometric shapes and non-symmetrical configurations

have been discussed either from pure academic interest, to achieve a specific performance change or because of the desire to use manufacturing technologies that are more suitable to non-standard electrode geometries.

Hayashi investigated the field characteristics produced by circular concave electrodes for both infinitesimal and infinite thickness electrodes [69]. Infinitesimal thickness circular electrodes can be formed on the inner surface of an insulating circular tube by selective vacuum deposition of metal films. With the correct pole angle it was shown that the A_6 term of the field could be eliminated providing a good approximation to the quadrupole field. Sakudo investigated the *multipole* fields produced by flat faced electrodes for two values of corner angles and obtained the conditions for approximating the ideal quadrupole field [70]. The field characteristics of a flat-plate quadrupole system were reported by Pearce [71]. He showed that over the central region a match to an ideal quadrupole field was possible to better than 0.1% accuracy. A QMF constructed from such electrodes demonstrated sufficient resolution to discriminate between masses of 17 and 18 amu. A ceramic single-piece hyperbolic quadrupole was constructed by Hiroki [72]. Four individual quadrants of Si_3N_4 were machined and sintered with the hyperbolic surfaces coated with 10 μm of metal thin films. They were then precisely joined together to provide a quadrupole field. Experimental results showed no difference in performance between the ceramic quadrupole and a conventional metal unit.

The magnitude of the *multipole* field components can be altered by changing the symmetry of the electrode geometry [38]. Ding added an A_4 field component by increasing the diameter of one pair of electrodes with respect to the other pair [73]. For a particular arrangement of the RF and DC voltages a considerable improvement in resolution was obtained.

2.9 Miniaturisation

Traditionally the majority of QMS applications have been for laboratory instrumentation and process monitoring. There is an increasing interest in the application of this technology for environmental, covert monitoring, deployment in harsh environments and on-going airborne and space applications. Characteristic requirements of these applications include small size, low weight and power, and for at least some of these instruments, low manufacturing cost would be advantageous.

Relatively large pumps and their high power requirements are required to achieve the low pressure operation for conventional systems. Henry reported that the National Aeronautics and Space Administration (NASA) scientists were "*working under a rule of thumb that an instrument should be no smaller than 1kg, occupy no more than 1 or 2 L, and consume less than 5 W for the complete system*" [74]. To minimise ion collisions with background gas molecules the dimensions of the QMF are arranged so that the mean free path (λ) of the background gas at the maximum operating pressure, is greater than the largest dimension of the QMF. Using Equation (2.1)

$$\lambda = \frac{k_B T}{\sqrt{2}\pi d^2 p} \tag{2.1}$$

where k_B is the Boltzman constant (1.3806488×10^{-23}) [75], T is the temperature (in K), d is the sum of the radii of the stationary molecule and the colliding ion (in m), p is the pressure (in Pa) and λ is the mean free path (in m) [1]. It can be calculated that for operation at a vacuum pressure of 1×10^{-1} Pa with a temperature of 300°K, a value of $\lambda \approx 5$ cm is obtained. Higher operating pressure can be achieved through size reduction, enabling smaller vacuum pumps to be used.

A number of options exist to miniaturise a QMF, some are suitable for low cost high volume manufacture, others using more traditional construction techniques are more suitable for low volume specialist applications. Conventional manufacturing processes such as centre-less grinding and wire and spark erosion, limit the size reduction possible due to handling difficulties and minimum process tolerances. The use of micro-electro-mechanical systems (MEMS) and/or micro-fabrication technologies create difficulties in realising hyperbolic shaped electrodes. They are in general more suited to producing rectilinear profile electrodes.

An early example of a miniaturised QMF was reported by Syms [76]. Four parallel cylindrical electrodes of 500 μm diameter formed from commercial silica rod with a 1000 Å Chromium surface coating were used. Pairs of the electrodes were mounted in V-grooves etched in a Silicon substrate. Two substrate assemblies separated by two additional cylindrical insulating spacers which are mounted in etched alignment grooves in the substrates form a quadrupole lens with a positional accuracy of 3%. Initial performance results for the 20 mm long device were reported

by Taylor [77]. A typical mass spectrum for Argon and Air mixture at a gas pressure of 6.67×10^{-3} Pa with an RF frequency of 6 MHz was shown. For an ion energy of 6 eV a resolution of 24 was obtained, close to the theoretically predicated value for operation in stability zone 1. An improved version of the QMF was reported by Syms [78]. Optimisation of the design to achieve good electrostatic performance was discussed and the use of kinematic mounts etched into the silicon wafers were shown to provide immunity to groove width variation. The performance improvements of this new design (MicroQuad) were presented by Taylor [79]. A directly coupled electrode drive was employed instead of the more common tuned load coupling. The same research groups later demonstrated improvements in performance of the device by the application of a transverse magnetic field providing an improvement in resolution with provision of an electron multiplier detector to compensate for low ion current [80]. Further changes to the control of the MicroQuad provided increased ion current output [81]. This was achieved through use of a pole bias to the electrodes and careful optimisation of the ion source voltage, producing an eight fold increase in ion current compared to previous results [81]. Operation at pressures up to 1.77 Pa and with reduced sensitivity to 4.53 Pa was also reported.

Researchers at MIT devised a MEMS quadrupole which used commercially available dowel pins with 5 μm diameter precision, for the electrodes [82]. The electrodes were held in position by two microfabricated plates, a top alignment plate and the springhead base (μGripper). The assembly was completed by a set of four ceramic spacers. The μGripper incorporates silicon DRIE-patterned deflection springs as an aid to precision hand assembly of the unit. The tested unit consisted of 1.58 mm diameter electrodes with an aspect ratio of 57. Operation was in stability zone 1 at a RF frequency of 1.44 MHz with a constant peak width scan line. A dynamic range of 650 amu and a peak width of 1.9 amu at 69 amu were reported.

A second generation of the μGripper was developed with the aim of enhancing performance and improving robustness during mechanical assembly [83]. To ensure equipotential surfaces, the substrates were highly doped with antimony. A final 1 μm silicon-rich nitride coating was deposited to ensure the springs were scratch resistant. This was operated in stability zone 1 with a constant peak width scan line at an RF frequency of 1.44 MHz. With 1.58 mm diameter electrodes and an aspect ratio of 57, peak widths of 1.9 amu at 69 amu and 2.2 amu at 219 amu were achieved. The peak widening at higher masses was attributed to the ultimate resolution of the device

being reached. Tests at RF frequencies of 2 MHz and 4 MHZ were also undertaken. Narrower peak widths with small precursor peaks and peak splitting on the high mass side were reported, the effects being worse at 2 MHz. Operation in stability zone 3 using 2 MHz provided almost perfect peak shape without any evidence of precursors or peak splitting. Transmission was much lower than for zone 1 with the signal-to-noise ratio reduced by a factor of 10. Using 1.00 mm diameter electrodes with an aspect ratio of 37 produced poor results. Operation in zone 1 at an RF frequency of 4 MHz produced a peak width of 4 amu at 69 amu. Reduced transmission with a signal-to-noise ratio comparable to zone 3 operation for the larger device was observed. Peak splitting was present on the mass peaks, attributed to the relative increases in electrode misalignment. No signal above the noise floor could be obtained for operation in zone 3.

Another example of a miniature QMF of similar dimensions to the MicroQuad but manufactured by a different process is attributable to Geear [84]. A wafer scale, batch fabrication process was used and included deep etched features with springs formed in the outer silicon layers for locating the precision-machined cylindrical metal electrodes in vertically etched slots. Integrated ion entrance and exit optics were similarly formed in the inner silicon layers. The completed QMF with 30 mm long 500 μm diameter stainless steel electrodes was tested. At an RF frequency of 6.1 MHz and operated in stability zone 1, a mass range of ≈ 400 amu was obtained, with a resolution of ≈ 219 at 219 amu.

A reduction in the dimensions of a QMF by a factor n produces an n^2 reduction in sensitivity [84]. Arrays of miniature QMFs [85-86] provide a means of achieving sensitivity comparable to more traditional QMFs and coupled with operation at higher frequency, provides a method of maintaining acceptable resolution with reduced length [85]. Ferran produced a QMF composed of a 4 by 4 grid array of identical electrodes precisely mounted and secured in a glass base, forming 9 QMFs operating in parallel, which they called a Micropole™ [86]. The electrodes were 10 mm long with a radius of 0.5 mm (r_0 = 0.435 mm) and the unit occupied a volume of 4 cm^3 with a weight of less than 25 g and was operated at 11 MHz. Additional supports were also mounted on the glass base for mounting filaments, lenses etc. A full width at half-maximum (FWHM) peak width of approximately 0.8 amu for components of air was obtained, with a mass peak at 17 amu being clearly resolved. The linearity of Argon partial pressure relative to the total pressure was linear up to

0.133 Pa; above this the linearity increasingly degraded before '*fold over*' [86] occurred. The non-linearity above 0.133 Pa was attributed to ion space charge in the ion source and ion background gas collisions in the QMF.

Another array was developed by the Jet Propulsion Laboratory [85]. The number of electrodes and configuration was the same as the Micropole but they were larger with a length of 25 mm and diameter of 2 mm. Two machineable ceramic (Macor) jigs, one at either end of the electrodes accurately located the electrodes. The accuracy of the electrodes was to 0.5% or better and positional accuracy was kept to 0.1%. The QMF was tested at two frequencies. The first, 7.1 MHz was used over the mass range 34 - 137 amu to obtain mass spectra for Argon, Krypton and Xenon at a resolution of 0.5 amu (FWHM) and operation up to 300 amu was tested with a sample of C_6F_{12}, of molecular weight 300 amu. A higher frequency of 12.9 MHz was used for analyses of Hydrogen and Helium, with peak widths of 0.1 amu (FWHM) for H_2 and Helium and 0.2 amu (FWHM) for the monatomic Hydrogen peak were obtained.

2.10 Alternative periodic voltage waveforms

QMFs are normally driven with an RF that is sinusoidal, but any time varying periodic waveform can be used [2]. For power sensitive applications and/or where small QMFs with integrated electronics are required, the ability to drive the electrodes with non-sinusoidal periodic waveforms maybe desirable [87]. Richards has shown the feasibility of using a periodic rectangular drive and the use of variable duty cycle to provide the mass scanning [88]. This removes the requirement to provide a closely matched ratio of RF to DC, replacing it with a variable timing parameter.

2.11 Conclusions

Whilst an extensive body of knowledge about the QMS and in particular the QMF exists there are specific areas where only limited information is available. Operation using stability zone 1 is the usual choice for the majority of manufacturers. There are

however certain demanding applications where the use of zone 3 provides the increased resolution and abundance sensitivity necessary.

Documented performance characteristics for zone 3 operation with hyperbolic and circular electrodes are very limited. For zone 1 operation an optimum value for r/r_0 is now widely accepted, no such value for zone 3 operation has been confirmed. The effects on performance of certain types of circular electrode displacements have recently been reported for zone 1 operation together with confirmation that using an unbalanced electrode drive can compensate for electrode displacement. Again, no similar information is yet available for zone 3 operation.

The use of stability zone 3 is emerging as a possible method of improving the limited performance envelope when operating with restricted length QMFs which are more likely when using micro-fabrication manufacturing techniques. Also associated with these manufacturing processes is the usage of rectilinear electrode profiles. Very little information about predicted performance for rectilinear electrodes for either stability zone 1 or zone 3 is available.

It is considered therefore that a better understanding of zone 3 operation and its associated performance sensitivities is an area that requires further investigation. At the same time the effects of electrode drive tolerances on achievable performance is another sphere requiring further investigation.

Chapter 3

3. QUADRUPOLE MASS FILTER

3.1 Summary

In this chapter the theory governing the ideal hyperbolic electrode QMF is introduced, together with the Mathieu stability diagram as an aid to understanding the operation and control of the QMF [2].

In practice it is more usual for QMFs to be constructed from non-hyperbolic (circular) shaped electrodes. Figure 3.1 shows the arrangement of electrodes for a circular electrode QMF [23]. The implications of using these '*non-ideal*' electrode geometries are discussed and the concept of multipoles is then introduced. To facilitate the calculation of ion trajectories in circular electrode QMFs, it is first necessary to solve the electric field within the QMF. One method of achieving this is

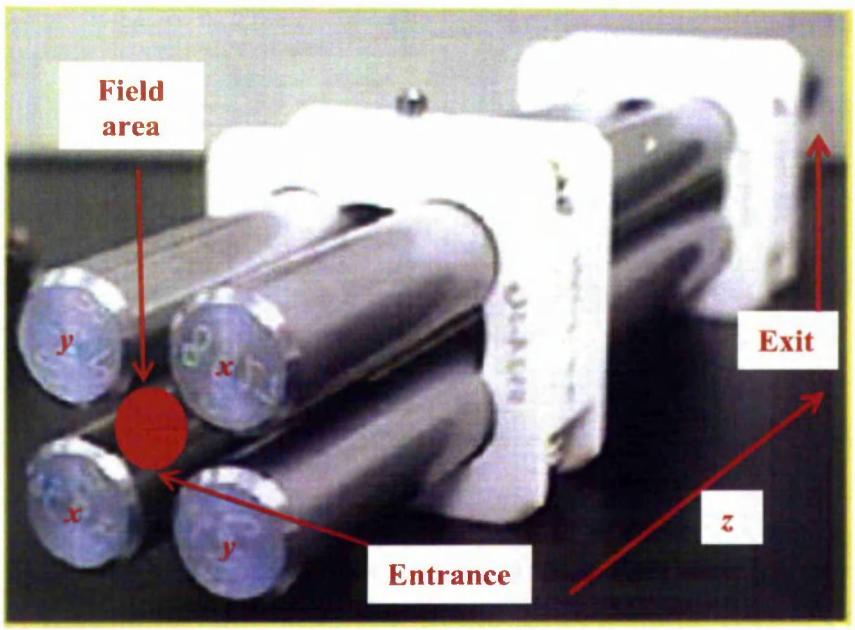

Figure 3.1. Photograph of a circular electrode quadrupole mass filter with the x and y electrodes, the central field area and ion entrance and exit positions identified. The outer enclosure has been omitted for clarity.

discussed, together with the numerical methods that are suitable for implementation in computer software. A public domain field solver program and the modules that have been used as part of this work are then reviewed. Finally, four custom computer programs that have been developed as part of this work are examined. These software packages provide tools for investigating the performance characteristics of hyperbolic and non-hyperbolic electrode QMFs.

3.2 Quadrupole Mass Filter

3.2.1 Hyperbolic electrodes

The ideal QMF would consist of a set of four hyperbolic profile electrodes of infinite size each one mounted on a side of an imaginary square to form a parallel array. In practice the closest approximation is obtained with finite sized hyperbolic electrodes as shown in Figure 3.2. With this electrode geometry, a quadrupole potential distribution in the central inter-electrode space is achieved by applying positive and negative potentials of equal magnitude to alternate electrodes [2], [89] and is defined by Equation (3.1)

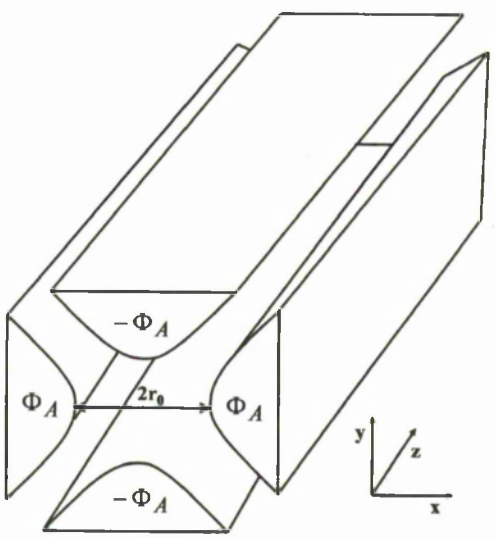

Figure 3.2. Hyperbolic electrode QMF arrangement showing applied potentials (see Equation 3.1).

$$\Phi(x,y) = \frac{\Phi_A(x^2 - y^2)}{2r_0^{\,2}} \tag{3.1}$$

where x and y define the position in the central aperture r_0 and Φ_A is the magnitude of the applied potential.

A quadrupole potential distribution produces an electric field that increases proportionally with increasing displacement from the central axis, and in the ideal case is independent in x and y, and invariant in the z axis and is defined by Equation (3.2).

$$E_x = \frac{\Phi_A x}{r_0^{\,2}}, \quad E_y = -\frac{\Phi_A y}{r_0^{\,2}} \tag{3.2}$$

where $E(x)$ and $E(y)$ are the electric field strengths for the x and y axes respectively, Φ_A is the magnitude of the applied potential to the x and y electrodes, r_0 is the field radius and x and y are the displacements from the central axis.

When Φ_A is a combination of a DC and an RF voltage as defined by Equation (3.3), the quadrupole potential distribution is still maintained while at the same time providing a time variant electric (electro-dynamic) field

$$\Phi_A = U - V\cos\omega t \tag{3.3}$$

where U is the DC component of the applied potential in Volts, V is the zero to peak amplitude of the applied RF potential in Volts, ω is the angular frequency of the RF in radians/secs and t is time in secs. With this applied composite potential the equations of motion for positive ions in the two axis are defined by Equations (3.4) and (3.5) [2], [89]

$$\frac{d^2x}{dt^2} + \frac{e}{mr_0^{\,2}}(U - V\cos\omega t) = 0 \tag{3.4}$$

$$\frac{d^2y}{dt^2} - \frac{e}{mr_0^2}(U - V\cos\omega t) = 0 \tag{3.5}$$

where e is the charge on an electron (1.602×10^{-19} C) [3] in Coulombs (C), m is the mass of the ion in atomic mass units (1 amu = 1.660538×10^{-27} kg) [90] and the remaining parameters are as previously stated. Equations (3.4) and (3.5) are in the canonical form of the Mathieu equation [27] as shown in Equation (3.6)

$$\frac{d^2u}{d\xi^2} + (a_u - 2q_u\cos(2\xi))u = 0 \tag{3.6}.$$

When $\xi = \frac{\omega t}{2}$ and the dimensionless Mathieu parameters a_u and q_u [2] are defined as follows

$$a_u = a_x = -a_y = \frac{8eU}{m\omega^2 r_0^2} \tag{3.7}$$

$$q_u = q_x = -q_y = \frac{4eV}{m\omega^2 r_0^2} \tag{3.8}$$

where u represents x or y and all other symbols are the same as previously defined.

By suitable rearrangement of Equations (3.7) and (3.8), the V and U voltages for a particular mass at an a_u and q_u value can be calculated by using Equation (3.9). This allows the Mathieu stability diagram to be transformed from a-q space to U-V space

$$V = \frac{q_u m\omega^2 r_0^2}{4e}, \quad U = \frac{a_u m\omega^2 r_0^2}{8e} \tag{3.9}.$$

The combination of the DC and periodically varying RF potential, produces differing time varying forces in the x and y direction. In the x-direction a net

repulsive force and in the y-direction a net attractive force is experienced by the positive ions. This combination results in the x-direction acting as a low pass mass to charge ratio filter and the y-direction acting as a high pass mass to charge ratio filter, producing a net band pass mass to charge ratio filter.

There are an infinite number of solutions to the Mathieu equation [27]. Each successive solution when applied to the QMF, results in the increasing magnitude of one or both of the Mathieu parameters [2], [27]. From Equation (3.9) it can be seen that as the Mathieu parameters a_u and q_u increase, there is a proportionate increase in the electrode voltages V and U. This imposes practical limitations on the suitability of these solutions because of the increasing operating voltages. The Mathieu stability diagram (see Figure 2.3) provides a convenient method of graphically presenting the theoretically stable and unstable operating zones. For an ion to successfully pass through the QMF, the ion must be stable in both the x and y direction, this occurs where the x and y stable regions overlap. Figures 3.3 shows the Mathieu stability diagram in more detail for zone 1 and figure 3.4 shows zone 3 in a similar level of detail.

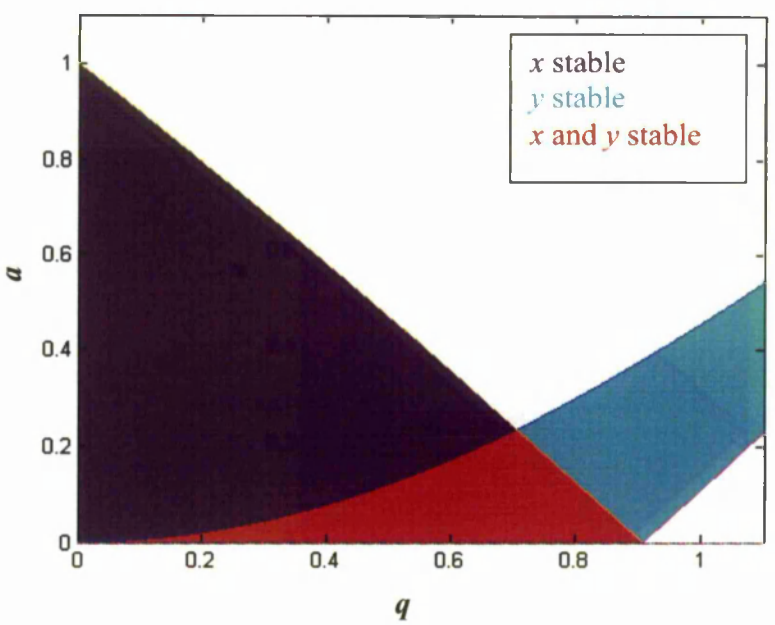

Figure 3.3. Detail of the Mathieu stability diagram showing areas of stable x, y and xy ion trajectories that form stability zone 1.

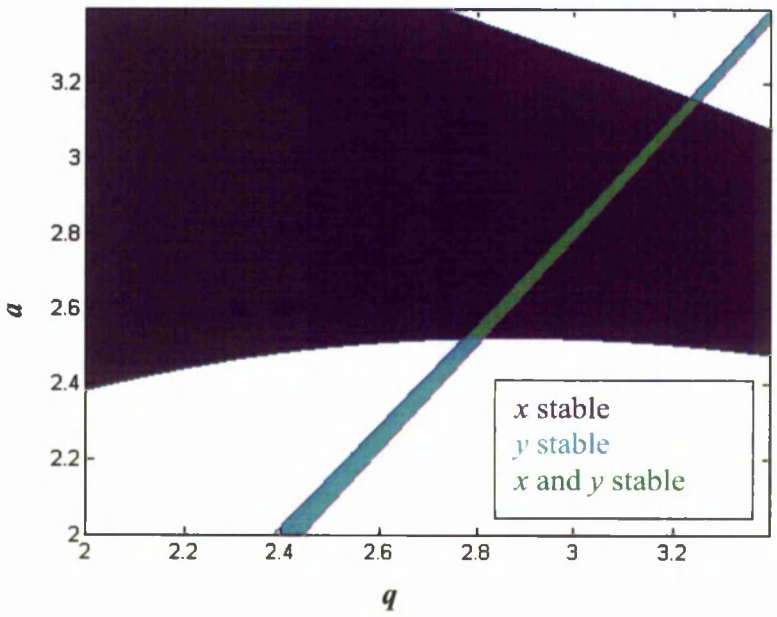

Figure 3.4. Detail of the Mathieu stability diagram showing areas of stable x, y and xy ion trajectories that form stability zone 3.

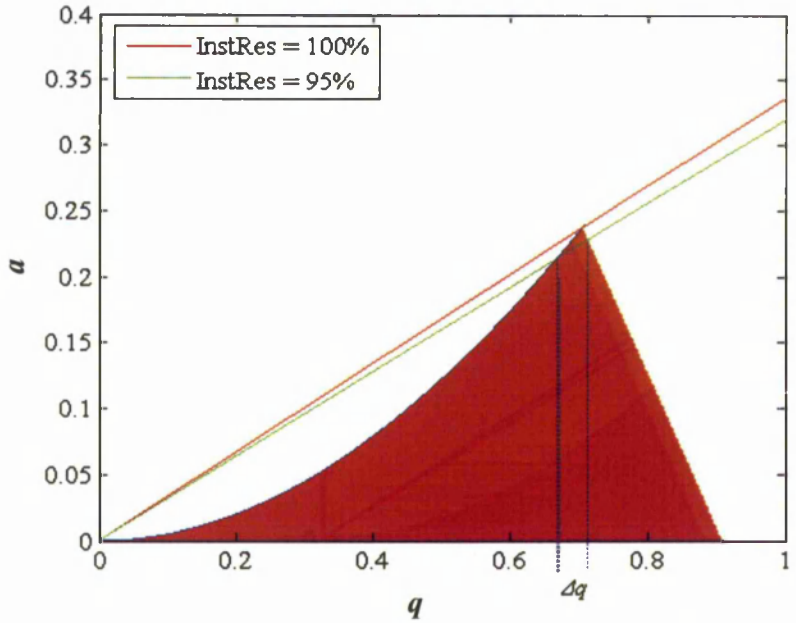

Figure 3.5. Mathieu stability diagram for zone 1 ($a_u \approx 0.237$, $q_u \approx 0.706$) with superimposed mass scan lines at two instrument resolution (*IntRes*) settings.

For practical mass filtering action the pass band of the QMF must be kept narrow in order to provide adequate species discrimination but not so narrow that insufficient ions are transmitted, resulting in inadequate ion detector signal current.

This trade-off between pass band and transmitted ions is achieved by varying the ratio of a/q. Increasing q, while keeping this ratio constant is termed a mass scan line. Figure 3.5 shows the approximately triangular zone 1 stability region, with two mass scan lines superimposed. The height of the stable area above the scan line gives a relative indication of the transmitted ions.

Instrument resolution (η) provides a convenient measurement [10] of the slope of the scan line and when equal to 100%, the scan line just touches the tip of the zone 1 stability region. By decreasing η, the slope of the scan line reduces, moving below the stability tip and increasing the pass band (Δq). This relationship can be seen in Equation (3.10),

$$a_{sl} = \eta \frac{a_{utip}}{q_{utip}} q_{sl} \tag{3.10}$$

where a_{sl} is the value of a at a particular value of q_{sl} on the scan line, a_{utip} is the value of a at the tip of the stability zone, q_{utip} is the value of q at the tip of the stability zone.

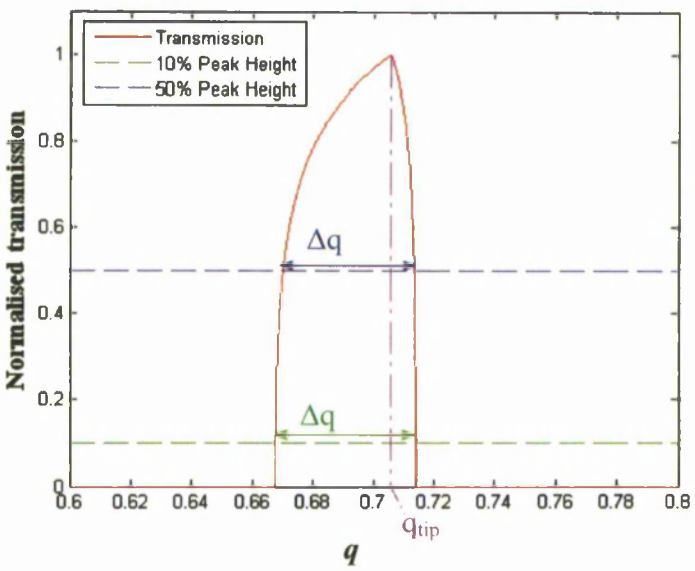

Figure 3.6. Normalised theoretical mass peak for an instrument resolution setting of 95% for operation in stability zone 1. Marker lines for Δq at 10% and 50% of peak height, and q_{tip} are also shown [91].

A theoretical indication of the mass peak for an instrument resolution of 95% (Figure 3.5) is shown in Figure 3.6. Observable in the figure is the narrowing peak width (Δq) with increasing amplitude. The Δq at 50% of peak height (Δq_{50}) is narrower than the Δq at 10% of peak height (Δq_{10}).

Mass resolution can be defined as $\frac{q_{tip}}{\Delta q}$ where Δq is measured at some percentage of the maximum peak height. More usually the resolution is quoted as the ratio $\frac{m}{\Delta m}$ which is effectively the same relationship scaled to the particular operating point of the instrument by (see Equation 3.11). This relationship indicates that as the mass is increased with a constant mass scan line slope, then the peak width Δm scales proportionally with m, producing constant mass resolution. Standard instruments are normally configured to operate with unit resolution i.e. Δm is 1 amu. This requires that the mass scan line is moved closer to the stability tip with increasing mass.

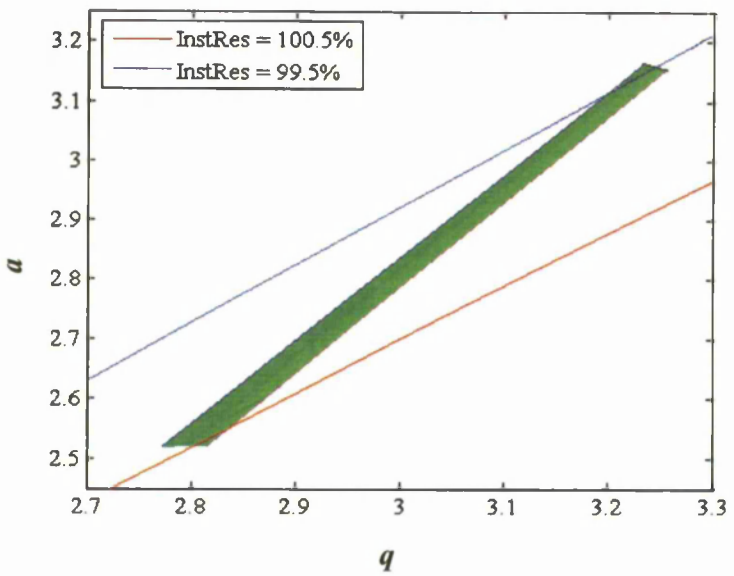

Figure 3.7. Mathieu stability diagram for zone 3 with superimposed mass scan lines at the lower and upper tips of the stability zone.

Similar mass scanning can be implemented with zone 3 where there are two tips that allow variable resolution control [59], [62], [92], the upper left hand tip ($a_u \approx 3.16$, $q_u \approx 3.23$) and the bottom right tip ($a_u \approx 2.52$, $q_u \approx 2.81$), and illustrated in Figure 3.7. It should be noted for the instrument resolution definition used above (see

Equation 3.9) values of η greater than 100% are needed to achieve a reduction in resolution at the lower tip of stability zone 3.

The instrument resolution control equation can be redefined in terms of U and V using Equation (3.11) [10]

$$U = \eta \frac{Va_{utip}}{q_{utip}} \tag{3.11}.$$

Alternatively the frequency for a given mass at a particular set of U and V voltages can be obtained by using Equation (3.12)

$$f = \sqrt{\frac{eV}{q_u m r_0^{\,2} \pi^2}} \tag{3.12}$$

where q_{utip} is the value of the Mathieu parameter at the tip of stability zone and U is set at a value to achieve the desired resolution.

These two sets of relationships enable the QMF to be mass scanned either by increasing the magnitude of the voltages U and V while keeping their ratio and the frequency constant. This is the method that is in common commercial usage and provides a linear relationship between the mass and voltages. Alternatively the frequency f can be decreased while keeping the magnitude of U and V constant. Frequency scanning exhibits a non-linear relationship between mass and frequency. Both these scanning methods allow successfully higher mass to charge ratio ions to pass through the QMF.

The achievable resolution for a QMF is determined by the number of RF cycles the ions experience on their passage through the QMF [37] and can be calculated using Equation (3.13)

$$\frac{m}{\Delta m} = \frac{1}{K} N_c^n \tag{3.13}$$

where N_c is the number of RF cycles experienced by the ions, m is the mass of the ion, Δm is the mass peak width at some percentage of the peak height. The constants K and n are dependent on the stability zone. For zone 1 a value of K $\approx$ 10 - 20 and n $\approx$ 2 has been found [93]. For zone 3, Titov found that the values for the constants K and n only hold for small values of N_c, and that for large values of N_c (> 100), $K \approx$ 0.5 and $n = 4/3$ [93] .

For voltage mass scanning, the number of RF cycles (N_c) experienced by the ions as they pass through the QMF increases with mass and is defined Equation (3.14)

$$N_c = Lf\sqrt{\frac{m}{2eE_{ion}}} \qquad (3.14).$$

Whereas for frequency mass scanning, the number of RF cycles experienced by the ions is independent of mass and is defined by

$$N_c = L\sqrt{\frac{V}{2q_u\pi^2 r_0^{\,2} E_{ion}}} \qquad (3.15)$$

where N_c is the number of cycles experienced by the ion, L is the length of the QMF in metres, E_{ion} is the energy of the ion in eV and the remainder of the parameters are as previously stated.

3.2.2 Non-hyperbolic electrodes

The use of circular electrodes enables manufacturing and assembly complexity to be minimised thereby reducing production costs. Figure 3.8 shows the end view of a QMF constructed from circular electrodes with the same drive potential as previously discussed. Circular electrodes produce a potential field distribution that degenerates from the quadrupole form and consists of a quadrupole term plus higher order terms [37], [94]. This is also true if the more general case of any shape electrodes is considered.

Whereas for the quadrupole term the resultant electric field component is linear with increasing displacement from the central axis, higher order terms produce non-linear electric field components. The multipole field can be represented by a multipole expansion [11] as defined in Equations (3.16) and (3.17),

$$\Phi(x,y) = \sum_{N=0}^{\infty} \frac{A_N \Phi_N}{r_o^N} \tag{3.16}$$

$$= \frac{A_0\Phi_0}{r_o^0} + \frac{A_1\Phi_1}{r_o^1} + \frac{A_2\Phi_2}{r_o^2} + \frac{A_3\Phi_3}{r_o^3} + ..+ \tag{3.17}$$

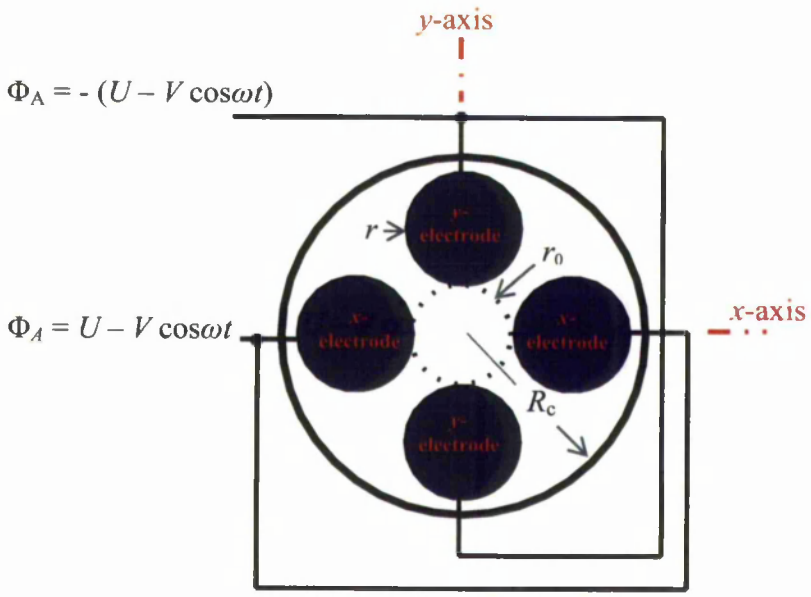

Figure 3.8. End section of a QMF constructed with circular electrodes where r is the radius of the electrodes, r_0 is the field radius, R_c is the radius of the enclosure.

where A_N is the amplitude of the multipole Φ_N consisting of 2N poles with A_0 Φ_0 defining the offset potential, A_1 Φ_1 defining the dipole potential, A_2 Φ_2 defining the quadrupole potential, A_3 Φ_3 defining the hexapole potential and continuing thereon. The electrode and drive voltage configuration of Figure 3.8 has two axis of symmetry and two of anti-symmetry and only multipole terms where $N = 4n + 2$ for $n = 0, 1, 2, 3, ..$ contribute to the field. For electrode configurations where electrodes are displaced or of different radii the degree of symmetry is reduced. These

geometrical imperfections will result in additional multipole terms being introduced and variations in the relative amplitudes of all the multipole components [38], [73].

3.3 Electric field solving - theory

3.3.1 Poisson and Laplace equations

To calculate the trajectories of ions in a QMF employing non-hyperbolic electrodes it is necessary to calculate the electric field for the area enclosed by the electrodes and in particular within the field radius r_0. Equation (3.18) shows Poisson's equation which enables a solution for an electrode structure to be obtained where volume space charge exists [95].

$$\nabla^2 V = -\frac{\rho}{\varepsilon_0} \tag{3.18}$$

If the area being considered is free of space charge then Poisson's equation simplifies to the Laplace equation as defined in Equation (3.19).

$$\nabla^2 V = 0 \tag{3.19}$$

For the case where the QMF electrodes are invariant in the z-axis and ignoring fringing fields at the entrance and exit of the QMF then Equation (3.20) is obtained. This represents the 2-D version of Laplace's equation which is an example of a second order partial differential equation (PDE). It is possible to solve this class of equation by analytical [95] or numerical methods [96].

$$\frac{\partial^2 V}{\partial x^2} + \frac{\partial^2 V}{\partial y^2} = 0 \tag{3.20}$$

3.3.2 Finite Difference Method

The finite difference method (FDM) [95], the finite element method (FEM) [97] and the boundary element method (BEM) [98-99] are all accepted methods for solving Laplace's equation. In this thesis, only the FDM method will be considered. The Finite Difference Method (FDM) is an iterative numerical method which relies on dividing the free space contained within the electrode system into a grid or mesh, commonly termed '*meshing*'. For the purposes of explaining the methodology of the process, the shape of the individual mesh elements are unimportant but commonly in commercial systems they are triangular as any polygonal region can be triangulated [100].

Figure 3.9 shows a small area of a 2-D potential field V. The potential gradient at a point on a grid line between two intersecting grid lines can be approximated to by the Equations (3.21) and (3.22).

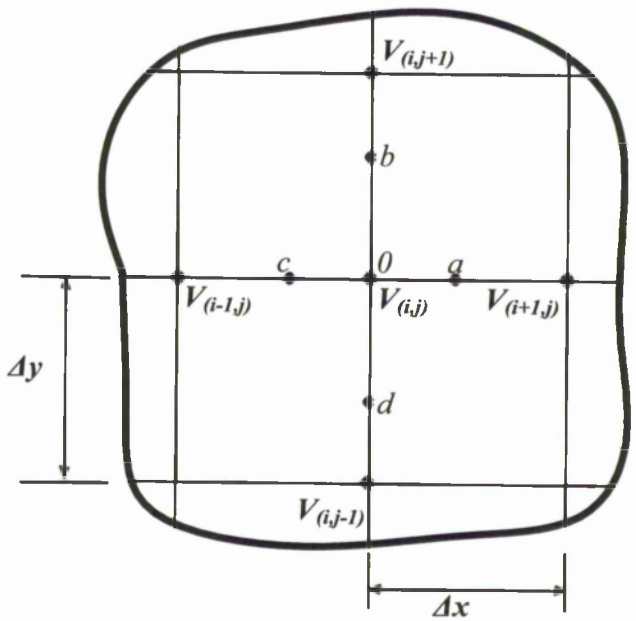

Figure 3.9. A small portion of a discretised region containing a 2-D potential field.

$$\left.\frac{\partial V}{\partial x}\right|_a \approx \frac{V_{(i+1,j)} - V_{(i,j)}}{\Delta x} \tag{3.21}$$

$$\left.\frac{\partial V}{\partial x}\right|_c \approx \frac{V_{(i,j)} - V_{(i-1,j)}}{\Delta x} \tag{3.22}$$

$$\left.\frac{\partial^2 V}{\partial x^2}\right|_0 \approx \frac{\left.\frac{\partial V}{\partial x}\right|_a - \left.\frac{\partial V}{\partial x}\right|_c}{\Delta x} \approx \frac{V_{(i+1,j)} + V_{(i-1,j)} - 2V_{(i,j)}}{\Delta x^2} \tag{3.23}$$

and

$$\left.\frac{\partial^2 V}{\partial y^2}\right|_0 \approx \frac{\left.\frac{\partial V}{\partial y}\right|_b - \left.\frac{\partial V}{\partial y}\right|_d}{\Delta y} \approx \frac{V_{(i,j+1)} + V_{(i,j-1)} - 2V_{(i,j)}}{\Delta y^2} \tag{3.24}$$

Letting $\Delta x = \Delta y = h$

$$\frac{\partial^2 V}{\partial x^2} + \frac{\partial^2 V}{\partial y^2} \approx \frac{V_{(i+1,j)} + V_{(i,j+1)} + V_{(i-1,j)} + V_{(i,j-1)} - 4V_{(i,j)}}{h^2} = 0 \tag{3.25}$$

As $h \rightarrow 0$ the following becomes true:

$$V_{(i,j)} = \frac{1}{4}(V_{(i+1,j)} + V_{(i,j+1)} + V_{(i-1,j)} + V_{(i,j-1)}) \tag{3.26}$$

An iterative process can be represented by Equation (3.27) which shows that the value of V(i,j) at step $(n + 1)$ is the average of the four grid point potentials that surround it at step (n). Using this, the sequence is repeated until the change in value between step n and n+1 is within acceptable limits. This method is commonly known as the Jacobian Iteration [97].

$$V_{(i,j)}^{(n+1)} = \frac{1}{4}(V_{(i+1,j)}^{(n)} + V_{(i,j+1)}^{(n)} + V_{(i-1,j)}^{(n)} + V_{(i,j-1)}^{(n)}) \tag{3.27}$$

A quicker convergence can be obtained with the Gauss-Siedel [97] method which is shown in Equation (3.28).

$$V_{(i,j)}^{(n+1)} = \frac{1}{4}(V_{(i+1,j)}^{(n)} + V_{(i,j+1)}^{(n)} + V_{(i-1,j)}^{(n+1)} + V_{(i,j-1)}^{(n+1)}) \tag{3.28}$$

A much increased convergence rate can be achieved through the use of successive point over relaxation (S.O.R.) which is the method adopted in the Poisson/Superfish suite of software [101] and is defined in Equation (3.29).

$$V_{(i,j)}^{(n+1)} = (1-\alpha)V_{(i,j)}^{(n)} + \alpha V_{(i,j)}^{(*)} \tag{3.29}$$

where α is termed the relaxation parameter and $\alpha V_{(i,j)}^{(*)}$ is an intermediate term calculated using Equation (3.27) or (3.28). Whereas the previous methods require approximately N^2 iterations, the SOR method requires approximately N iterations providing a significant improvement in operational speed [97].

3.4 Electric field solving - software

Poisson/Superfish [102] are a public access suite of programs for solving a range of magneto-static problems. They were originally written by R. F. Holsinger in collaboration with K. Halbach for particle accelerator design. Three modules from the Poisson/Superfish suite were used when undertaking this computer simulation work; Automesh, Poisson and SF7. Figure 3.10 illustrates the operational flow path and the use of the binary solution file for passing intermediate results between the various modules. Wsfplot, a utility program provided within Poisson/Superfish, was also used to generate check plots and the Figures. 3.11 and 3.12.

Automesh provides for the problem geometry; material electrical characteristics, electrode voltages and meshing grid pitch to be defined in a text file (see Appendix A). Geometric models were created for the range of electrode geometries that have been investigated. Automesh divides the free space between the electrodes and the problem boundary (a circular enclosure forms the problem boundary of the circular electrode QMFs considered) into a 2-D triangular grid. Figure 3.11 shows a plot of a

low resolution discretisation of a QMF with the triangles that comprise the meshed area visible.

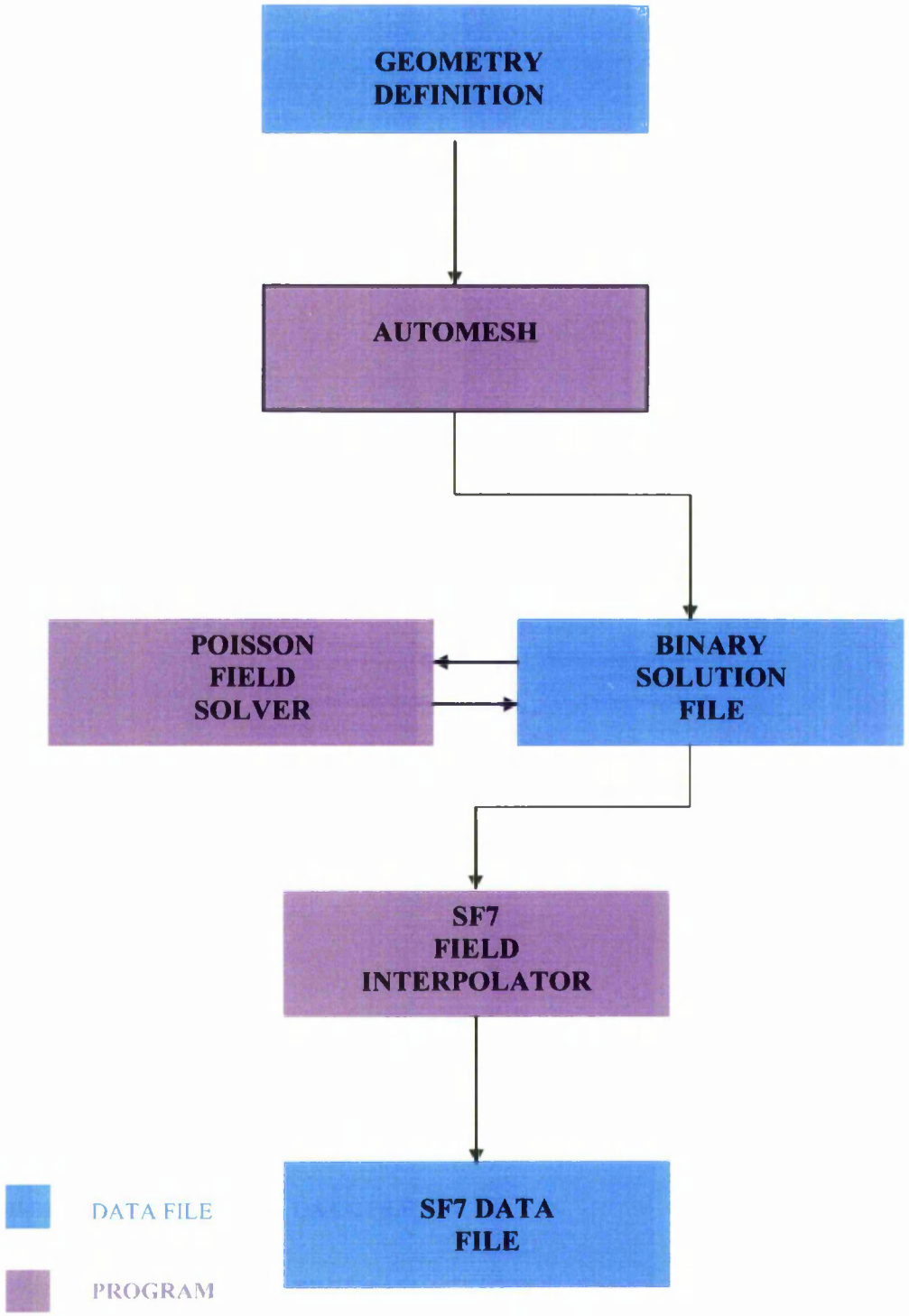

Figure 3.10. Poisson/Superfish operational flow chart.

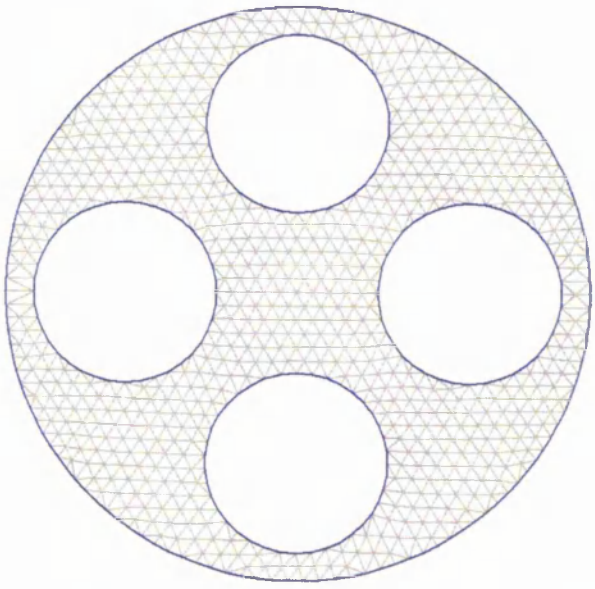

Figure 3.11. Automesh plot showing mesh triangles with a low resolution mesh used for clarity.

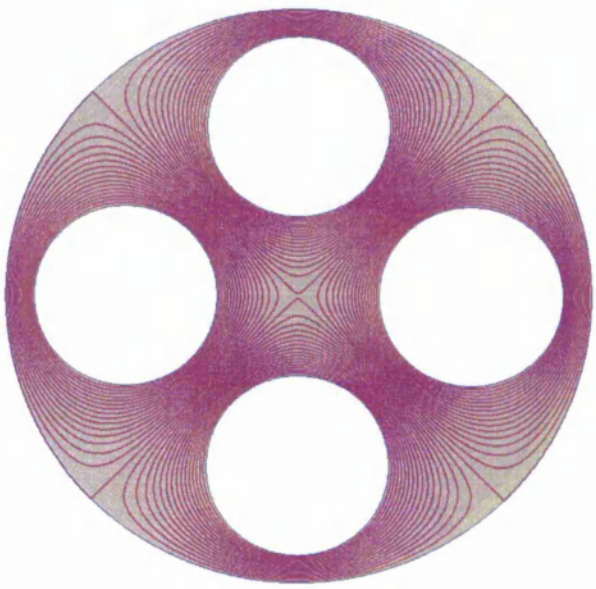

Figure 3.12. Poisson plot showing equipotential field contours.

The field interpolator program SF7, is used to process the Poisson field data to produce a user defined rectangular grid of electric field values. The resultant electric field values are written to a new SF7 data file. Figure 3.13 shows the SF7 GUI with the user control parameters entered.

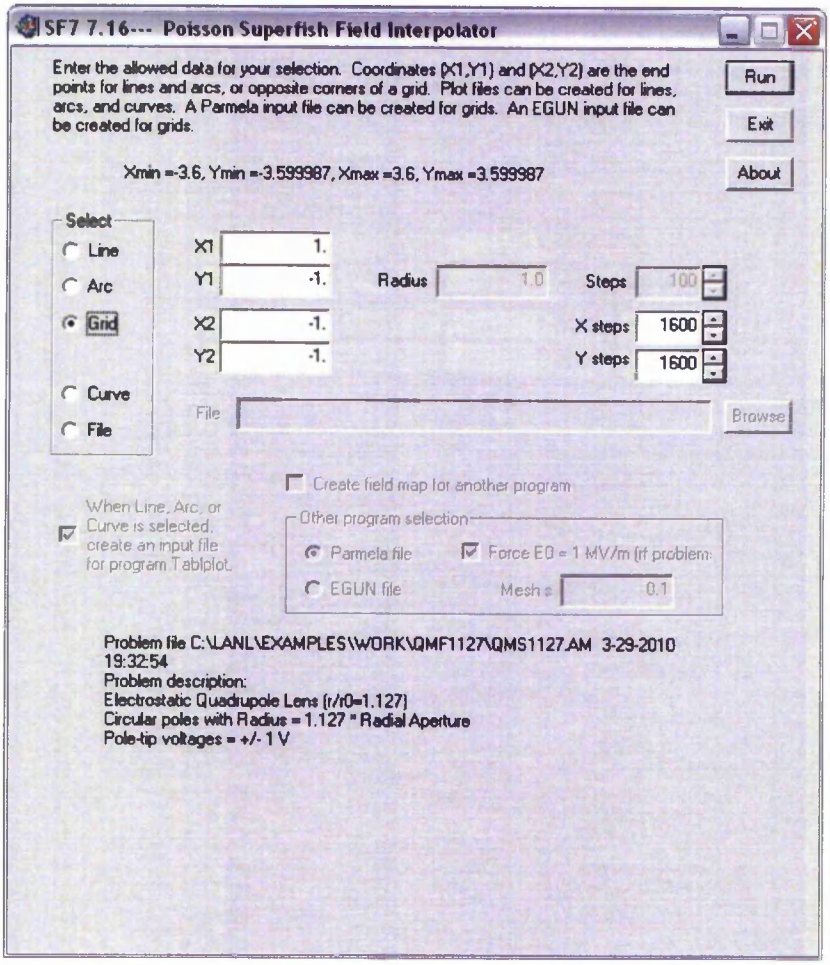

Figure 3.13. Poisson/Superfish SF7 field interpolator GUI.

The resultant SF7 data file was then processed by a custom developed post-processor FieldCalc program, to format the data to the same standard as previously reported field files [43] enabling comparison and validation of the processes used.

3.5 Ion trajectory simulation software

3.5.1 Overview

Previously reported results [4], [43] have utilised custom software developed in a legacy version of the Microsoft development environment (Visual C++ 6.0). It was considered timely to develop a new suite of programs using initially Microsoft Visual Studio.Net 2003 development environment, then Microsoft Visual Studio

2005. Advantages of this undertaking were the ability to provide greatly enhanced user controls through an extensive graphical user interface (GUI). This GUI facilitated the easy configuration of control parameters and in the case of the ion trajectory programs, display of both mass spectra and individual ion trajectories. Further advantages were the provision of a range of output reports enabling post processing by Matlab for the generation of mass spectra and ion trajectory spatial power frequency graphs. The QMS2 suite of programs consists of an ion source program and three ion trajectory simulation programs.

The ion source generation program QMS2-ION (QMS2-I) is based closely on the program first reported by Gibson et al [10]. It has been rewritten where necessary for compatibility with later Microsoft development environments with some additional functionality added. The two major variants of the ion trajectory simulation software are called QMS2-Hyperbolic (QMS2-H) and QMS2-Field (QMS2-F), used for the simulation of hyperbolic and non-hyperbolic electrode QMFs respectively. For QMS2-F the ability to utilize field files produced by Poisson/Superfish has improved computation times and enabled asymmetric electrode geometries to be efficiently handled. A further simulation program QMS2F-H was developed, this is a modified form of QMS2-H enabling frequency scanning of hyperbolic electrode QMFs to be investigated. It is not mentioned in any more detail in this chapter as it is operationally virtually identical to QMS2-H.

The design philosophy applied to the specification and development of these programs has been to keep as near as possible the same GUI for all the versions of the ion trajectory software, thereby minimising the users learning curve when moving between different programs.

3.5.2 QMS2-Ion

A GUI is provided to allow the user to control the physical and operating characteristics of the ion source. Additional facilities have been added to allow automatic generation of ion files for a range of values of a selected parameter (parametric). The ion source generation program generates the entry conditions for a large number of ions, 10^6 being the default value. User control is provided for larger numbers of ions to be generated ($>10^7$), this being added to support further research. Figure 3.14 shows the QMS2-I GUI with parameter entry fields for the source radius,

nominal energy, energy spread and beam spread visible. In the example of the GUI shown the parametric sweep facility has been enabled for the ion energy parameter.

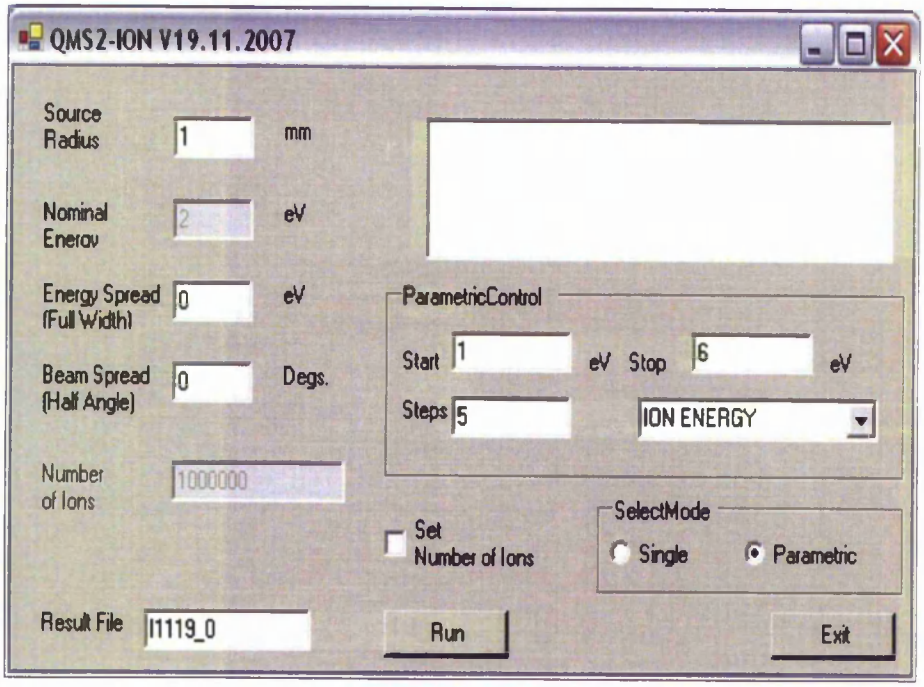

Figure 3.14. QMS2-Ion graphical user interface.

The spatial entry conditions for the ions are bounded by the user defined source radius, with each ion entry point being completely random with respect to every other, generating a top hat profile for the ion beam. The ion beam is symmetrical about an origin which aligns with the central axis of the QMF. There is no provision within QMS2-I for introducing mechanical misalignments between the ion source and the QMF, this functionality is provided by the QMS2 ion trajectory simulation programs. The user can also specify a random spread in ion energy and a beam spread. The ion entry conditions generated by each run cycle are written to a separate ion file, which provide the ion entry conditions to the ion trajectory simulation software.

3.5.3 QMS2-Hyperbolic

The QMS2_H program simulates the ion trajectories of a large number of ions enabling the performance of hyperbolic electrode QMFs to be characterised. Figure 3.15 shows the program's GUI which provides the user the ability to control the operational window of the QMF being investigated. As reported by Gibson and Taylor [10], much earlier simulation work relied on characterisation of the QMF based on a relatively small ensemble of ions and they suggested that a much greater number of ions were required to isolate more subtle performance characteristics. In producing these programs those previous comments have been noted and the facilities to handle a much greater number of ions have been provided. A large number of ion trajectories ($>10^6$) can be computed at each mass step of the specified mass scan range and within practical limits the mass scan step size is unbounded.

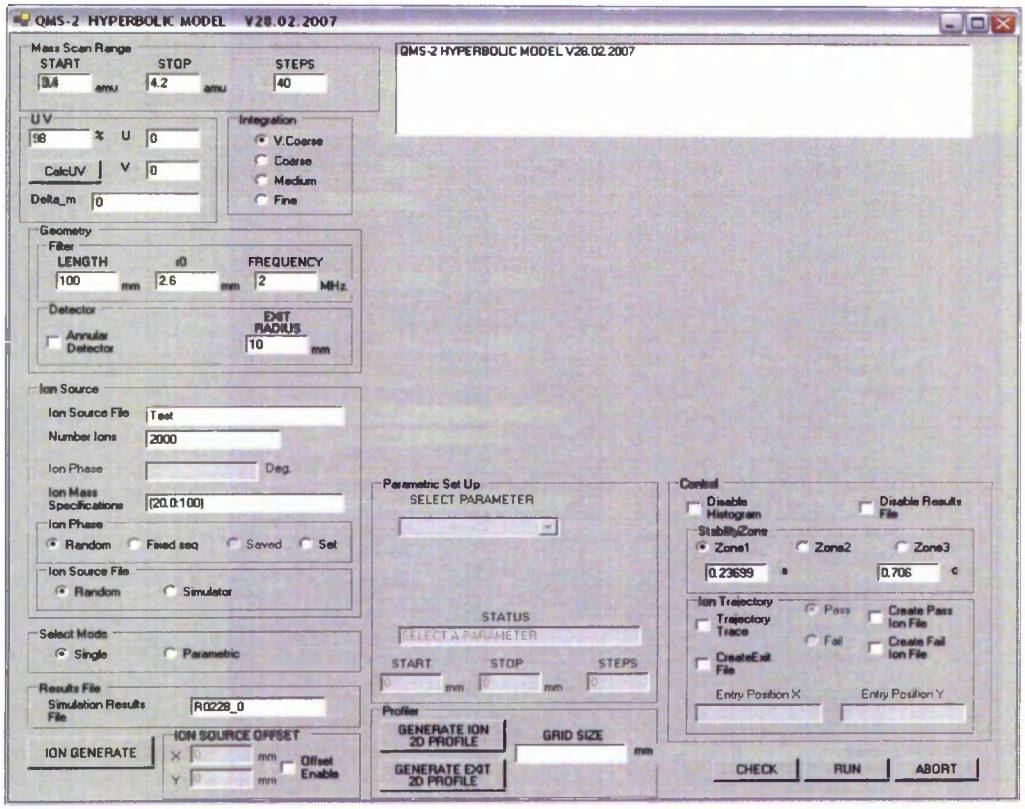

Figure 3.15. GUI for the QMS2-Hyperbolic program

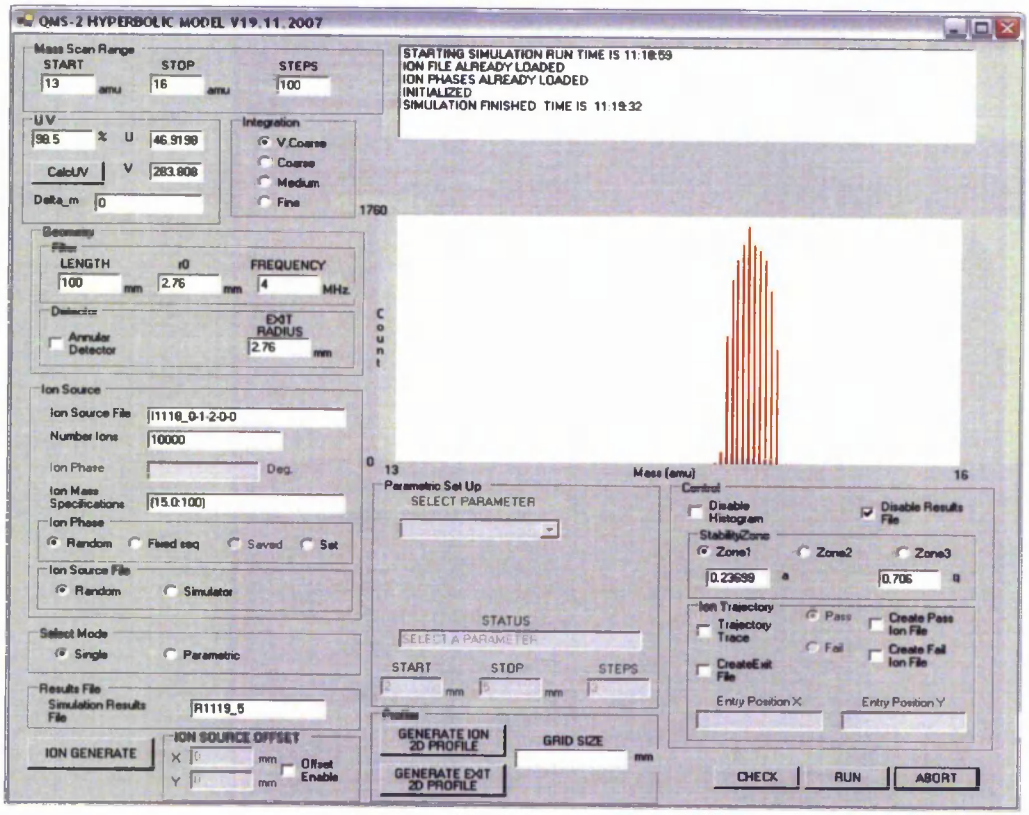

Figure 3.16. QMS2-Hyperbolic graphical user interface showing the result of a mass scan simulation.

The spatial entry condition of each ion together with its velocity in the three axes x, y and z are read from the specified ion file. The phase of the ion with respect to the RF electrode potential is controlled by the program and in the default setting this is totally random. The ion trajectory as it progresses through the QMF is calculated by solving the Mathieu equation using a fourth order Runge-Kutta algorithm for the x and y axis independently. The core Runge-Kutta routine is largely based on previous software developed at the University of Liverpool [10] with the remainder of the software being specifically developed for this project.

Ions are deemed to have successfully passed through the QMF if they do not exceed the r_0 of the QMF and their position at the end of the QMF falls within the radius or annular portion of the detector. If the ion is successful, the total successful ion count is incremented. At the completion of the simulation cycle for each mass

scan step, the mass and the total successful ion count are written to a results file and if enabled the mass spectra on the GUI is updated (see Figure 3.16).

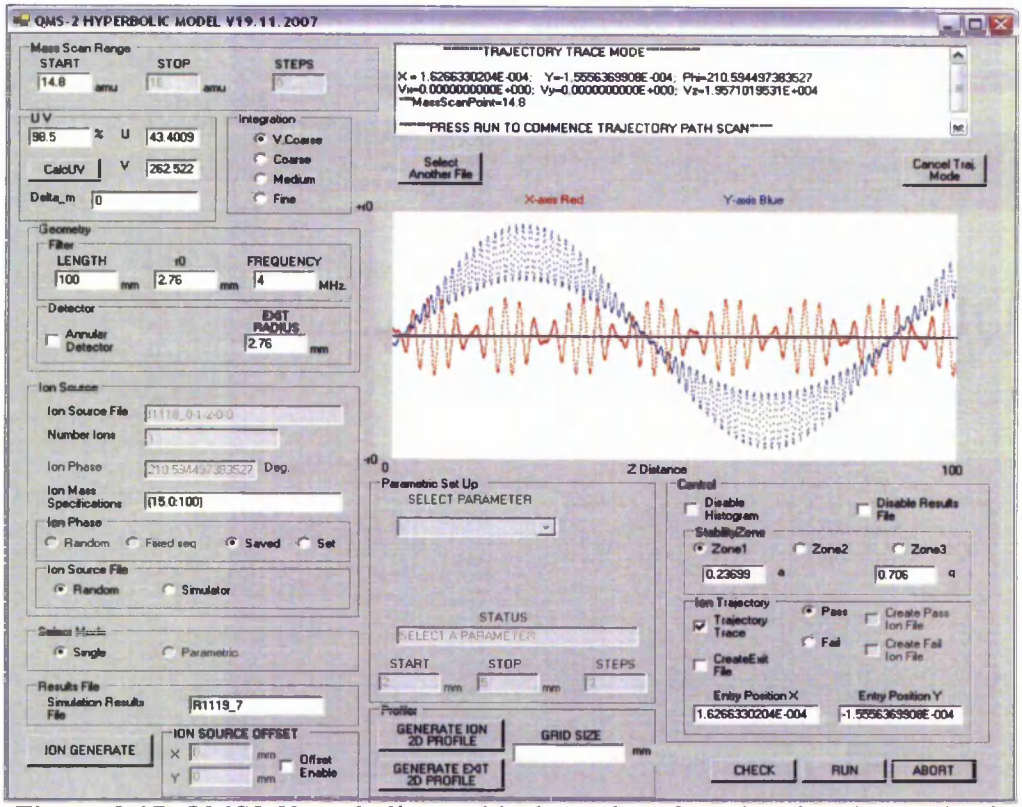

Figure 3.17. QMS2-Hyperbolic graphical user interface showing the result of an individual ion trajectory simulation.

The user interface provides controls for the generation of additional ion files which contain the initial conditions for each successful and/or unsuccessful ion of the mass scan. The program also supports the simulation and display of individual ion trajectories (see Figure 3.17) enabling the effects of phase entry position and operating point to be investigated with an immediate indication viewable on the GUI. The spatial position of the ion as it progresses through the QMF can be saved to a file. The text box above the ion trajectory window contains the initial conditions for the ion trajectory being displayed.

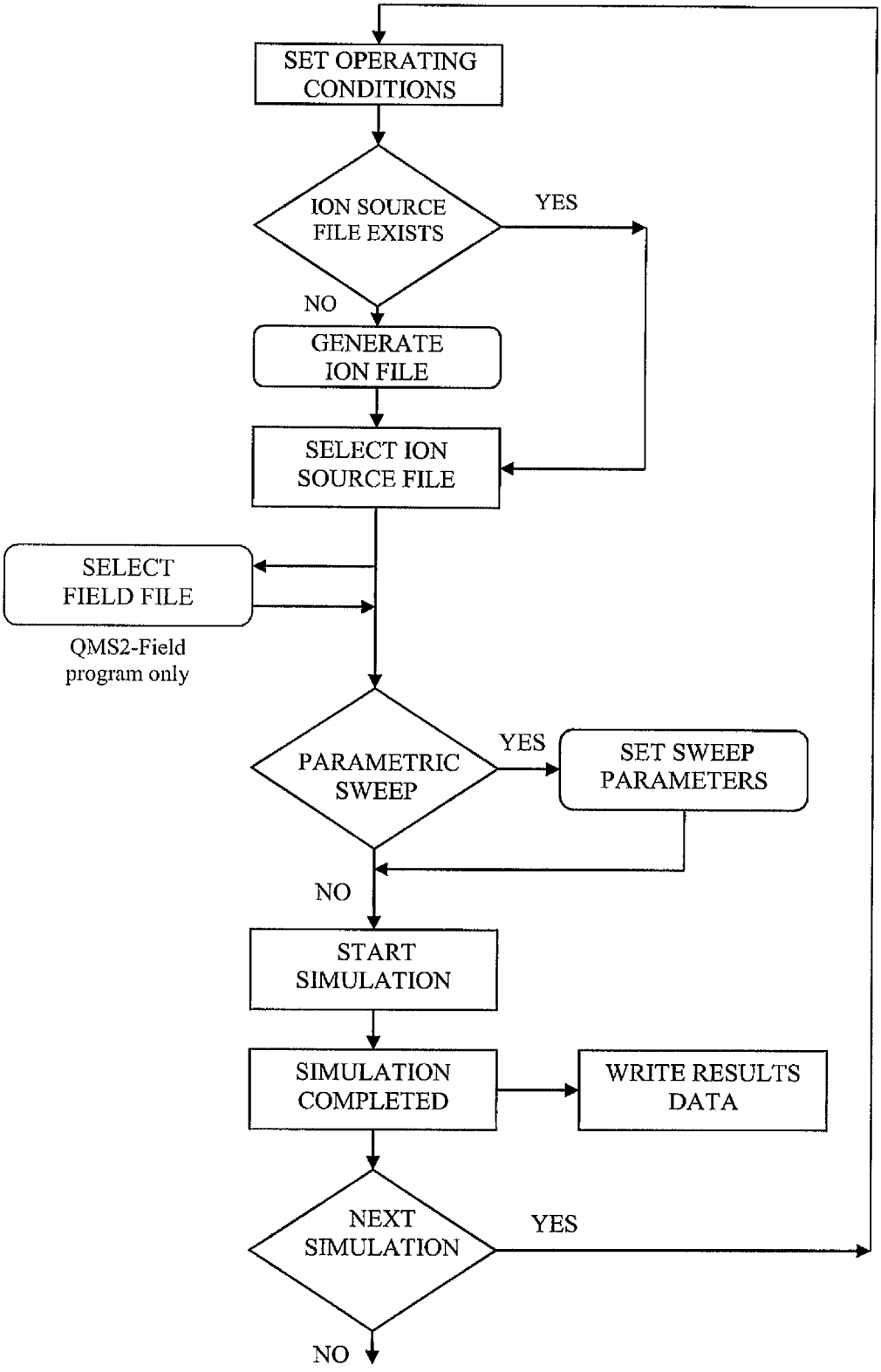

Figure 3.18. Operational flow chart for QMS2- Hyperbolic and QMS2-Field programs.

For extended simulation a parametric sweep facility is provided allowing a large number of simulations to be undertaken without user intervention. At completion of each mass scan a user selected parameter is incremented by a defined amount and the next mass scan is commenced. An operational flow chart for the QMS2 ion trajectory programs is provided in Figure 3.18.

3.5.4 QMS2-Field

Ion trajectories for QMFs constructed from circular and other shaped electrodes were simulated using QMS2-F. This is a completely new custom program developed

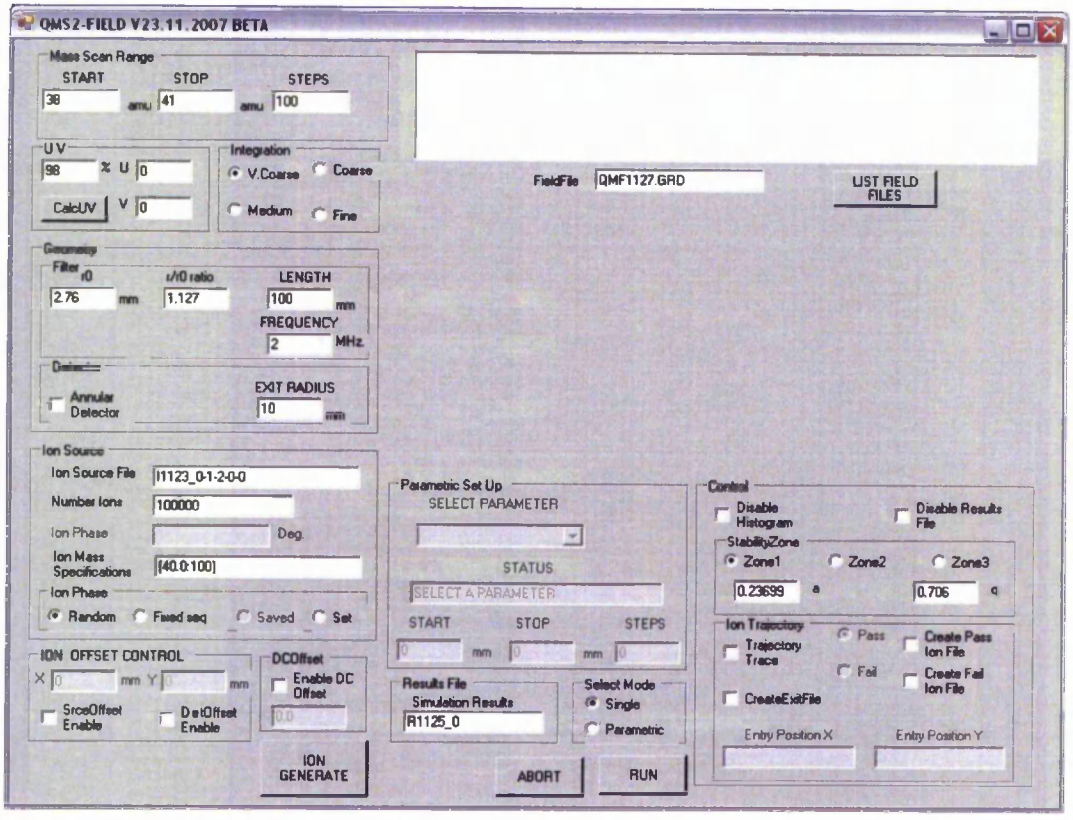

Figure 3.19. GUI for QMS2-Field program

by the author as part of the research work reported in this thesis. It was developed in the Visual Studio C++. NET and Visual Studio 2005 development environments using managed C++. Figure 3.19 shows the GUI for QMS-Field. It is very similar to

QMS2-Hyperbolic GUI but with additional fields to accommodate differences in control requirements such as field file selection.

The handling of the ion source simulation through the use of pre-generated ion source files is the same as for QMS2-H. The display of mass spectra and individual ion trajectories is also the same and GUI displays of these are not repeated in this section. The major difference between the QMS2-H and QMS2-F is the method of calculating the ion trajectories.

3.5.4.1 Ion trajectory calculation

Assuming that the geometry is consistent throughout the length of the QMF and ignoring the effects of fringing fields the 2-D field model used in Poisson/Superfish can be used in calculating the ion trajectories. A further assumption is made, that the x and y fields are uncoupled; this is valid if small incremental movements of the ion are considered. With these assumptions the ion trajectories for circular and other shaped electrodes were calculated by solving the following pair of equations.

$$m\frac{\partial^2 x}{\partial t^2} = -e\frac{\partial \Phi_{(x,y)}}{\partial x} \tag{3.30}$$

$$m\frac{\partial^2 y}{\partial t^2} = -e\frac{\partial \Phi_{(x,y)}}{\partial y} \tag{3.31}$$

where e is the charge on the ion, $\frac{\partial \Phi_{(x,y)}}{\partial x}$ is the instantaneous electric field strength E_x at the ions position (x, y), $\frac{\partial \Phi_{(x,y)}}{\partial y}$ is the instantaneous electric field strength E_y at the ions position (x, y).

These equations for ion motion are solved using a fourth order Runge-Kutta algorithm. To ensure that the assumption of small incremental movements of the ion is achieved, the incremental time step for successive evaluation of the Runge-Kutta algorithm is kept small. The values for the time interval were arrived at by

undertaking a number of mass scans and comparing the results. A value for the time increment of 150.1 steps for an RF period was found to more than adequate to satisfy this requirement. The software does make provision for varying the time step size through the integration control, and when set at the lowest value, 75.1 steps for an RF period is used. At the highest of the four available integration settings, the number of time steps is 300.1 for an RF cycle. The non-integer values for the step sizes are to avoid beat effects [103].

3.5.4.2 Field file

The SF7 field interpolator (see section 3.4) was used to create a 1600 x 1600 square grid of electric field values for the central field area between the electrodes from the data contained in the binary results file created by Poisson. Figure 3.20 shows the end view of a circular electrode QMF. The corner points of the square grid are x_1y_1, x_2y_2, x_3y_3, x_4y_4 as shown in the figure.

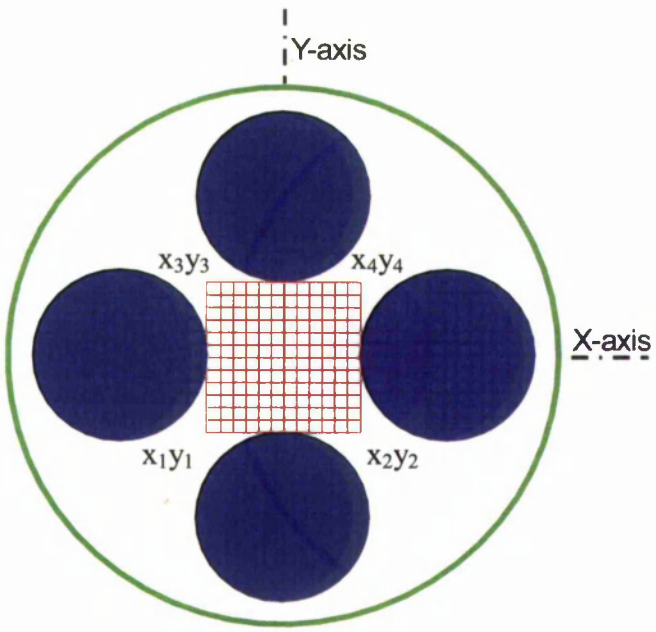

Figure 3.20. End section of circular electrode QMF showing electric field grid.

The custom utility program FieldCalc was then used to format the data suitable for use by QMS2-F. FieldCalc was also used to generate field files analytically for hyperbolic electrode QMFs.

The electric field values E_x and E_y provided by Poisson are calculated for unit voltage applied to the electrode pairs, positive to the x-axis electrodes and negative to the y-axis electrodes. For ions that are not directly on a grid point, the actual value for the electric field is calculated using bilinear interpolation [104]. The values of E_x and E_y at the ions position are then multiplied by the instantaneous voltage of the RF and DC combination that is applied to the electrodes, thereby obtaining the actual instantaneous electric field values.

3.6 Runge-Kutta algorithm

To calculate the ion trajectories for both hyperbolic and non-hyperbolic electrode QMFs, it is necessary to solve second order ordinary differential equations (ODE) with known initial values. These equations can be reduced to first-order differential equations by suitable manipulation. Numerical integration methods provide a computer compatible procedure to obtain solutions to the above class of differential equation, and the fourth-order Runge-Kutta formula (see Equation 3.32) is an accepted numerical integration method [104], [105].

$$y_{n+1} = y_n + \frac{1}{6}(k_1 + 2k_2 + 2k_3 + k_4)s \tag{3.32}$$

where

$$k_1 = f(x_n, y_n)$$
$$k_2 = f(x_n + \frac{1}{2}s, y_n + \frac{1}{2}k_1 s)$$
$$k_3 = f(x_n + \frac{1}{2}s, y_n + \frac{1}{2}k_2 s)$$
$$k_4 = f(x_n + s, y_n + k_3 s)$$

and s is the integration step size.

Appendix B contains example code for the implementation of the Runge-Kutta method for the QMS2-F program.

3.7 Software validation

Validation of QMS2-H was undertaken by comparison of mass spectra obtained with previously reported simulation software [10] and by examination of individual ion trajectories with typical published data for zone 1 [9] and zone 3 [6]. QMS2-F validation was undertaken in two stages. Firstly an analytically generated field file was used in conjunction with the program to simulate mass spectra. These mass spectra were compared with ones simulated by QMS2-H and close correlation of the two was observed (see Figure 3.20). The second stage compared mass spectra obtained when using a field file created by a previous field solver [4] with one generated with Poisson/Superfish. Figure 3.21 shows the result of these simulations.

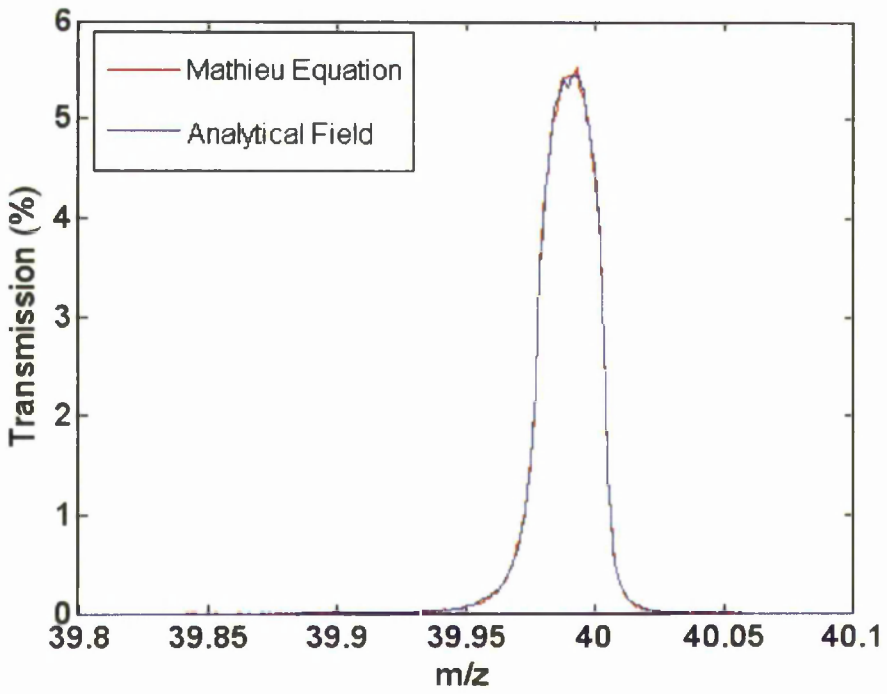

Figure 3.21. Mass spectra for operation in zone 1 with hyperbolic shaped electrodes using the QMF2-H and QMS2-F simulation programs.

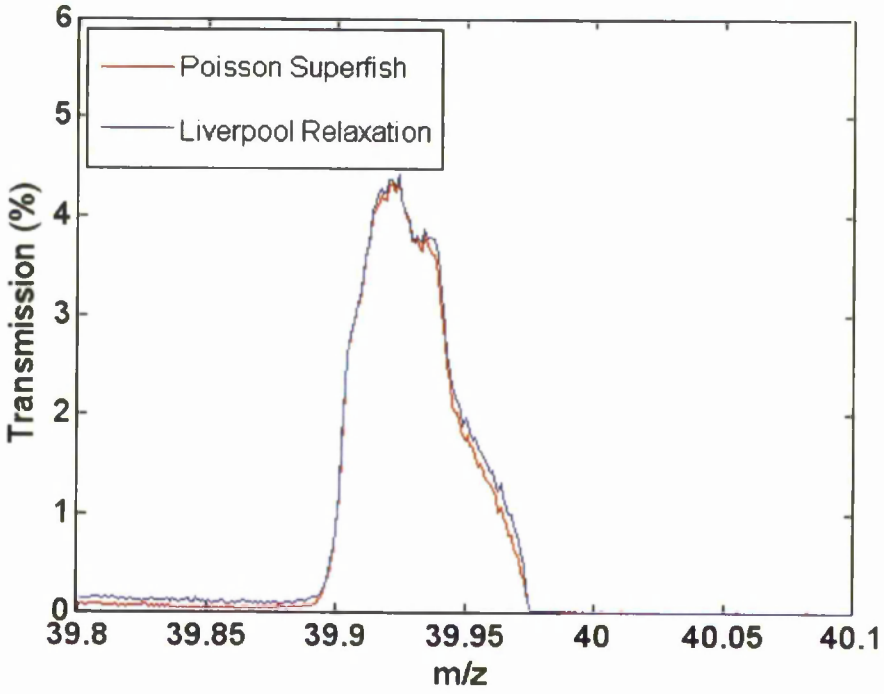

Figure 3.22. Mass spectra for operation in zone 1 with circular shaped electrodes using the QMS2-F simulation program for two differently derived field files.

QMF PARAMETER	CONDITION
Length	254 mm
r_0	2.76 mm
Frequency	2 MHz
Detector radius	2.76 mm
Housing radius	$3.6 \times r_0$
Ion Source	
Ion energy	2.00 eV
Ion source radius	0.5 mm
Ion energy spread	0
Ion angular spread	0
Operating point	
a_{tip} (zone 1)	0.237
q_{tip} (zone 1)	0.706
Instrument resolution (η)	0.9995
Ion species	Argon (40 m/z)

Table 3.1. Test conditions for simulations contained in Figures 3.22 and 3.23.

The two simulations exhibit very similar characteristics, corresponding to results obtained by Taylor and Gibson [49]. The test conditions employed for the two comparative tests shown in Figures 3.21 and 3.22 are contained in Table 3.1.

3.8 Ion motion

The ion motion is oscillatory as it traverses the RF field of a QMF, consisting of a dominant secular oscillation (low frequency) modulated by micro-motion (high frequency oscillation) [94]. The component frequencies are determined by the value of β_x and β_y at the operating point. Equation (3.33) was used for calculating the spatial frequencies for zone 1:

$$\Omega_{Z1un} = (2n + \beta_u)\frac{\omega}{2} \tag{3.33}$$

where Ω_{Z1un} is the set of secular spatial frequencies for $u = x$ or y, $n = 0, 1, 2, 3$ the frequency ranking, $\beta_u = f(a_x, q_x)$ or $f(a_y, q_y)$ and ω = RF excitation angular frequency.

For zone 3 the fundamental frequency at the upper stability tip are defined by Equations (3.34) and (3.35) [62]:

$$\Omega_{Z3x} = (2 - \beta_x)\frac{\omega}{2} \quad \text{for } 1.5 \leq \beta_x < 2 \tag{3.34}$$

$$\Omega_{Z3y} = \beta_y \frac{\omega}{2} \qquad \text{for } 0 \leq \beta_y < 0.5 \tag{3.35}.$$

The values of β for zone 1 and 3 can be calculated from formulae quoted in Dawson [2] or March [94] and from published tables [106].

3.9 Discrete Fourier transform

The ion trajectories generated by the QMS2-H and QMS2-F programs are in the time domain. Applying the Discrete Fourier Transform (DFT) [107] as shown in

Equation (3.36) to these trajectories it is possible to obtain the relative spatial power frequency components of the these trajectories.

$$X(m) = \sum_{n=0}^{N-1} x(n) e^{-j2\pi nm/N} \tag{3.36}$$

where Xm is the m^{th} DFT component and xn is the discrete sequence of time domain sampled values.

The ion trajectory power frequency spectra were obtained by first simulating a single-ion trajectory and saving the discrete xy coordinates for each incremental time step to a results file. A custom MatLab script was written which uses the MatLab DFT and PLOT functions to generate the relative power frequency spectra for the x and y ion trajectories held in the results file.

3.10 Conclusions

A combination of public domain and custom developed software has been developed which provides the toolset for the investigation of the performance characteristics of hyperbolic and non-hyperbolic electrode QMFs. In the next two chapters this toolset will be utilised to investigate the behaviour of the '*ideal*' QMF, and QMFs that are constructed from circular and more novel electrode geometries.

Chapter 4

4. PERFORMANCE CHARACTERISTICS OF NON-IDEAL QMFs

4.1 Introduction

Non-ideal QMFs are classed as QMFs which are constructed from any electrode profile other than hyperbolic or QMFs whose electrode arrangement exhibit some form of imperfection such as asymmetries in their electrode geometry [38], [108]. In this chapter only QMFs constructed from circular electrodes are considered.

Firstly the effects of the ratio r/r_0 on QMF performance is investigated for operation in stability zone 3. From these results an optimum value for r/r_0 is deduced. An alternative method of qualitatively identifying the optimum value of r/r_0 using the spatial power frequency spectra of ion trajectories is introduced and examples provided for operation in stability zone 1 and zone 3.

Finally the effects on QMF performance that arise from different types of electrode mechanical tolerances for operation in zone 3 are investigated. The results are used to provide acceptable production limits for the manufacturing process. Also examined is a method of compensating for certain types of electrode mechanical tolerance through the use of unbalanced electrode drive.

4.2 Methodology

4.2.1 Background

Investigation of the effects of the ratio r/r_0 and/or misaligned electrodes is extremely difficult to achieve by experiment, due to the need to dismantle the QMS to change or alter the position of the electrode(s). Errors introduced due to the disassembly/reassembly cycle can introduce significant performance effects which cannot be isolated from the effects that are being investigated. Manufacturing a QMF

for each r/r_0 and tolerance condition is a possible alternative which would remove the errors associated with assembly and disassembly. Each unit would be a custom build, requiring closer tolerance limits than those being characterised and would incur significant costs. Numerical simulation methods overcome these experimental and manufacturing cost burdens, enabling the effects of mechanical errors to be investigated and recommendations made on acceptable tolerance limits.

4.2.2 Computer simulation

The methods that have been adopted herein are based on the application of computer simulation techniques using custom software. The QMS2D-Hyperbolic program (see Ch. 3.5.3) was used for the investigation of a QMF with hyperbolic profile electrodes. The QMS2D-Field (see Ch. 3.5.4) software together with the public domain software Poisson/Superfish [102] was used to characterise circular electrode QMF performance for a range of r/r_0 ratios and for a range of electrode displacements. Previous research carried out by the University of Liverpool Mass Spectrometry Research Group [43], [45], [49] and other reported research [11] have previously reported on certain aspects of these effects when operating a QMF in zone 1. When investigating the effects of the ratio of electrode radius r to field radius r_0 and the effects of mechanical tolerance on positional accuracy of the four electrodes, a common set of operating and simulation conditions have been used (see Table 3.1 and Table 4.1). These values have been selected to enable direct comparison with previously reported results.

All simulations use 500 steps across the mass range with $2\text{x}10^5$ ions traced at each mass step. The QMF control setting η (InstRes) = 1 (see Equation 3.12), corresponds to the peak of the stability diagram (i.e. $a_{tip} \approx 3.16$, $q_{tip} \approx 3.23$ for zone 3. Decreasing η so that it is less than 1, moves the operating point below the stability tip increasing the mass pass band and decreasing the resolution (see Figure 3.5 and 3.7). No account has been taken of fringing fields at the entrance or exit of the QMF and ion velocity v_z is constant through the QMF with ion velocity components $v_x = 0$ and $v_y = 0$ on entry to the QMF. An ion is successfully detected when its trajectory does not exceed the field radius over the length of the QMF and on exit falls within the active area of the detector.

OPERATING POINT	ZONE 1	ZONE 3
a_{tip}	0.237	3.16
q_{tip}	0.706	3.23

Table 4.1. Tips of stability zones for r/r_0 investigation.

4.2.3 Ion trajectory power frequency spectra

Simulations of mass spectra with a large number of ions (2×10^5) at each mass step are computationally intensive, requiring up to 24 hours or more on a high performance PC. It was considered that a faster method of converging on an optimum electrode geometry would prove a useful tool. The concept of ion trajectory power frequency spectra as a fast method for identifying an optimum value for r/r_0 was investigated with this in mind.

4.3 Performance characteristics - hyperbolic electrodes

To provide benchmark performance characteristics of a QMF, hyperbolic profile electrodes were first investigated using computer simulation both for operation in stability zone 1 and zone 3. This was undertaken using the custom software program QMS2D-Hyperbolic.

Figure 4.1 shows typical mass spectra for a hyperbolic electrode QMF operating in stability zone 1 and zone 3 for a single ion species of 40 m/z. Evident are certain differences between the two spectra. Zone 1 provides approximately three times greater transmission than zone 3 and a peak width at 50% peak height that is narrower than zone 3. However when considering the ability to resolve a low abundance species closely adjacent to a high abundance species then the peak width at 10% peak height is a more relevant parameter. For this parameter, zone 3 is superior due to the absence of the low and high mass tails that are present on the zone 1 spectra.

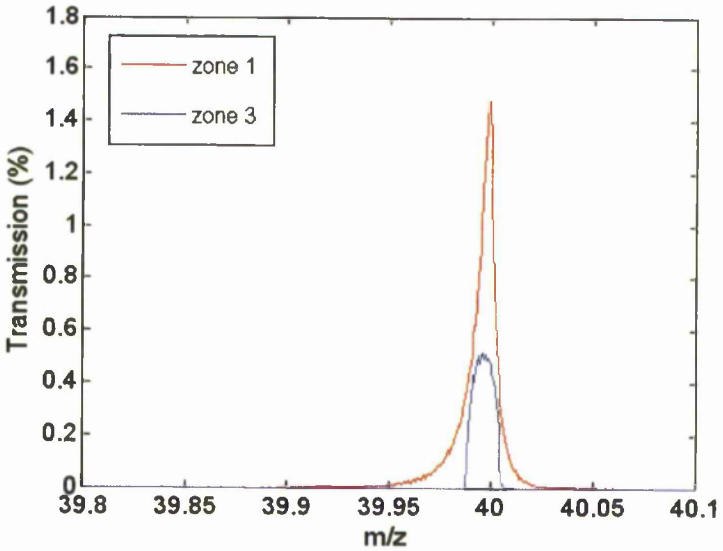

Figure 4.1. Computer simulated spectra for a QMF with hyperbolic electrodes for operation in stability zone 1 and zone 3 at an instrument resolution setting of 0.9999 with the ions experiencing 164 cycles of RF.

4.4 Methodology validation

The computer simulation techniques were validated by comparison with previously reported results for operation in stability zone 1; firstly for the performance changes as r/r_0 was varied, then for the effects of electrode displacement. Finally a comparison was made between computer simulated and experimental data.

4.4.1 Simulated data (circular electrodes)

Figure 4.2 shows the mass spectra for a range of r/r_0. It can be observed that as the ratio of r/r_0 is varied the mass peak changes in character. In general as the ratio increases the peak transmission reduces with the shoulder moving from the high mass side to the low mass side. Also in evidence is a significant low mass tail whose amplitude and width increases with increasing ratio. Accompanying this is an

increasing main peak width and a progressive shift to a lower mass position. These all confirm previously reported results [43], [45].

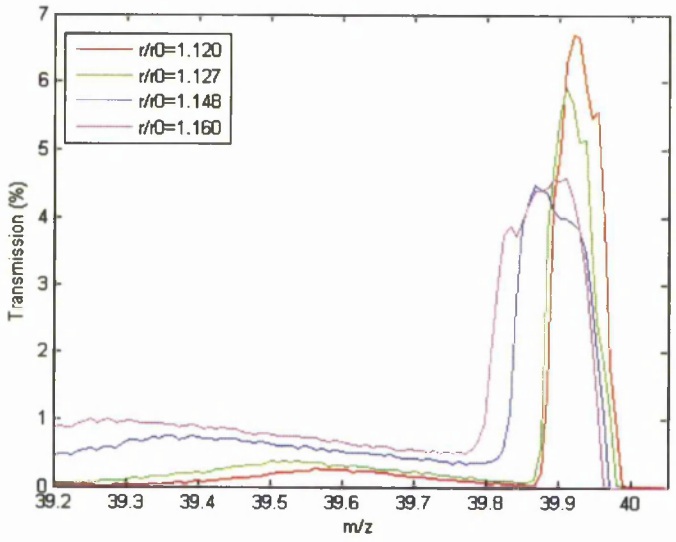

Figure 4.2. Simulated spectra for Ar^+ ion (m/z = 40) single ion species operating in stability zone 1 at a fixed instrument resolution for a range of r/r_0 ratios.

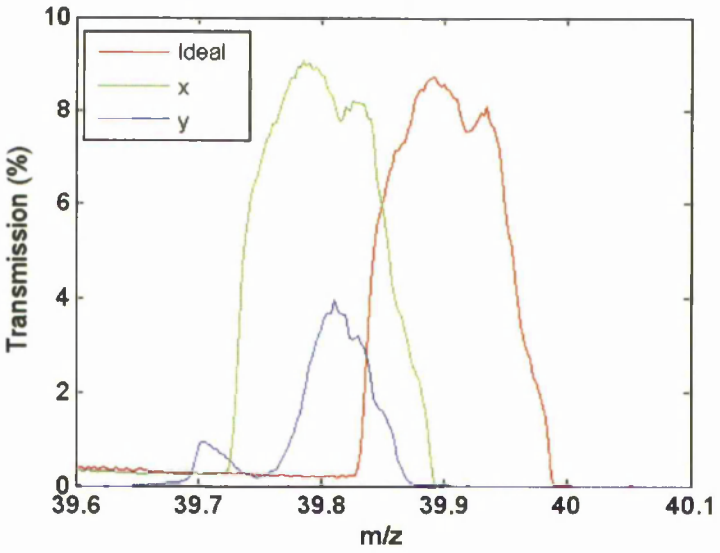

Figure 4.3. Simulated mass spectra for Ar^+ ion species (m/z = 40) for operation in stability zone 1 with no electrode displacement and for inward radial displacement of 0.005 × r_0 of a single x or y electrode.

The software was further validated by examining the resultant effects of the displacement of individual x and y electrodes when operating in zone 1. Figure 4.3 shows the results of these simulations. For a shift of an x-electrode the mass peak shifts to a lower point on the mass scale accompanied by minor changes to the mass peak tip. For a displacement of a y-electrode the mass peak again shifts to a similar position on the mass scale but is accompanied with a significant decrease in the transmission and the emergence of a secondary peak on the low mass side confirming previously reported results [49].

4.4.2 Experimental data

Experimentally obtained mass spectra for $^{59}Co^{+}$ ions with an energy of 63 eV are shown in Figure 4.4 which are derived from [62].

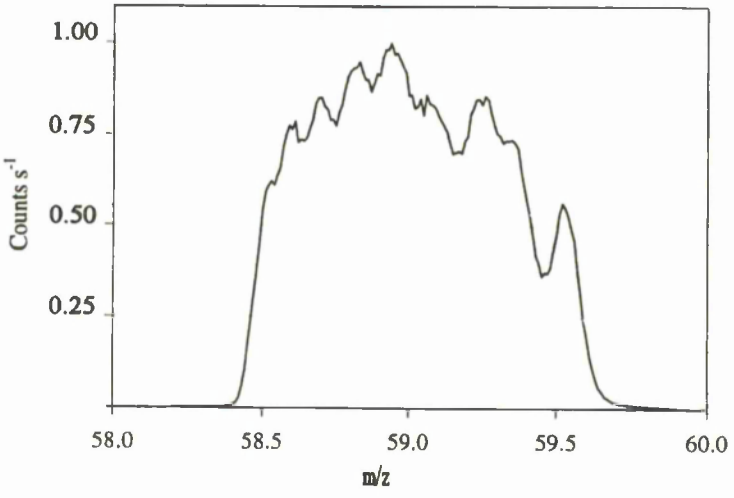

Figure 4.4. Zone 3 experimental mass spectra constructed from data in [62] for $^{59}Co^{+}$ ions with an ion energy of ~63 eV.

The simulated mass spectra for the QMF section of this instrument obtained using QMS2D-Field is shown in Figure 4.5. Simulated results show very good agreement with the experimental peak but do contain detailed differences. The low mass side contains an additional peak; there are detailed differences across the peak tip with

smaller peak amplitude on the high mass side. The simulation model assumed: uniform ion source illumination about the centreline, ions enter parallel to the *z*-axis, no entry or exit fringing fields, parallel electrodes and a faraday cup detector. Similar simulations have shown that peak structure is highly dependent on; alignment of the ion source and detector, ion energy spread and on focusing effects. The exact data on the instrument operating point were unavailable, resulting in possible differences between the actual instrument and computational operating conditions. A number of simulations were undertaken and the results presented reflect the character of the peak shape previously reported. Any differences that do exist between the two spectra can be attributed to uncertainties in the chosen operating conditions.

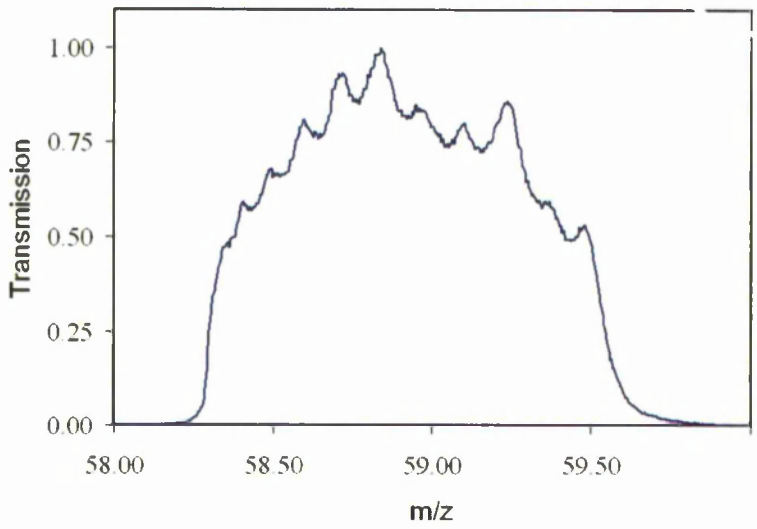

Figure 4.5. Zone 3 simulated mass spectra for the QMF for $^{59}Co^{+}$ ions with an ion energy of ~63 eV.

4.5 QMF performance – the effects of r/r_0

4.5.1 Overall impact

Mass spectra for a circular electrode QMF for a range of r/r_0 ratios when operating in zone 3 are shown in Figure 4.6. A number of discernible characteristics are present which result in degraded performance when compared to hyperbolic electrodes. Peak position shifts along the mass scale as r/r_0 is increased, corresponding to

the hyperbolic electrode peak position only when $r/r_0 \approx 1.120$. The peak height varies by a factor of 3 to 1 for the range of r/r_0 considered with a minimum occurring at $r/r_0 = 1.127$.

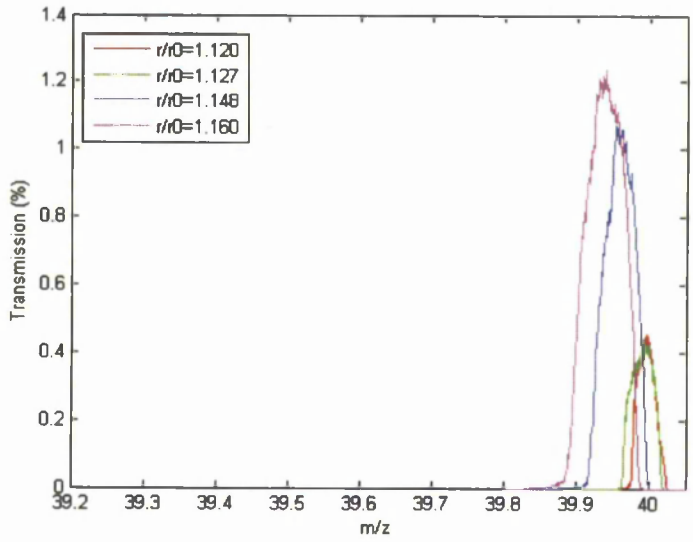

Figure 4.6. Simulated mass spectra for Ar^+ ion (m/z = 40) single ion species operating in stability zone 3 at a fixed instrument resolution for a range of r/r_0 ratios.

The mass peak edges are less sharp due to a broadening of the peak base and increased structure is present across the peak tips. Artefacts are discernible on the low and high mass peak sides, more apparent on the low mass side. For the range of r/r_0 ratios examined there is evidence of low mass tailing but not as significant as produced when operating in zone 1.

4.5.2 Multipole coefficients

Multipole coefficients (Table 4.2.) generated by the Poisson/Superfish software show that the dominant multipole (A_2) coefficient varies from 1.0009 for $r/r_0 = 1.117$ to 1.0037 for $r/r_0 = 1.160$. The quadrupole component (A_2) of field strength increases with increasing r/r_0, resulting in a proportionally higher field strength for a given excitation voltage when compared to that generated by hyperbolic electrodes. This shifts the mass scan line operating point to a lower mass value as r/r_0 increases. The additional multipole components in the field result in distortions to the ideal stability diagram. These distortions produce a defocusing of the stability boundaries, the

effect being accentuated near the stability tip (two boundaries converging) and results in a spreading of the transition region between rejection and acceptance. This produces a spreading out of the mass spectral peak base resulting in less steep peak edges and more apparent mass spectral tailing. Defocusing near the stability tip also produces increased structure in the peak (noise) and distortions in peak shape.

4.5.3 Mass peak shape

Figure 4.7 shows a set of simulated mass spectral peaks for a range of r/r_0 at two instrument control settings (η) for operation in zone 3. A number of observable mass spectra characteristics are dependent on the value of r/r_0. Operation at η = 0.9995 produces non-monotonic characteristics on the rising edge of the mass peak, greatest at r/r_0 = 1.140 and reducing either side of this ratio. At η = 0.9999 these characteristics are not apparent. Similar characteristics are just evident under certain operating conditions on the falling edge again at η = 0.9995. For all test conditions, structure is present across the mass peaks, adding uncertainty to the mass peak position. This structure is marginally greater than that observed for hyperbolic electrodes. Experimental results previously reported have demonstrated similar characteristics including the presence of peak splits [6]. Peak splitting can occur because of misalignment of the ion detector, ion collection effects due to fringing fields at the exit of the QMF coupled with minimum and maximum amplitudes of the ion trajectory [62], and non-linear resonances. Simulations were undertaken for a range of ion energies from 2 eV to 40 eV at η = 0.9995 for both constant U/V and constant U scanning. For these test conditions, the mass split amplitude (marked P in Figure 4.7.) decreased with increasing ion energy with no measurable shift in the position of the split on the mass scale. As ion energy is increased, ions experience fewer RF cycles resulting in a reduction in the strength of any non-linear resonance effects that may be present. These non-linear resonances are associated with particular lines on the stability diagram and any characteristics associated with these resonances will not shift on the mass scale as ion energy is varied. The observed behaviour of the mass peak split (Ps) conforms to that expected of a mass peak split due to non-linear resonances in the ion trajectories. Low mass tails are present at the two extremes of r/r_0, the most pronounced occurring at an r/r_0 = 1.160 for η = 0.9995

A_N	r/r_0					
	1.117	**1.120**	**1.127**	**1.130**	**1.140**	**1.160**
A_2	1.0009×10^{0}	1.0011×10^{0}	1.0016×10^{0}	1.0018×10^{0}	1.0024×10^{0}	1.0037×10^{0}
A_6	1.8914×10^{-3}	1.6714×10^{-3}	1.2004×10^{-3}	9.9978×10^{-4}	3.3623×10^{-4}	-9.6720×10^{-4}
A_{10}	-2.4200×10^{-3}	-2.4241×10^{-3}	-2.4323×10^{-3}	-2.4356×10^{-3}	-2.4453×10^{-3}	$-2.4596\text{E}\times10^{-3}$
A_{14}	-3.0404×10^{-4}	-3.0164×10^{-4}	-2.9650×10^{-4}	-2.9431×10^{-4}	-2.8700×10^{-4}	-2.7252×10^{-4}

Table 4.2. Multipole coefficients for a range of r/r_0 values generated from Poisson/Superfish.

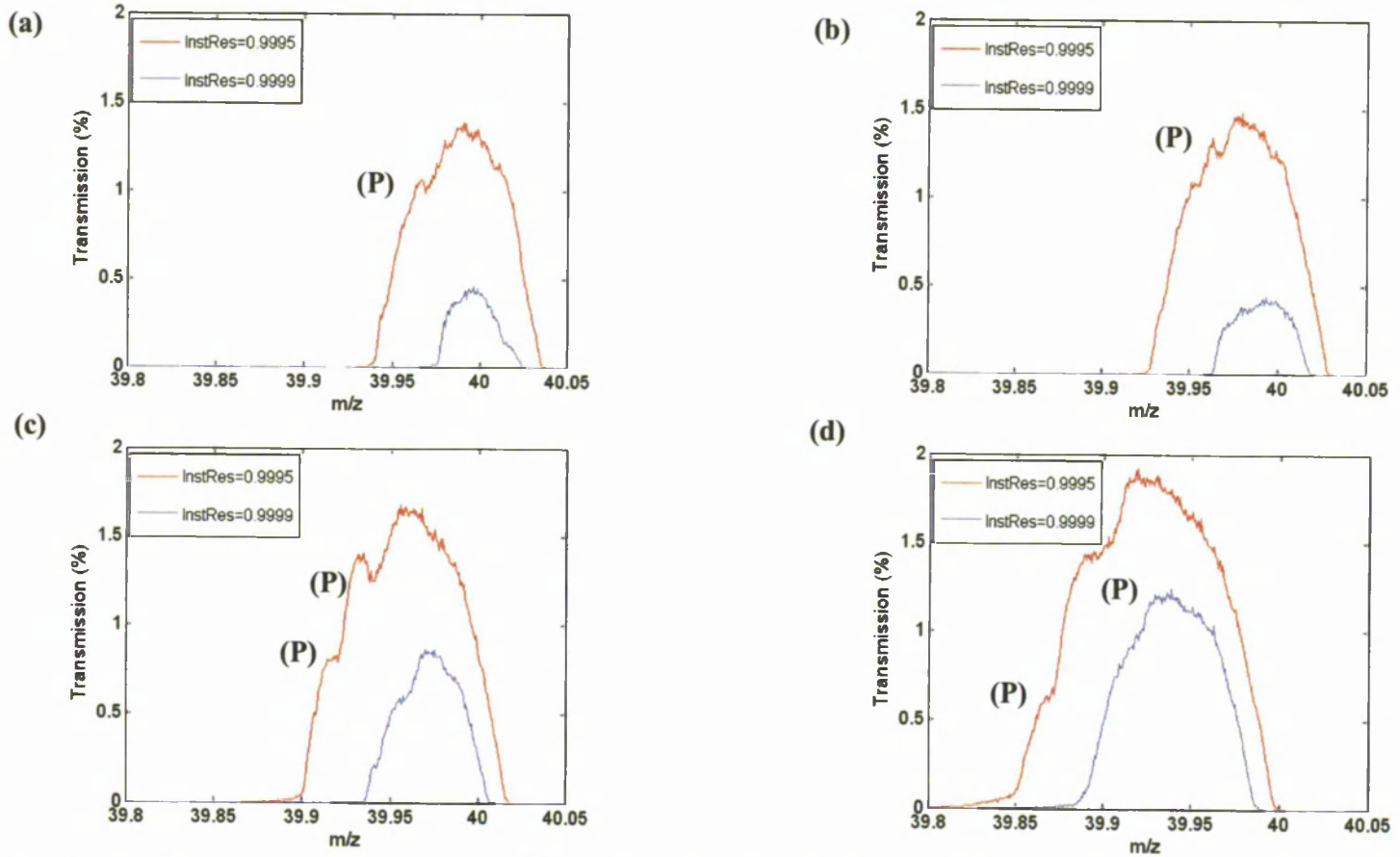

Figure 4.7. Set of simulated mass spectra for Ar^+ (40 *m/z*) single ion species for four r/r_0 ratios at two instrument resolution settings; (a) $r/r_0 = 1.120$, (b) $r/r_0 = 1.127$, (c) $r/r_0 = 1.140$, (d) $r/r_0 = 1.160$.

with an amplitude of ≈ 0.06%, insufficient to influence actual resolution. As r/r_0 moves away from these two extremes the low mass tail reduces, becoming barely detectable at $r/r_0 = 1.127$. Zone 3 performance exhibits a marked improvement over zone 1 where extensive low mass tails were evident which had a detrimental effect on abundance sensitivity and resolution. Results for zone 3 clearly indicate the improved abundance sensitivity that is obtainable due to the increased baseline peak separation provided by the minimal low mass tails confirming previously published experimental results [56-57].

4.6 Performance sensitivities

A performance sensitivity parameter σ is now introduced as a method of quantifying the susceptibility of QMF performance parameters to variations in r/r_0. Peak height sensitivity σ_{PH} is defined in Equation (4.2)

$$\sigma_{PH} = \frac{\delta(PH)}{\delta(\frac{r}{r_0})} \tag{4.2}$$

where σ_{PH} is the peak height sensitivity, PH the transmission peak height of a mass peak and r/r_0 is as stated previously.

4.6.1 Transmission sensitivity

Peak height transmission (see Figure 4.8.) varies with r/r_0 and is dependent on η. This dependency or performance sensitivity (σ_{PH}) is most marked at the highest setting of η. Here transmission increases by the greatest percentage either side of a minimum at $r/r_0 \approx 1.120$. At the lowest value of η considered, peak height varies almost linearly, decreasing with decreasing r/r_0, with a lower percentage change and no obvious optimum setting. Performance sensitivity σ_{PH} increases as η increases, and is dependent on the value of r/r_0. These results show that the QMF acceptance is also dependent on r/r_0, with acceptance staying smaller than the field radius over the range tested.

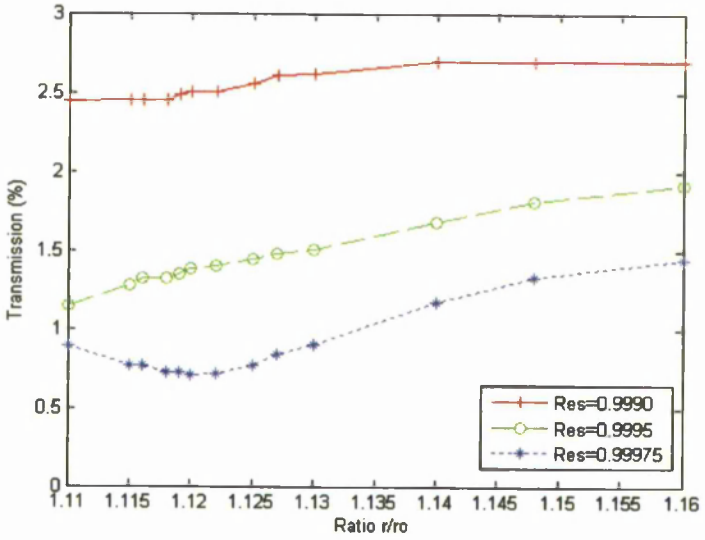

Figure 4.8. Variation of transmission (peak height) for a range of r/r_0 ratios at different instrument resolution settings for a single species Ar ion.

4.6.2 Peak width sensitivity

Figures 4.9 and 4.10 show the variation of peak width at 50% PH and 10% PH respectively for a range of r/r_0 values at three settings of η. A peak width minimum is observable for all settings of η at peak width definitions. These occur within a range

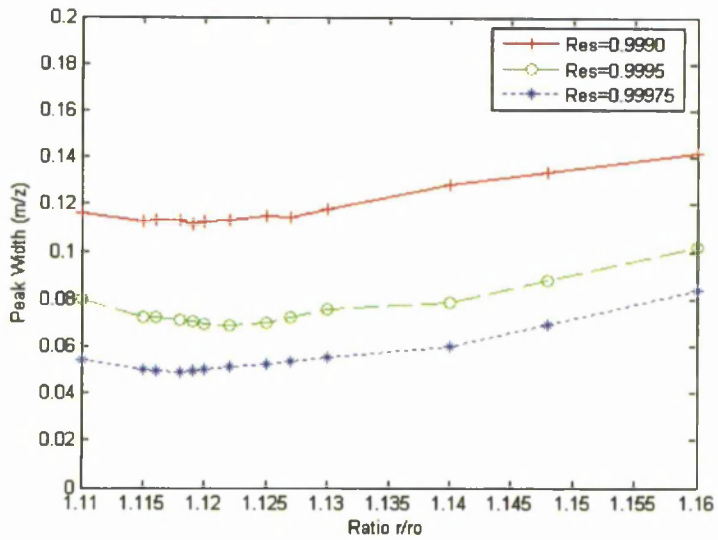

Figure 4.9. Variation of peak width at 50% PH for a range of r/r_0 ratios at different instrument resolution settings for a single species Ar^+ (40 *m/z*) ion.

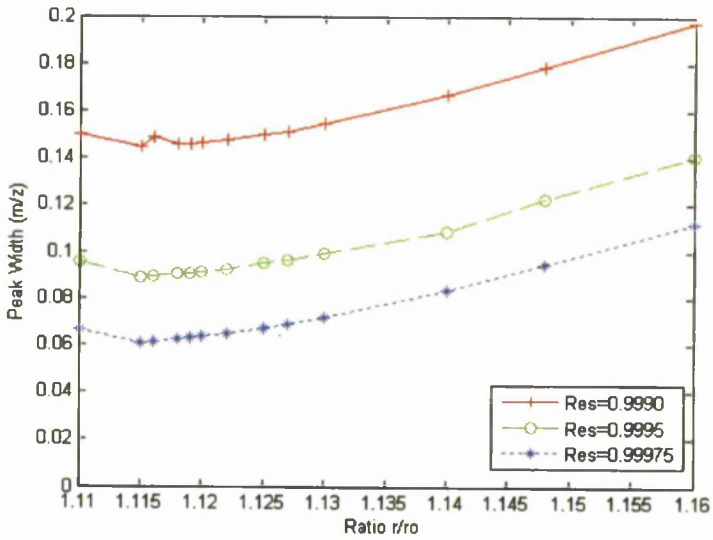

Figure 4.10. Variation of peak width at 10% PH for a range of r/r_0 ratios at different instrument resolution settings for a single species Ar^+ (40 *m/z*) ion.

of r/r_0 = 1.117-1.122, the actual value being dependent on η and the peak width definition. In a similar manner to equation (4.2) we can define a peak width sensitivity parameter σ_{PW} as

$$\sigma_{PW} = \frac{\delta(PW)}{\delta(\frac{r}{r0})} \tag{4.3}$$

where σ_{PW} is the peak width sensitivity, PW the peak width of a mass peak and r/r_0 is as stated previously. A maximum for σ_{pw} occurs when the peak width is measured at 10% PH and due to small changes in mass tailing which is r/r_0 dependent. The value of η has little influence on the magnitude of σ_{pw}.

4.6.3 Peak position sensitivity

The variation of the mass peak position with r/r_0 is shown in Figure 4.11. The mass peak position changes with r/r_0, moving from a value equal to or just greater than the nominal of 40 *m/z* at r/r_0 = 1.11 down to a value of 39.94 *m/z* or less at a r/r_0 = 1.16. This shift reflects the change in the magnitude of the A_2 multipole coefficient as

discussed previously in this chapter. A peak position sensitivity parameter σ_{pp} is defined by Equation (4.4)

$$\sigma_{PP} = \frac{\delta(PP)}{\delta(\frac{r}{r0})} \tag{4.4}$$

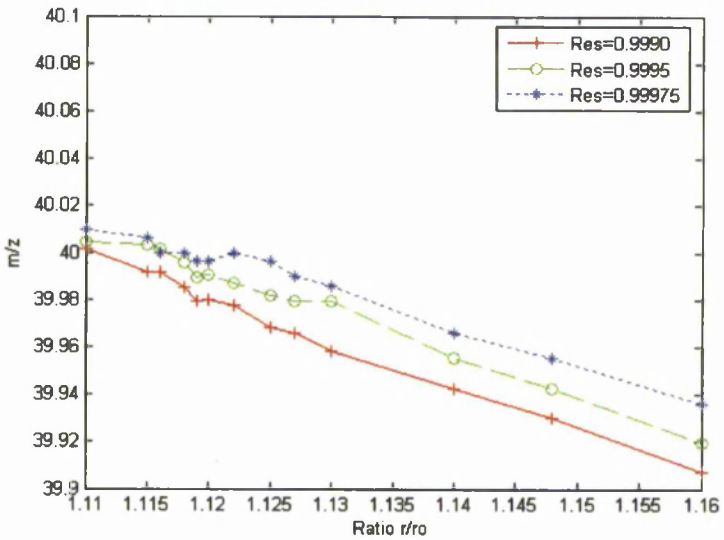

Figure 4.11. Variation of peak position for a range of r/r_0 ratios for different instrument resolution settings for a single species Ar^+ (40 *m/z*) ion.

where σ_{PP} is the peak position sensitivity parameter, PP the peak position on the mass scale and r/r_0 is as stated previously. The sensitivity (σ_{pp}) to r/r_0 is largely constant for the range of r/r_0 considered with the absolute value being dependent on the value of η, indicating that calibration of the instrument would be required when η changed.

4.6.4 Resolution sensitivity

QMF resolution is determined from the ratio of mass spectral peak width (Δm) at a given mass (m). Resolution ($m/\Delta m$) is defined with Δm measured at 10% of the mass spectral peak height (10% PH) or 50% of the peak height (50% PH). Figures

4.12 and 4.13 show the variation of resolution with r/r_0 for 50% PH and 10% PH respectively.

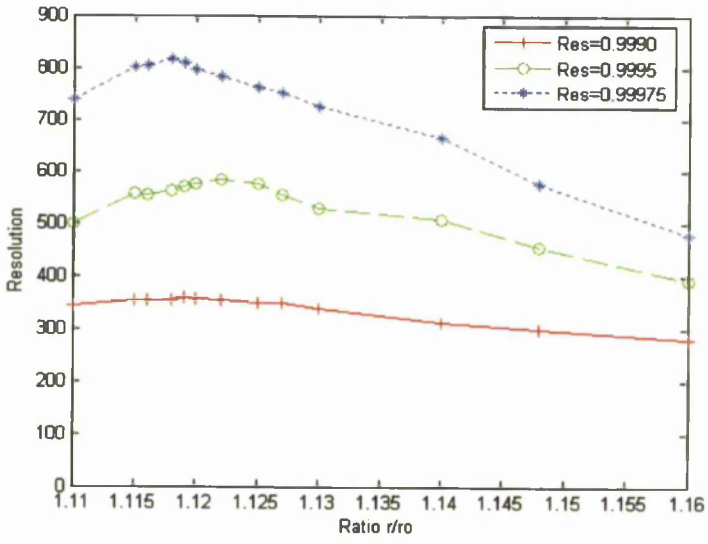

Figure 4.12. Variation of resolution at 50% peak height with r/r_0 for a range of instrument resolution settings for a single species Ar^+ (40 *m/z*) ion.

For both peak width definitions, resolution varies with r/r_0 with a maximum value occurring for a range of r/r_0 = 1.115 and 1.122 with the value being dependent on peak width definition and the value of η. The mass resolution sensitivity parameter σ_{RES} is defined by

$$\sigma_{RES} = \frac{\delta(RES)}{\delta(\frac{r}{r0})} \tag{4.5}$$

where σ_{RES} is the mass resolution sensitivity parameter, RES the mass resolution and r/r_0 is as stated previously. The performance sensitivity σ_{RES} is greatest for the highest setting of η and when using the 50% PH definition. The value of σ_{RES} decreases as η is decreased for both definitions. In all cases the spread in measured mass resolution is greatest for values in the range r/r_0 = 1.115 to 1.122 and the least when r/r_0 = 1.16.

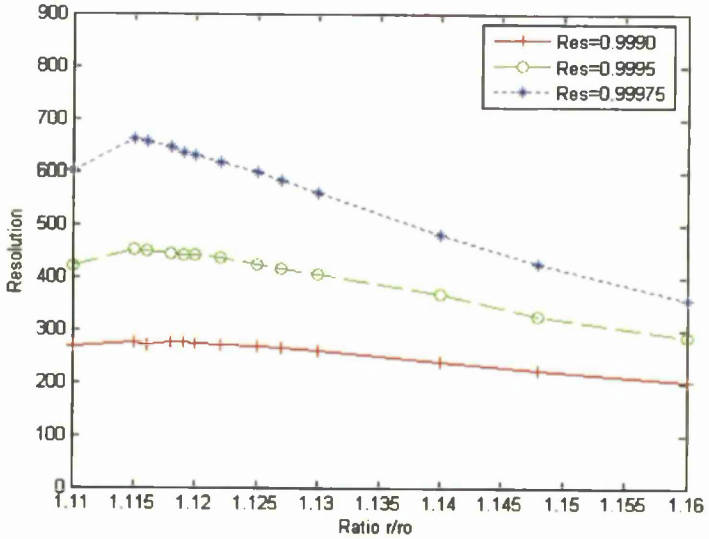

Figure 4.13. Variation of resolution at 10% peak height with r/r_0 for a range of instrument resolution settings for a single species Ar^+ (40 m/z) ion.

4.7 Power frequency spectra

4.7.1 Hyperbolic electrodes

Figure 4.14 shows a typical ion trajectory when operating in zone 1 confirming previously reported results [9]. The x-trajectory ion motion consists of a waveform of sinusoidal appearance which is amplitude modulated to a depth of approximately 100% by a second lower frequency periodic waveform. The y-trajectory ion motion consist of a periodic waveform with a higher frequency superimposed on it. The peak excursion from the central axis is greater for the x-trajectory.

The ion trajectory power-frequency spectra for hyperbolic electrodes operating in zone 1 are shown in Figure 4.15. Dominant x and y-direction spatial frequencies of ~ 993 kHz and 18 kHz respectively can be observed. At the operating point, a = 0.236813, q = 0.7060, the iso-β line values are β_x = 0.988491 and β_y = 0.0151852 [109]. The analytically calculated values for the fundamental frequencies using Equation (3.33) are Ω_{Z1x0} = 988.491 kHz and Ω_{Z1y0} = 15.1852 kHz. These compare favourably with the results obtained through simulation.

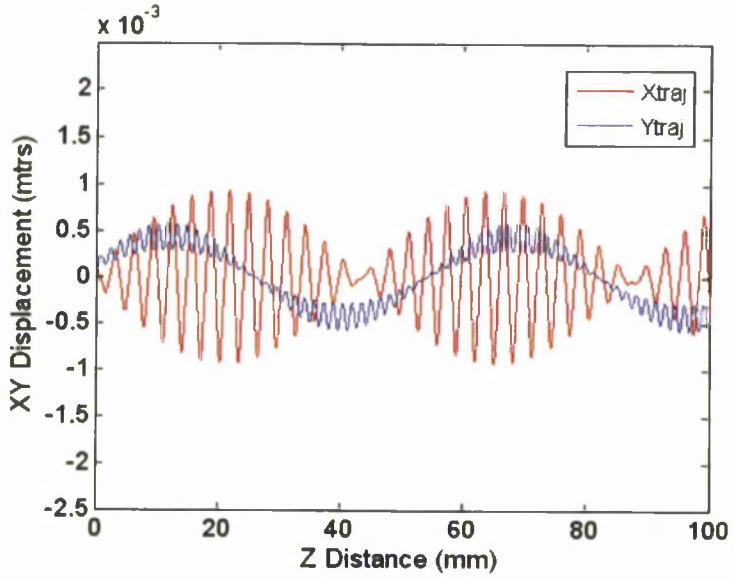

Figure 4.14. Ion trajectory of an Ar^+ (40 *m/z*) ion for operation in stability zone 1 at $a = 0.236813$ and $q = 0.7060$.

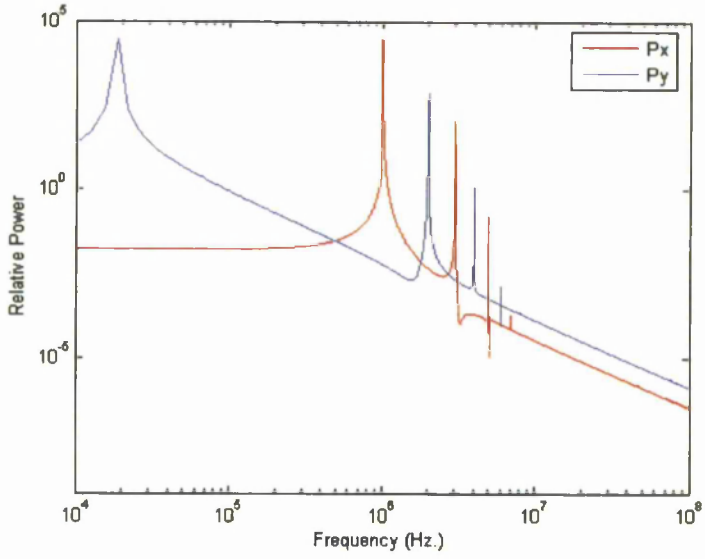

Figure 4.15. Spatial power frequency spectra for trajectory of a Ar^+ (40 *m/z*) ion operating in stability zone 1 at $a = 0.236813$ and $q = 0.7060$ for a QMF with hyperbolic electrodes.

Differences are due to the resolution of the DFT algorithm and simulated data. Higher order spatial frequencies correspond to those obtained through analytical calculation. For both directions, the lowest spatial frequency component exhibits the highest relative power, with each higher order spatial frequency decreasing in relative power.

A computer simulated ion trajectory for a hyperbolic electrode QMF operating in zone 3 is shown in Figure 4.16, confirming ion trajectories reported by Hiroki [59]. For the chosen *a-q* operating point, they are markedly different to zone 1. Both *x* and *y* trajectories have similar appearance but with detailed differences. For both directions, the overall appearance is that of a sinusoidal waveform with a large harmonic content. Figure 4.17 shows the resultant power frequency spectra for the ion trajectory shown in Figure 4.16. At the selected zone 3 operating point, ion trajectory power spectra, display differences from those of zone 1. The lowest spatial frequency now occurs for the *x*-direction and exhibits a much sharper peak. The *x*-direction second order spatial frequency ($n = 1$) is now dominant and for the *y*-

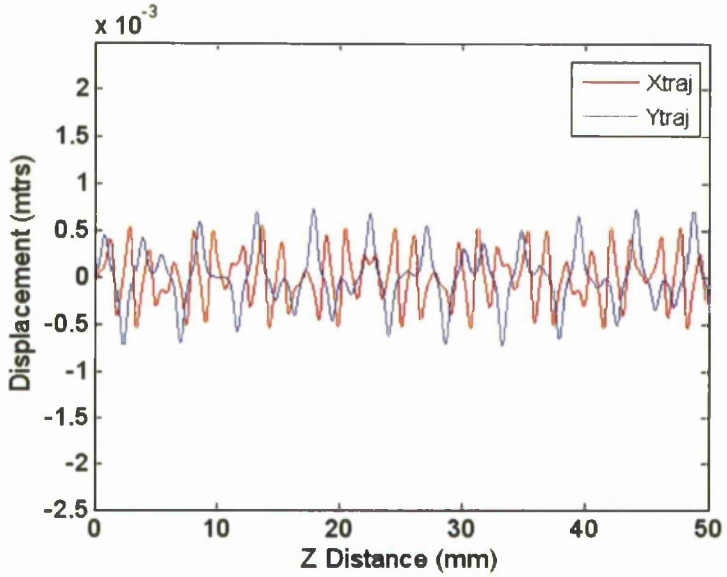

Figure 4.16. Ion trajectory of a Ar^+ (40 *m/z*) ion for operation in stability zone 3 for a QMF with hyperbolic electrodes at $a = 3.023$ and $q = 3.154$.

direction the fundamental spatial frequency ($n = 0$) is still dominant but is only marginally greater than the second order one. A larger number of frequency peaks

are apparent, reflecting the less sinusoidal (higher harmonic content) character of the zone 3 ion trajectories.

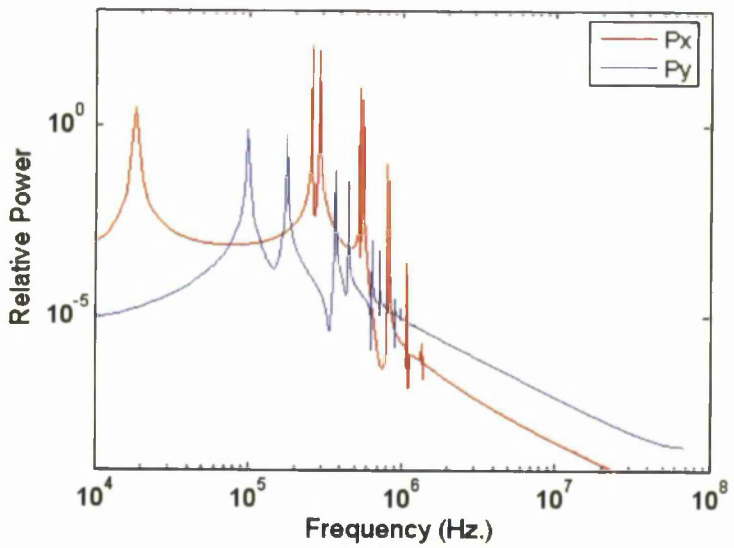

Figure 4.17. Spatial power frequency spectra for trajectory of a Ar^{+} (40 *m/z*) ion operating in stability zone 3 at $a = 3.023$ and $q = 3.154$ for a QMF with hyperbolic electrodes.

4.7.2 Circular electrodes

An analytically derived hyperbolic field was used to validate ion trajectories simulated using QMS2D-Field. The trajectories obtained, and their associated power frequency spectra compared very strongly to those obtained by solving the Mathieu equations. This demonstrates that field derived ion trajectories do not introduce significant additional components to the power frequency spectra. Ion trajectories for a range of operating conditions and r/r_0 ratios were simulated for operation both in zone 1 and zone 3. Broadly, they reflect the general characteristics presented for hyperbolic electrodes.

4.7.2.1 Zone 1

For operation in zone 1 with circular electrodes (Figure 4.18.) base power levels are

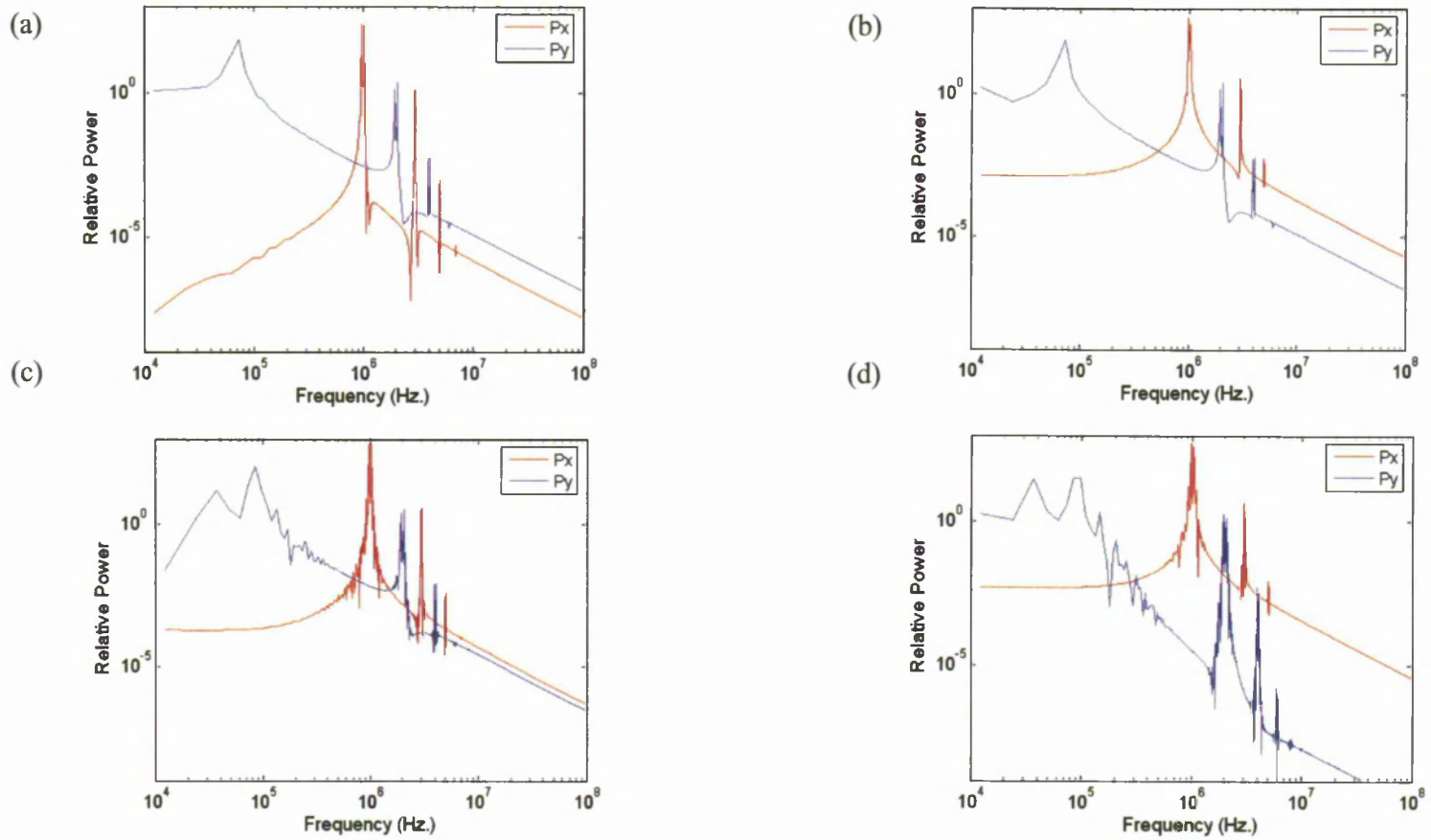

Figure 4.18. Set of ion trajectory spatial power frequency spectra for an Ar+ (40 m/z) ion for four r/r_0 ratios operating in stability zone 1at a = 3.023 and q = 3.154; (a) r/r_0 = 1.120, (b) r/r_0 = 1.127, (c) r/r_0 = 1.140, (d) r/r_0 = 1.160.

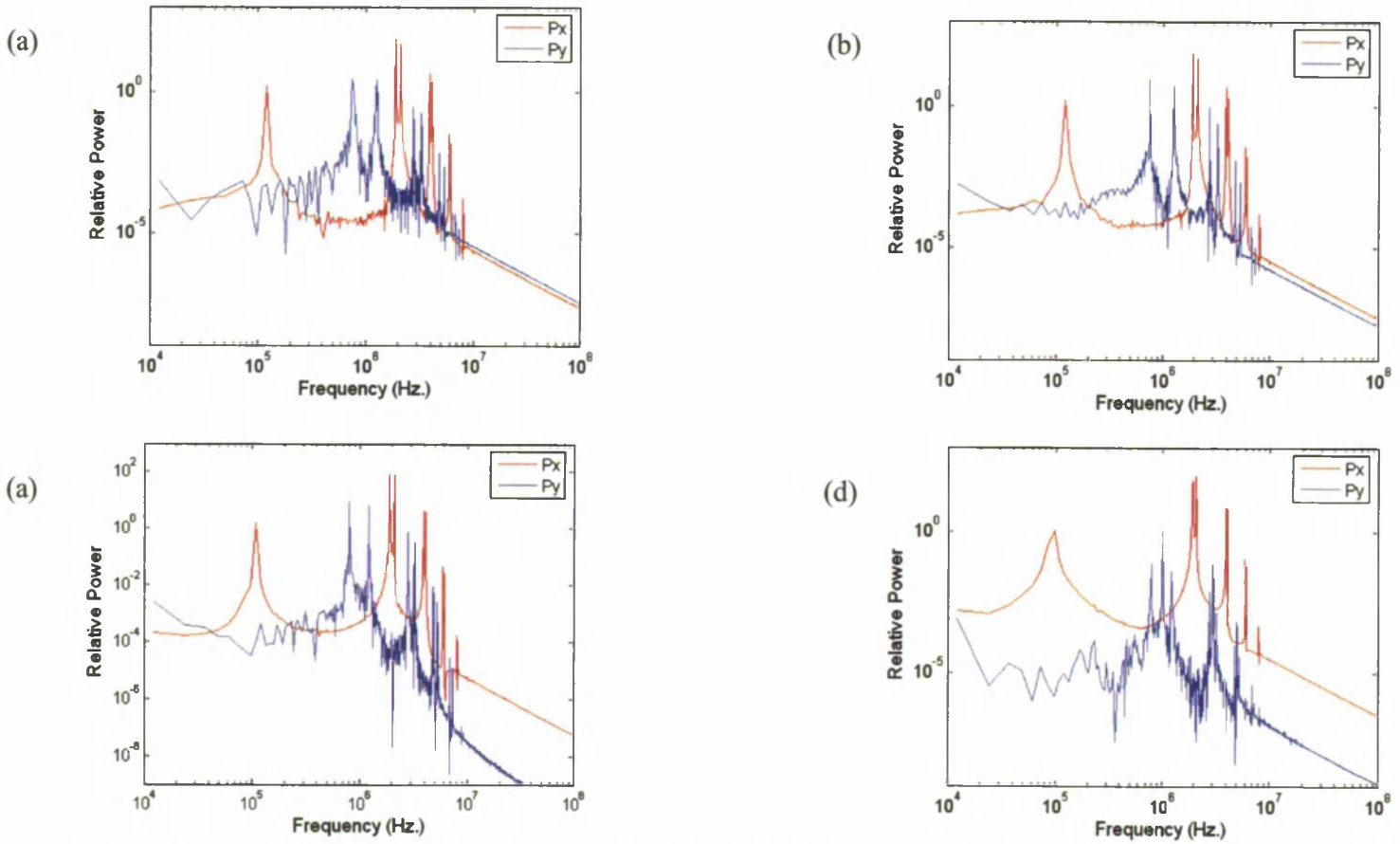

Figure 4.19. Set of ion trajectory spatial power frequency spectra for an Ar^+ (40 *m/z*) ion for four r/r_0 ratios operating in stability zone 3 at $a = 0.236813$ and $q = 0.7060$; (a) $r/r_0 = 1.120$, (b) $r/r_0 = 1.127$, (c) $r/r_0 = 1.140$, (d) $r/r_0 = 1.160$.

increased, accompanied by increases in the x and y direction peak relative power as r/r_0 is increased when compared to those obtained for hyperbolic electrodes. Small changes to the peak frequencies and their general character are also discernible. The power spectra are not as clean; there are additional spatial frequency components present. These additional frequency components increase in number and relative power the further r/r_0 deviates from 1.127. The power frequency spectra for zone 1 with r/r_0 = 1.127 shows very strong correlation to that obtained for hyperbolic electrodes.

4.7.2.2 Zone 3

For zone 3 (see Figure 4.19.), the spatial frequency spectra are not as well defined, due to the added clutter of additional spatial frequencies. It is still possible to identify an optimum value for r/r_0 but there is not such a strong correlation to the hyperbolic power spatial frequency spectra. The additional spatial frequency peaks observed for circular electrodes arise from non-linear resonances occurring due to the non-linear multipole fields. As r/r_0 deviates from the ideal, the net effect of these multipole fields varies, resulting in varying non-linear resonances. These manifest themselves as variations in the amplitude and number of spatial frequency peaks present in the power spatial frequency spectra.

4.8 Asymmetric electrode geometry

4.8.1 Introduction

In addition to identifying an optimum value for the ratio of r/r_0, it is also necessary to quantify acceptable limits for manufacturing tolerances for the electrode radius and for the positional accuracy of the electrodes. Manufacturing processes are not ideal; tolerances exist, which cause the instrument performance to deviate from the optimum [37]. For a QMF, these manufacturing tolerances result in variations in

QMF PARAMETER	CONDITION
Length	254 mm
r_0	2.76 mm
r/r_0	1.127
Frequency	2 MHz
Detector radius	2.76 mm
Housing radius	$3.6 \times r_0$
Ion Source	
Ion energy	50 eV
Ion source radius	0.5 mm
Ion energy spread	0
Ion angular spread	0
Operating point	
a_{tip}	3.16
q_{tip}	3.23
Ion species	40 m/z

Table 4.3. Computer simulation test conditions for electrode displacement investigation.

electrode radii due to tool wear and accuracy limits of the production machinery; misalignments of the electrodes arise from the electrode mounting systems and limitations of the assembly process. In the case of longer length QMFs, non-parallel alignment of the electrodes can arise due to bowing of the electrodes and/or slight differences in the mounts, all of which contribute to changes in the performance characteristics of a QMF. Additionally, the mechanical design of the instrument has to minimise any thermo-mechanical effects that arise from thermal cycling of the instrument during bake-out and usage.

Investigation of the effects of misaligned electrodes is extremely difficult to achieve by experiment, due to the need to dismantle the QMS/QMF to change or alter the position of the electrode(s). Errors introduced due to the disassembly/reassembly cycle can introduce significant performance effects which cannot be isolated from the effects that are being investigated. Manufacturing a QMF for each tolerance condition is a possible alternative which would remove the errors associated with assembly and disassembly of the QMF but still may leave alignment issues between the ion source and detector assemblies. Each unit would be a custom build, requiring closer tolerance limits than those being characterised and would

incur significant costs. Numerical simulation methods overcome these experimental and cost burdens, enabling the effects of mechanical errors to be investigated and recommendations made on acceptable tolerance limits. Table 4.3 shows the computer simulation conditions used for the investigation of electrode displacement and the actual electrode displacements are contained in Table 4.4.

4.8.2 Effects on resultant field

When one or more electrodes are displaced, the symmetry of the electrode geometry is altered. For the case of on-axis displacements, only one axis of symmetry is retained. A reduction in the degree of symmetry introduces additional multipole field terms that are not produced by an optimum QMF [38]. Previously published research has demonstrated the effects of multipole field differences on the resultant mass spectra by selective introduction of multipole field components. Examples include; making the radii of the electrode pairs different to introduce an octopole field component [73], [110]; shifting one of the electrode pairs further out from the axis centre to introduce a number of different multipole components of similar magnitude [110] and rotational shifts of the y-electrode to introduce a hexapole term [111]. These investigations used electrode displacements in excess of what could be expected as normal production tolerances and resulted in multipole terms several orders of magnitude greater than those considered here.

4.8.3 Single electrode radial displacement

The effects of an inward radial displacement of a single x and y electrode were firstly investigated for a range of displacements up to $0.005 \times r_0$, at which point an isolated satellite peak is identifiable in the case of a y-electrode displacement.

Figure 4.20 shows the results of inward axial displacement of a single x-electrode. We can observe that an increasing displacement produces an increasing shift of the mass peak to a lower mass position. From inspection of the data in Table 4.4 it can be observed that the incremental mass peak shift is approximately proportional to the incremental electrode displacement. Accompanied with this shift there is a decrease in resolution and an increase in peak height (sensitivity) as inward displacement is

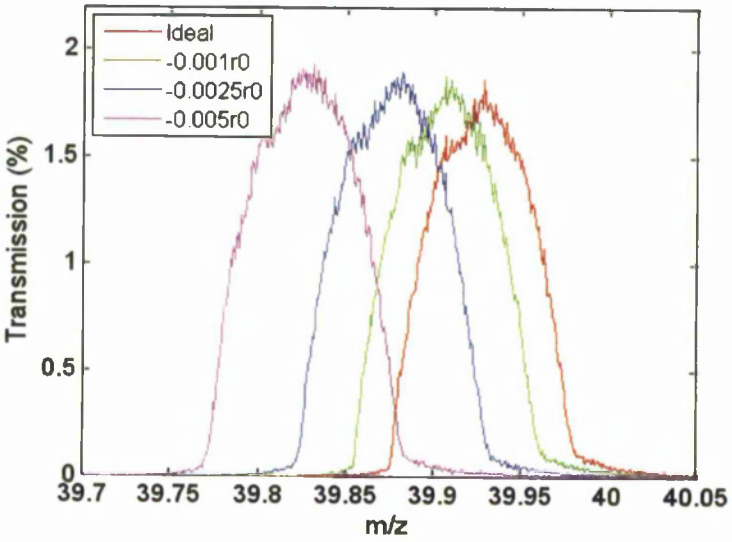

Figure 4.20. Simulated mass spectra for Ar^+ ion species ($m/z = 40$) for a range of inward radial inward radial displacements of a single x-electrode when operating in zone 3.

increased. The shift on the mass scale would be correctable through calibration. As the sensitivity increases with increased displacement, it may be possible to increase the instrument resolution (η) to compensate for the reduction in actual resolution, without the sensitivity decreasing below that of the optimum QMF. Slight changes to the structure of the noise on each of the mass peaks are observable, but no significant change in the low and high mass tails is observable.

A radial inward displacement of a single y-electrode produces significant changes to the mass spectra as can be seen in Figure 4.21. An increasing inward displacement of a y-electrode produces a proportional shift of the mass peak to a lower mass value. This shift is approximately the same as for a displacement of an x-electrode. Decreasing peak height and a reduction in the steepness of the edges are observable as the y-electrode displacement increases. For small y-displacements, a shoulder emerges on the low mass side of the mass peak. The higher mass side of this shoulder decreases in amplitude while the low mass side increases with increasing electrode displacement.

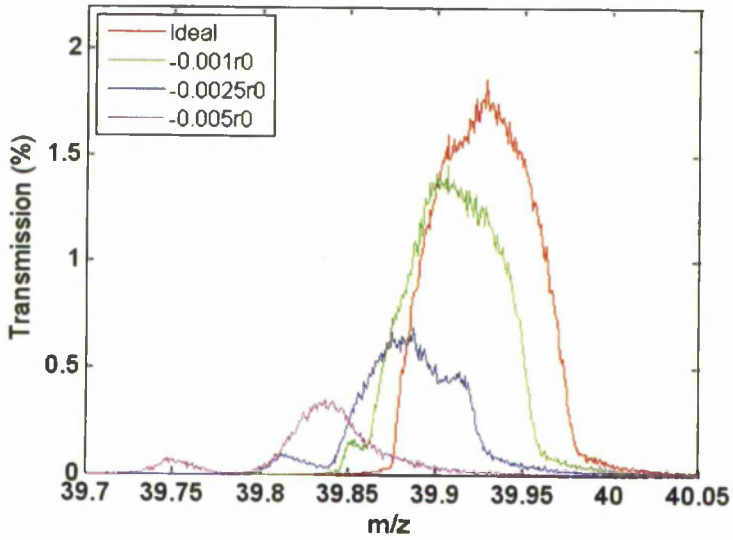

Figure 4.21. Simulated mass spectra for Ar^+ ion species (m/z = 40) for a range of inward radial displacements of a single y-electrode for operation in zone 3.

Displaced Electrode	Parameter	Displacement (on-axis)			
		0	-0.001×r_0	-0.0025×r_0	-0.005×r_0
x	Peak position (m/z)	39.93	39.909	39.88	39.82
	Peak height (%)	1.79	1.83	1.86	1.89
	Resolution 50% PH	524	514	497	476
	Resolution 10% PH	394	388	378	369
y	Peak position (m/z)	39.93	39.904	39.89[1]	39.84[1]
	Peak height (%)	1.79	1.38	0.65[1]	0.33[1]
	Resolution 50% PH	524	544	595[1]	937[1]
	Resolution 10% PH	394	368	301[1]	248[1]

Table 4.4. Mass spectra characteristics for a range of radial inward displacements (negative) for x and y electrodes (Note [1] main peak value, PH = peak height).

At the extremes of the displacement range, the shoulder separates from the main peak forming an isolated peak. On the high mass side of the main peak a secondary peak appears and disappears finishing with the formation of a concave edge at the limits of the displacement. Outward displacements of the x and y electrodes result in very similar changes to those obtained for inward displacements of x and y electrodes except that the mass peak shifts to a higher mass position.

4.8.4 Single electrode radius error

Differences in the radius of an electrode can also occur due to mechanical tolerances of the manufacturing process and can result in electrodes of different radii being present in a QMF assembly. Simulations undertaken for a single x or y-electrode of differing radius with all the electrodes mounted on a common pitch centre, resulted in mass peak changes similar to those obtained with electrode displacement. Increasing the electrode radius resulted in mass peak changes corresponding to an inward electrode displacement of the corresponding x or y-electrode and decreasing the electrode radius produced results similar to those for an outward electrode displacement of the same electrode.

4.8.5 Single electrode orthogonal displacements

Figure 4.22 shows the results of mounting errors which produce orthogonal shifts of an electrode with respect to its reference axis. For an x-electrode with a displacement in the y-direction, distortions to the mass peak were observable together with a reduction in transmission and the emergence of a secondary peak at the extremes of the displacement.

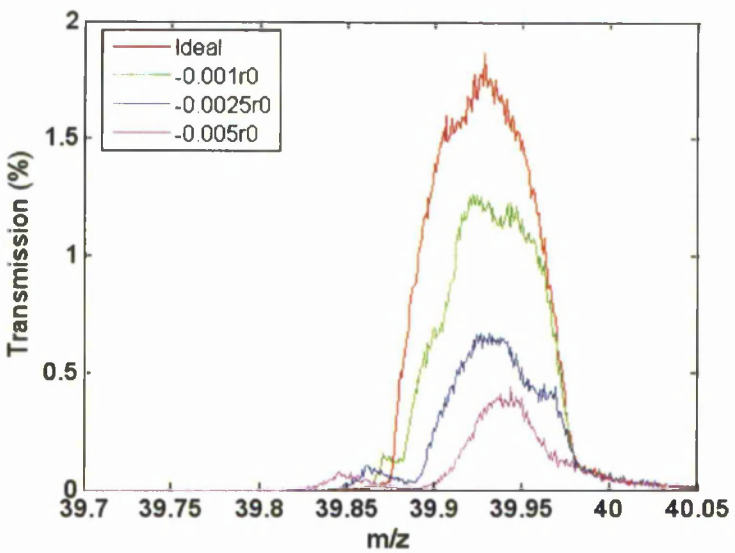

Figure 4.22. Simulated mass spectra for Ar^+ ion species ($m/z = 40$) for a range of orthogonal displacements of an x-electrode for operation in zone 3.

The characteristics of the secondary peak are very similar to that observed for radial displacement of a *y*-electrode. No significant shift in the position of the main peak was observable. For progressive increases in the orthogonal displacement there was an accompanying reduction in the slopes of the mass peaks and a decrease in the peak width at 50% PH. For the case of a *y*-electrode shifted in the *x*-direction (Figure 4.23), changes in peak structure with a variation in a peak split on the low mass side are observable. Peak position and peak width both stay approximately the same for the range of displacement investigated.

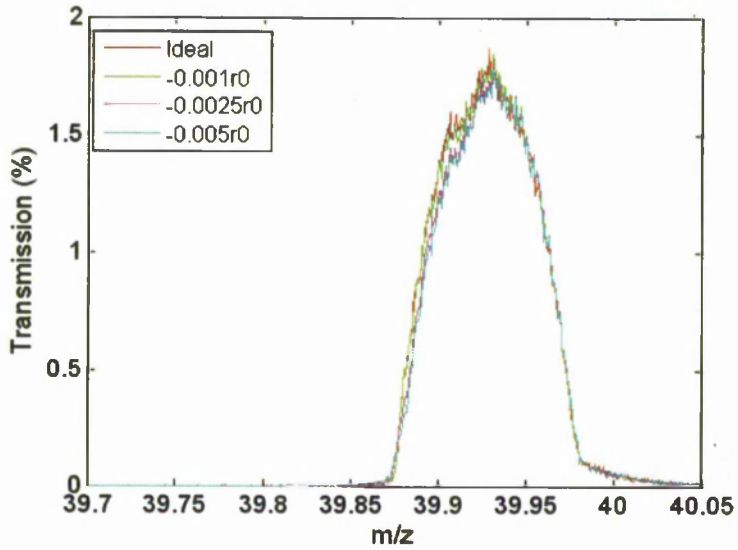

Figure 4.23. Simulated mass spectra for Ar^+ ion species ($m/z = 40$) for a range orthogonal displacements of a *y*-electrode for operation in zone 3.

4.8.6 Compound radial displacement

Figure 4.24 shows the effects of compound misalignments, where both *x* and *y* electrodes are displaced. The resultant mass peak shapes are similar in character to those obtained for an inward displacement of a single *y*-electrode. However, there are differences that are worth noting. Table 4.5 shows that when the *x* and *y* electrodes both have inward radial displacements, the peak position shift is greater. It is approximately equivalent to the sum of the individual shifts obtained for individual *x* and y displacements. The satellite peaks move slightly closer to the main peak, the peak heights are marginally greater and there is increased noise on the main peak. An

inward displacement of a *y*-electrode coupled with an outward displacement of an *x*-electrode, results in the main peak being close to the optimum position. The relative peak positions of the main and satellite peak stay the same with a decrease in their peak heights. These effects demonstrate that the electrode tolerances of individual electrodes can self-compensate for the quadrupole term but the effects of the higher order field components on peak shape, are only marginally altered.

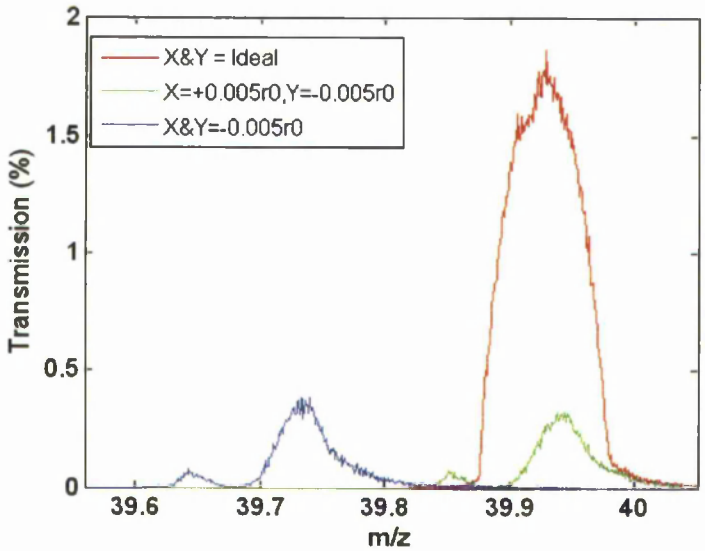

Figure 4.24. Simulated mass spectra for Ar^+ ion species (m/z = 40) for a range of compound inward radial displacements of an *x* and a *y* electrode.

Parameter	Displacement (on-axis)		
	x = 0 y = 0	**x = +0.005×r_0 y = -0.005×r_0**	**x = -0.005×r_0 y = -0.005×r_0**
Peak position (amu)	39.93	39.95	39.74
Peak height (%)	1.79	0.31[1]	0.36[1]
Res 50% PH	524	907[1]	968[1]
Res 10% PH	394	391[1]	358[1]

Table 4.5. Mass spectra characteristics for compound radial displacements of an *x* and *y* electrode (Note [1]main peak value).

4.8.7 Effects of RF frequency with displaced electrodes

The number of RF cycles an ion experiences determines the quality of the mass peak [34], [48]. For zone 1 operation, this relationship is also true when the

electrodes are displaced [49]. Figure 4.25 shows this relationship for zone 3. At 1 MHz (lowest number of cycles) the main peak is very wide not decaying to the 0.1% transmission value on the high mass side within the range of the graph. An isolated peak is apparent with the isolated peak to main peak valley greatly raised above the baseline.

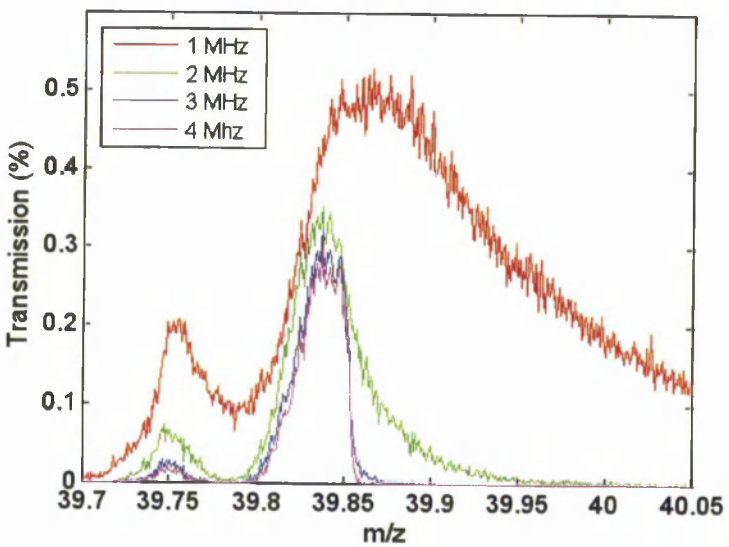

Figure 4.25. Simulated mass spectra for Ar^+ ion species ($m/z = 40$) for a $0.005 \times r_0$ inward radial displacement of a y-electrode for a range of RF drive frequencies.

As the frequency is increased, (number of cycles the ion is exposed to increases) the relative height of the isolated peak decreases more rapidly than the main peak with a defined base line separation appearing. Above 4 MHz (corresponding to 65 cycles), the incremental changes are much smaller and above 8 MHz (130 cycles) no discernible difference can be detected with increasing frequency. This limiting condition occurs at a much lower value than for zone 1 [49].

4.9 Compensation techniques

The significant difference in the effects of x and y displacements has been recognised within the industry for a number of years [49]. The practice of swapping the drive voltage feeds to the x and y electrode pairs have been used as an attempt to overcome problems of asymmetries in the electrode geometry. As can be deduced

from the previous results, this will only be effective for certain asymmetry situations. Modification of the drive voltage on the displaced electrode is a method of compensation that has previously been reported for zone 1 operation [49] and is the subject of a number of patents [52-54]. For an inward or outward displacement of an electrode, changes to the multipole components of the field will occur. Decreasing or increasing the drive voltage to the displaced electrode(s) provides a method of compensating for these electrode displacements. Simulated mass peaks when employing this compensation method for operation in stability zone 3 are shown in Figure 4.26. Comparing this figure to the uncorrected mass peak in Figure 4.20, shows that decreasing the electrode drive voltage alters the mass peak

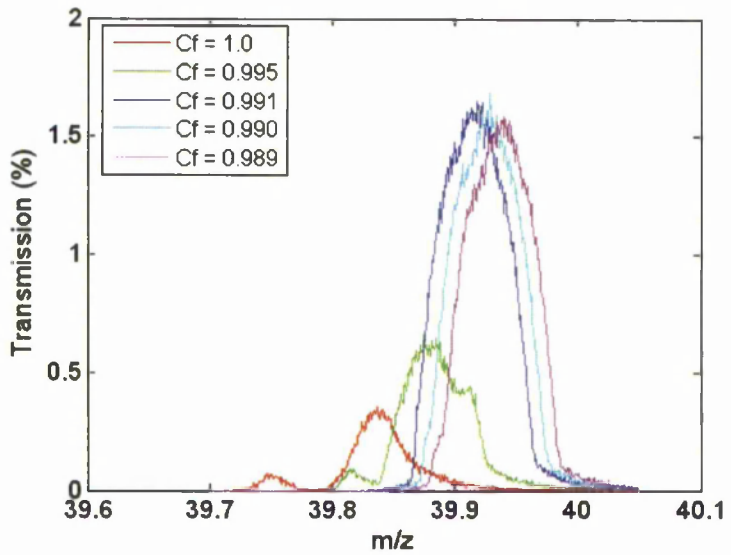

Figure 4.26. Simulated mass spectra for Ar^+ ion species ($m/z = 40$) for a $0.005 \times r_0$ inward radial displacement of a y electrode for a range of compensation factors (Cf). A voltage $Cf \times (-U + V \cos \omega t)$ is applied to the displaced y electrode. (See Figure 4.20 for a comparison with the optimum mass spectra.

and with $Cf = 0.990$ (where the applied voltage is $Cf \times (-U+V\cos\omega t)$,) a close match to the optimum is obtained. This confirms the previously reported correction factor of twice the displacement error [49] for zone 1 and demonstrates that the electric field is defined by the electrode geometry and the relative magnitude and sign of the

electrode voltages. It is therefore possible when considering the overall QMS system that a trade-off between the mechanical accuracy and electrode drive system complexity can be made. An important consideration when employing this method of correction is the stability and accuracy of the drive voltages, as a deviation in the relative *y*-electrode drive voltage will cause the mass peak to degrade in a similar fashion to that produced by a displaced electrode. These simulations suggest that the total error budget for the drive voltage should not be greater than +/- 0.1%.

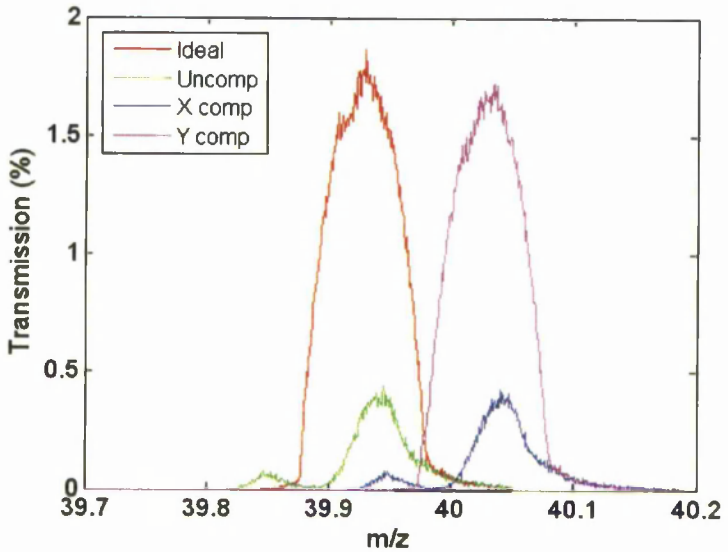

Figure 4.27. Simulated mass spectra for Ar+ ion species (m/z = 40) for a displaced x electrode shifted by 0.005 × r_0 in the y-axis, showing the effects of compensation (Cf = 0.990) applied to the *x* and *y* electrodes individually.

Figure 4.27 shows the results of applying the compensation technique described previously for attempting to compensate *y*-displacements of an *x*-electrode by applying the correcting voltage to one of the *y*-electrodes. The compensating voltage is applied to the upper electrode for a positive *y*-displacement and the lower electrode for a negative *y*-displacement. This compensation restores the mass peak shape and is accompanied by a marginal reduction in peak height and a shift to a higher mass position for both types of displacement. Application of the correcting voltage to the misplaced *x*-electrode, results in a shift in the mass peak but with no accompanying correction to the mass peak shape.

4.10 Asymmetrical behaviour

When one or more electrodes are displaced, the symmetry of the electrode geometry is altered. This reduction in the degree of symmetry introduces into the field the 4N multipole terms that are not present in the optimum QMF field [11], [38]. Table 4.6 contains the multipole coefficients for the range of electrode displacements investigated. For the optimum circular electrode geometry only the A_2, A_6, A_{10} and A_{14} terms are present. Firstly, consider the changes to these components. The A_2 multipole coefficient increases with increasing electrode displacement for both x and y electrode displacements. Outward on-axis displacements exhibit a comparable decrease in this term. This increase/decrease in A_2 has an equivalent effect to an increase/decrease in Φ_A, and is the major contributor to the observable shift on the mass scale.

Considering next the remaining 4N+2 multipole terms A_6, A_{10} and A_{14}, our results show that these vary by a very small amount. Previous research has shown that these terms depend on the r/r_0 ratio and that possibly A_6 and A_{10} act in a way to self-compensate [11]. As these three terms do not vary significantly, it can be assumed that they do not contribute in any major way to the effects that are observed for displacements of an electrode. Examination of Table 4.6 shows that for these displacements the A_4, A_8 and A_{12} multipole (4N terms) become non-zero and all are of the same sign and increase with increasing displacement. The magnitude of the A_4 and A_8 terms are approximately two orders of magnitude less than A_6 and A_{10} and an order of magnitude greater than the A_{12} term. It can be deduced that the presence of the A_4, A_8 and A_{12} terms result in the shoulder forming and for the isolated peak appearing when the y-electrode is displaced. It is not possible to deduce from these results the exact contribution each of these terms make to the overall effect. It may well be the case that the three terms reinforce each other to achieve the overall effect or more likely given the non-linear nature of these coupled terms they interact in a more complex manner.

The results show that the effect of changes due to electrode displacement are not the same for x and y electrodes. Although the optimum electrode geometry is symmetrical about the x and y axis there is asymmetry due to the average (mean)

Displacement	Multipoles						
	A_2	A_4	A_6	A_8	A_{10}	A_{12}	A_{14}
0	1.0016×10^{0}	-	1.20×10^{-3}	-	-2.43×10^{-3}	-	-2.96×10^{-4}
$-0.001\times r_0$	1.0021×10^{0}	1.58×10^{-5}	1.18×10^{-3}	1.17×10^{-5}	-2.43×10^{-3}	1.90×10^{-6}	-2.97×10^{-4}
$-0.0025\times r_0$	1.0029×10^{0}	3.98×10^{-5}	1.16×10^{-3}	2.96×10^{-5}	-2.44×10^{-3}	4.79×10^{-6}	-2.98×10^{-4}
$-0.005\times r_0$	1.0042×10^{0}	8.10×10^{-5}	1.11×10^{-3}	5.99×10^{-5}	-2.46×10^{-3}	9.69×10^{-6}	-3.00×10^{-4}

Table 4.6. Multipole coefficients obtained using Poisson/Superfish for radial displacements of a single x or y electrode.

potential that is applied to the electrodes and the charge on the ion. The mean potential averaged over a number of cycles is negative for the y-electrodes and positive for the x-electrodes. Due to the positive charge on the ions they will on average be repelled by the x-electrodes and attracted to the y-electrodes. This results in an increased instability of the ions in the y-axis with a distortion of the low mass side of the y stability region. These observed effects on peak shape are due to a combination of the A_4, A_8 and A_{12} multipole terms and the average polarity of the electrode potential. This inter-relationship between the effects of electrode displacement and electrode potential has been previously reported [73]. The relationship is also confirmed by the industry practice of exchanging the voltage drive to the x and y electrodes as a method of improving QMF performance [49].

4.11 Conclusions

A toolbox has been developed using a combination of public domain and custom written software that provides a flexible method for investigating performance characteristics of QMF.

Results obtained using this toolbox has shown that zone 3 provides improved immunity from the effects of variations in the nominal value of r/r_0. The increase in mass tail amplitude and width, as r/r_0 moves away from the optimum which is a characteristic of zone 1, are negligible for zone 3. It has also been demonstrated that ion trajectory power spectra provide a quick and useful method of finding an approximate optimum value for r/r_0.

Asymmetries in the QMF electrode geometry introduced due to variations in the individual electrode radii or through electrode displacements produce degraded performance. The effects depend on the plane of the displacement. Displacements in the y-direction or radii errors of the y-electrode result in the most serious performance degradation.

These results also demonstrate that the previously reported method of compensation for axial displacement of an electrode by adjustment of the electrode drive voltages is also valid for a QMF operated in zone 3. This also holds for orthogonal shifts of an electrode. As this method of compensation can introduce peak

shape errors similar in character to displaced electrodes, it is therefore necessary to maintain tight control of the differential electrode voltages.

The actual ratio r/r_0 is important in maximising the resolution and/or sensitivity of a QMF. However ensuring the symmetry of the electrode structure is more important as the errors introduced through poor symmetry have a more detrimental effect on QMF performance. The results obtained so far suggest that an acceptable range for r/r_0 is 1.12 to 1.13 which equates to +/- 0.005 $\times$ r_0 on the nominal value. While results show that a tighter asymmetry budget of +/- 0.001 $\times$ r_0 is required. These values demonstrate that when designing a QMF and the manufacturing process, more consideration should be given to maximising the quality of the electrode symmetry than the absolute value of r/r_0.

Chapter 5

5. QMFs – HIGH RESOLUTION AND MINIATURISATION

5.1 Introduction

In this chapter, two particular but very different specialised implementations of a QMF are considered. The first is a high resolution instrument for in situ process monitoring of gases over the mass range 1 to 6.2 amu. The second is an investigation of the performance characteristics of QMF fabricated using Micro Engineered Electro-Mechanical Systems (MEMS) technology.

5.2 Measurement of low mass isotopes

In the previous chapter the effects of mechanical tolerances on QMF performance were investigated. In undertaking that investigation consideration was given to single species performance. For most practical applications a QMS/QMF is usually applied to identifying a number of species that compose the sample under investigation [112-113]. The actual application dictates the minimum performance requirement of the QMS/QMF to be used. Most commercial manufacturers make the performance specification as general as possible in order to target the maximum possible pool of end users. For certain specialised applications this generic specification will not be acceptable. For example the detection of traces of Helium (He) in a sample of CO_2 can easily be achieved with a standard unit mass resolution (constant peak width of 1 amu) QMF and would be considered a relatively benign application given the large mass differences between the species. If the presence of diatomic Hydrogen (H_2) is introduced into the sample, the application becomes more onerous due to the reduced mass difference between H_2 and Helium. It is still achievable with a unit mass resolution QMS. If the presence of the Hydrogen isotopes Deuterium (D_2) and

Tritium (T_2) are included, along with their molecular combinations, the application becomes much more exacting. This final scenario forms the basis of an application that is now investigated in more depth.

5.3 Operational requirement

This application was considered as part of a feasibility study carried out for the Atomic Weapons Establishment (AWE) under their outreach program. The study investigated the feasibility of manufacturing a QMS for use as an on-line hydrogen isotope process monitoring and surveillance system on a gas process line at AWE. The vacuum side of the QMS would have to be capable of being mounted within a Nitrogen filled glovebox to ensure safe containment of the process gases. This in turn places restrictions on the maximum dimensions of these elements of the QMS. A length of 300 mm was considered an acceptable maximum for the QMF section.

Table 5.1 shows the species that would comprise the process sample together with their masses and the calculated minimum resolution to separate them. The data shows that a maximum mass range of approximately 6.2 amu with a minimum resolution of 931 to achieve separation of HT from D_2 is required. The next highest resolution of 513 is required for the separation of ^{3}He and HD.

A number of similar but less demanding applications requiring high resolution for low mass ions already exist include Helium (^{4}He) leak detection in the presence of high deuterium partial pressures D_2 [114] and the separation of ^{4}He and D_2 [57], [59], [115-117]. The majority of commercial QMSs and in particular residual gas analysers (RGA) are designed to provide a mass range of 64 amu and upwards, combined with a fixed unit mass resolution, making them unsuitable for this application. The inability of standard commercial QMSs to resolve ^{4}He and D_2 is an easier task and has been observed by Winkel [114] and Day [5]. A specially modified QMS where the ions where shielded from the entrance fringing field with a higher specification RF control was successful in separating ^{4}He and D_2 [115], [118]. More recently Day applied a modified Balzers GAM400 to successfully separate ^{4}He and D_2 [5]. This was achieved by decreasing the mass range to achieve a decreased mass step size, thereby increasing the achievable resolution of the QMS to a maximum of 400, which is still insufficient for this application.

Species		H_2	^3He	HD	^4He	HT	D_2	T_2
	Mass (amu)	2.01565	3.016029	3.021927	4.002602	4.0238743	4.028204	6.032099
		MINIMUM RESOLUTION REQUIRED						
H_2	2.01565	NA	3.0	3.0	2.0	2.0	2.0	1.5
^3He	3.016029	2.0	NA	512.4	4.1	4.0	4.0	2.0
HD	3.021927	2.0	511.4	NA	4.1	4.0	4.0	2.0
^4He	4.002602	1.0	3.1	3.1	NA	189.2	157.3	3.0
HT	4.0238743	1.0	3.0	3.0	188.2	NA	930.5	3.0
D_2	4.028204	1.0	3.0	3.0	156.3	929.5	NA	3.0
T_2	6.032099	0.5	1.0	1.0	2.0	2.0	2.0	NA

Table 5.1 Mass values [119] and minimum resolution required to discriminate between the each of the gas species present (see also Fig. 2.9 for additional information).

5.4 Choice of stability zone

The maximum resolution of a QMS is limited by; the constructional accuracy [37], the accuracy and stability of the drive electronics [93], and by the number of RF cycles the ions experience [37], [93]. For a QMF length of 300 mm and operated at an RF frequency of 6 MHz a ^{4}He ion with an energy of 5 eV would experience approximately 116 cycles of RF. However, for zone 1 operation the ions would have to experience 200 cycles or greater to achieve a resolution in the order of 1000 [37]. Therefore, achieving high resolution with zone 1 with the physical constraints imposed by the application is not a practical proposition. Zone 3 is an alternative stability zone of approximately rectangular shape offering potentially higher resolution at two tips, the upper tip ($a_\mu \approx 3.16$, $q_\mu \approx 3.23$) and the lower tip ($a_\mu \approx 2.52$, $q_\mu \approx 2.81$) [93]. The upper tip provides potentially the greater resolution with marginally less sensitivity when compared with the lower tip, with a resolution of up to 4000 at 59 amu reported [120]. These characteristics were the basis for choosing to investigate the suitability of zone 3 for this application.

5.5 Factors affecting mass separation

In the previous chapter it was demonstrated that when using circular electrodes the ratio of r/r_0 and the tolerance on the asymmetry of the electrode geometry were contributory factors to the maximum achievable resolution. It was also demonstrated that differences in the drive potential applied to the electrodes had a similar effect to that of a displaced electrode and from this it can be inferred that accuracy of the drive potentials are also important in maximising performance.

Most modern instrumentation systems use a combination of digital and analogue techniques to measure and acquire information on the process variables they are measuring. In the case of a QMS, the process variable is a gas phase sample which is converted by ionisation into an ionic current. This is then measured by means of a Faraday Cup or Electron Multiplier. The ionic current is measured at discrete points as the mass scan line is varied. This enables mass spectra for the sample to be acquired. Normally the mass data would be assembled as a series of digital words, each word representing one point on the mass scale. This data acquisition system can

be considered as a sampling system and must as a minimum satisfy the Nyquist criterion to capture the data without introducing aliasing effects [121-122]. This can be interpreted as the number of samples across the mass scan line must be sufficient to resolve the components present in the sample. The mass scan line sets the resolution of the QMF within the limits set by operational characteristics, such as the number of RF cycles the ion experiences. Any unintended shift in the scan line due to drift in the electronic control electronics will change the instantaneous resolution and affect the resultant mass spectra.

5.6 Comparison of circular and hyperbolic electrodes

Circular electrodes and their mounting systems are less costly to manufacture, although they have the disadvantage of inferior performance [4], [37] when compared with the more expensive hyperbolic electrodes.

	CIRCULAR		HYPERBOLIC	
	RESOLUTION			
Length (mm)	**10% PH**	**50% PH**	**10% PH**	**50% PH**
125	258	863	206	629
250	686	944	755	1678
300	702	944	915	1777

Table 5.2. Variation of resolution with length, for circular and hyperbolic electrodes operating at 5 MHz with ion energy of 15 eV for a HD^+ (3.02 *m/z*) ion operation in zone 3.

Table 5.2 contains results of a number of simulations undertaken to quantify the achievable resolution for both hyperbolic and circular electrodes for operation in stability zone 3. Circular electrodes show increasing resolution as the length of the QMF is increased for 10% PH resolution, whereas at 50% PH the resolution does not improve for lengths above 250 mm. For hyperbolic electrodes there is no such limiting effect they provide superior performance for lengths of 250 mm and above. Although this initial test is for a single species of HD^+, even when operating with hyperbolic electrodes of a length of 300 mm at 10% PH, the resolution just fails to achieve the requirement for separation of HT^+ and D_2^+.

5.7 Instrument resolution control

Applying Equation 3.9 the Mathieu stability diagram can be transformed into *U-V* space. Figure 5.1 shows a composite zone 3 stability diagram for ^{4}He and D_2 with scan lines at two instrument resolution (η) settings superimposed. The two mass species have a small difference in their respective mass values ($\approx$ 0.0256 amu) this results in an overlap in their respective stable zones for certain combinations of U and *V*. For the values of η shown the scan line does not enter this overlapping stable area, a clear separation between the two scanned areas exists. If the scan line is shifted negatively in the *U* direction by greater than -0.65 volts with η = 0.9995 or -0.81 volts with η = 0.9999 the scan line intersects the overlapping area. This situation increases the probability that ions of both types would pass through the QMF concurrently.

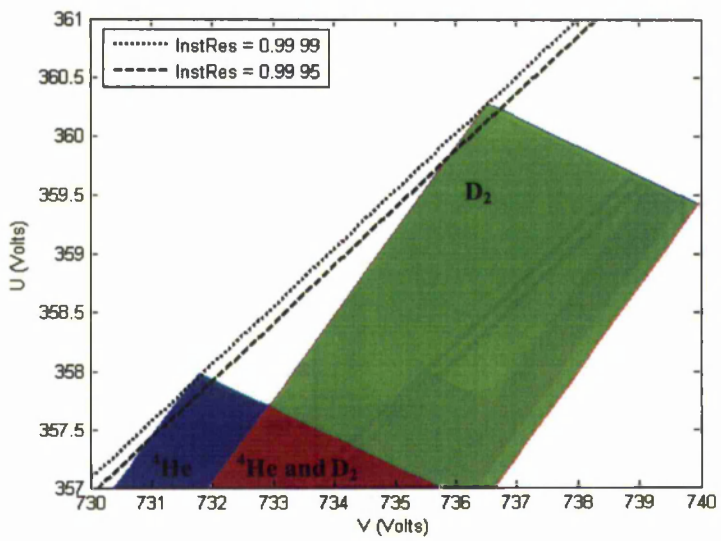

Figure 5.1. Zone 3 stability diagram in *U-V* space for ^{4}He and D_2 showing non-overlapping and overlapping areas with superimposed scan line for two settings of η.

Figure 5.2 shows a similar diagram for the species HT and D_2 whose mass difference is much less ($\approx$ 0.00433 amu). The same two scan lines are again superimposed and it can be seen that when η = 0.9995 the scan line intersects the area where both species are stable. Only with η = 0.9999 is there clear separation

between the unique stable areas. With η = 0.9999, there is a margin of -0.1 Volt to the point where the scan line intersects the overlapping stable area. The margin in the positive direction is the same for both cases at +0.05 volt for η = 0.9999.

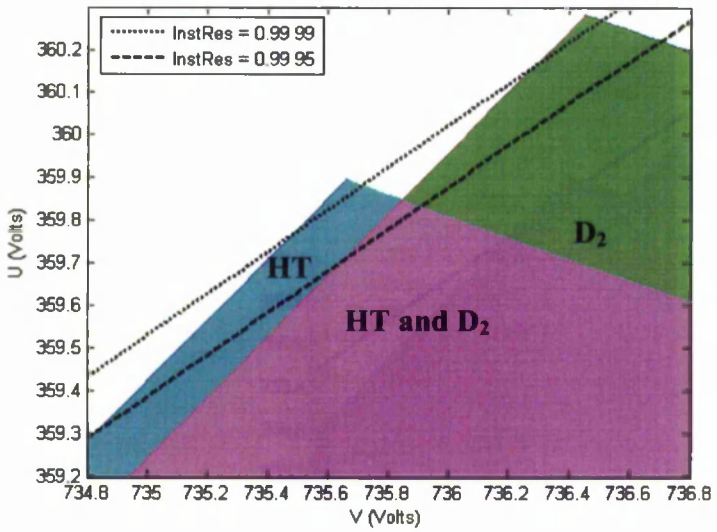

Figure 5.2. Zone 3 stability zone in *U-V* space for HT and D_2 showing non-overlapping and overlapping areas superimposed scan line for two settings of η.

The effect of voltage offsets in *U* for η = 0.9999 with an equal abundance of HT and D_2 is demonstrated through computer simulation. The resultant mass peaks are shown in Figure 5.3. As the mass scan is shifted lower (*U* reduced by a negative offset); the transmission increases, the resolution decreases and the inter-peak valley minimum increases. At the extreme of the offset the valley becomes an additional peak with an amplitude greater than the individual HT or D_2 peaks. This additional peak corresponds to where the scan line passes through the overlapping area (HT and D_2 stable). This is very similar to the outcome that would be seen for a scan line with η = 0.9995; where first the HT stable area is traversed, followed by the HT and D_2 stable area, then finally the D_2 stable area. Additional simulations for a scan line shift in the opposite direction result in a reduction in the peak amplitude and width, to a point where the ion transmission becomes so low that the QMS would be unusable.

This is the equivalent of operating the QMS at $\eta \geq 1$. This effect is similar to that reported by Gibson and Taylor for a QMF operating in zone 1 [4].

a)

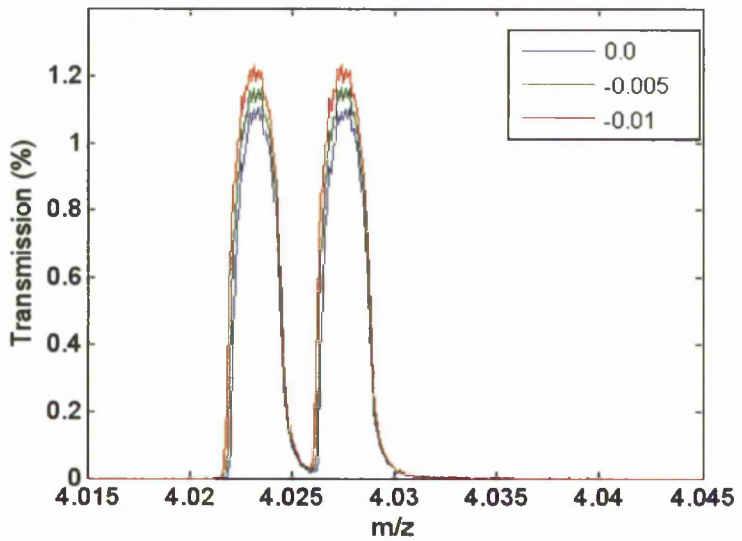

b)

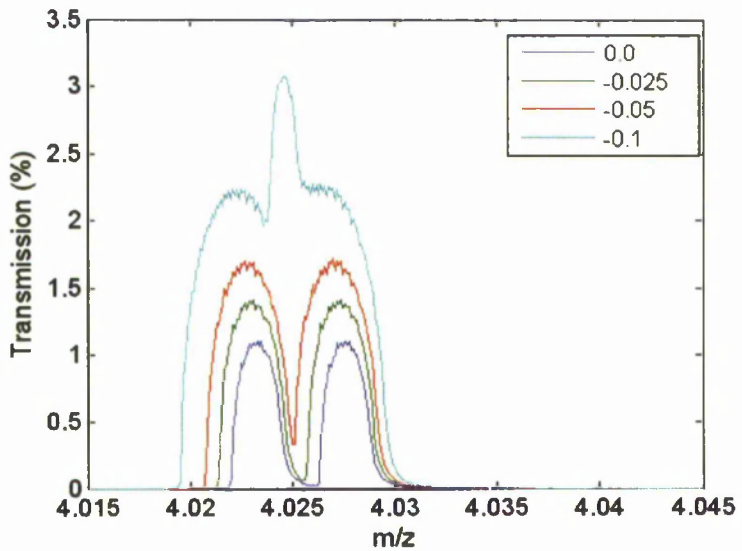

Figure 5.3. Mass spectra for ^4He and D_2 for a range of U voltage offsets: with QMF length (L) = 300mm, field radius (r_0) = 2.76 mm, ion source radius (R_s) = 0.4 mm, ion energy (E_i) = 15 eV, a) acceptable offsets, b) increasingly unacceptable offsets.

The scan line operating point and the tolerance on this setting is dependent on the application. The higher the resolution required by the application the smaller the

acceptable operational tolerance. A similar situation exists for the RF amplitude. The important criterion is the maintenance of the ratio of the RF and the DC amplitudes i.e the ratio of U/V must be maintained to close limits.

5.8 Mass scan step size

As previously mentioned, the mass scan line can be viewed as a sampling system with respect to the gas phase sample. If the mass step size is too large with respect to the mass differences between the species to be separated, a species may be missed or an incorrect abundance may be measured. Sampling theory dictates that to preserve the information contained in a continuous signal a sampling rate of twice the minimum period is required [121-122]. For the requirement of a minimum resolution of 930 or a baseline width of 0.004329288 amu, then a maximum step size of 0.004329288/2 amu = 0.002164644 is required to achieve the desired separation. Figure 5.4 shows a set of simulated mass spectra for HT and D_2. This figure clearly demonstrates the effect of mass step size on the ability to separate adjacent species. For the case of a step size of 0.003 amu, only a single peak can be observed. Reducing the mass step size to 0.0015 amu (less than required by sampling criteria) two mass peaks are now visible but with limited peak shape and an imbalance between their relative abundances. At a step size of 0.001 amu the peak amplitude is approximately the same, with the peak shape possessing observable differences. Further reduction of the mass step size produces improvements in the peak shape, peak height and resolution. For a step size of 0.00025 amu the two peaks are nearly identical in shape and with similar peak structure in evidence.

The above results demonstrate that the mass step size required to adequately discriminate between the adjacent peaks of HT and D_2 and provide an accurate abundance measurement is less than that calculated using sampling theory. However, additional information over and above basic separation is required in the form of the peak height and peak position. Because of the shape of the mass peaks, higher frequencies are present than those indicated by the baseline resolution. To sample these higher frequencies requires a much smaller mass step size.

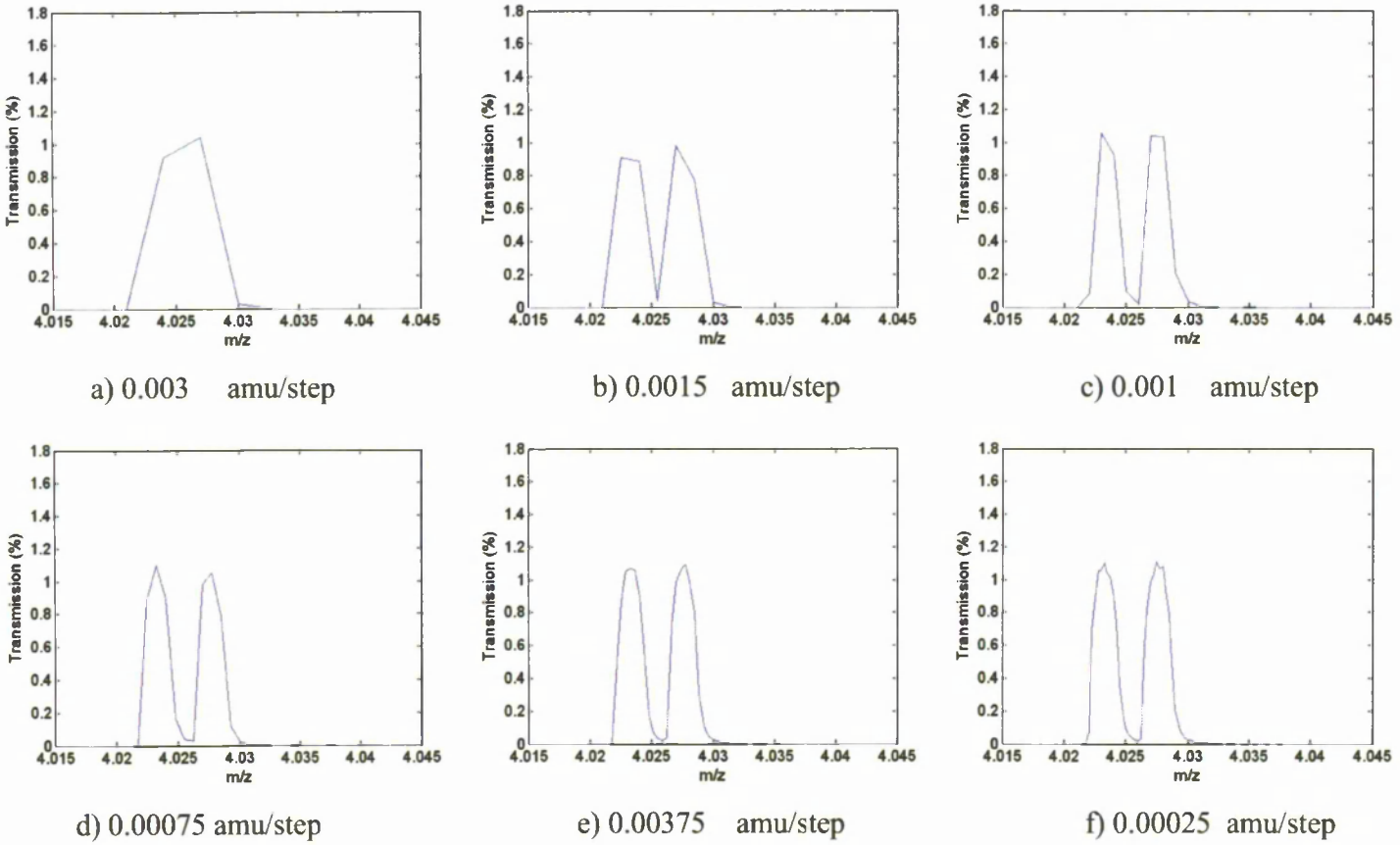

Figure 5.4. Effects of mass step size on peak shape and mass discrimination performance for an equal mixture of HT and D_2 (mass separation = 0.0043292 amu), L = 300mm, r_0 = 2.65 mm, F = 6 MHz, E_i = 15 eV.

5.9 Effects of RF frequency on peak shape

When considering the quality of performance provided by a QMF, the abundance sensitivity is important as this provides a measure of the contribution an adjacent species makes to the measured abundance of its nearest neighbour(s). Figure 5.5 shows computer simulated spectra for HT for a range of RF frequencies. Figure 5.5a shows the full mass peak. For the operating conditions investigated the peak width at

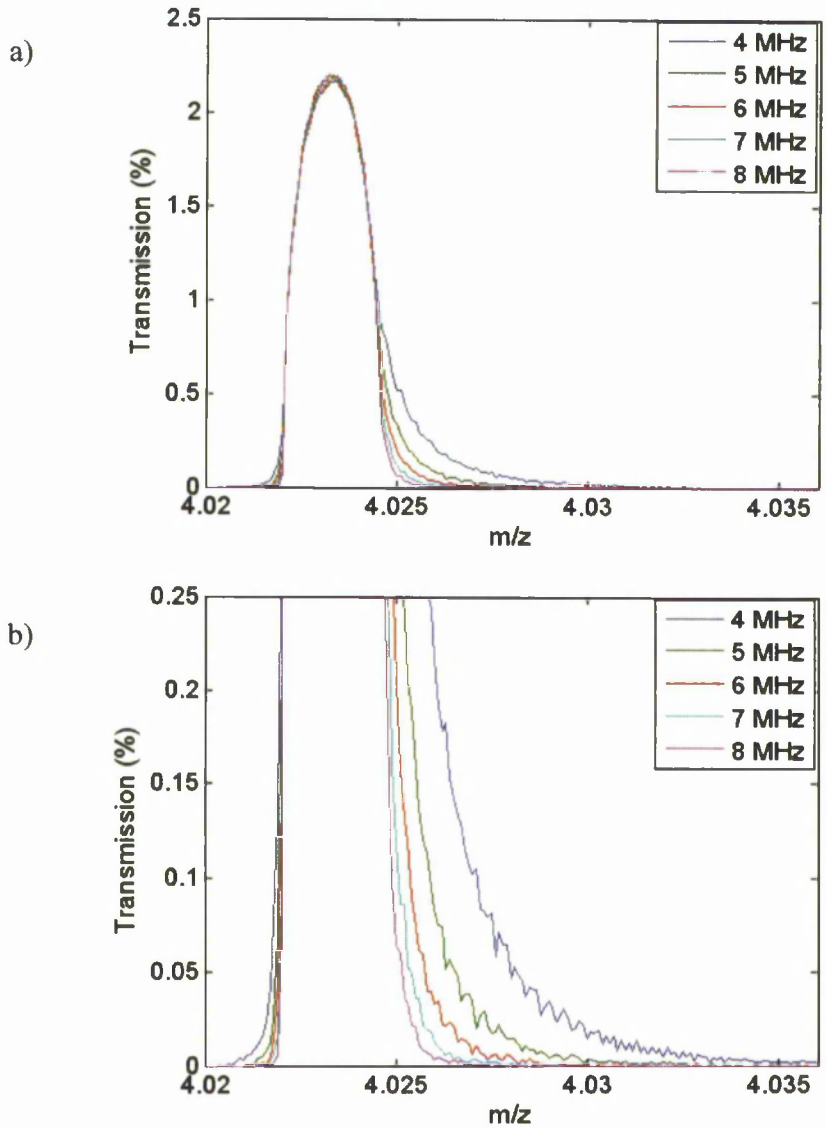

Figure 5.5. Variation of HT mass spectra with frequency (L = 300 mm, r_0 = 2.76 mm, E_i = 15 eV, R_s = 0.276 mm; a) complete mass peak, b) detail of high and low mass tails.

a)

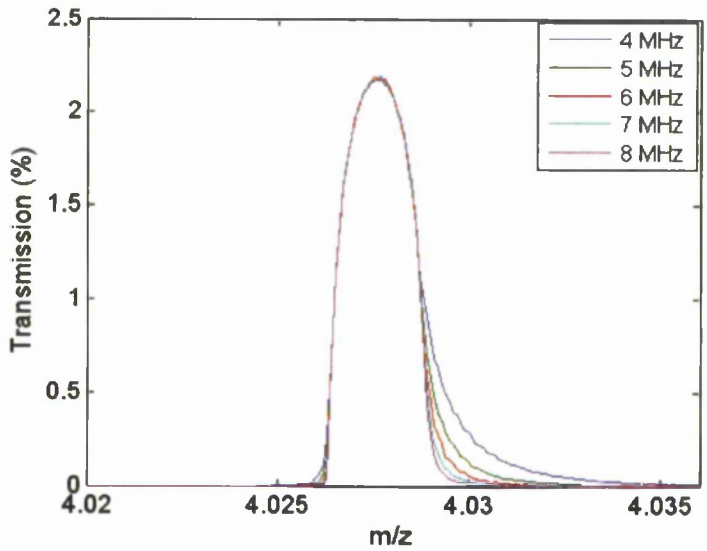

b)

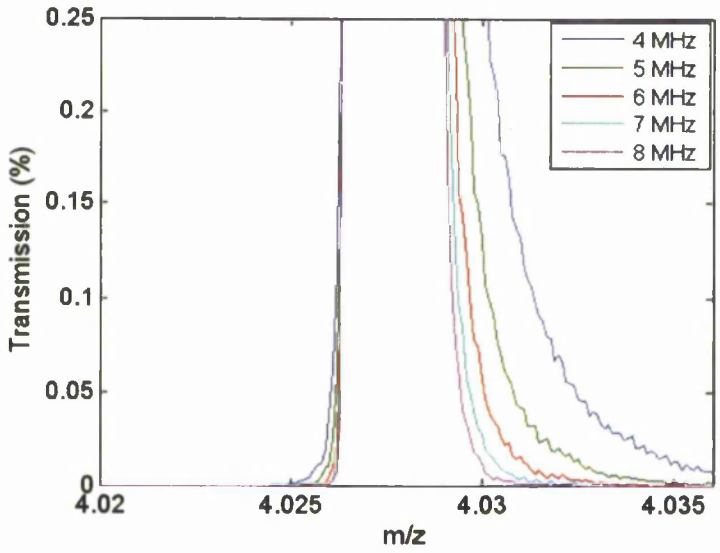

Figure 5.6. Variation of D_2^+ mass spectra with frequency (L = 300 mm, r_0 = 2.76 mm, E_i = 15 eV, R_s = 0.276 mm; a) complete mass peak,b) detail of high and low mass tails.

50% PH does not change, whereas at 10% PH the peak width decreases as the RF frequency is increased. The reduction in the high mass tail is the contributory factor to the peak width decreasing. This indicates that the main influence on abundance sensitivity will be between HT and the next higher mass species. This is different to the lower tip of zone 3 [67] where the low mass tail is more dominant. Figure 5.5b shows these mass tails in more detail. If the effect of the HT high mass tail on the D_2 (4.0282036 amu) peak is now considered. At an RF frequency of 4 MHz the

contribution to a D_2 mass peak at 4.0282036 amu on the mass scale is a transmission of 0.05% which if the relative abundances are the same, represents a 2.27% contribution to the total peak height. At a frequency of 5 MHz this contribution decreases by a fifth to 0.45%, progressively decreasing as the frequency is increased further. Above 6 MHz the contribution becomes negligible. The contribution is greater for lower mass points on the D_2 peak but decreases more rapidly with increasing frequency due to the simultaneous contribution of a decreasing high mass tail amplitude and an increase in high mass side slew rate. The significance of this effect depends on the relative abundances of the two species. For a very small abundance of HT and large abundance of D_2 the effect is not as severe as when the relative abundances are reversed. The extent that the low mass tailing spreads is such as not to influence the next lower mass (^{4}He).

A similar set of simulations are shown in Figure 5.6 for D_2. They exhibit very similar characteristics. For this application the presence of the high mass tail will not influence the abundance of the next higher species T_2, as the separation is over 2 amu. The low mass tail will however make a small contribution to the high mass peak edge of HT as there is minimal baseline separation between the two peaks for the range of frequencies tested. Overall, the abundance sensitivity effects are due to the high mass tail contributing to the next heavier species. This is most severe for HT and D_2, as these two species have the least mass separation.

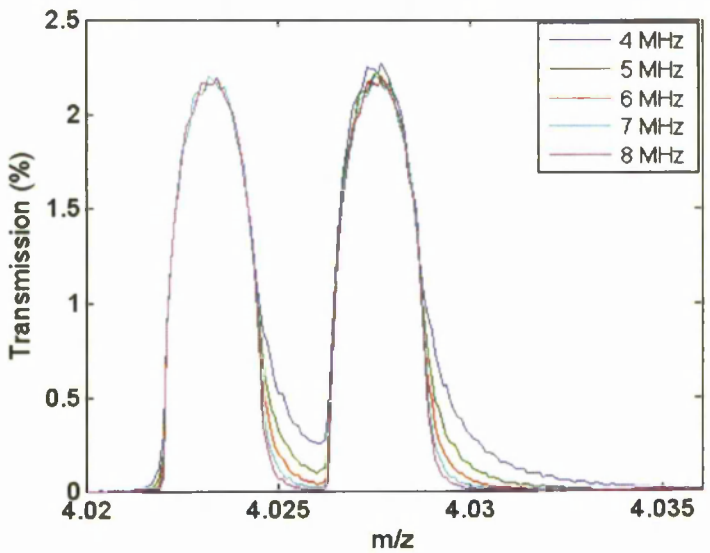

Figure 5.7. Mass spectra for HT^+ and D_2^+ for a QMF with L = 300 mm, r_0 = 2.76 mm, E_i = 15 eV, R_s = 0.276 mm for a range of frequencies.

Figure 5.7 shows the simulated results of HT in the presence of an equal abundance of D_2. The influence of the high mass HT tail on the valley between the two species can be seen. As the frequency is reduced the floor of the valley lifts to above 10% of peak height at a frequency of 4 MHz. Resolution for the two species is nearly identical reflecting the close mass values and the result that the two species of ions experience very similar numbers of RF cycles. Limiting of the 50% peak height (PH) resolution occurs at approximately 6 MHz, indicating the maximum resolution that is achievable for this instrument setting. The 10% PH resolution still increases with increasing RF frequency. The rate at which the 10% PH resolution increases slows above 6 MHz, but it still is significantly higher than the 50% PH resolution.

		Frequency (MHz)				
Species	**Resolution**	**4**	**5**	**6**	**7**	**8**
HT	**10% PH**	914	1087	1183	1219	1257
	50% PH	1749	1829	1829	1829	1829
D_2	**10% PH**	915	1118	1220	1258	1299
	50% PH	1751	1831	1918	1918	1918

Table 5.3. Comparison of HD and D_2 resolutions for a 300mm length QMF with E_i = 15 eV for a range of RF frequencies operating in zone 3.

5.10 Ion source alignment

The ion source provides the mechanism whereby the sample species are converted to positively charged particles or ions. In this section, the effects of mechanical misalignment of the ion source are investigated. This provides an understanding of how mechanical tolerance of the ion source to QMF alignment may impact on the performance of the QMF. Figure 5.8 shows computer simulated mass spectra for a range of x and y direction displacements of the ion source with respect to the QMF axis. Both x and y displacements exhibit similar characteristics, with the y-displacement producing the greater decrease in transmission for a given displacement. These characteristics can be explained by the difference that exist between the x and y acceptances [123]. It was also found that concurrent displacements in x and y produce a cumulative decrease in transmission. Also in

evidence are decreases in the slopes of the peak edges, more marked on the high mass side. This is accompanied by a reduction in peak width as displacement is increased. The relationship between these peak characteristics and displacement are the same irrespective of the direction of displacement. These characteristics indicate that the acceptance is symmetrical about the x and y axis and is greater than the ion source radius (R_s) of 0.4 mm. For the conditions tested, a tolerance of +/- 0.2 mm in each axis is considered acceptable.

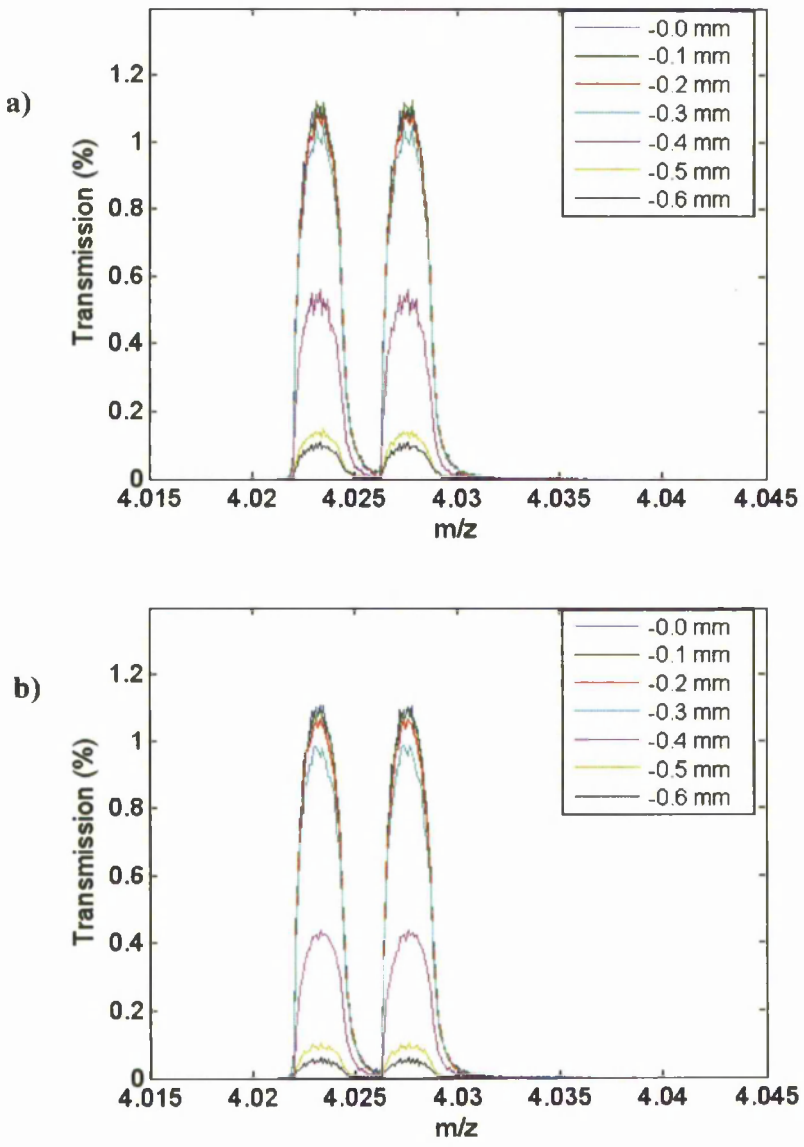

Figure 5.8. Effects of misplaced ion source for L = 300 mm, r_0 = 2.76 mm, R_s = 0.4 mm, F = 6 MHz, E_i = 15 eV; a) x-direction displacement, b) y-direction displacement.

5.11 Miniaturisation

Traditional machining techniques used in the manufacture of a QMS may be suitable for low volume production and for equipment that is deployed in locations such as laboratories, process plants and land based vehicles. These traditional production techniques are characterised by weight, volume, power dissipation and manufacturing costs. For certain applications such as airborne, space and covert monitoring, the magnitude of these characteristics may be a barrier to their use. Therefore, alternative methods of manufacturing are actively being sought [78], [80], [84], [124-125] to achieve a reduction in the magnitude of some or all of these physical characteristics. To achieve these goals, mature process technologies that enable accurate electrode profile definitions to be manufactured are a lower risk option. One possible technology is used by the semiconductor industry in the manufacture of integrated circuits. These process technologies enable feature sizes down to the sub-micron level to be constructed. Miniaturisation also brings the additional advantage of higher pressure operation, thereby reducing the vacuum pumping requirements. Higher pressure may also compensate to some extent for the loss of sensitivity that occurs when the field radius (r_0) is scaled down [37].

While modern semiconductor processes are very accurate (absolute terms), at least when compared to traditional manufacturing processes, there are certain disadvantages in using them. The process is much more suited to the manufacture of QMFs with rectilinear profile electrodes [126] whose performance characteristics are not as well understood as their more conventional cousins.

5.11.1 A QMF with rectilinear electrodes

The effect of electrode geometry has been discussed in previous chapters where the effects of circular electrodes and the ratio of their radius (r) to the r_0 were assessed. Attempts to use other electrode profiles until recently have only attracted limited interest. Hayashi and Sakudo (Figure 5.9a) [69], Sakudo and Hayashi (Figure 5.9b) [70], Pearce and Halsall (Figure 5.9c) [71], have all reported on non-standard electrode geometries.

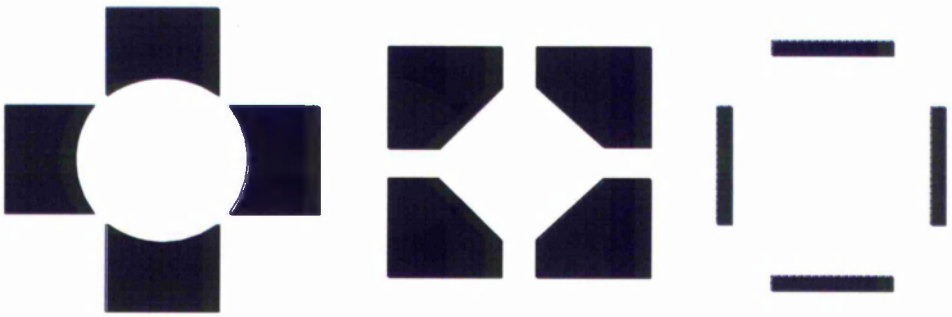

a) b) c)

Figure 5.9. Alternative electrode profiles; a) concave electrodes, b) flat faced electrodes, c) flat bar electrodes.

In addition to these researchers, Sillon and Baptist reported on the use of silicon micro technologies to fabricate a low cost miniature mass spectrometer which was capable of working at a high vacuum pressure (>0.999 Pa). A quadrupole mass spectrometer, and a Wein filter had both been developed by them but only the Wein filter was reported [127]. A Wien filter uses simultaneous crossed electric and magnetic fields to produce a trajectory in the direction of a detector for ions of one particular *m/z* value. Other masses can be obtained by varying one or both of the fields. A micro-machined all silicon process was used to produce wafers containing the rectilinear electrode array. Channels were formed by bonding two wafers together with selective metallization and laser drilling to complete the device. The rectilinear electrodes are used to produce the electric field with strong external magnets for the magnetic field. Tests confirmed that for the applied operational conditions Helium ions behaved in the correct manner. The resolution was poorer than anticipated but sufficient to separate Helium from Hydrogen and Nitrogen. Another example of a micro-engineered mass filter is described in a patent by Baptist [128]. The patent covers the application of electrodes of polygonal section for the generation of multi-polar fields to act as a mass filter. Also covered is the use of standard semiconductor processing processes to fabricate polygonal shaped micro-electrodes.

5.11.2 An example of a micro-fabricated QMF

Cheung investigated the relationship between the aspect ratio of rectilinear cross-section electrodes, the central field area and the resultant electric field [129]. The potential field was solved with MAXWELL-2D and a MatLab script used to extract the multipole expansion for the potential fields [129]. For the particular case of square electrodes the odd terms of the multipole field were minimised reflecting the four fold symmetry of the electrode geometry. For square electrodes, a minimum for the ratio of the even multipoles A_6, A_{10} and A_{14} and the quadrupole term was found to occur when the spacing between the electrodes equalled the dimension of one side of an electrode. These findings were used by Cheung in his development of the MEMS Quadrupole Mass Filter. This new device was named the Micro-Square Electrode Quadrupole Mass Filter (MuSE-QMF). A diagram of the physical arrangement of the device can be seen in Figure 5.10. The device measured 4 mm × 15 mm × 33 mm and consisted of a QMF and associated inlet and outlet ion optics. Fabrication of the device was undertaken at the Massachusetts Institute of Technology (MIT) Microsystems Technology Laboratories. A photograph (Figure 5.11) of the completed device can be seen alongside a U.S.A. $0.25 coin to give a sense of scale. Integration of the electrodes, ion optics and housing into one monolithic block eliminates (minimises) the electrode to housing misalignments providing improved performance [129].

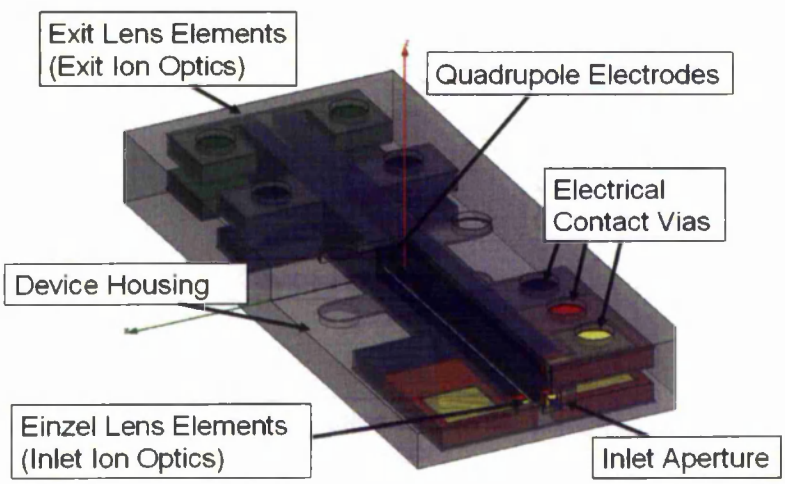

Figure 5.10. General arrangement of a micro-fabricated QMF [128].

Figure 5.11. Fabricated MuSE-QMF alongside a U.S.A. $0.25 coin [128].

5.12 Simulation and experimental methodology

Computer simulation studies were undertaken using QMS2-Hyperbolic and QMS2-Field (section 3.5.3 and 3.5.4) with the test conditions as stated in Table 5.4 unless otherwise stated. For the experimental rig the MuSE-QMF was mounted in a much larger diameter housing 80.6 mm diameter to enable the mounting of the MuSE-QMF on a conventionally scaled test assembly. Figure 5.12 shows a cross section for a circular QMF and the MuSE-QMF with the relevant axis and other definitions shown. For a similar definition for hyperbolic electrodes see Figure 3.2.

Cheung characterised the quadrupole mass filter experimentally by measuring the residual gases from a leak of room air into a vacuum chamber in which the quadrupole was mounted on a flange mounted mass filter configuration [129]. In this configuration, an axial molecular beam ionizer was mounted onto the quadrupole housing, which was then mounted to a detector housing containing a continuous dynode electron multiplier. This complete assembly was then mounted to a feed-through flange. The emissive area of the ionizer was larger (9 mm diameter ionization region, and a 3 mm diameter extraction lens) than the acceptance of the quadrupole which had a 2 mm entrance lens positioned 1.00 mm from the front of the device followed by a 1×1 mm^2 aperture in the micro-fabricated housing. The integrated optics at the front and back of the device are positioned 0.1 mm from the

housing and the electrodes. The exit lens of the quadrupole was positioned 1.00 mm from the end of the device and had a 1 mm aperture, followed by a 9 mm diameter focusing lens and conventionally scaled detector.

QMF PARAMETER	CONDITION
Length	30.6 mm
r_0 (all)	0.707 mm
r/r_0 (Circular)	1.127
MuSE-QMF electrode dimensions	1 mm×1 mm
Housing radius (Hyp and Cir)	$3.6 \times r_0$
Housing dimensions (MuSE-QMF)	3.2 mm×3.2 mm
Frequency (Zone 1)	4 MHz
Frequency (Zone 3)	2 MHz
Detector radius	0.707 mm
Ion Source	
Ion energy (E_i)	See results
Ion source radius	0.3 mm
Ion energy spread	0
Ion angular spread	0
Operating tip	
a (zone 1, zone 3)	0.237, 3.16
q (zone 1, zone 3)	0.706, 3.23
Ion species	See results

Table 5.4. Computer simulation test conditions (electrode comparison)

An Extrel CMS Merlin [130] data acquisition system and control electronics, with a prototype Ardara Technologies [131] quadrupole power supply operated at 2 MHz. was used to control the QMF assembly. For optimum sensitivity higher ion energies were required for operation in zone 3 than for zone 1. For the zone 3 experiments, ion energy was maintained at 18 eV by biasing the ionization grid to +18 Volts and maintaining the pole bias offset of the quadrupole at 0 Volts.

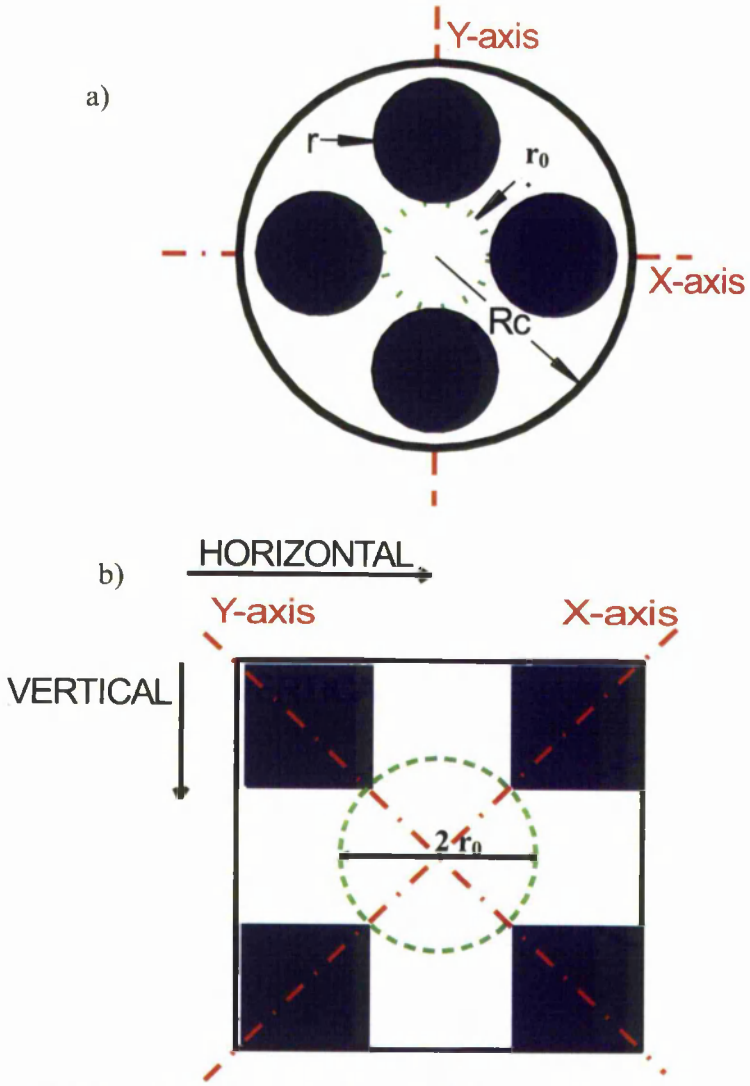

Figure 5.12. End section views of a QMF constructed from; a) circular electrodes, b) MuSE-QMF.

5.13 Multipole differences

The dependency of the multipole coefficients of square electrode QMFs on electrode geometry and the resultant performance characteristics are not well documented. For a micro-engineered QMF constructed from circular electrodes, the effects of electrode to substrate distances are known to affect field asymmetries and hence the magnitude of the multipole field coefficients [78]. The previously reported optimisation [126] of the square electrode QMF used in these experiments demonstrated similar characteristics, finding that the optimum value for the electrode

geometry was dependent on the distance of the electrode from the substrate and also on the ratio of the electrode size to the effective device aperture radius r_0. Table 5.5 shows the relative magnitudes of the multipole coefficients for the optimum rectilinear electrodes and for equivalent size circular electrodes. It can be seen there are significant differences; use of square electrodes results in a decrease of approximately 22% in the quadrupole coefficient (A_2) with the next three higher terms all positive with much increased magnitudes. These significant differences suggest that there may well be a considerable degradation in the performance associated with the MuSE-QMF when compared with a more conventional QMF with similar dimensions.

A_N	CIRCULAR ELECTRODE	SQUARE ELECTRODE
2	1.0016×10^{0}	0.78381×10^{0}
6	1.2000×10^{-3}	8.0909×10^{-2}
10	-2.4325×10^{-3}	3.2235×10^{-2}
14	$-2.9680\text{E}\times10^{-4}$	1.8101×10^{-2}

Table 5.5. Multipole coefficients at radius r_0, for circular and square electrode geometries, extracted from Poisson/Superfish for dimensions defined in Table 5.4.

5.14 Operation in zone 1

5.14.1 Hyperbolic and circular electrode QMFs

To provide a performance benchmark for comparison, computer simulations for hyperbolic and circular electrode QMFs for operation in zone 1 were first undertaken. Both electrode profiles are of the same length and with a comparable field radius to the MuSE-QMF that is discussed later in the chapter. The mass spectra for Oxygen (O) for these two electrode types are shown in Figure 5.13 and quantitative performance data is provided in Table 5.6.

The two mass spectra are very similar with the exception of the sensitivity (peak height) which is slightly lower for circular electrodes. The low resolution and the

lack of a significant difference between the two electrode types is attributable to the low number of RF cycles the ion experiences under the operating conditions tested (20 cycles at 3eV). The low number of RF cycles experienced by the ion results in a low resolution and the presence of significant low and high mass tails.

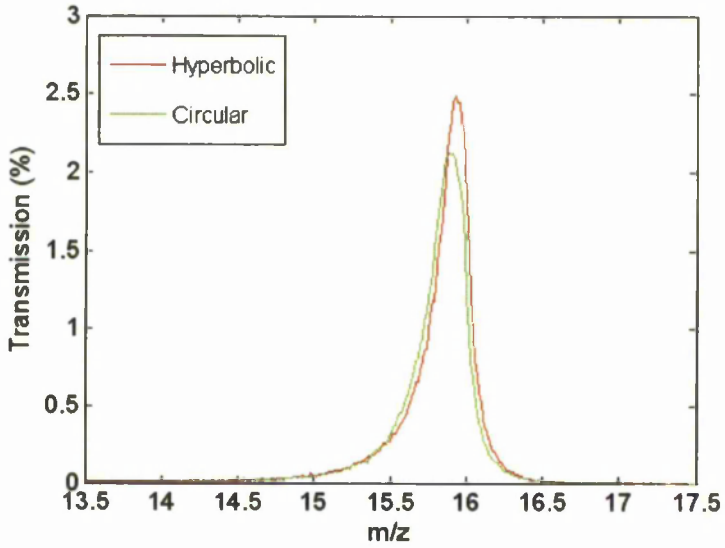

Figure 5.13. Computer simulated mass spectra for Oxygen ions for a QMF with hyperbolic and circular electrodes for operation in stability zone 1.

5.14.2 MuSE-QMF

Figure 5.13 shows the simulated mass spectra for zone 1 operation for the MuSE-QMF operated with the same instrument resolution setting as for the hyperbolic and circular electrodes. Table 5.6 contains relevant quantitative performance data for the MuSE-QMF. Several characteristic differences are apparent when compared to the previous results for hyperbolic and circular devices: peak height is greater, the peak width is increased, the low and high mass tails are greater and the peak position is shifted to a higher point on the mass scale. The MuSE-QMF has a much-reduced mass filtering performance. This results in nearly a nine fold reduction in the 50% PH resolution when compared to hyperbolic electrodes for operation at an E_i of 3 eV. The shift in the mass scale can be largely attributable to the much reduced

quadrupole coefficient (A_2) produced by the MuSE-QMF (A_2 (MuSE-QMF) = 0.78381, A_2 (circular) = 1.0016).

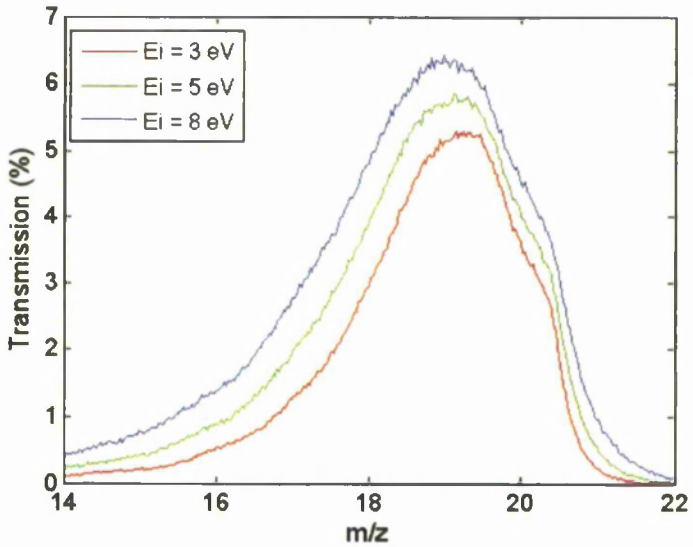

Figure 5.14. Computer simulated mass spectra for Oxygen ions with a square electrode QMF and operating in stability zone 1 with an uncorrected mass scale.

5.15 Operation in zone 3

Computer simulated mass spectra for the MuSE-QMF operating in zone 3 are shown in Figure 5.15. These exhibit a better formed mass peak shape when compared with zone 1. The low and high mass peak tails reduce significantly as does the sensitivity, with the peak position shifted a little higher up the mass scale. Operation in zone 3 requires higher ion energies than for zone 1 to maximise the transfer of the ions through the increased fringing field in the proximity of the QMF entrance. As a result, ion velocity is increased and the ions spend less time in the QMF and experience a lower number of RF cycles (5 cycles at E_i = 12 eV for F = 4 MHz) compared with zone 1 (20 cycles at E_i = 3 eV for F = 2 MHz). In spite of the ions exposure to a reduced number of RF cycles, zone 3 provides improved performance compared to zone 1. The MuSE-QMF achieves a 10% PH resolution of 20.4 for an E_i of 12 eV for zone 3 operation compared to 22.52 for an E_i of 3 eV for hyperbolic electrodes operating in zone 1. This demonstrates that operation in zone 3 provides a

means of improving the resolution of electrode geometries that generate electric fields that are far from the 'ideal' quadrupole field.

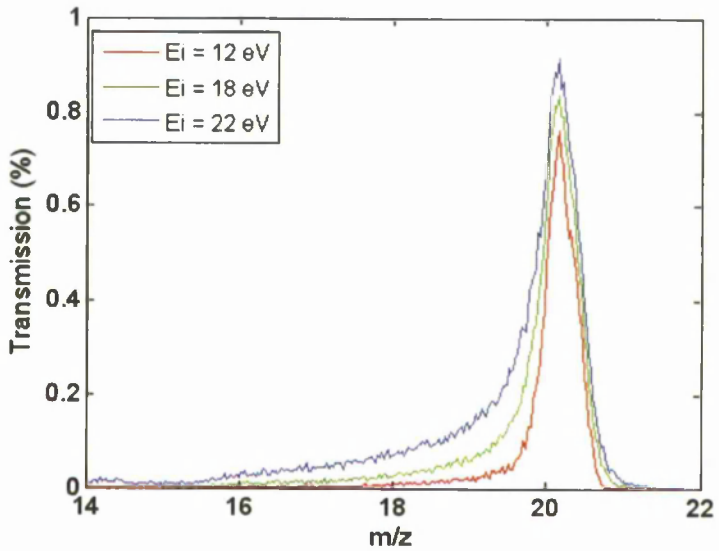

Figure 5.15. Computer simulated mass spectra for O^+ (m/z = 14) ions for the MuSE-QMF for operation in stability zone 3 (with uncorrected mass scale).

Except for very special cases, the QMF is required to discriminate between co-existing species in the sample. Figure 5.16 shows experimentally obtained spectra for air when operating in zone 3 with the MuSE-QMF. The gain of the experimental system is set to show the peaks for diatomic Nitrogen (N_2), diatomic Oxygen (O_2), Argon (Ar) and Carbon Dioxide (CO_2). Simulated mass spectra for the same gas sample are shown in Figure 5.16. Comparing Figure 5.16, with the simulated mass spectra in Figure 5.17, we can observe that the simulated data shows the correct abundances for the four species simulated. For the experimental results we observe approximately correct abundances for N_2 and O_2 with Ar and CO_2 showing higher than expected peaks. The sample abundances of Ar and CO_2 are very much smaller than the two major species and therefore more sensitive to background signal levels and electron multiplier noise (signal to noise ratio). The measured 10% peak height resolution for N_2 is 16.6 (experimental) and 22.6 (simulated), which are of the same order. A well-formed valley between the N_2 and O_2 peaks is observable for both

ELECTRODES	ZONE 1					ZONE 3		
	HYPERBOLIC	CIRCULAR	MuSE-QMF			MuSE-QMF		
Ion Energy (eV)	3	3	3	5	8	12	18	22
Peak Position (amu)	15.91	15.87	19.25	19.09	18.96	20.13	20.11	20.11
Peak Height (%)	2.46	2.11	5.28	5.80	6.35	0.72	0.81	0.88
Resolution at 10% PH	22.52	21.26	4.03	3.44	2.95	20.4	13.96	8.29
Resolution at 50% PH	66.31	54.10	7.68	6.69	5.88	39.73	35.91	30.16
Number RF cycles	20.4	20.4	20.4	15.8	12.5	5.1	4.2	3.8

Table 5.6. Performance characteristics for hyperbolic, circular and MuSE-QMF quadrupole mass filter. (Note PH = peak height)

cases but better defined for the simulated spectra. Low mass tailing is also more evident for the simulated N_2 peak.

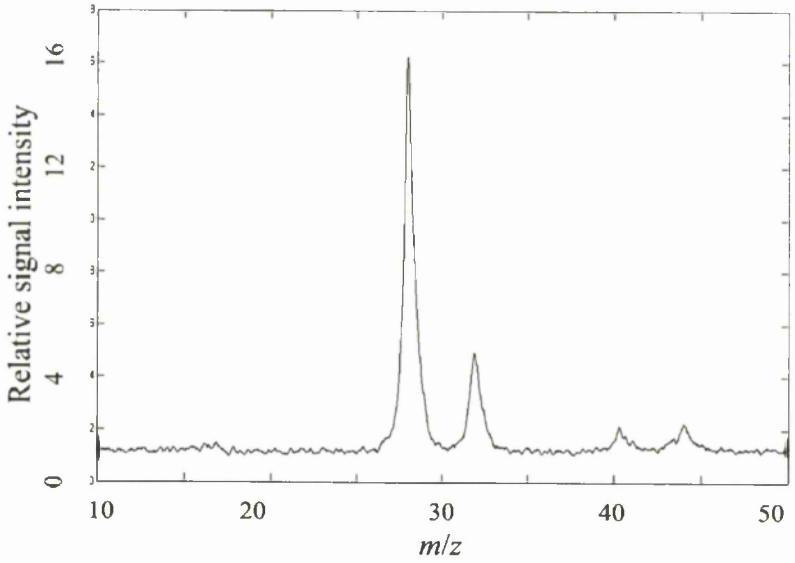

Figure 5.16. Experimental data for a square electrode QMF for operation in zone 3 with E_i equal to 18 eV [36].

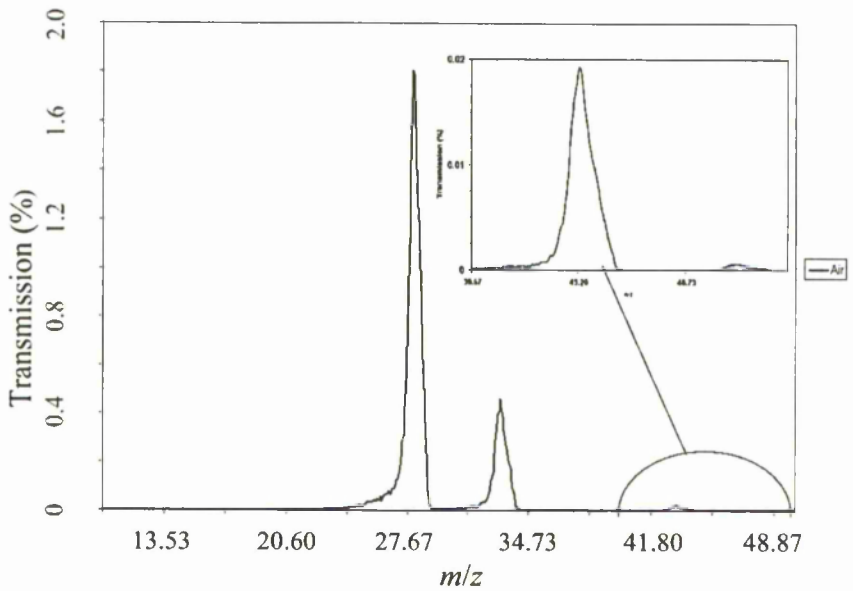

Figure 5.17. Computer simulated mass spectra of air for a QMF with square electrodes.

The differences that do occur are attributable to scan line, baseline and ion source variations between the experimental equipment and the computer simulation model. In both cases a mass scale calibration has been performed and for the simulated data this was linear across the mass range. There is an increase in the low mass tail of the major peak which is possibly due to ion source alignment differences which are known to have a marked effect on this aspect of performance [43]. There is a very strong similarity between the simulated and experimental results, providing validation of the computer simulation methodology. The performance obtained for relatively closely spaced species does not completely characterise the performance. This is especially valid where a relatively short QMF length is employed resulting in the ions experiencing a small number of RF cycles. This can result in differences between the low and high mass performance due to the differing number of RF cycles experienced across the ion mass range. The effect is accentuated in this case by the very low number of RF cycles experienced at the bottom end of the mass range (5 cycles at an E_i of 18 eV for a 20 amu ion). Use of the QMF over a large mass range enables the mass scan linearity to be quantified and an accurately calibrated mass scan line to be defined. A calibration compound FC-43 as used previously [132], provided the range of species required and was used to experimentally verify this aspect of performance [129].

5.16 Effects of process tolerances on performance

As discussed in 4.8.1 the manufacture of a QMS instrument and in particular the QMF component requires careful consideration of the positional tolerances of the electrodes. The particular characteristics of the MEMS process can result in different combinations of electrode positional tolerances. When MEMS is used in conjunction with square electrodes the accepted tolerance limits for a conventionally engineered QMF with circular electrodes may no longer apply.

The effects of imperfect electrode position on QMF performance [49] have indicated that +/- 0.001 × r_0 is an acceptable tolerance limit for the displacement of a single circular electrode of a QMF. This relationship shows that the maximum acceptable value of the electrode tolerance scales with the field aperture of the QMF. It was demonstrated in Chapter 4 that for positional tolerances that occur on more

than one electrode concurrently, a cumulative effect on QMF performance is observed. The absolute tolerance limits associated with MEMS processes are generally smaller but percentage tolerances can be larger than those achievable using traditional manufacturing methods. MEMS devices are usually much smaller with an accompanying smaller r_0. Therefore, if the above field radius relationship holds, careful control of the tolerance is necessary to maintain adequate performance.

In the first instance the effects of a single electrode displacement was examined. The manufacturing process used for the construction of the MuSE-QMF would not result in this class of electrode displacement due to the particular two wafer construction process. However, alternative manufacturing processes for achieving miniaturisation may well exhibit similar forms of misalignment that are also found in traditionally manufactured QMFs. Figure 5.18 shows the end view of the MuSE-QMF for two examples of electrode displacement. Figures 5.19 and 5.20 show the effects on the mass peak for inward and outward displacements of a single *y*-electrode respectively.

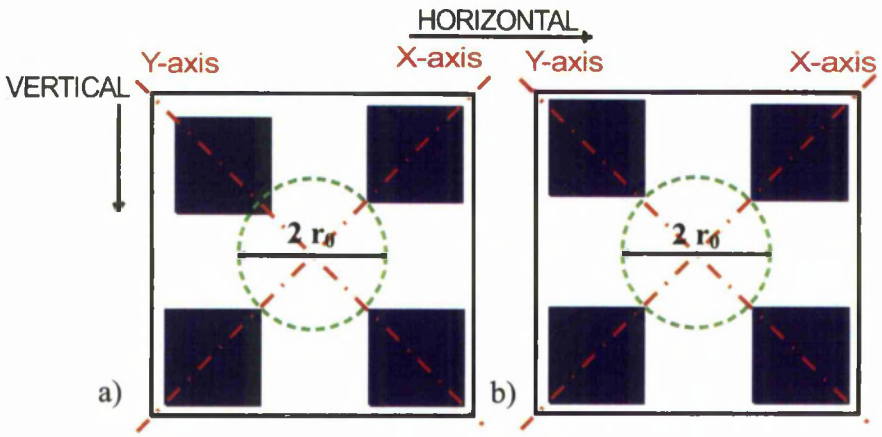

Figure 5.18. End view of the MuSE-QMF showing single *y*-electrode; a) shifted inward in the *y* direction, b) shifted outward in the *y* direction.
(Note the electrode shift is not to scale)

For N_2, as the *y*-electrode is displaced outwards on-axis, the mass peak shifts to a higher mass value in response to the decreased field strength. There is also an accompanying decrease in peak transmission and resolution as the electrode

displacement increases accompanied by an alteration in the peak shape. For displacements below +25 μm, there are only fine detail changes to the mass peak shape and accompanied by an increase in peak width both at 10% PH and 50% PH.

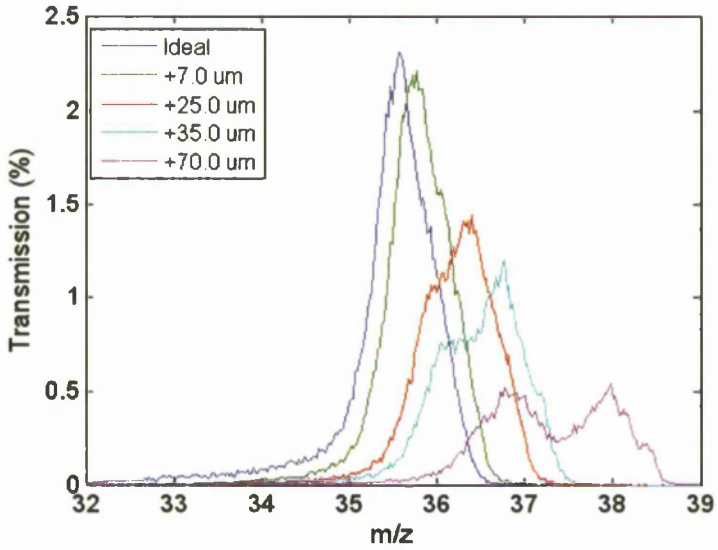

Figure 5.19. Computer simulated zone 3 mass spectra of N_2^+ (28 *m/z*) ions for outward displacements of the upper *y*-electrode (see Figure 5.17) for E_i = 18 eV with uncorrected mass scale.

At +35 um a definite shoulder emerges on the low mass side of the peak which by +70 μm has developed into two very similar peaks separated by a valley. The valley has a transmission of over 50% of the individual peak height. For inward on-axis displacements of a *y*-electrode a similar result is observable with the main exception being that the peak shifts to a lower mass point. The decrease in peak height is less for a -7 μm displacement than for a +7 μm displacement. Above this magnitude of displacement, the decrease in peak height with displacement is approximately the same for both positive and negative displacements. For a -70 μm displacement there are again two peaks but they have structural differences. Their transmissions are different with the valley between them greater than for a +70 μm displacement. For the ideal electrode geometry and with electrode displacements, the low mass tailing is much greater than the high mass tailing.

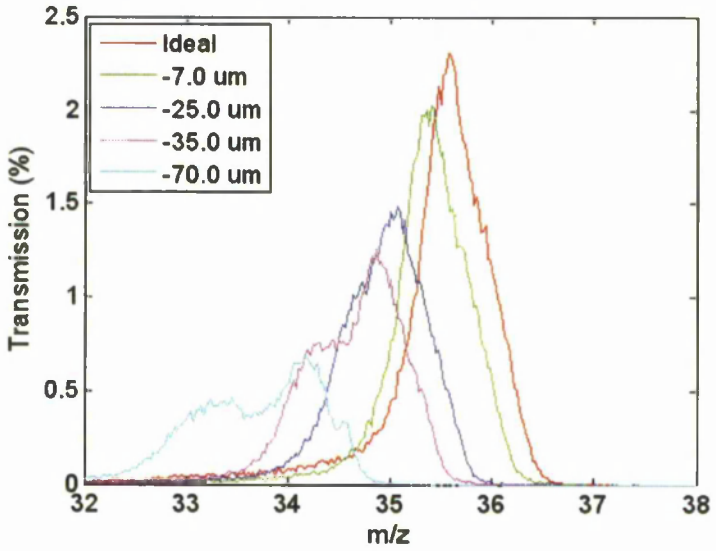

Figure 5.20. Computer simulated zone 3 mass spectra of N_2^+ (28 amu) ions for an inward displacements of the upper *y*-electrode (see Figure 5.17) for $E_i = 18$ eV with an uncorrected mass scale.

Figure 5.21 shows the resultant mass spectra for C_4F_9 for a range of inward displacements of a *y*-electrode. In all cases the overall transmission is less than observed for N_2. A definite shoulder now emerges at the much lower displacement of -7 μm. While at -25 μm a distinct secondary peak has formed which by -35 μm has nearly separated from the main peak. For outward displacements of the *y*-electrode, peak position again moved to a higher position on the mass scale and the general characteristics of the peaks are the same as for inward displacements. Table 5.7 contains quantitative data for inward displacements for both N_2^+ and $C_4F_9^+$.

From these results it is considered that for the lower mass ion the acceptable maximum displacement equates to a tolerance of +/- 0.035 × r_0, and for the higher mass ion the acceptable tolerance is +/- 0.01 × r_0. These results demonstrate that the maximum acceptable process tolerance for this class of positional error is dependent on the required maximum operational mass of the QMF at the particular operational RF frequency. They can also be interpreted in terms of the maximum number of RF cycles that the ions experience (Table 5.7).

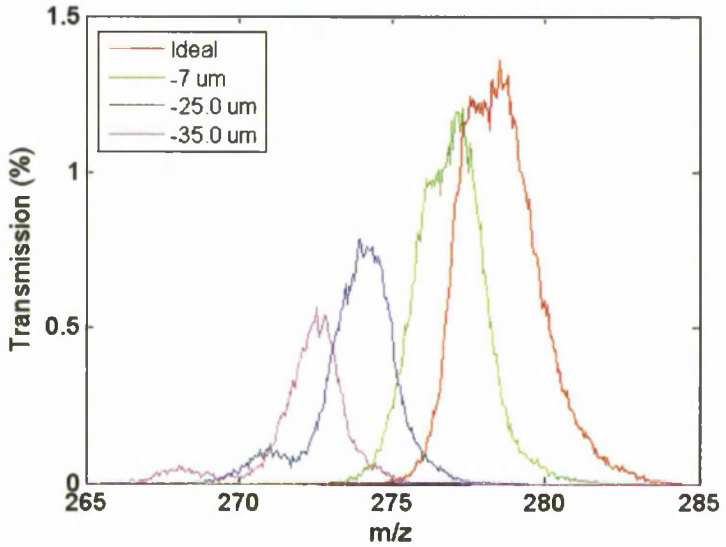

Figure 5.21. Computer simulated zone 3 mass spectra of C_4F_9 (219 amu) for inward displacements of the upper *y*-electrode (see Figure 5.17) for an E_i of 18 eV with an uncorrected mass scale.

ION TYPE	ELECTRODE DISPLACEMENT (microns)	0	-7	-25	-35
N_2^+ (28 amu) (≈ 5 RF cycles)	Peak position	35.57	35.36	35.03	34.82
	Peak Height (%)	2.27	1.99	1.45	1.21
	Res 10% PH	22.75	23.68	20.57	18.66
	Res 50% PH	49.18	47.36	35.75	31.09
$C_4F_9^+$ (219 amu) (≈ 15 RF cycles)	Peak position	278.47	277.17	273.93	272.42
	Peak Height	1.31	1.18	0.76	0.53
	Res 10% PH	52.01	60.39	39.50	68.17
	Res 50% PH	95.50	111.58	126.82	152.87

Table 5.7. Performance parameters for differing inward displacements of the *y*-electrode for operation in zone 3 with an E_i of 18 eV for N_2^+ and $C_4F_9^+$.

For the process used in the construction of the MuSE-QMF device two of the most dominant misalignments are due to: a horizontal shift between the upper and lower electrode pairs during bonding; differential wafer thickness resulting in a

vertical shift of the upper electrodes with respect to the lower electrodes. The bonding process can also introduce rotational shifts between the upper and lower electrode pairs resulting in the horizontal misalignment mentioned, as well as a misalignment in the *z*-axis. The tolerance of this form of misalignment is within +/- 10 um, while the vertical shift is limited by the tolerance of the wafer thickness, which is within +/- 5 um. The rotational shifts will result in varying degrees of horizontal misalignments along the length of the device. To investigate the effects of these requires 3D simulation software which is outside the scope of this work.

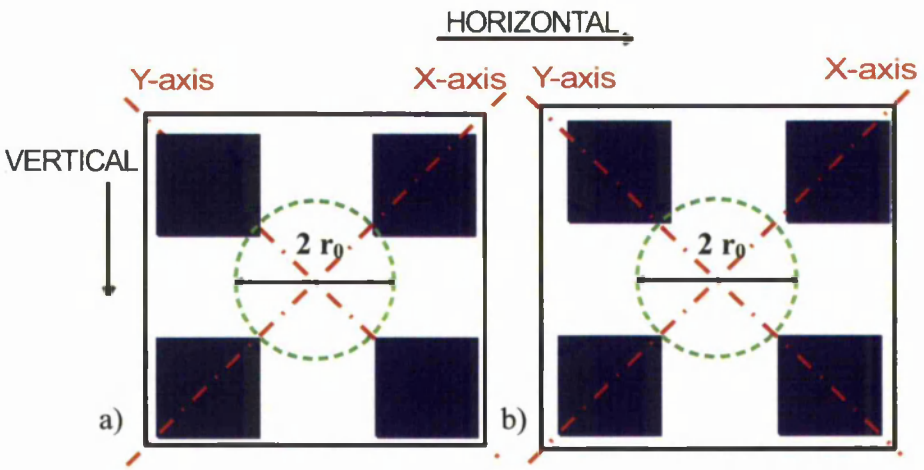

Figure 5.22. End view of the MuSE-QMF showing; a) vertical shift of a *x* and *y* electrode, b) horizontal shift of a *x* and *y* electrode.
(Note the electrode shift not to scale)

The process tolerance axis are at 45° to the electrode field axis (Figure 5.22) and result in compound displacements of the electrodes with respect to the field axis. Figure 5.23 shows the effects of these two types of electrode displacements on the resultant mass peak. For the +50 μm and +100 μm horizontal shifts, there is little observable difference between the mass spectra for a correct electrode placement and the displaced electrodes. The mass peak shifts by small increments to a lower mass position with increasing electrode displacement and a small progressive increase in peak height is also observable. With this class of process error, both the *x* and *y* electrodes are displaced in the *x* and *y* field axis simultaneously. The *x* and *y* field

axis displacements are in the opposite direction and self-compensate, thereby minimising the resultant effect on the mass peak. A vertical and inward shift of the upper electrodes results in a more marked effect on the mass peak. The mass peak now shifts with greater increments to an increasingly lower mass position. These increments are approximately proportional to the electrode positional shift and are accompanied by a decrease in the peak height (transmission). This type of misalignment results in a compound displacement of both electrodes in both the field axis. The x and y field axis displacements are of the same magnitude and in the same direction for both electrodes. As a result, the effect on the mass peak is cumulative; a much greater mass peak shift occurs and is accompanied by a reduction in transmission, this has been observed for simulations of circular electrodes.

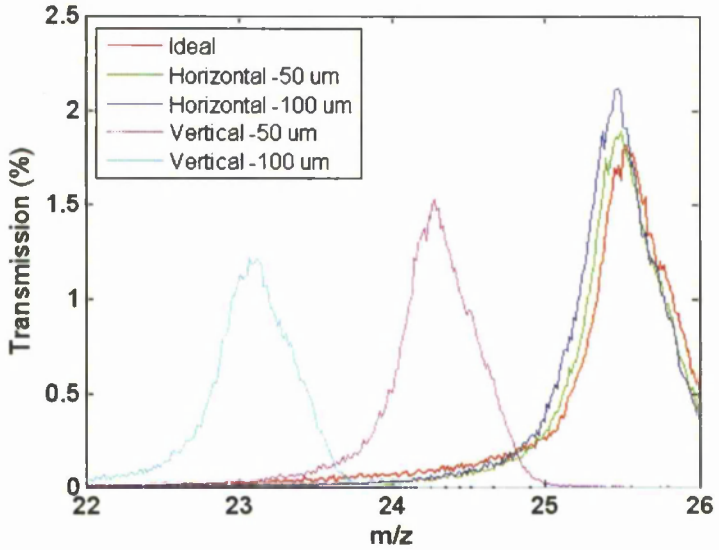

Figure 5.23. Computer simulated zone 3 mass spectra of Ne for horizontal and vertical displacements of the upper electrodes (see Figure 5.21) for an E_i of 18 eV with uncorrected mass scale.

5.17 Conclusions

Certain QMS applications create barriers to achieving the desired performance window. In the examples that have been investigated they are due to the low number

of RF cycles experienced by the ions. The reasons for this are different in the two examples investigated.

5.17.1 Low mass isotopes

The separation of closely spaced low mass ions is particularly troublesome because of their high relative velocity resulting in the exposure of ions to a relatively low number of RF cycles. The factors influencing this are the ion energy, RF frequency and QMF length. For this particular application it is not possible to increase the length and RF frequency sufficiently to provide adequate performance in zone 1. It was found that zone 3 operation provides a promising method of achieving the desired performance within the desired maximum length of the QMF electrodes. Reduced abundance sensitivity when using zone 3, is still an important consideration. For closely spaced species careful choice of operating frequency is required, the exact value being dependent on the abundance sensitivity required. Over a certain number of cycles the 50% PH resolution limits while the 10% PH resolution continues to increase due largely to the high mass tail decreasing in amplitude and width.

5.17.2 MEMS devices

These experimental and computer simulation techniques have demonstrated that the use of zone 3 operation for a QMF with square electrodes provides improved mass filtering action compared to that achievable with zone 1. The use of zone 3 enables acceptable performance to be obtained even though the QMF produces a non-ideal electric field and its short length results in the ions being exposed to a relatively low number of RF cycles.

A displacement of a single electrode in the y direction over a certain limit will result in a secondary peak before the main mass peak. The acceptable limit of the displacement is determined by the velocity of the ion, which for a given ion energy is mass dependent. Therefore, as the mass range is increased a reduction in the process tolerance is required (all other operating conditions being the same). Increasing the

ion energy as the mass scan line is increased would provide a method of compensating or reducing this effect. Another approach would be through the use of RF scanning instead of the more common voltage scanning. This would ensure that for constant ion energy ions would experience the same number of RF cycles irrespective of their mass (see 3.15). However it does introduce complications in the coupling of the RF drive stage to the QMF due to the normal reliance of a tuned coupling stage to provide voltage gain.

The more common process errors associated with the manufacture of the MuSE-QMF are a concurrent displacement of both the upper x and y electrodes. This produces equal magnitude shifts in both the field axis and does not result in a secondary peak over the range of displacements of interest. A mass scale calibration will negate the effects of the observable mass peak shifts that do occur. The expected range of the dominant process tolerances does not adversely affect the achievable performance of the QMF.

The lower quadrupole coefficient (weaker quadrupole field) produced by the square electrodes results in the drive voltage being approximately 1.28 times greater than for a comparable hyperbolic or circular electrode device operating under the same conditions. This results in a lower achievable maximum mass for the square electrode QMF for a given safe maximum operating voltage.

More simulation studies could be undertaken to investigate other aspect ratio electrodes. This work was based on a device that was designed with the criteria of minimising specific multipole terms. This has been previously shown not to provide the best performance when considering circular electrodes. This may also be the case for rectilinear electrodes.

Chapter 6

6. QMS ELECTRONIC CONTROL UNIT

6.1 Introduction

This chapter firstly examines the operational requirements for an implementation of a QMS ECU and supporting application software capable of running on a standard laboratory computer. Requirements from two different target applications have been considered; firstly that required to support a commercial RGA application, and secondly the specific requirements to support experimental research including the validation of the computer simulation work reported on in this thesis and elsewhere [6], [49]. The operational requirement for a typical RGA application has been arrived at from examining manufacturer data sheets [133-135] and from information provided by a typical RGA user [136].

The aim of designing a custom QMS ECU was to provide a much wider range of user control than can be achieved with available commercial instruments and secondly to provide the facilities for operation in stability zone 3. At the same time the QMS ECU should support operation in a fall-back mode where the user would be unaware of the greater control that is available.

In undertaking this design certain novel facilities have been included both at a system level and at the circuit level and these are discussed in the relevant sub sections.

The electronic control unit (ECU) provides the overall control of the other modules that comprise a quadrupole mass spectrometer (QMS). To facilitate user control and interfacing to other controllers in a system, additional inputs and outputs (I/O) are usually provided. These additional I/O take the form of: optically-isolated inputs for monitoring of external conditions; volt-free relay contact outputs for controlling external equipment and/or indicating status; universal serial bus (USB) or

alternatively an Ethernet for bi-directional communication with a host computer interface. There is no definitive method of implementing such an ECU and published research targets specific areas of the ECU design; RF generation and electrode drive [137-141], ion source control [142], high voltage amplifiers for driving capacitive loads [143-145], electrometer amplifiers [146-148]. One possible route to implementation is the use of a proprietary computer in conjunction with a collection of standard and custom designed add-on controllers. Alternatively, a custom designed standalone control unit with a USB port for communication to a commercial computer is another possibility. From a commercial viewpoint a custom designed controller is a superior choice as it maximises the added value to the QMS product as well as the control that the developer can exercise over the overall product design philosophy. This was the philosophy that was chosen.

6.2 Operational requirement

The two major requirements were to meet or exceed present commercially available ECUs and secondly to provide additional functionality so that the ECU would provide a flexible platform for future research.

6.2.1 Minimum requirement

Figure 6.1 (see also Figure 3.1) shows a top level block diagram for a quadrupole mass spectrometer showing the connectivity between the ECU and the remainder of the QMS modules and external units. The ECU provides control or interfaces to the following modules;

a) Electron impact ion source.
b) Quadrupole mass filter.
c) Ion detector
d) Optional user interface
e) Other instrumentation.
f) Computer.

The optional user interface provides facilities for displaying mass spectra and a keypad for setting up the operating conditions of the QMS. More usually this functionality is provided by an attached computer connected via a USB or Ethernet communications link. In this mode an application program running on the computer would provide a GUI for a user to control the QMS, display mass spectra and handle data storage.

As well achieving the functional requirement for the QMS, the requirement of a user has to be taken into account. In doing so, the instrument does not usually sit in isolation but usually forms part of a bigger system which may provide the process monitoring and instrumentation system for a plant. Alternatively, it may sit independently and collect data which is then stored on a supporting computer and sent to other parts of the system via a network.

A typical application of a small QMS is that of a vacuum quality monitoring instrument and is often called a Residual Gas Analyser (RGA). A typical operational requirement for such a device has been kindly supplied by The Vacuum Science Group at Daresbury and is reproduced in Appendix C [136]. This is comparable with the specification of commercially available equipment offered by manufacturers such as Thermo Fisher [133], Extrel [134] and Stanford [135].

6.2.2 Additional facilities to support research

For research applications there is usually a requirement to exercise more control over an instrument in order to investigate interrelationships between operating conditions and realisable performance. An additional set of operating controls to facilitate these requirements is contained in also Appendix D.

6.3 Electronic control unit

6.3.1 Overview

To achieve the greatest flexibility for the user interface and data processing, it was decided that a standalone ECU connected to a standard computer offered the best solution. To maximise the intellectual property reuse for the ECU, an architecture

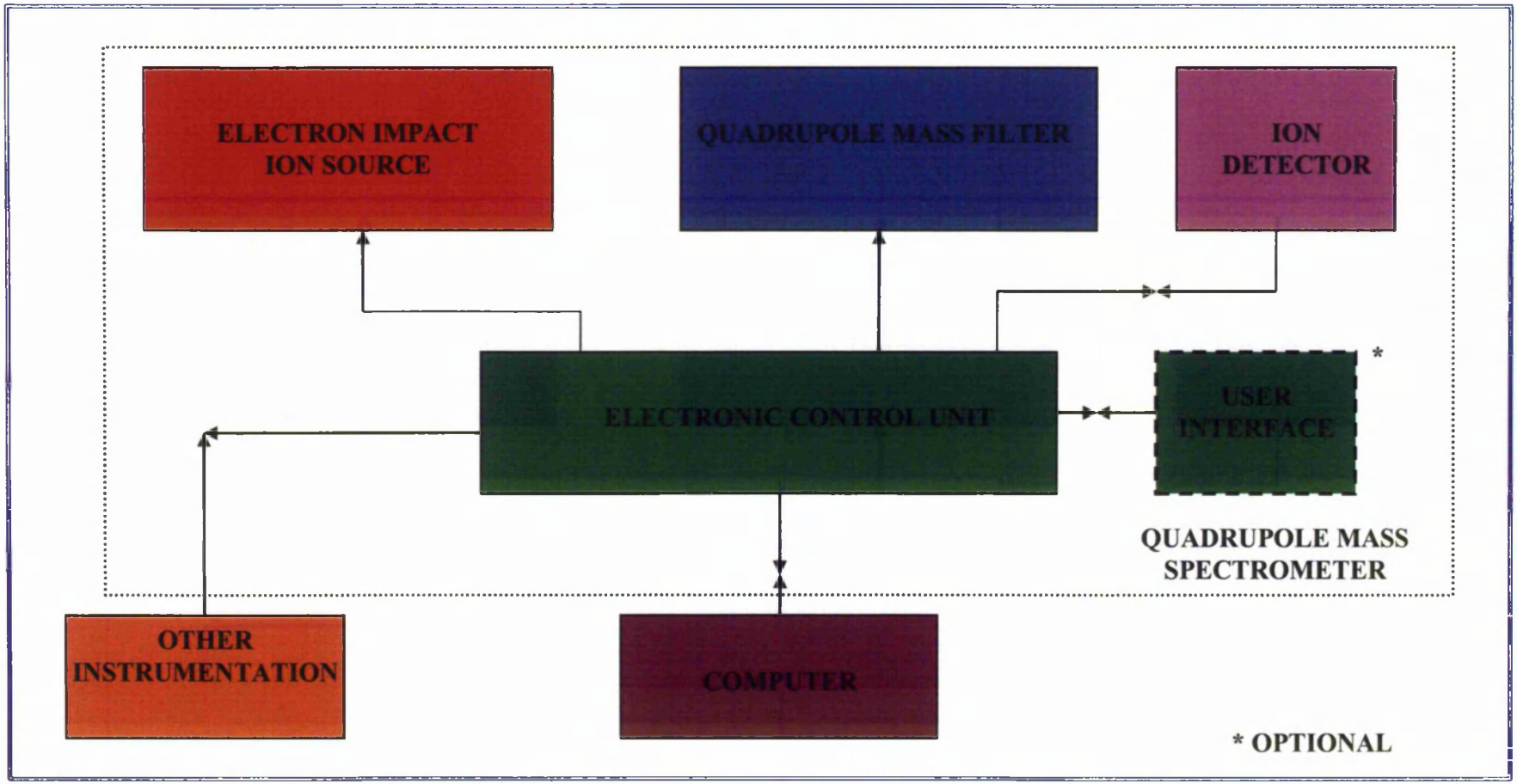

Figure 6.1. Top level block diagram for a quadrupole mass spectrometer and peripheral modules.

based on a number of individual controllers each associated with one of the major functional blocks was selected. Although this does result in a certain degree of redundancy, it does offer a greater degree of flexibility for reconfiguring the ECU. Furthermore by judicious selection of the microcontroller, the design offers a relatively easy route to creating standalone controllers for the ion source, mass scan and data acquisition functions. These would then be capable of independently interfacing to a computer. Figure 6.2 contains a top level system block diagram for the ECU showing the main functional blocks which are:-

a) System controller-motherboard
b) Ion source controller
c) Mass scan controller
d) Data acquisition controller
e) Drive controller
f) Power output.

The complete ECU consists of six printed circuit boards. Four of these (a – d) are intelligent controllers and each incorporates an on-board microcontroller. The other two (e - f), consist of solely analogue circuitry.

6.3.2 Microcontrollers

The Microchip PIC32MX family of microcontrollers was chosen for their low cost coupled with flexible options for the number of SPI and USB interfaces that are available on the different variants [149-150]. A further consideration was the availability of low cost in-system programming and debugging equipment, together with the availability of a free cross assembler and C cross compiler. The central processing unit (CPU) of the PIC32MX3XX/4XX family of microcontrollers is based on the MIPS Technologies Inc. MIPS32® M4K 32 bit synthesisable core [151-152]. Also integrated into the device is an; non-volatile program memory, random access memory (RAM) together with a range of on-chip peripherals. The peripherals include universal serial bus (USB), serial peripheral interface (SPI), timer counters, digital input-output (DIO), interrupts and a multiplexed analogue to digital convertor

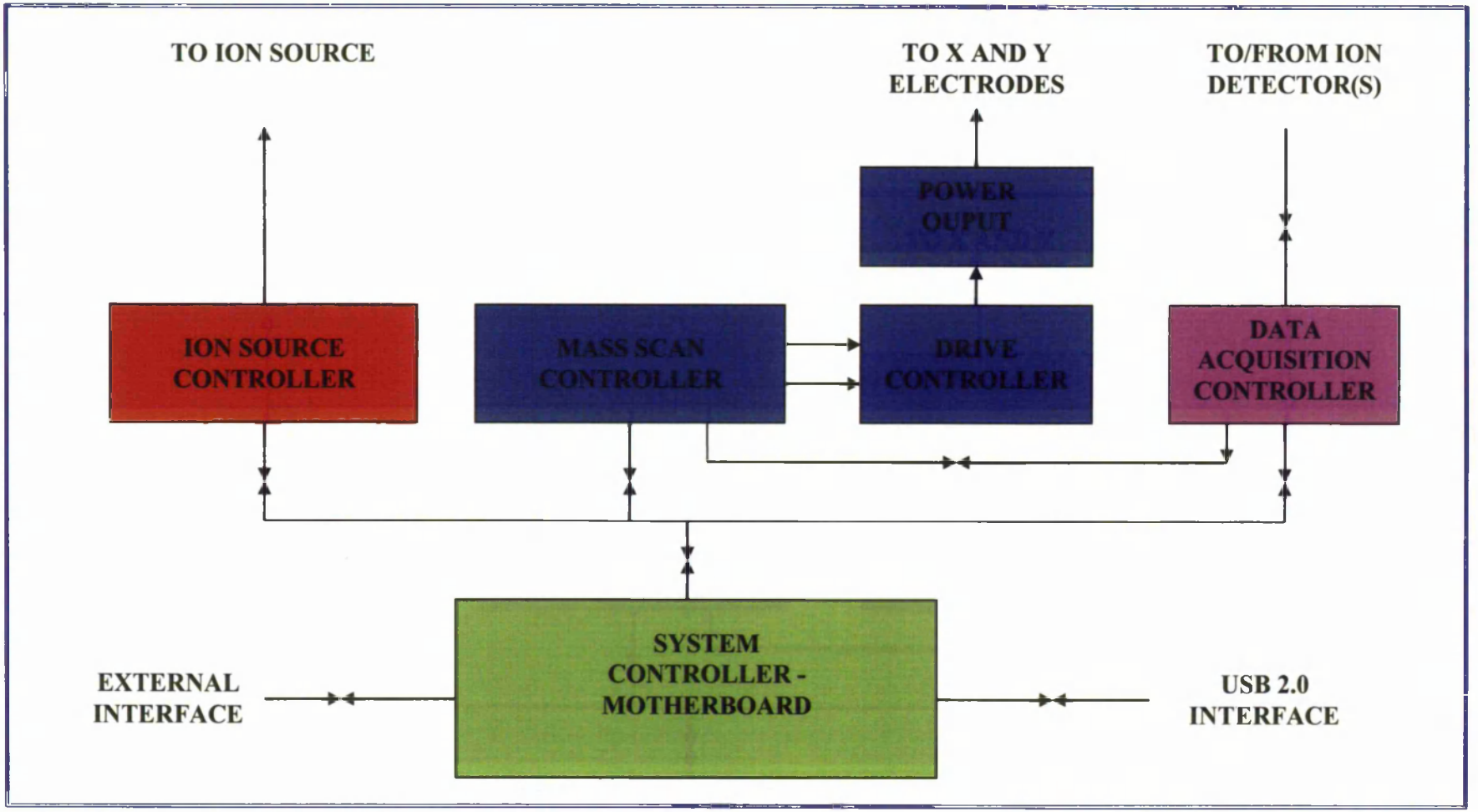

Figure 6.2. Top level system block diagram of electronic control unit.

(MUX-ADC). The PIC32MX has two on-chip phase lock loops (PLL), programmable dividers and a crystal controlled oscillator. This clock control circuitry enables a large range of processor clock speeds and peripheral bus speeds to be programmed from a single crystal frequency.

Two variants of the PIC32MX are used. The PIC32MX440F512 (PIC32-4) is used in the system controller and motherboard (SCM) and the PIC32MX340F512 (PIC32-3) is used in the other three intelligent controllers (SSC). The major difference between the two is that the PIC32-4 incorporates one USB port and one SPI port whereas the PIC32-3 has two SPI ports but no USB port. The USB port on the SCM provides the communications link between the ECU and the computer.

Each intelligent controller is equipped with a connector to support in system programming (ISP) and debugging of the firmware using an ICD3 [153] and if fitted with programmable logic, a connector to support ISP of these devices using a USB-Blaster [154, 155].

6.3.3 Inter-controller communication

The SPI port of the SCM is buffered and routed through to four backplane connectors [156-157]. Each connector provides a position that a SCC can be plugged into. Four slave select lines derived from the PIC32-4 are also routed to each of the connectors. On board links on the SCCs provide a method of allocating a unique salve select to the SSCs. For SCM to SCC transfers the SCM always acts as master. An SSC can indicate to the SCM that it requires servicing by asserting its own unique request line. These act as interrupt request inputs to the PIC32-4 on the SCM and also form part of the backplane signalling.

Data transfer size is dependent on the target device for on-board transfers but is always 32 bits for backplane transfers. For backplane transfers the most significant bit (MSB) is bit 31 and is always transmitted first. The 32 bit word is divided into three fields with bit 31 determining the action (read or write) of the transfer. The next field, bit 30 down to bit 24 determines the source or destination of the transfer and the third field bit 23 down to bit 0, is the data.

For on board transfers, the organisation and size of the transfer is dependent on the peripheral being addressed.

6.3.4 Internal controller peripheral control

Control within a specific controller is achieved through a number of mechanisms. For the SCM the SPI and the PIC32-4 DIO are used to control the on-board peripherals. In the case of the SCCs the first SPI port is used for backplane communication with SCM. While the second SPI port and i/o are used for general on-board control. For the mass scan (MSC) and the data acquisition controllers (DASC) there is additional control provided through dedicated programmable logic controllers.

6.3.5 Universal serial bus

The PIC32-4 provides a universal serial bus (USB) [158] which meets the USB 2.0 standard [159-160]. Implementation of the USB PIC32-4 firmware was based around the USB stack [161] provided by Microchip. A human interface device class was used as this offered the option of using the Windows® inbuilt drivers [162-163]. This has saved considerable effort in developing custom drivers. An improvement in the effective USB bandwidth could be achieved by providing customised drivers.

6.3.6 Miscellaneous

An on-board light emitting diode (LED) and a programmable link are provided on each intelligent controller and are directly connected to the microcontroller digital i/o. They are intended as an aid to testing and development.

6.4 System controller-motherboard

6.4.1 Introduction

The system controller-motherboard (SCM) provides the overall control of the ECU, providing the link between the applications program running on the computer, the external interfaces and the SCCs that comprise the ECU. A schematic for the top

level hierarchy is shown in Figure 6.3 and an image of a completed printed circuit board is shown in Figure 6.4. The SCM hierarchy is comprised of five functional blocks; the main processor, analogue interface, panel input-output, USB connector and the backplane.

6.4.2 Main processor

This block contains the PIC32-4 microcontroller, ISP connector, SSC slave select lines, SCC request lines and SPI interface to the backplane. Provision is also made for fitting a serial electrical erasable programmable read only memory (EEPROM) [164], which can be used to store a board serial number and other ECU specific data.

In addition to connecting to the backplane the SPI port provides the interface between the PIC32-4 and EEPROM with digital outputs from the PIC32-4 which provide other control functions. The USB interface provides a communications channel between the application program running on the computer and the ECU.

6.4.3 Panel input output

The panel input/output block contains the external interface signal conditioning for the input and output signals that are available via the on-board 15 way D-type connector. This connector provides the method of connecting external signals to the ECU. Three optically isolated inputs are provided. One, a fast vacuum interlock (FSTVIL) enables the ion source filament to be powered down in the event of a high pressure vacuum situation being detected. The other two, are general purpose and can be defined by the PIC32-4 firmware. Two sets of normally closed volt free relay contacts are provided whose functionality can be user defined. A connector is also provided for four general purpose LEDs.

6.4.4 Backplane

The backplane area consists of 4 off 15+15 way connectors mounted vertically with respect to the SMC PCB allowing up to four SSCs to be connected. The

connectors provide access to a SPI interface, four SSC slave select lines (SEL[0..3] and four SSC request lines (REQ[0..3]), the digital +3.3 and +5 voltage rails together with the main ±24 Volt rails. A system reset signal (_SYS_RESET) and a fast vacuum interlock signal (_FSTTINL) complete the available signals. Also included in this functional block are the connections for the main power input feed for the ECU. The ECU requires ± 24 volts from an external power supply. The physical arrangement of the PCBs also allows for an internal mains power supply to be fitted in the space between the front panel and the position of the first SSC if so required. Filters are provided on the power input to attenuate external power noise and to minimise conducted noise out of the ECU. A XP Power JCA series dc-dc convertor [165] and a LM340S linear regulator produce the +3.3 and +5.0 Volt supply rails respectively.

6.4.5 USB connector

A USB type B connector is provided to support the USB 2.0 port. A transient voltage suppressor (TVS) is mounted adjacent to the connector providing protection for the data lines.

6.4.6 Analogue interface

Two types of analogue interface are provided. The first consists of a buffer amplifier feeding a high resolution single integrated circuit ADC. This provides a method of controlling the mass scan ramp via an external analogue signal. The second consists of a set of resistive networks for signal conditioning of the ECU voltage rails. The outputs of the networks connect to some of the multiplexed analogue inputs of the PIC32-4. This allows the PIC32-4 to monitor the voltage rails for correct operational voltage limits and provide status information back to the connected computer.

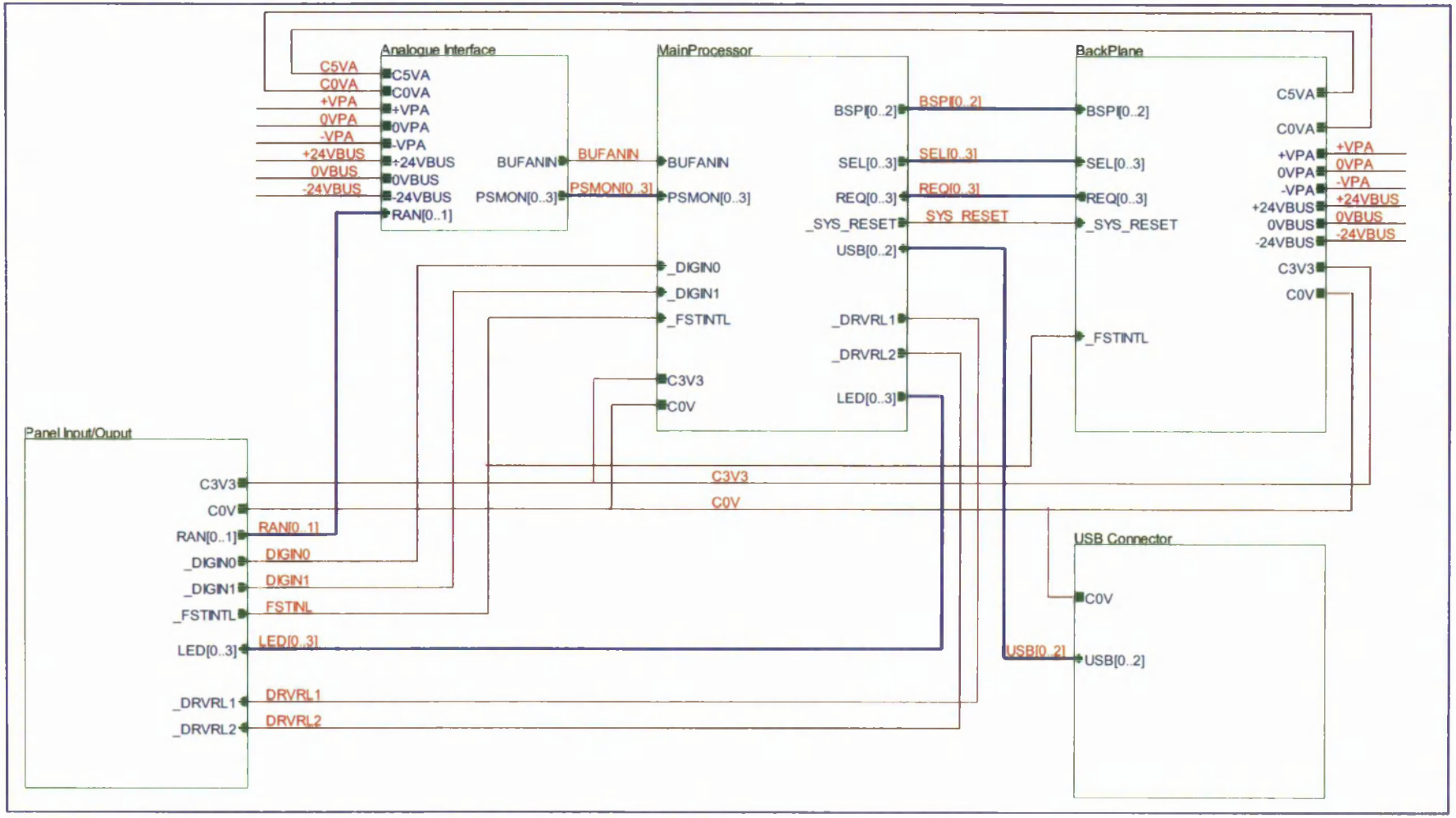

Figure 6.3. Top level schematic diagram for system controller and motherboard.

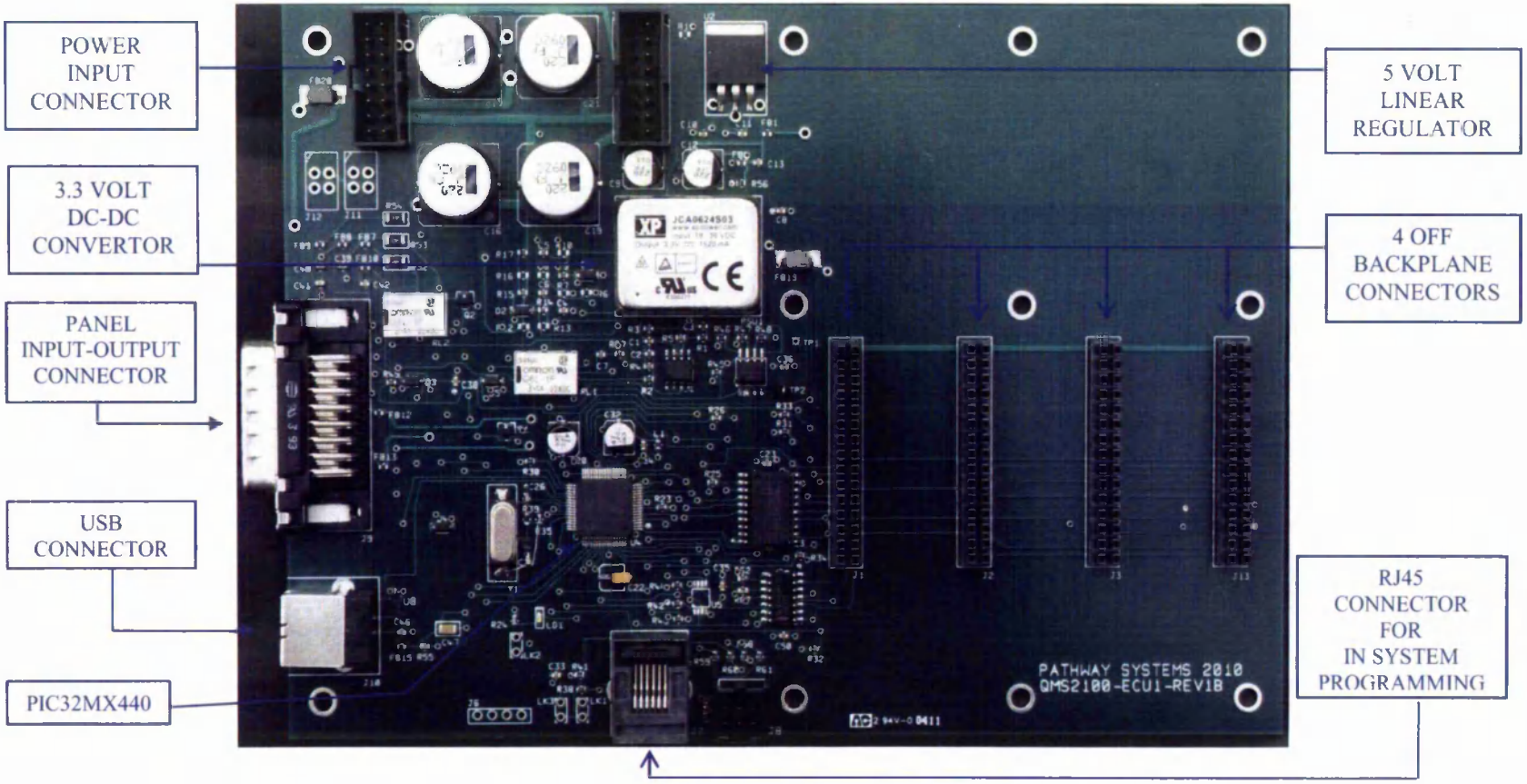

Figure 6.4. Image of system motherboard controller with major functional features identified.

6.5 Ion source controller

6.5.1 Overview

The ion source controller (ISC) is one of the SSCs that form the ECU. The ISC provides control of the ion source emission current and the voltages required for the ion source. An optional power supply is provided for generating an electrode pole bias supply if required. A top level schematic of the ISC is shown in Figure 6.5.

6.5.2 Main processor

This block contains a PIC32-3 microcontroller, a four channel digital to analogue convertor (DAC), a two channel analogue to digital convertor (ADC) and an optional EEPROM. The DAC is used to control; the set point for the cage voltage, the repeller voltage, the filament current and the optional pole bias voltage. The ADC is used to read the magnitude of the emission and filament currents. The FSTVIL from the backplane is connected to a digital input line of the PIC32-3 which is configured as an interrupt input. This allows the ISC to react quickly to a critical increase in vacuum pressure if an external pressure sensor is used.

The SPI-1 port of the PIC32-3 connects to the backplane via a transceiver and always operates in slave mode. The SPI-2 port of the PIC32-3 is used to control the on-board ADC, DAC and EEPROM.

6.5.3 Filament drive

The filament drive (FIL_DRV) together with a software control algorithm which is part of the firmware developed for the ISC PIC32-3 forms a three term controller (PID) [166-167] for maintaining the desired emission current. The filament current is controlled by a voltage controlled pulse width modulated (PWM) fly-back convertor operating at approximately 200 kHz. A schematic for part of the circuit is shown in Figure 6.6. A DAC controlled by the PIC32-3 generates a voltage which controls the output pulse width of the modulator U14 (Linear Technology LTC6922). The modulator output is buffered by U13 a metal oxide silicon field effect transistor (MOSFET) gate driver (National Semiconductors LM5112) before being fed to the

gate of the power MOSFET Q3 (ST Micrelectronics STD15NF-10). Q3 controls the current switching through the primary of transformer T1 (Coilcraft FA2677). Two of the secondary windings of the transformer are fed to a half wave rectifier and filter circuit comprising Schottky diode D2 (ON Semiconductors MBRD1035CTL) and low equivalent series resistance (ESR) capacitors C37–C39 (Kemat Corporation C0805C106K8PACTU), inductor L4 (Vishay Dale IHLM2020CZERR10M11) and bulk capacitor C40 (Rubycon 10TZV220M6.3X8). The positive output of the filter is connected via a Hall-Effect current sensor to one side of the filament with the filament common (repeller) connected to the negative output of the filter. The Hall-Effect sensor provides galvanic isolation of the filament circuit from the signal conditioning and ADC current monitoring circuit.

A feedback stabilised voltage controlled dc-dc convertor (not shown) is used to float the filament common (repeller) at a nominal -70 volts with respect to ground. The magnitude of the voltage can be varied between 20 to 100 volts providing a facility for soft ionisation or appearance potential methodology [168]. Figure 6.7 contains the results for an efficiency test undertaken for a nominal 1 ohm filament resistance for operation centred about a nominal 2 amp filament current.

6.5.4 Cage control

A DAC controlled cage voltage circuit controls the ion energy(together with the pole bias if provided) of the ions exiting the ion source. A sense resistor is provided on the output of the circuit across which is connected a high side current-sense amplifier (Analog Devices Inc. ADM4073). This generates a voltage proportional to the emission current and feeds into one channel of an ADC providing a measurement of the emission current for use by the software emission current control algorithm.

6.5.5 Lens 1 control

The lens 1 control consists of a voltage controlled dc-dc convertor (EMCO High Voltage Corporation, Model Q01-24) to provide a bias voltage for one of the lenses. The output from the Q01-24 is controlled by a high speed gating system. The on-time

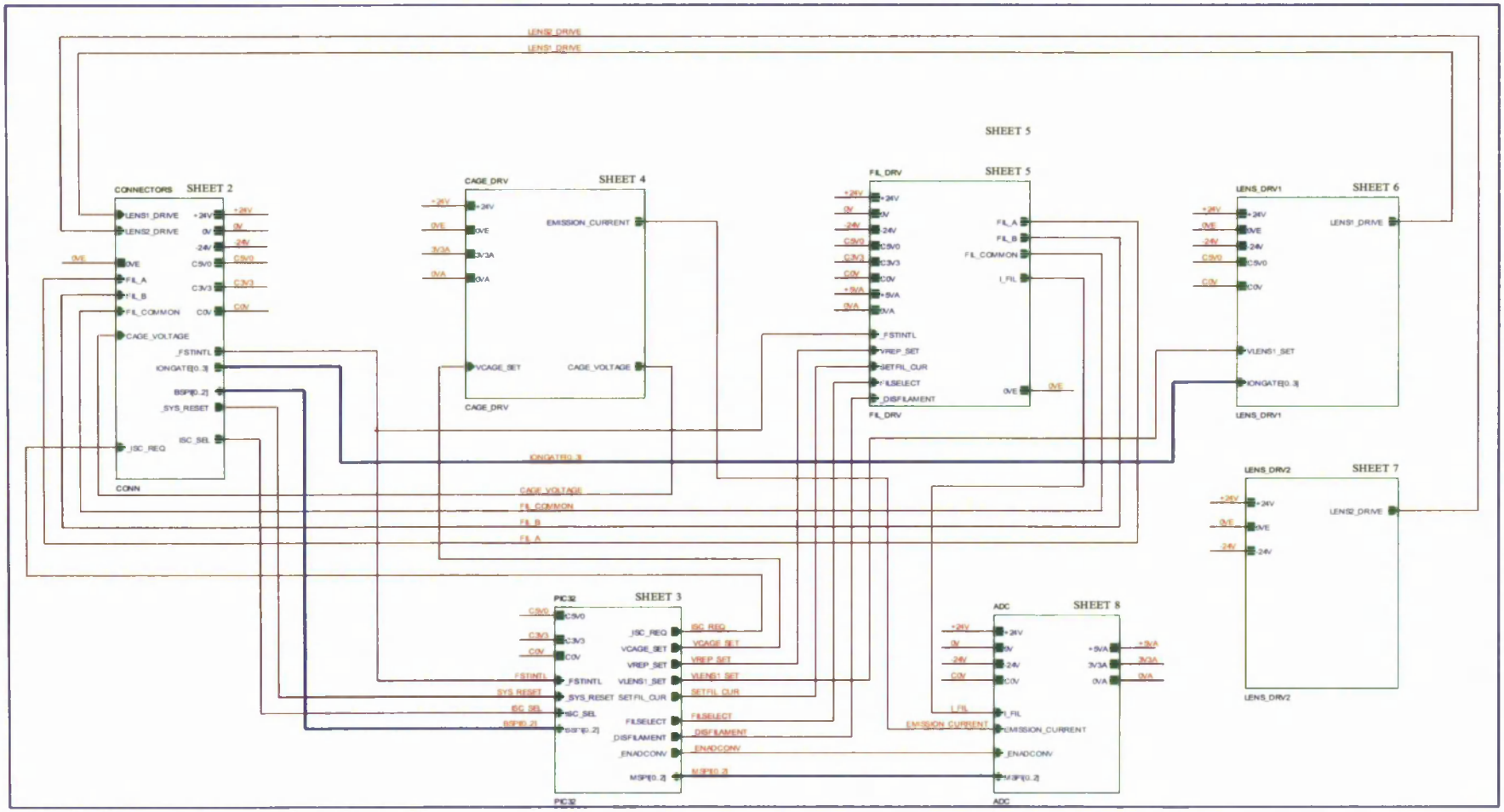

Figure 6.5. Top level schematic diagram for the ion source controller.

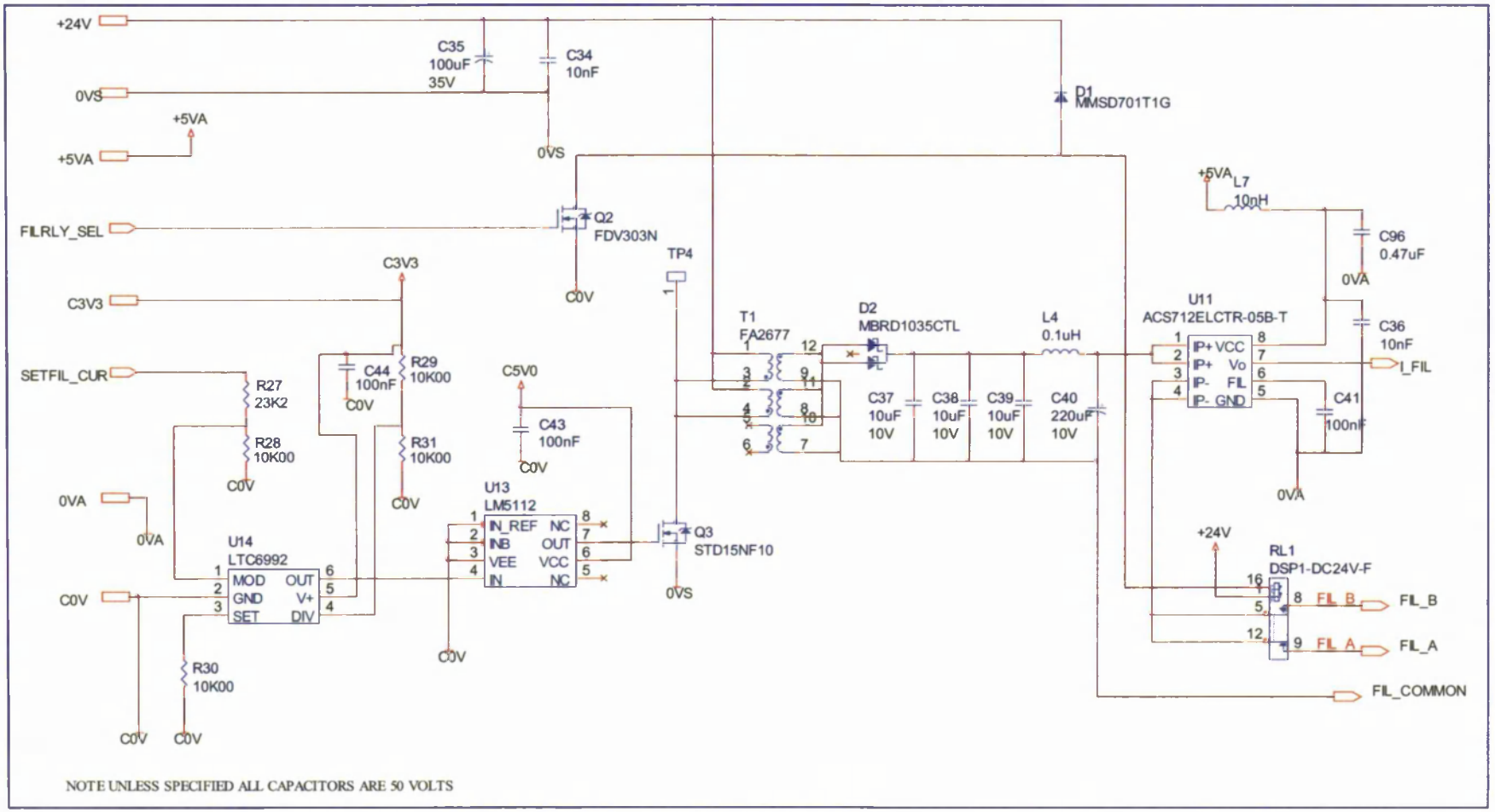

Figure 6.6. Schematic showing the major components of the filament current drive circuit.

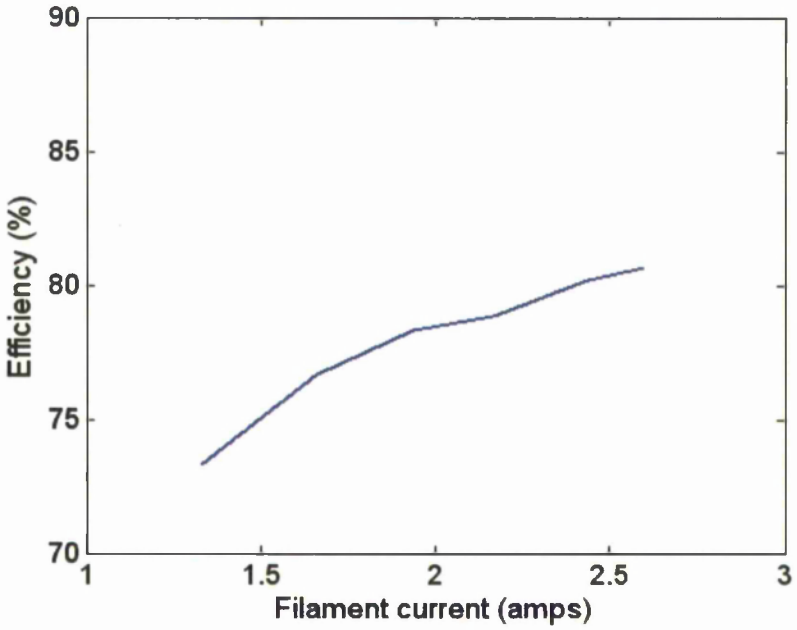

Figure 6.7. Efficiency characteristics obtained for a typical filament current centred about the nominal operating current.

of the gate can be varied in phase relative to the RF frequency providing for phase synchronised pulsed ion injection. This provides support for an investigation of the relationship between the RF phase at the entry point of ions into the QMF and the resultant mass peak tailing [123].

6.5.6 Pole bias control

A facility to generate a pole bias offset voltage is incorporated onto the ISC. This has been included on this controller as the pole bias voltage together with the cage voltage determines the overall ion energy at the entrance to the quadrupole mass filter. A similar circuit to the lens1 circuit is used to generate this voltage.

6.5.7 Analogue to Digital convertor

This block contains the analogue to digital convertor (ADC) which digitises the voltages that represent the filament and emission current magnitudes. A dual channel

12 bit ADC (Analog Devices Inc. AD7887) with a three wire SPI interface to the PIC32-3 is used. Each of the analogue signals are buffered by operational amplifiers (OPAMPS) and processed by anti-aliasing filters before connection to the ADC input pins. Two linear regulators provide low noise voltage rails for the OPAMPS and an accurate voltage reference provides the voltage rail for the ADC from which the reference voltage is also derived.

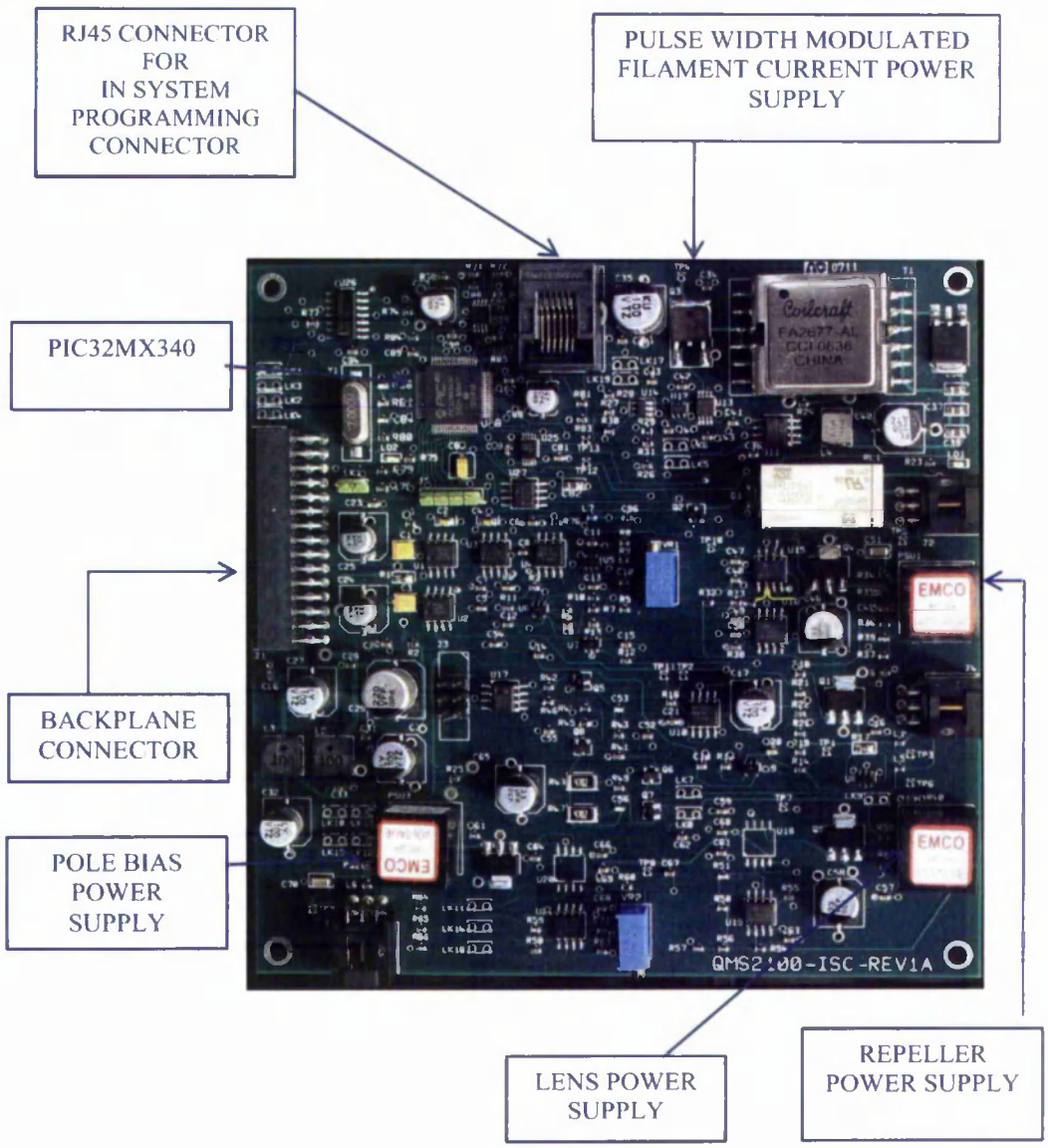

Figure 6.8. Photograph of the ion source controller with major functional blocks identified.

6.5.8 Connectors

A 15+15 way plug provides connection to the mating connector on the SMC for access to the backplane. Provision for accessing the various control signals are provided by means of edge mounted connectors. An edge mounted RJ45 connector is provided for connecting an ICD3 for program development and programming the PIC32-3. Additional Molex connectors are provided on the other edges of the board. A set of links are provided to select one of the slave select lines to as the ISC select.

6.5.9 Physical appearance

A photograph of the assembled ISC with the main functional blocks annotated is shown in Figure 6.8.

6.6 Data acquisition controller

6.6.1 Overview

The data acquisition controller (DASC) together with the ion detector provides the functionality to capture the magnitude of the ionic current exiting from the quadrupole mass filter at each step of the mass scan. The ionic current is measured using either a faraday cup (FC) or an electron multiplier (EM) mounted near the exit of the QMF. The output of the ion detector is connected by coaxial cable to the input of the high input impedance amplifiers on the DASC before being further processed, digitised then stored in the PIC32-3 on-chip random access memory (RAM). These stored values are passed onto the SCM and then finally to the computer for display and storage. The input amplifiers, gain switching relays, selectable inverting/non-inverting amplifiers are contained within a grounded screened enclosure to minimise stray coupling from other parts of the ECU. Figure 6.9 shows a high level schematic of the DASC.

6.6.2 Input amplifier

There are two input amplifier blocks providing for two input amplifiers (Analog Devices Inc. AD549) although only one is required if enhanced auto-ranging is not a requirement. The amplifiers are very low input bias current amplifiers with external switchable feedback resistor networks. The feedback switching is achieved with low thermal EMF reed relays (COTO Technology Inc. 3500 series). The amplifier input leads are mounted on Teflon standoffs (Cambian Ltd. 570-1510-01-05-19) to minimise stray leakage paths at the amplifiers inputs. The output from each of the input amplifiers is fed via an additional operational amplifier (OP-AMP). On-board links are provided to configure the OP-AMP as inverting or non-inverting, thereby accommodating the different polarity of the FC and EM output currents. The output from these OP-AMPs feed into the input multiplexor. A circuit schematic showing the major components for one of the input amplifiers and gain switching circuit is shown in Figure 6.10. Also shown is a low temperature coefficient 2.5 Volt reference voltage to correctly bias the output of U11 for compatibility with downstream circuits.

The dual input amplifier configuration provides the facility to interface to two detectors or can be configured to provide an auto-ranging font end providing faster response than the more conventional single switched gain amplifier which can have a significant recovery time if overdriven. By using two input amplifiers it is possible with the correct gain options to switch between the amplifiers allowing one amplifier to recover while using the other amplifier.

In an RGA it is relatively common for both a Faraday Cup (FC) and an Electron Multiplier (EM) to be provided with their outputs both connected to the QMF output pin. The FC is mounted on-axis and the EM off-axis and with no bias applied to the EM, ions exiting the QMF will hit the surface of the FC. This results in a current flowing into the input of the DASC input amplifiers. With a negative bias voltage applied to the EM, ions are attracted off-axis away from the FC and hit the EM. The EM amplifies the ion current through a conversion to an electron current and results in a current flowing out of the input amplifier. The dual input amplifier can be configured to provide software controlled switching between the FC and the EM increasing the available dynamic range of the measured partial pressures.

6.6.3 Input multiplexer

The input multiplexer (Analog Devices Inc. ADG1219) allows the input signal to be dynamical, sourced from the output of either input amplifier. This forms part of the auto-ranging facility of the DASC or dynamic switching between the FC and EM. The input multiplexer is controlled by a digital output from the DASC microcontroller. If only one input amplifier is fitted the firmware sets the input multiplexer source accordingly. The output from the multiplexer feeds the input to the analogue to digital convertor (ADC) block.

6.6.4 Analogue to digital convertor

This block takes the single ended output from the input multiplexer and using an OP-AMP (Analog Devices Inc. AD8021) and anti-aliasing filters converts the single ended signal to a differential signal compatible with the input requirements of the sigma-delta analogue to digital convertor (Analog Device Inc. AD7765) [169-171]. A number of local linear voltage regulators and voltage references are provided to achieve a set of low noise voltage rails and references for the OP-AMP and AD7765.

6.6.5. Controller

A programmable logic controller (Altera Corporation EPM570) provides the digital interface between the microcontroller, the ADC block and the synchronisation of the ADC operation with the mass scan controller to achieve programmable dwell time at each mass sample point. A local crystal oscillator provides the reference timing clock for the CPLD which generates the timing clocks for the AD7765. The PIC32-2 provides overall control using both SPI communication and control through the digital i/o lines.

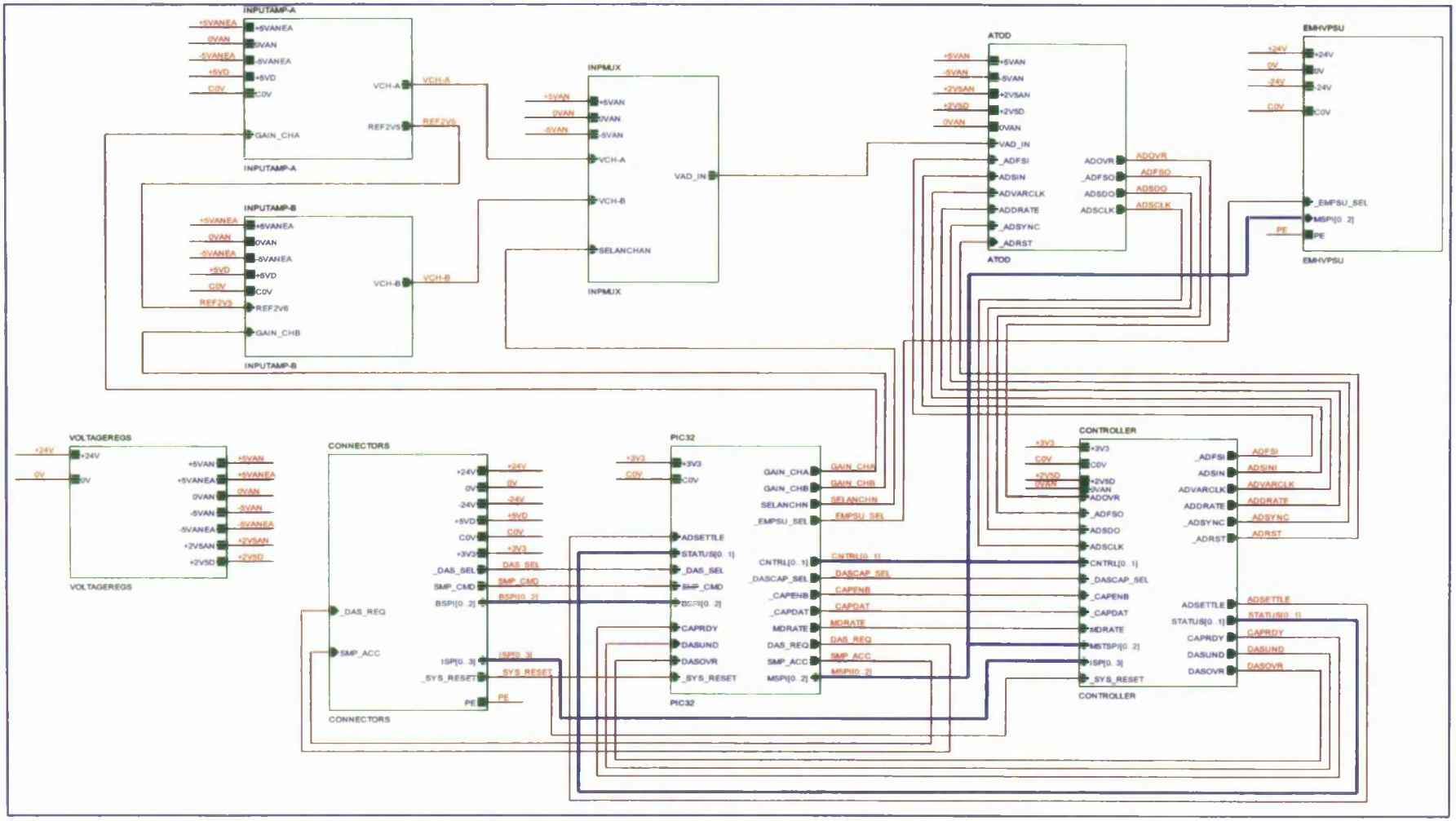

Figure 6.9. Top level schematic for the data acquisition system controller.

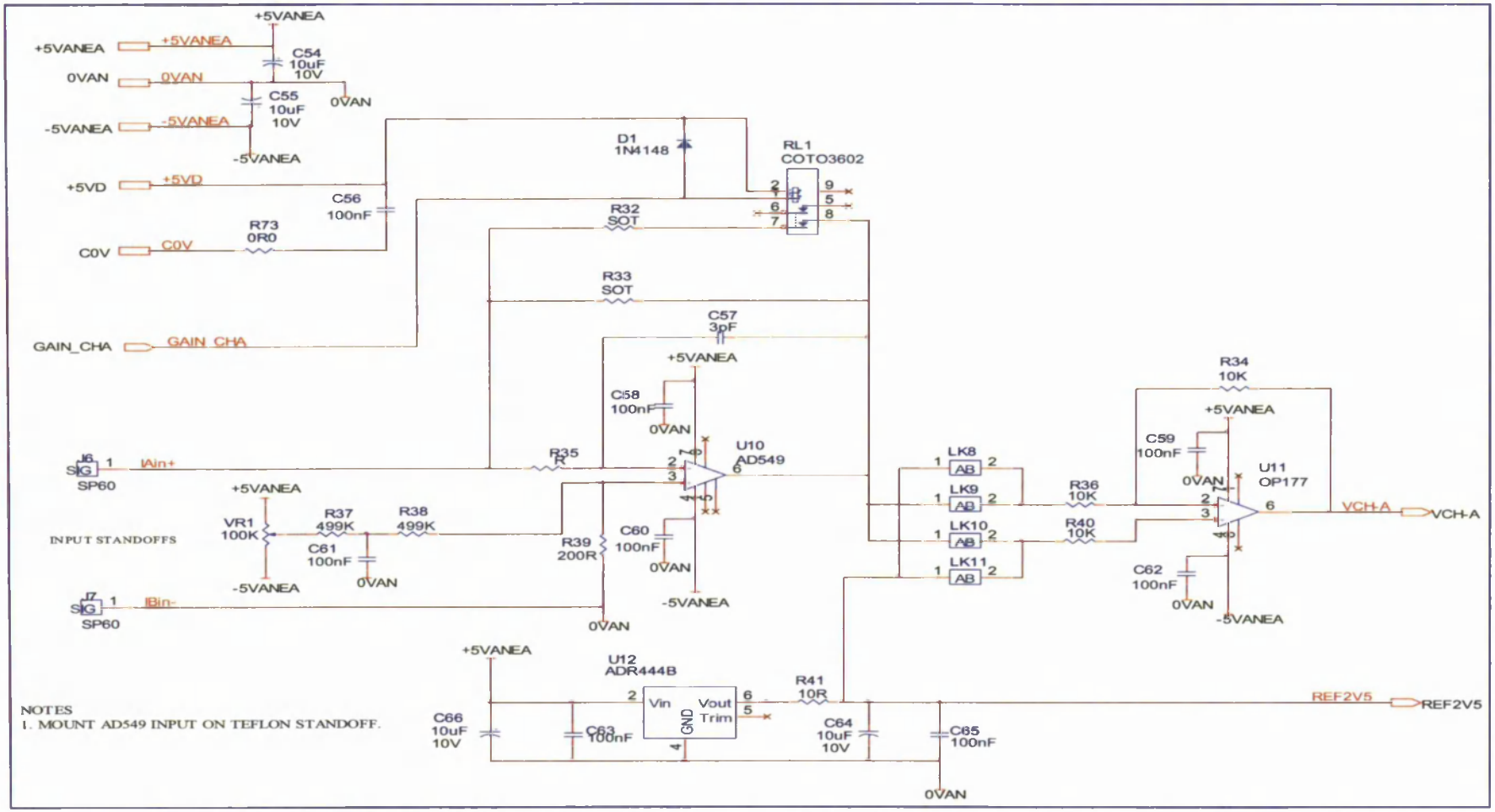

Figure 6.10. Schematic circuit for one of two DASC input amplifiers showing major components including the gain switching relay and precision voltage reference.

6.6.6 Electron multiplier bias voltage

For operation with an EM detector a high voltage negative bias is required for correct operation and gain control. A voltage controlled programmable DC-DC convertor (EMCO High Voltage Corporation Model Q25N-24C) generates the 0 to -2500 bias voltage. A DAC controlled by the PIC32-3 provides the controlling voltage for setting the bias voltage. Load stability of the bias is achieved using a high impedance sense network coupled with an OP-AMP. A high voltage cable directly soldered to the PCB provides the output connection to the ECU flange connector.

6.6.7 Voltage regulators

A JTC series DC-DC convertor (XP Power plc Model JTC0624D09) generates the intermediate voltage rails from the +24 Volt backplane rail. These intermediate voltage rails are post regulated by linear regulators and further filtered to achieve low noise analogue voltage rails.

6.6.8 Connectors

A 15+15 way plug provides connection to the mating part on the SMC for access to the backplane. An edge mounted RJ45 connector is provided for connecting an ICD3 for program development and programming of the PIC32-3. A board link area enables the one of the slave select lines to be selected as the DASC select.

6.6.9 Microcontroller

A microcontroller section virtually identical to that used on the ISC is implemented on the DASC.

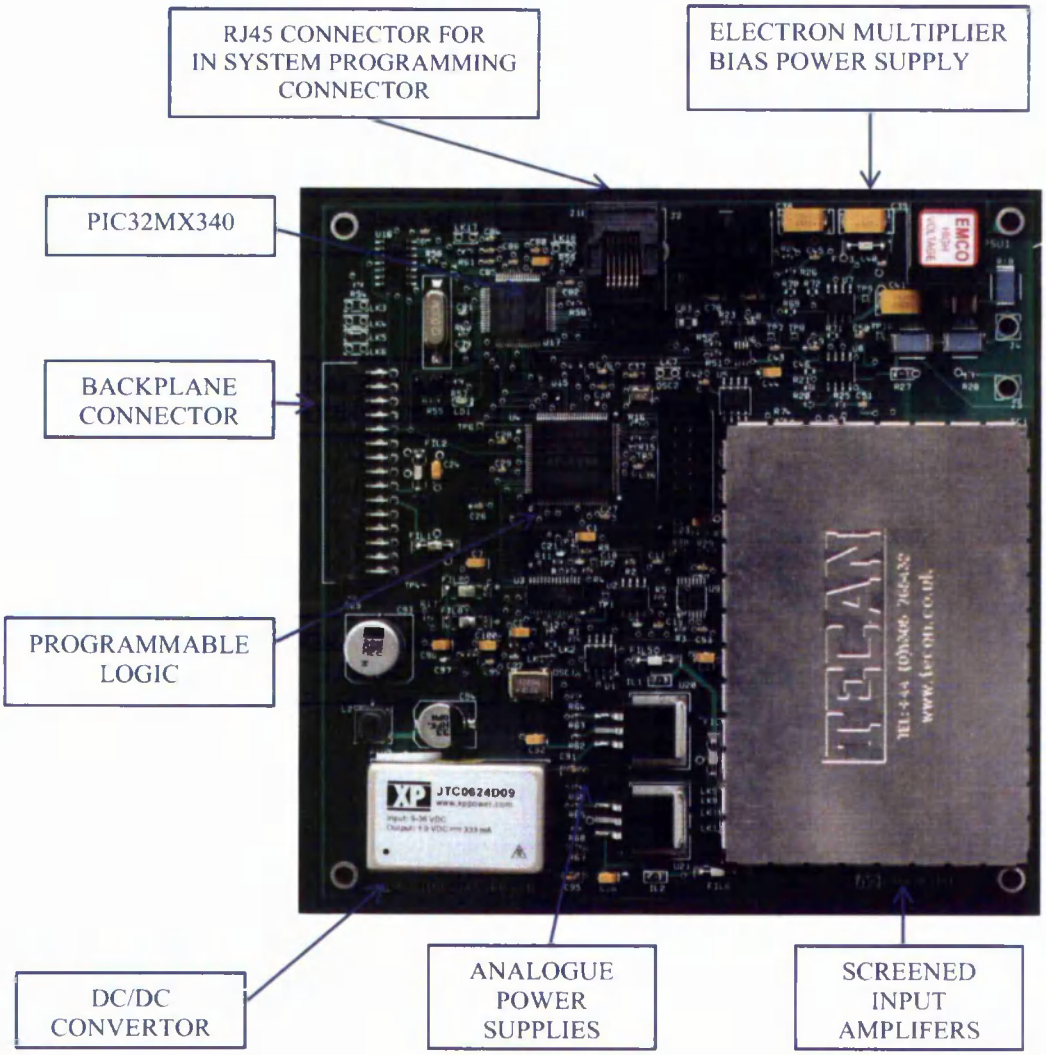

Figure 6.11. Photograph of the data acquisition systems controller.

6.6.10 Physical appearance

An photograph of the assembled DASC with the main functional blocks annotated is shown in Figure 6.11.

6.7 Mass scan controller

6.7.1 Overview

The mass scan controller (MSC) provides the source of the RF and DC ramps required to produce the analytical mass scan required for correct operation of the

quadrupole mass filter (QMF). A top level schematic for the MSC is shown in Figure 6.12 and an image of a completed PCB is contained in Figure 6.13.

A proprietary dual channel direct digital synthesis (DDS) [172] provides the reference RF signal (Analog Devices Inc. AD9958). Each DDS RF output is transformer coupled to a reconstruction filter to minimise the harmonic content of the RF signal. Harmonic content has been shown to degrade QMF performance [35]. Only one DDS channel is required for basic QMF operation. The second channel offers the facility for investigating the effects on QMF performance of differential phase between the x and y electrode RF drives. It also provides a mechanism for correcting for certain mechanical tolerances in the QMF electrode geometry [49].

Each output of the DDS module feeds into the input of a variable gain amplifier (National Semiconductors LM6503) which is used to generate the variable amplitude RF signal under control of the mass sequencer module. These amplifiers can be used in standalone mode or in conjunction with the Drive controller to provide automatic gain control for amplitude stabilisation. A schematic of the mass sequencer module is shown in Figure 6.14.

A PIC32-3 is included on-board together with an interface to the backplane which perform a similar function to those already described for the other SSCs. A number of on-board regulators and voltage references are derived locally to improve noise performance and to support standalone operation.

6.7.2 Mass sequencer

The mass sequencer module consists of a complex programmable logic device (CPLD) Altera MAXII EPM570, a dual channel 16 bit DAC (Analog Devices Inc. AD5547), voltage references and operational amplifiers.

The CPLD contains a SPI port allowing the PIC32-3 to write to the internal control registers and read status information back from the CPLD. The value of the mass scan start, mass scan step size and the mass scan end points are contained in registers within the CPLD and are set by the PIC32-3. At the end of each mass scan step the CPLD calculates the next mass step value and when the mass scan end point is reached indicates to the microcontroller the completion of the active mass scan. The MSC sequencing is interlocked with DASC by the SMP_CMD and SMP_ACC

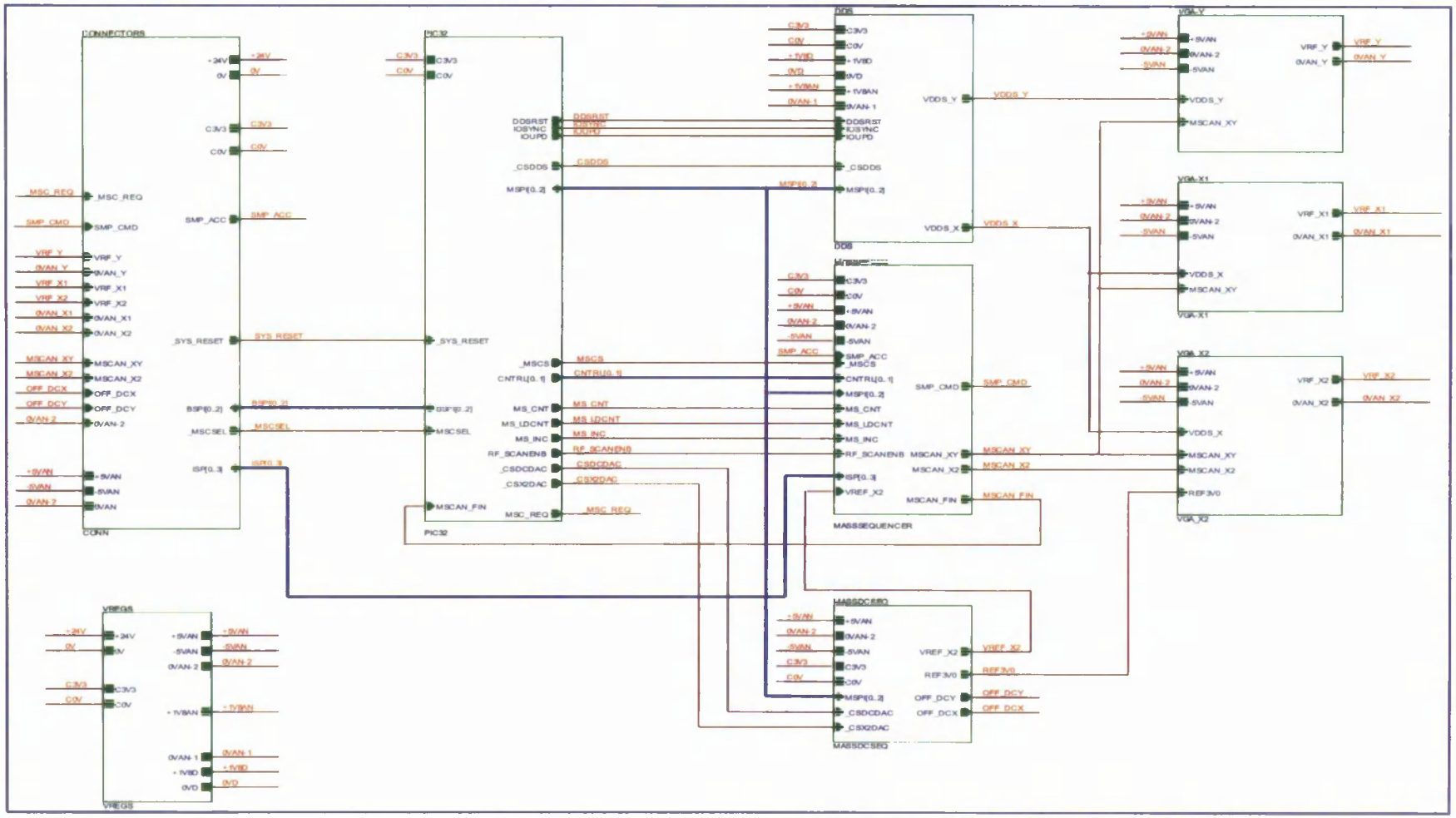

Figure 6.12. Top level schematic for the mass scan systems controller.

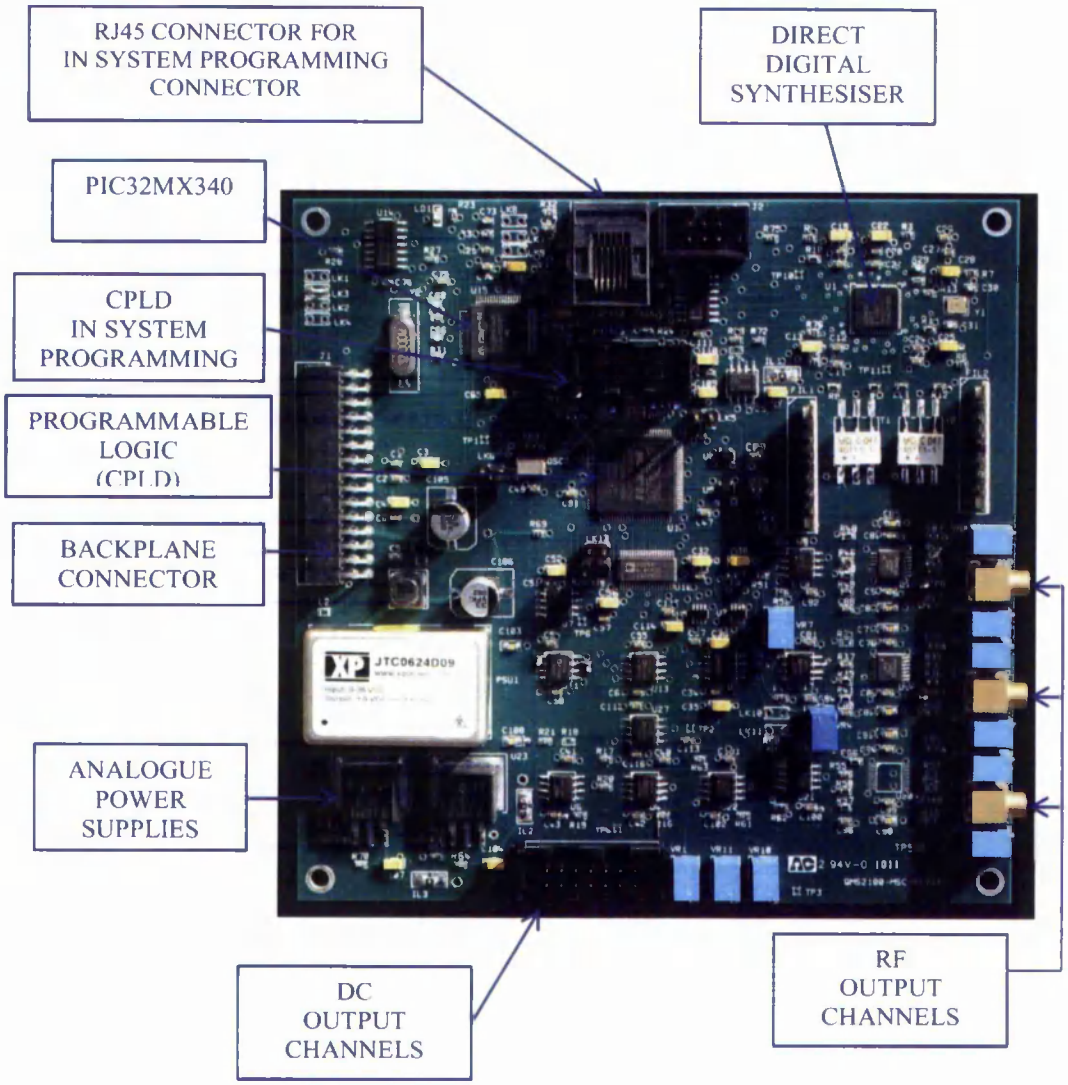

Figure 6.13. Photograph of the mass scan controller.

signals so that MSC dwells on a scan point until the DASC has acquired data. The flexibility in control offered by these programmable registers enables non-linear scan line generation and variable mass scan step size to be achieved. This flexibility also enables zone 1 and zone 3 scan lines to be achieved through firmware control.

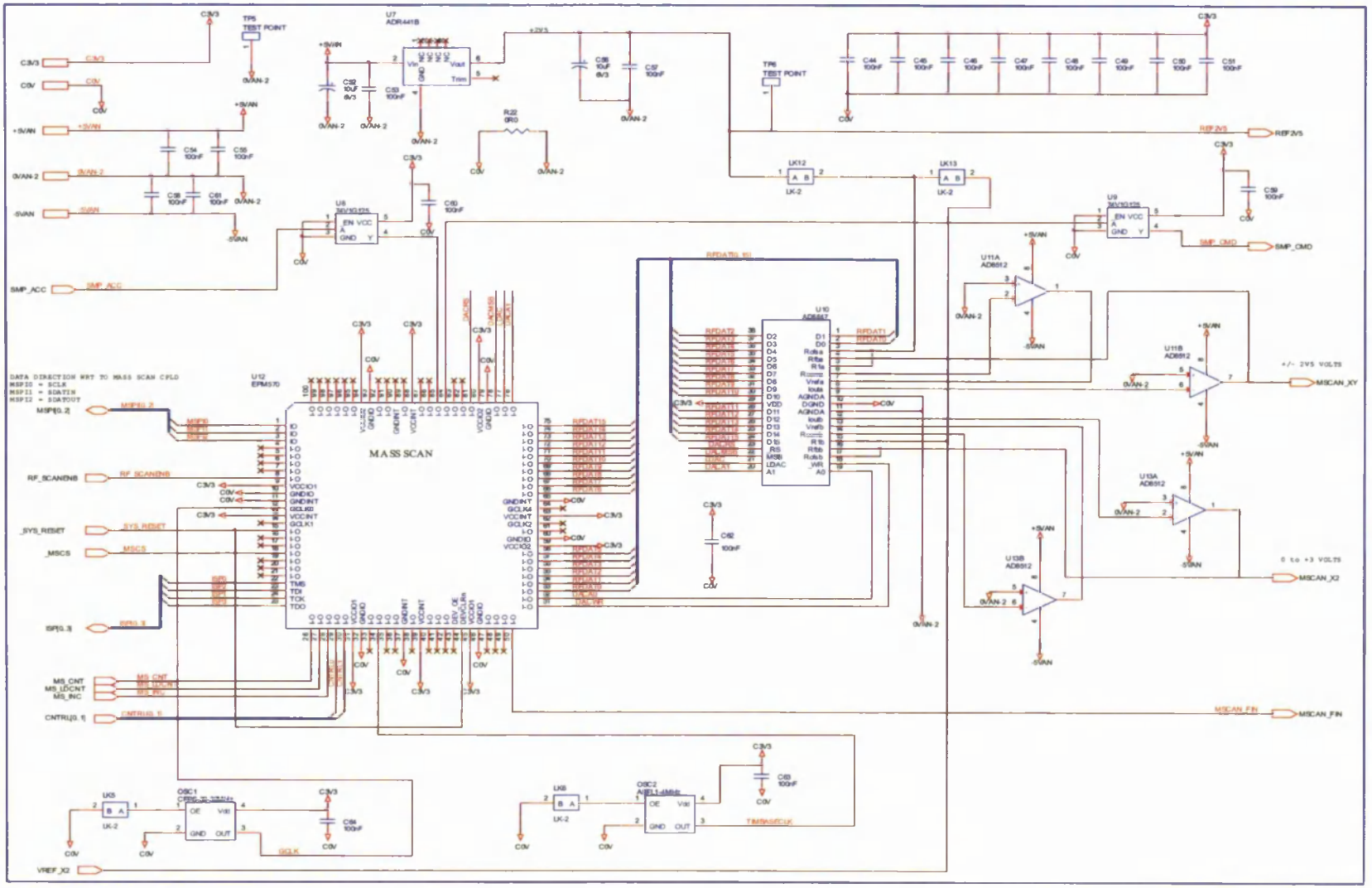

Figure 6.14. Schematic showing major components of mass scan ramp generation

6.8 Drive controller

6.8.1 Overview

The drive controller (DRVCON) consists of two identical channels for providing stabilisation and the correct ratio between the RF and DC ramps. It also provides the buffer amplifiers required for introducing the DC component onto the RF voltage applied to the x and y electrodes. The controlling ramps are sourced from the output of the MSC. The DC signal paths allow for the introduction of a variable pole bias and a mass scan offset voltage to achieve an approximation to a unit resolution mass scan if required.

A standard backplane connector is fitted to the board to derive voltage rails from the backplane and provide a means of mechanical registration with respect to the remainder of the system. No backplane signalling is required for operation of the DRVCON. On-board regulators are used to generate a number of local voltage rails. Figure 6.15 shows a schematic for the top level hierarchy of the DRVCON which consists of a total of nine modules.

6.8.2 DC drive control

The DC drive control consists of a common module DCGEN connected to the electrode specific modules DCDRIVE_X and DC_DRIVE_Y. The DCGEN provides signal conditioning and level shifting of the ramp control signals derived from the MSC. The two outputs (DCSCAN_X and DCSCAN_Y) each act as an input to the DCDRIVE_X or DCDRIVE_Y modules respectively. The DCDRIVE_X and DCDRIVE_Y modules are identical and provide an OP-AMP based summing circuit for introducing the common pole bias (VPOLE) and the mass scan offset voltage OFF_DCX or OFF_DCY. The output of the summing circuit is buffered by a PA240 high voltage power amplifier before connecting to the DC input of the respective channel of the PA.

6.8.3 Peak detection

It is possible to use a number of different methods to measure the amplitude of RF electrode drive signals; root mean square (RMS) detection [173], precision rectification [174], peak detection [175]. The RF drive signal for reasons already discussed is required to be kept free of harmonic content so can be assumed to be a pure sine wave. It is therefore possible to use any of the above methods for measuring the RF amplitude. In general, commercially available RMS measurement integrated circuits (IC) are suitable for frequencies less than 1 – 2 MHz or much higher frequencies. Similarly for precision rectifiers and peak detectors no standard ICs are suitable due to their limited frequency response. A custom design based on one originally proposed by J. McLucas [176] was designed and a schematic showing part of this circuit is contained in Figure 6.16. Two peak detector modules are provided PKDET_X and PKDET_Y. If single channel RF drive with transformer coupling to the QMF is employed only one peak detector circuit needs populating. A sense network in each channel of the PA generates the RF feedback signals VSENSE_X and VSENSE_Y which act as input to their respective peak detectors. The output of each peak detector VPEAK_X and VPEAK_Y feed into their respective gain control modules. A prototype circuit was built to optimise the design but it is considered that there will in all probability be a need for additional development work during the testing and development phase.

6.8.4 RF Amplitude control

The RF amplitude control system is comprised of the four modules VGA_X and VGA_Y together with their respective peak detectors PKDET_X and PKDET_Y. These form a dual channel RF amplitude controller. The purpose of these controllers is to maintain a constant relationship between the mass ramp control signal produced by the MSC and the amplitude of the RF electrode drive voltage. By achieving this, the ratio between the RF amplitude and the DC amplitude can be maintained.

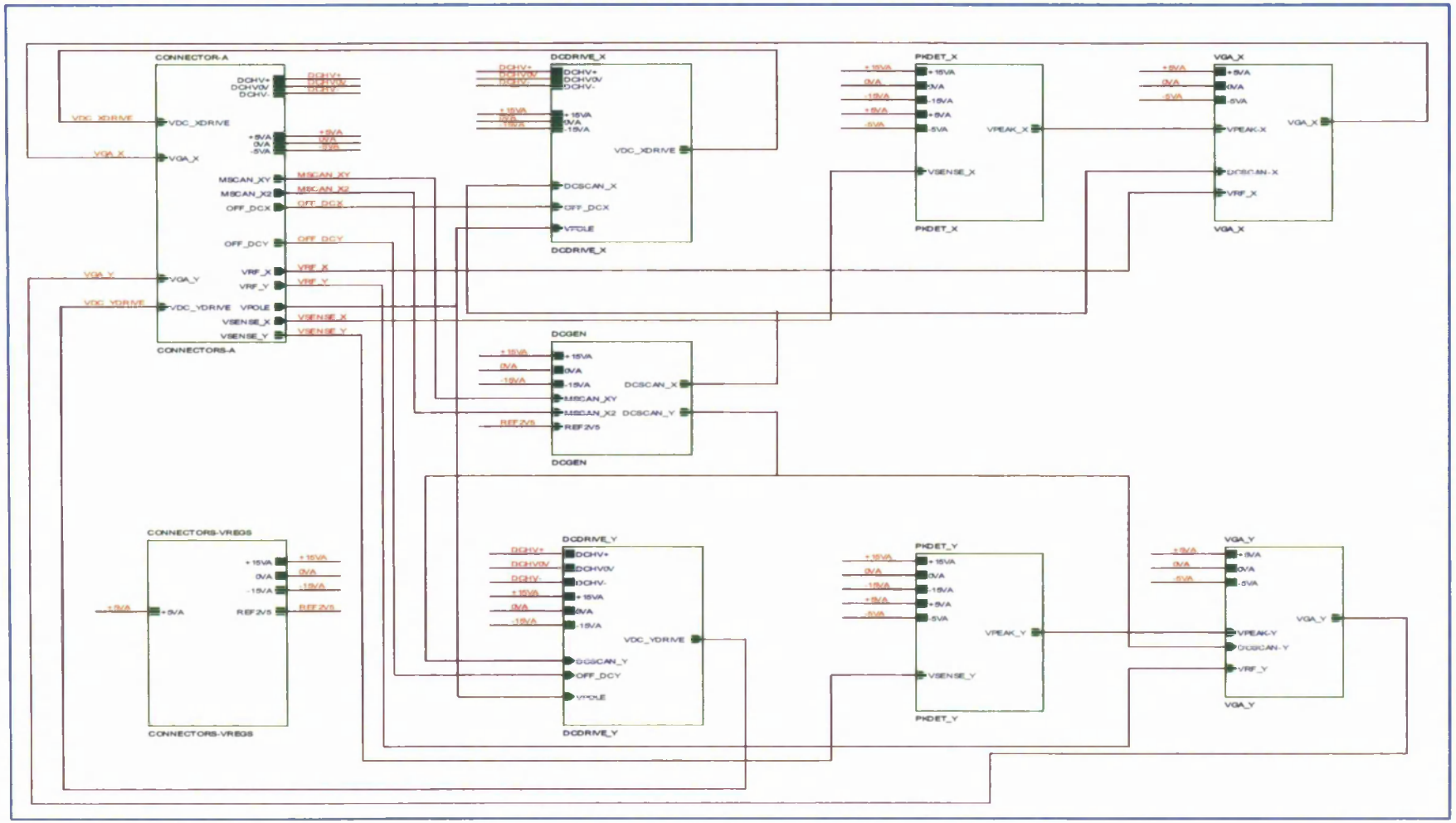

Figure 6.15. Top level schematic for the drive controller.

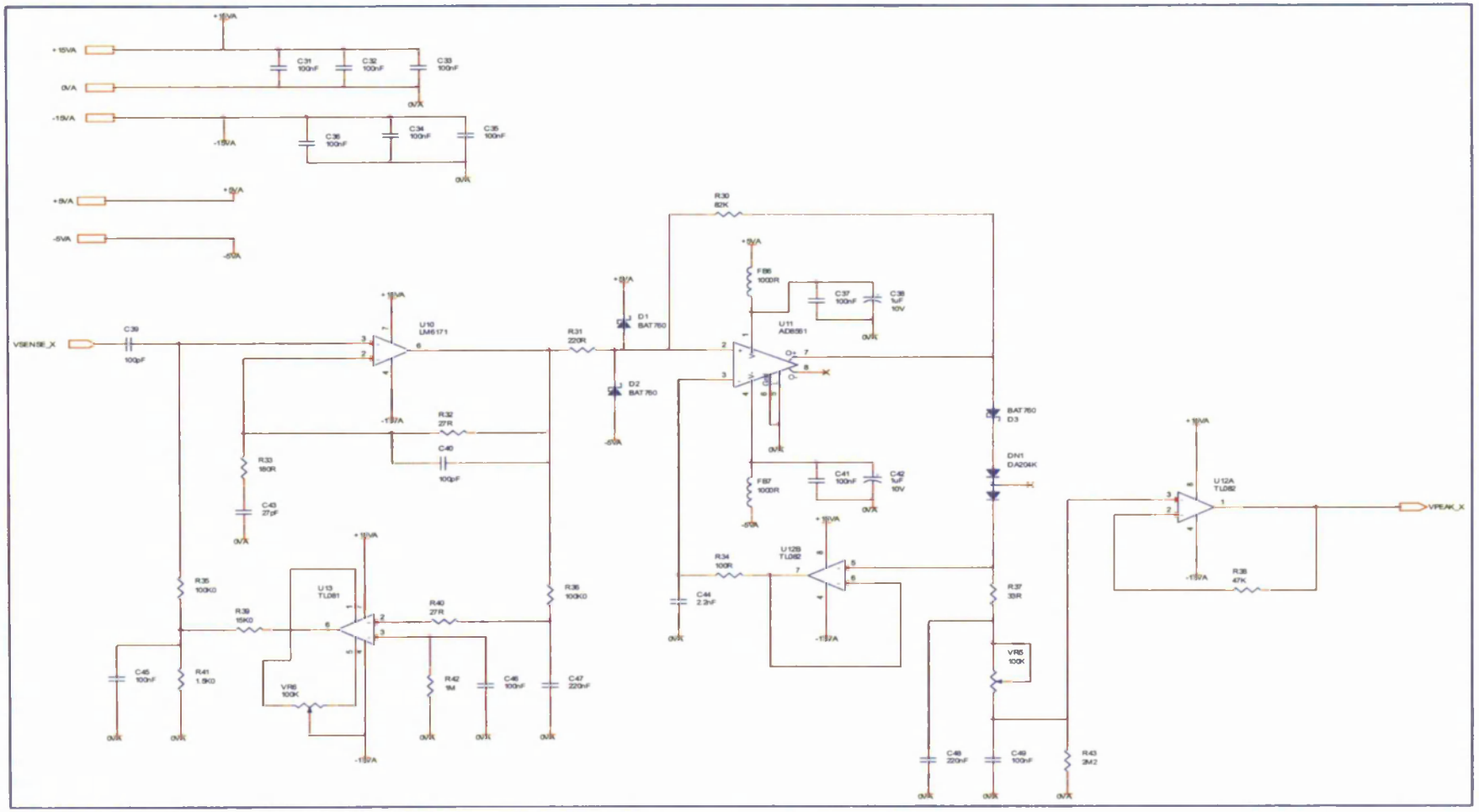

Figure 6.16. Schematic diagram of RF peak detector showing significant components for one channel.

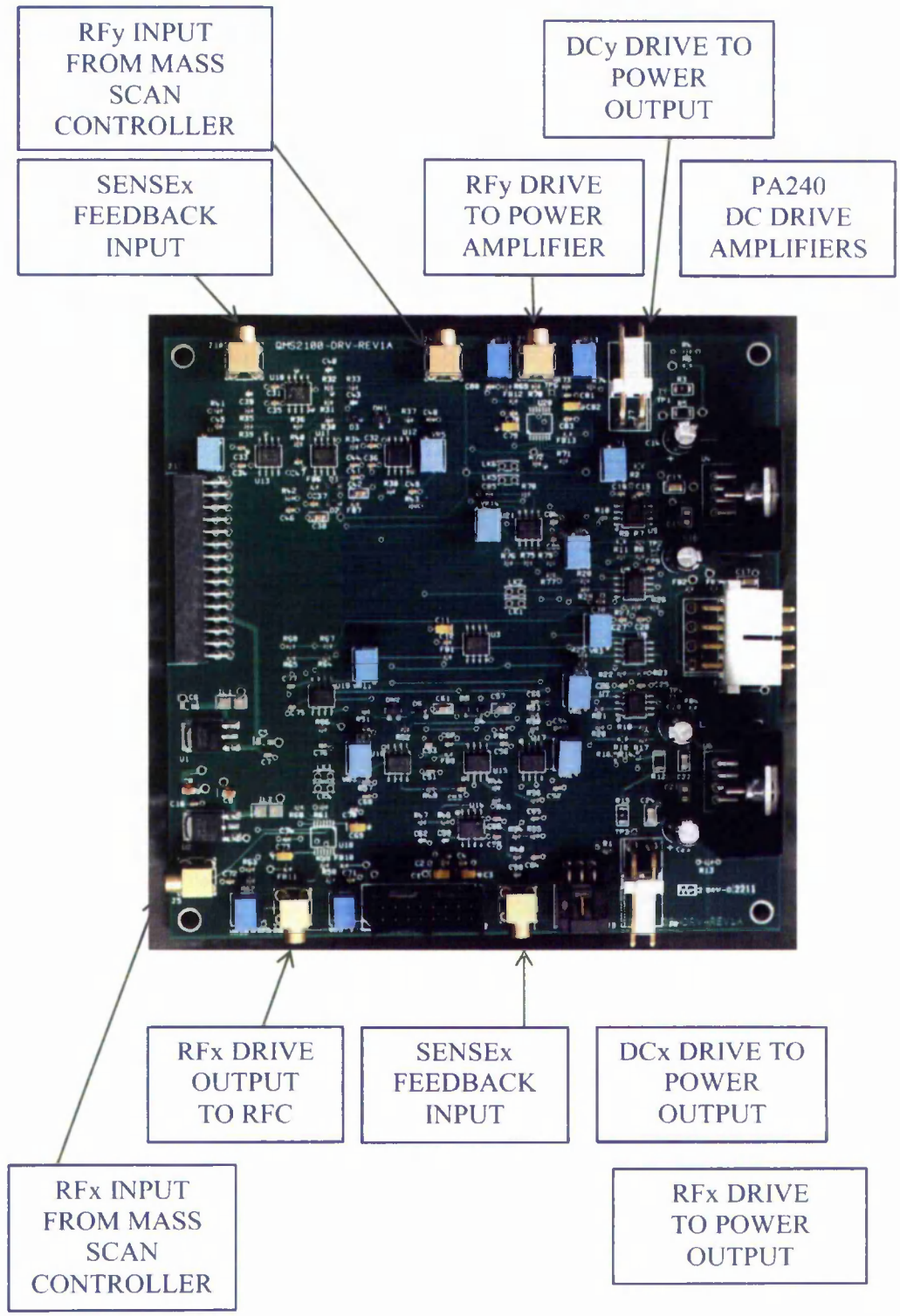

Figure 6.17. Photograph of the drive controller.

Each peak detector output and the mass scan ramp control signal are used to form an error signal which acts as a gain control signal for a voltage controlled gain amplifier.

6.8.5 Physical appearance

Figure 6.17 shows a photograph of the completed DRVCON with each of the connectors identified.

6.9 Power amplifier

6.9.1 Overview

The power amplifier (PA) provides a dual power output stage for driving the QMF electrodes together with filtering networks for coupling the RF and DC voltages to the QMF electrodes. A PA119 (Apex Microtechnology Corp.) is used for each of the RF power amplifier output, two are required if independent x and y electrode drive is being used. The circuit also allows either direct coupling using separate series tuned circuits to achieve voltage amplification or if much higher output voltages (> 350 Volts peak to peak) are required transformer coupling can be employed. Two pi-network filters are provided for coupling the x and y electrode dc voltages to their respective electrodes. This provides protection for the dc driving circuits from the RF drive voltages but still maintain a low source impedance source for the DC electrode drive thereby maximising scan speed. Figure 6.18 shows a schematic for a single power output channel.

6.9.2 RF amplitude sensing

A capacitive potential divider network is provided for each of the output channels to generate feedback to the RF amplitude control on the DRV PCB. The PCB

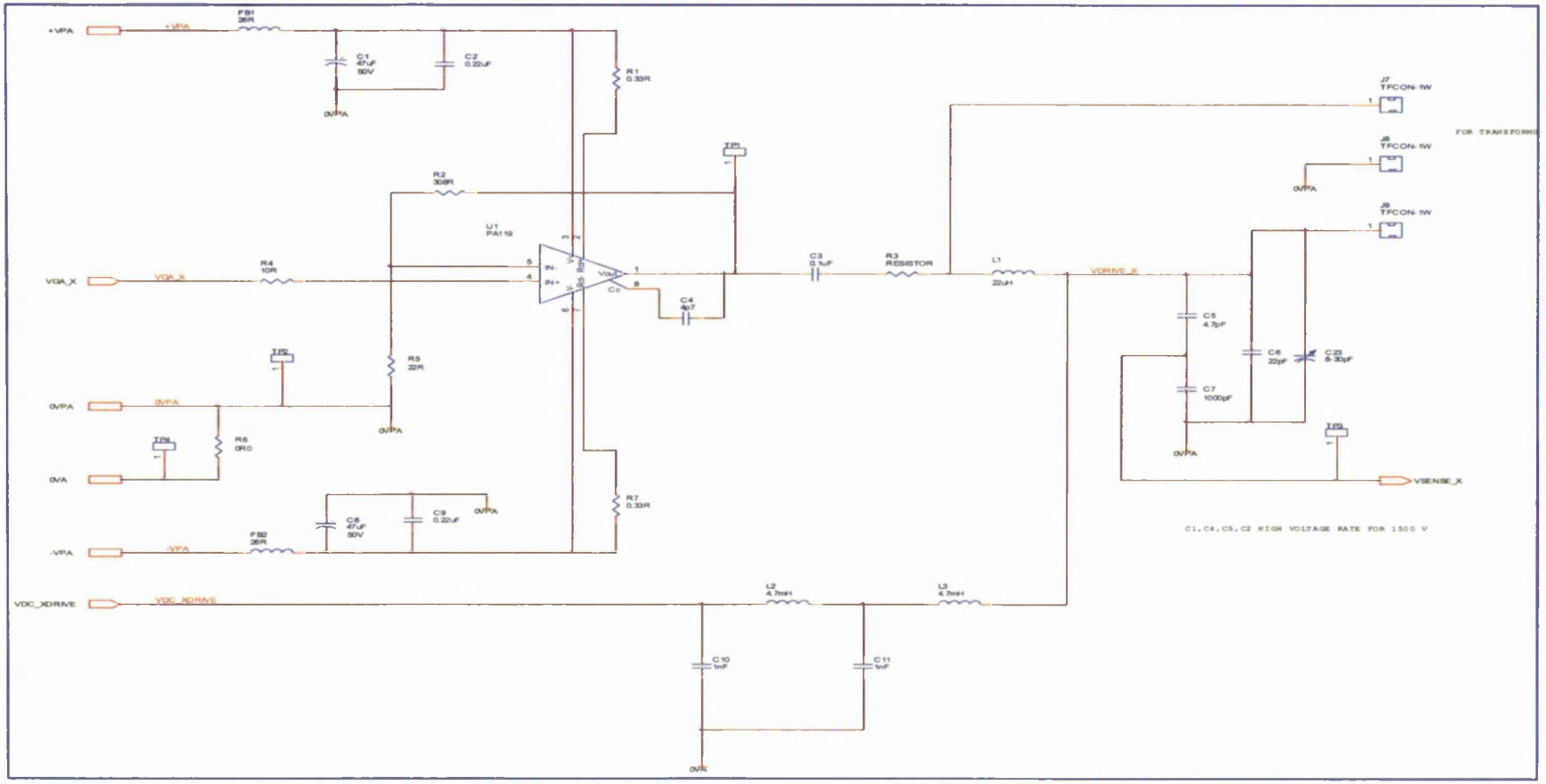

Figure 6.18. Schematic of one power output channel showing major components include PA119, tuned coupling and DC drive isolation filter

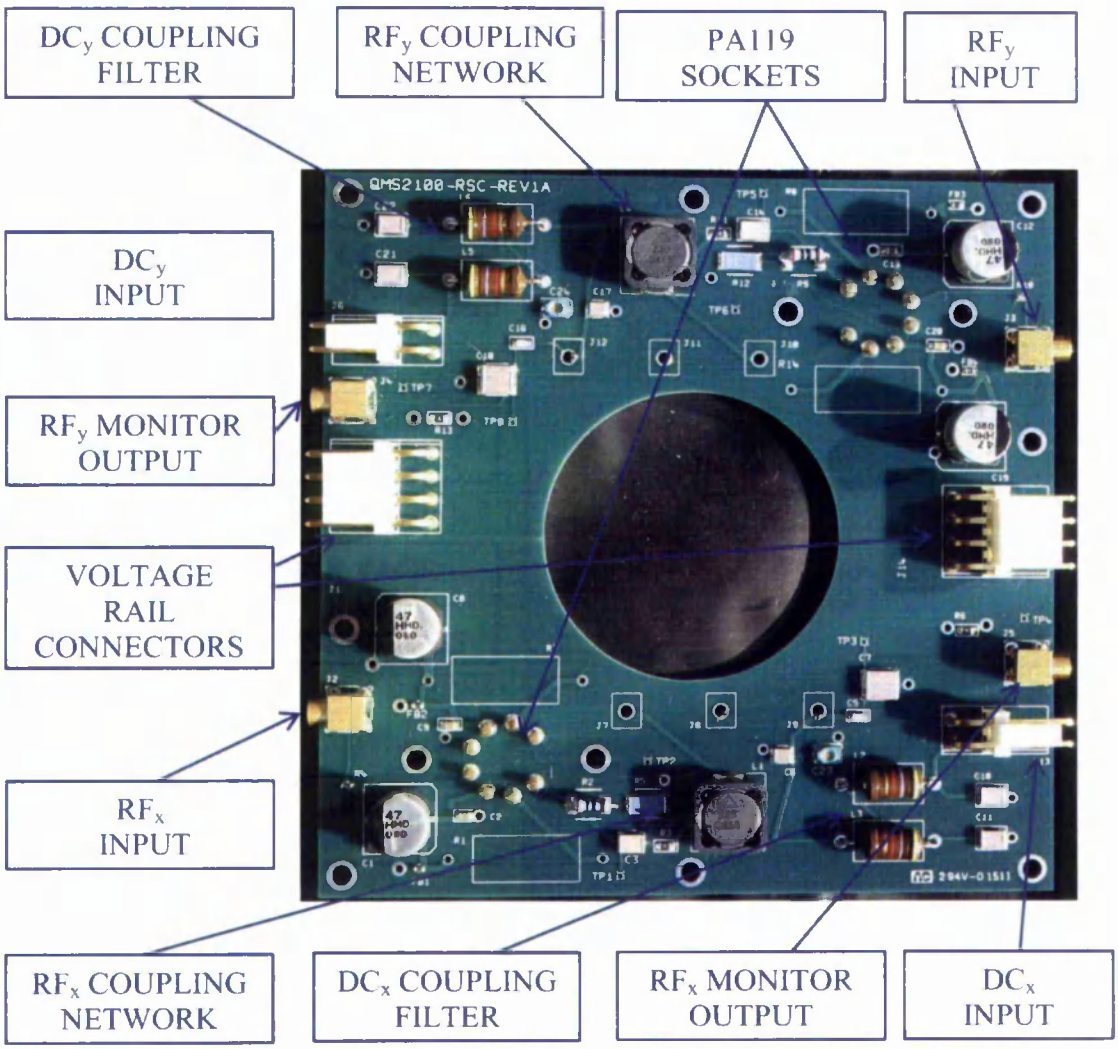

Figure 6.19. Photograph of the main component side of the dual channel power amplifier.

tracking arrangement enables the network to monitor the output of the PA when operating in direct coupled mode or the output from the transformer secondary if transformer coupling is employed. Two trimmer capacitors are fitted one for each sense network to compensate for tolerances in the capacitive divider.

6.9.3 Power supply requirements

The boards are designed to run from the ±24 Volt main voltage rails or from a separate voltage supply of up to ±36 Volt allowing higher electrode drive voltages to be achieved. Current limit resistor positions are provided on the PCB and if the resistors are fitted the PA119s are capable of sourcing up to 4 amps peak output current. When not fitted the current output is determined by the internal current limit of the PA119 which is set to provide 0.5 amps. Power line LC filtering is provided to minimise conducted noise to the rest of the ECU.

6.9.4 Physical arrangement

The PCB is designed so as to allow for the board to be mounted on the back-plate of the enclosure where the vacuum flange interface connector would be mounted. This arrangement enables the co-axial cables used for coupling the board to the connections feeding the QMF electrodes to be kept short, thereby minimising the additional capacitive load of the interconnection system. The PA119 amplifiers are mounted on the back-plate to allow their heatsinks to make direct contact with the back-plate so as to minimise the thermal resistance between the PA119 package and ambient.

6.10 Physical implementation

6.10.1 Printed circuit board material

All of the printed circuit boards (PCB) are constructed to a similar mechanical standard. The PCBs are of four layer construction using 35 micron copper laminate on FR4 base material. The external two copper layers are used for signal traces with the inner two layers providing the power and ground planes. All the PCBs are of a nominal 1.6 mm thick laminate with the exception of the PA which is 2.4 mm. To minimise effects of the coupling of circulating currents into sensitive circuit areas the power and ground planes are split into isolated areas with single point connections

between them. The mechanical characteristics for the individual PCBs are contained in Table 6.1.

Controller	Part identification	Size length × width (mm)	Height (mm)	Weight (gms)
SMC	QMS2100-ECU1	175 × 125	20	142
ISC	QMS2100-ISC	125 × 125	21	115
MSC	QMS2100-MSC	125 × 125	19	102
DASC	QMS2100-DAS	125 × 125	21	136
DRV	QMS2100-DRV	125 × 125	33	106
PA	QMS2100-RSC	125 × 125	47	170[1]

Table 6.1. Physical characteristics of the controller printed circuit boards.
([1] excludes rear panel mounted heatsinks)

6.10.2 Printed circuit board assembly

The majority of components are mounted on the upper layer of the PCB but a number of PCBs also have a small number of components mounted on the lower surface. In the majority of cases these are decoupling capacitors and are placed there to achieve more localised decoupling of power rails. In general all components are of surface mount construction the exceptions being; the connectors, high powered components such as the PA119 and PA240, power supplies and a small number of high power resistors.

Assembly of the PCBs was carried out by EFS Ltd Cambridge using conventional hand placement and soldering. For this prototype batch, this was significantly cheaper than using automatic placement and reflow soldering due to the one off set-up charges associated with this manufacturing process.

6.10.3 Complete assembly

Figure 6.20 shows an image of a complete ECU housed in a skeleton enclosure. The heatsinks associated with the dual PA119 amplifiers are visible on the external

surface of the backplate. A space between the left most SSC and the front edge of the enclosure can be used to house an internal power supply if required.

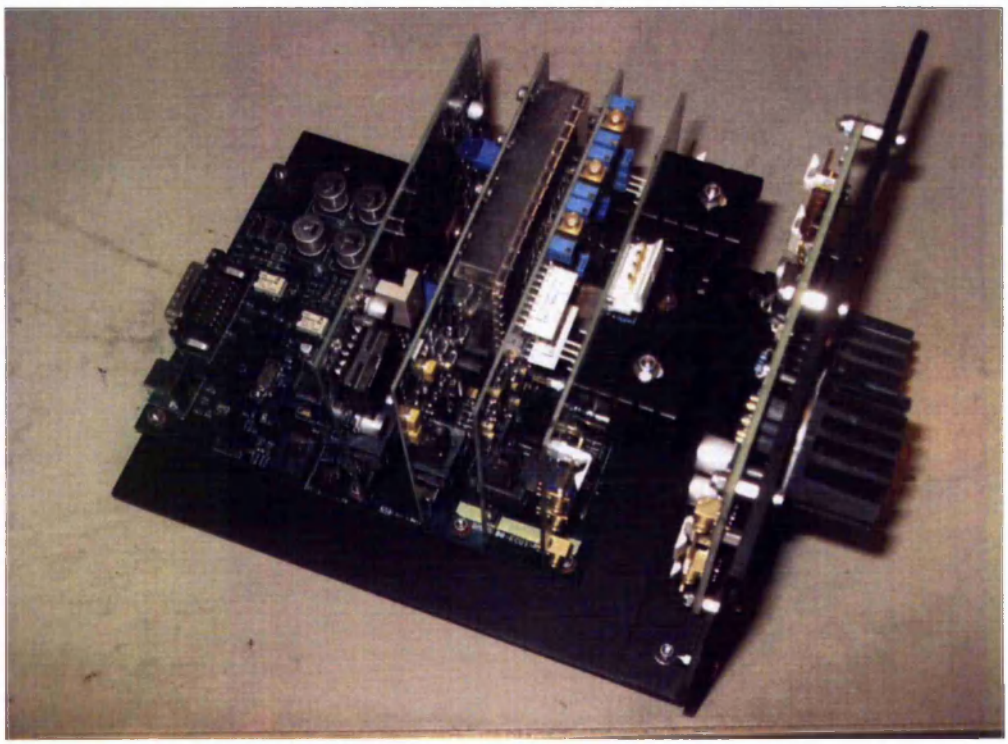

Figure 6.20. Photograph of the assembled electronic control unit mounted in a skeleton enclosure with internal cabling omitted for clarity.

6.11 Design tools

To support the design, development and manufacture of the ECU a number of software packages were utilised. These split logically into three groups; schematic capture and printed circuit layout, programmable logic design, software and firmware development.

6.11.1 Schematic capture

The schematic drawings were produced using Cadence OrCad Capture [177-178] software. Each of the control boards are specified in a hierarchical manner and from

the top level it is possible to drill down to the individual circuits. The package allows the design to be verified against a set of design rules. On satisfactory completion of the design rule checking (DRC) a bill of materials was generated. Finally a net list was generated which provides a connectivity list and footprint identification for the circuit. The net list provides the mechanism for data exchange between the schematic capture and pcb layout systems.

6.11.2 PCB layout

Vutrax produced by Computamation Systems Ltd. [179] was used to design the PCB layouts and to generate their manufacturing. Firstly for each footprint used in the circuit, a physical shape was generated and stored in the project physical library. At this stage a board outline was also generated which incorporates any fixed mounting holes and/or routing cut-outs that are required. Next a set of appropriate design rules were generated. These specify the required attributes of the PCB such as minimum track thicknesses, minimum track clearances, names for power plane signals. Next the net list produced in Orcad is imported and associated with the physical library to produce a rats nest. This is a database which contains all the design information.

Each electronic component is physically located in a position within the board outline taking into account signal path lengths and physical constraints. A ripup and retry autorouter is then run to obtain an initial track routing solution. Manual editing was then used to achieve a completed layout. Power and groundplane layers were then designed. The designs were then checked against the design rules. Finally the Gerber photoplot and computer numeric control (CNC) drilling plots required to generate the manufacturing artworks are obtained by running the plotting module.

6.11.3 Programmable logic design

The DAS and MSC controllers use Max II EPM570 (Altera Corporation) complex programmable logic devices (CPLD) to provide some of the real time control functionality. Design entry of these was specified using the Very High Speed

Integrated Hardware Description Language (VHDL) [180-181] in the Altera Quartus 11.0 Web base edition [182] development environment. The waveform entry tools were used to generate a test bench for functional and timing analysis. A USB Blaster (Altera Corporation) was used to program the devices using the controllers ISP at the initial controller testing stage.

6.11.4 Microcontroller firmware development

The firmware for each of the controllers was written in C using the Microchip C compiler and developed within the Microchip MPLAB IDE environment. As the PIC32 is a common microcontroller to each of the controllers, certain high level functions are made common to all them. This provides for easier development and on-going maintenance.

Testing and development of the firmware was carried out using the software simulator MPLAB SIM then the MPLAB ICD3 for final code optimisation and development on the target controller. When the code was completed, the ICD3 was used to program the flash program memory on each of the PIC32 microcontroller.

6.11.5 PC software development

To support user control, data extraction and storage a PC based application software package was developed. It provides a graphical user interface (GUI) to enable a user to; control the operation of the ECU, retrieve mass scan data, and display and store the data. To support this development and also as a manufacturing aid, a test harness was developed to facilitate testing and debugging of the hardware and associated firmware.

The GUI is shown in Figure 6.21 and consists of a number of group boxes on the left to enable an operator to enter the operating conditions of the QMS. Control switches are provided along the bottom of the GUI to start a mass scan, save results, abort a scan and to exit the program. The largest white rectangular area on left of the GUI provides a means of displaying the results of a mass scan. The program was developed in the Visual.Net environment and has been tested on Windows® XP professional and Windows® 7 64 bit professional [183].

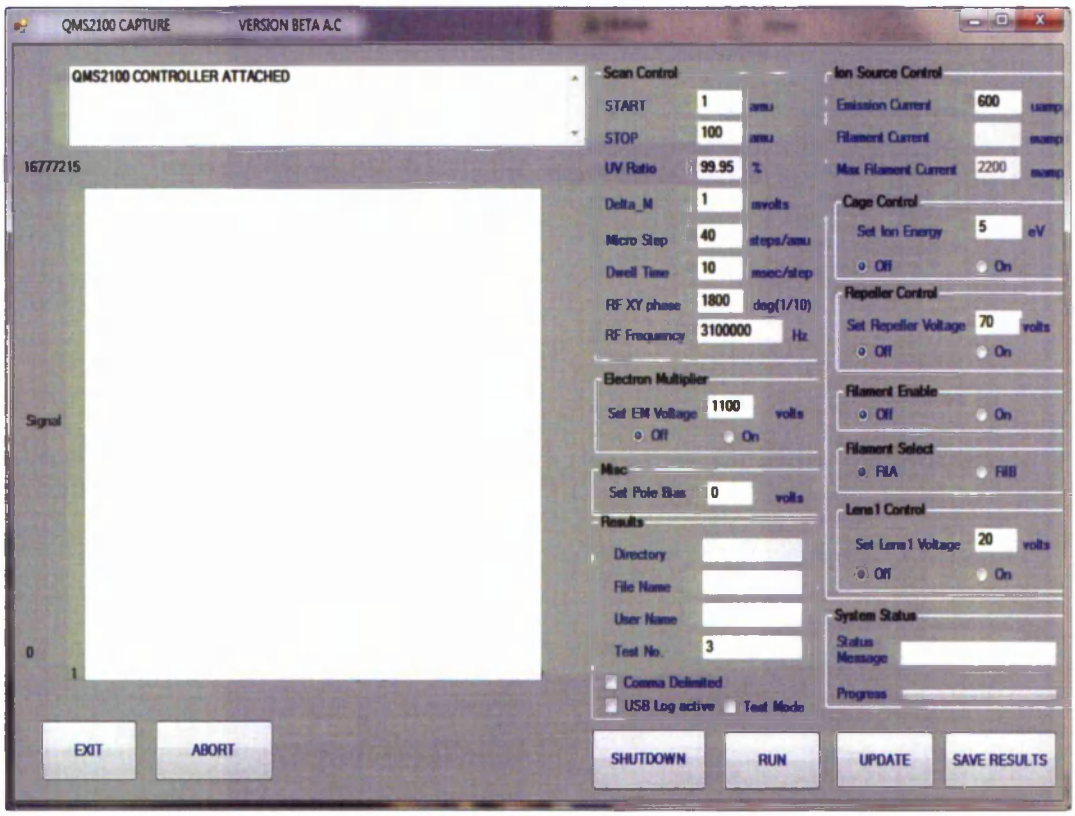

Figure 6.21. Graphical user interface for QMS2100 capture program for use with QMS2100 electronic control unit.

6.12 Testing

6.12.1 Controllers

For each of the controllers, firmware test harnesses were developed and if necessary hardware test boxes designed and built. Each controller was then tested individually to check for correct functionality. Then each of the SCCs were connected to the SMC to verify correct communication between the computer, SMC and SCC.

6.12.2 System testing

Initial testing of the ECU coupled to the remainder of the modules that form the QMS has commenced. Figure 6.22 shows a QMS system with the ECU loosely

coupled to the flange connector together with bench power supplies that were used in the used in the tests. Details of the equipment associated with the suitcase are contained in Appendix E and the pin allocation for the vacuum flange connector in Appendix F.

Firstly the ISC was connected to the Ion source and tests confirm that an emission current in excess of 1 milliamp was obtained at a total pressure of 1×10^{-6} Torr. Additional tests were carried out to characterise the change in emission current against total pressure while keeping the filament current constant. The results of these tests are shown in Figure 6.23. As expected, the emission current measured is proportional to the filament current and falls with increasing pressure due to the electron collisions with the neutral gas molecules. Additional tests are required to characterise the response characteristics of the ion source and tune the control loop.

The dual channel PA was connected to the two sets of electrodes and frequency and coupling network adjusted to maximise the peak to peak RF voltage at a frequency of 3.1 MHz derived from the DDS on the MSC. With suitable changes to the tuning components, the ECU can be operated at lower or at higher frequencies up to approximately 5 MHz. The relative phase parameter of the DDS was adjusted to ensure correct 180° relative phase between the x and y electrode RF drive was obtainable.

An initial value for the gain of the electrometer amplifier has been set based on tests carried out with a fixed RF voltage and no DC voltage on the QMF electrodes and using the FC as the ion detector. A value of 1G ohm for the electrometer amplifier feedback resistor was selected based on these initial measurements. Further total pressure tests were carried out for approximate emission currents of 200 and 400 micro-amps and are displayed in Figure 6.24. From these tests it can be calculated that the ion current is approximately 0.3×10^{-9} A and 0.65×10^{-9} A at 200 and 400 micro-amps emission current respectively for a total pressure of 4×10^{-5} Torr. This corresponds to a sensitivity in the order of 1×10^{-5} A/Torr which compares well with commercial instruments [133]. The non-linearity of the output voltage against pressure in the case of the emission current of 400 μ A is attributed to the variation in emission current when undertaking the tests.

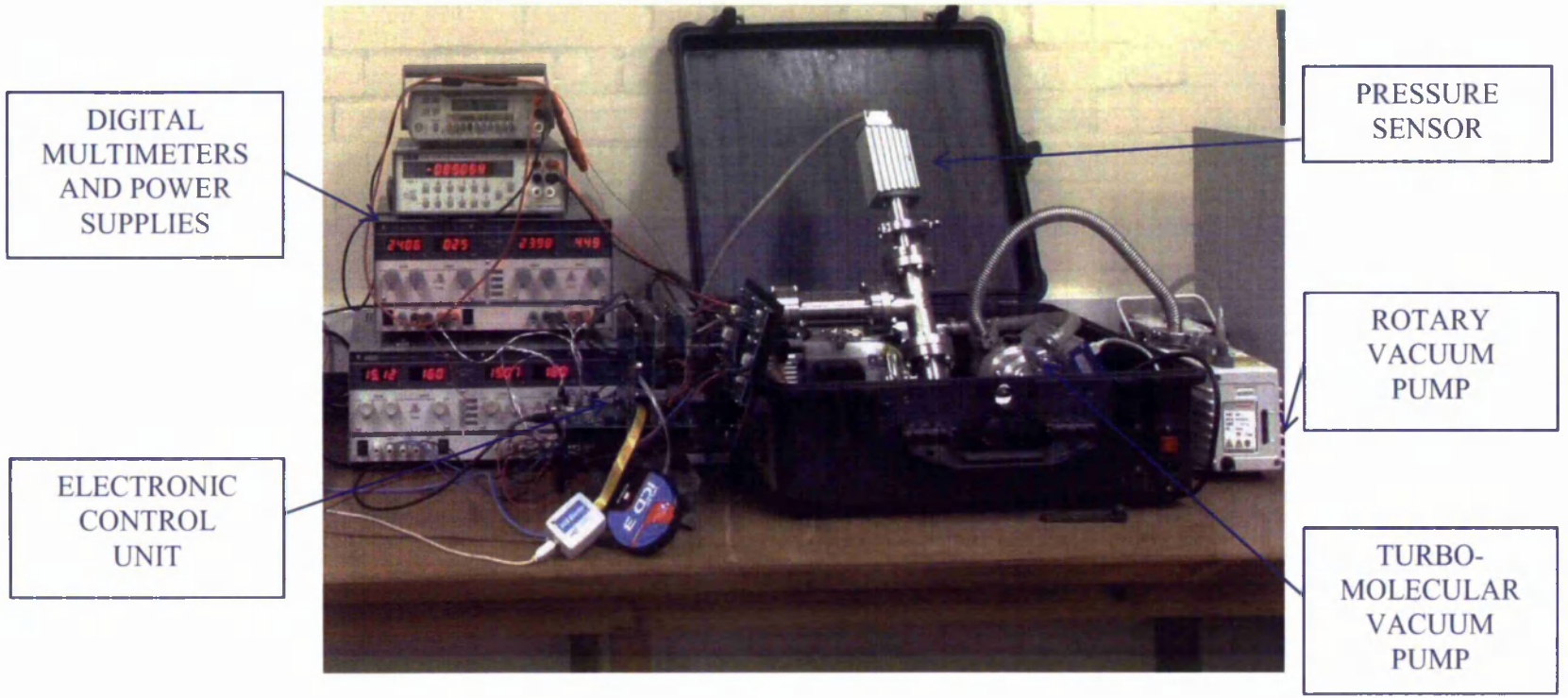

Figure 6.22. Initial test set showing ECU connected to a QMS and vacuum system.

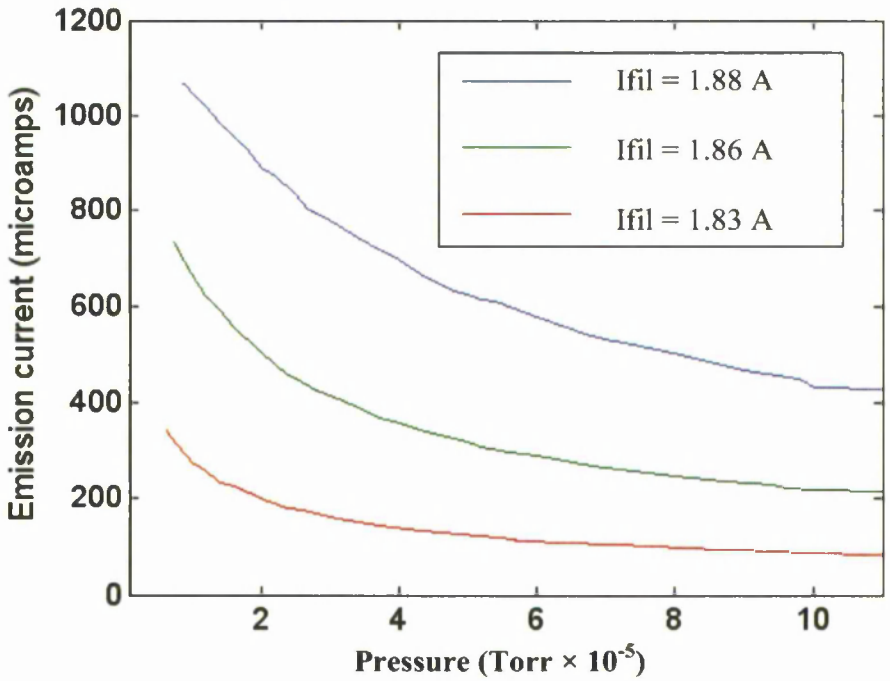

Figure 6.23. Variation of emission current against total pressure for three a constant values of filament current (Ifil) .

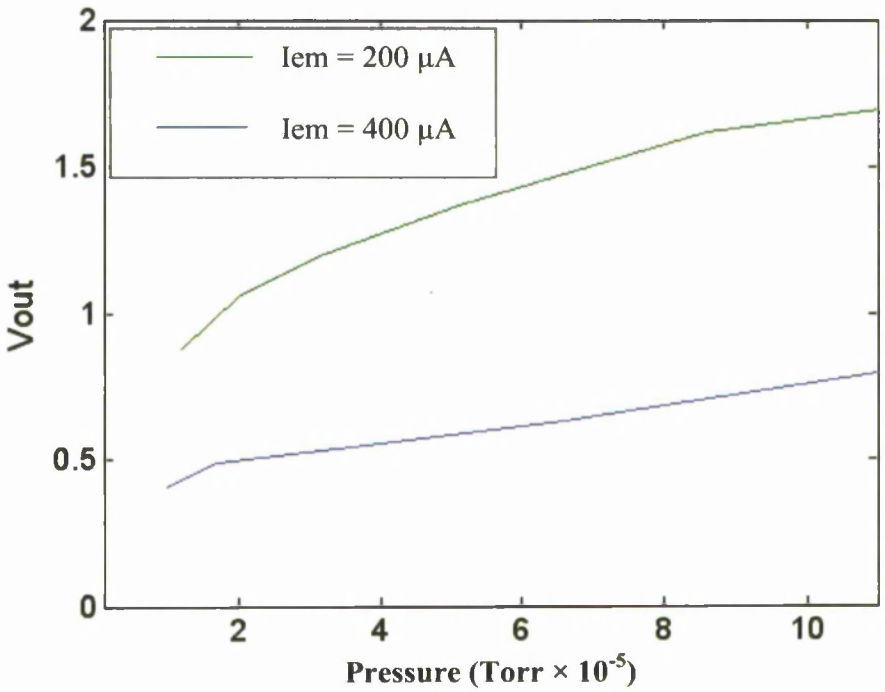

Figure 6.24. Variation of electrometer amplifier output voltage against total pressure for two different values of emission current (Iem).

6.13 Conclusions

A QMS ECU controller has been designed, developed and manufactured which takes into account the knowledge gained from the simulations reported upon in this Thesis. This has enabled the desired flexibility in terms of mass scan step size and U/V ratio to be provided. These are important characteristics when attempting to resolve the Hydrogen isotopes and their molecular combinations that were discussed in Chapter 5. The existence of a QMS ECU with this functionality opens up the possibility of undertaking experimental validation of the AWE feasibility study conclusions which are also discussed in Chapter 5.

The provision of a dual channel mass scan controller and dual RF power amplifiers provides the functionality required to investigate the effects of differential phase offsets between the x and y electrode drive. It also provides the functionality required to investigate the effects of differential electrode drive as a method of compensating for electrode positional tolerances.

These novel features are not provided by commercially available QMS ECUs and it would be very difficult, if impossible to modify a commercial unit to provide this functionality in order to undertake the experimental investigations mentioned above.

Chapter 7

7. CONCLUSIONS AND FUTURE WORK

It has been demonstrated that the combination of public domain software and custom designed software provides an efficient method for developing a software toolkit targeted at understanding and investigating a range of operational conditions that influence the performance window of a QMF and in turn the QMS. The effects of different electrode geometries on the performance of a QMF when operating in stability zone 3 have been investigated and it has been demonstrated that zone 3 provides a method of reducing the effects of non-optimum electrode radii.

The investigation of displaced electrodes showed that these effects can have a cumulative effect on QMF performance. It was also shown that asymmetric electrode drive voltages can contribute in a similar manner and their effects can reinforce or compensate for the displaced electrodes. These characteristics indicate that when specifying the QMS the inter-relationship of each of the modules must be considered.

The demand for miniaturisation of the QMS means that non-traditional manufacturing processes are being considered. These do not always lend themselves to realising the classic hyperbolic or circular electrode geometry but more novel electrodes of rectilinear profile. This profile coupled with the reduction in the length, results in very poor performance if stability zone 1 is used. The results obtained with stability zone 3 indicate that this is a more suitable operating mode and provides adequate performance for at least some applications.

The importance of the ECU in achieving the required QMF performance has also been investigated. Results obtained demonstrate that the accuracy of the electrode drive voltages and the mass scan step size used for generating the mass scan are very important in determining the maximum realisable mass resolution. These results have also been important inputs to the specification, design and development phase of the ECU.

Additional operational facilities have been incorporated into the ECU to support future experimental investigations. The symmetry of the inter-relationship between asymmetric electrode geometry and asymmetric electrode drive voltages has been

demonstrated. The ability of the ECU to provide unbalanced electrode drive voltages enables experimental data to be obtained on the resulting QMS performance. From these results it will then be possible to draw conclusions about experimental performance of a QMS incorporating a QMF with displaced electrodes. The provision of a DDS RF generator provides a basis at least for miniature QMFs to investigate the characteristics of frequency scanning as an alternative scanning mode.

One aspect of the QMF that was considered for investigation was that of a comparison between the effects of mechanical accuracy for hyperbolic and circular electrode QMFs. This was attempted but the Automesh module of Poisson/Superfish exhibited a problem when using the hyperbolic shape definition command. Contact was made with Los Alamos National Laboratories who accepted that a problem existed but they did not have the resource to correct the problem at that time. This is still an interesting study to carry out as it would provide quantitative data enabling a costing of the relative merits of the two electrode profiles (circular and hyperbolic) to be made.

The development and commissioning phases of the ECU are not yet finished but are continuing and is hoped that these will be concluded satisfactorily over the next few months. Higher levels of circuit integration could take the form of soft or hard processer cores and a DDS module integrated into a field programmable logic array (FPGA). This may lead eventually to a QMF and control electronics integrated into a multi-chip module.

The information that has been collected while undertaking this work confirms that Wolfgang Paul's statement "*There are many examples in physics showing that higher precision revealed new phenomena, inspired new ideas or confirmed or dethroned well established theories*" is as relevant today as when he made it over thirty years ago.

References

[1] E. de Hoffman, V. Stroobant, "Introduction," in *Mass Spectrometry Principles and Applications*, Chichester: Great Britain: Wiley, pp. 1- 9, 2003.

[2] P. H. Dawson, "Principles of operation," in *Quadrupole Mass Spectrometry and its Applications*, Amsterdam: Holland: Elsevier, pp. 9-64, 1976.

[3] W. Paul, H. P. Reinhard, U. von Zahn, "Das Elektrische Massenfilter als Massenspektrometer und Isotopentrenner, " *Z. f. Physik*, vol. 152, pp. 143-182, Jul. 1958.

[4] J. R. Gibson, S. Taylor, "Prediction of quadrupole mass filter performance for hyperbolic and circular cross section electrodes," *Rapid Commun. Mass Spectrom.*, vol. 14, no. 18, pp. 1669-1673, Sep. 2000.

[5] C. Day, "The use of a high-resolution quadrupole gas mass spectrometer system for selective detection of helium and deuterium," *Vacuum*, vol. 51, no. 1, pp. 21-30, Sep. 1998.

[6] S. Hiroki, T. Abe, Y. Murakami, "Development of a quadrupole mass spectrometer using the second stable zone in Mathieu's stability diagram," *Rev. Sci. Instrum.* vol. 62, no. 9, pp. 2121-2124, Sep. 1991.

[7] R. F. Lever, "Computation of ion trajectories in the monopole mass spectrometer by numerical integration of Mathieu's equation," *IBM J. Res. Develop*, vol.10, no. 1, pp. 26-40, Jan. 1966.

[8] P. H. Dawson, "Appendix E," in *Quadrupole Mass Spectrometry and its Applications*, Amsterdam: Holland: Elsevier, pp. 339-340, 1976.

[9] J. H. Batey, Quadrupole gas analysers, *Vacuum*, vol. 37, no. 8-9, pp. 659-668, Aug. 1987.

[10] J. R. Gibson, S. Taylor, J. H. Leck, "Detailed simulation of mass spectra for quadrupole mass spectrometer systems," *J. Vac. Sci. Technol. A*, vol. 18, no. 1, pp. 237-243, Jan. 2000.

[11] D. J. Douglas, N. V. Konenkov, "Influence of the 6th and 10th spatial harmonic on the peak shape of a quadrupole mass filter with round rods," *Rapid Commun. Mass Spectrom.*, vol. 16, no. 15, pp. 1425-1431, Aug. 2002.

[12] W. Paul, Electromagnetic traps for charged and neutral particles, Nobel Lecture, Dec. 1989.

[13] M. Hedenus, "Eugen Goldstein and his laboratory work at Berlin Observatory," *Astron. Nachr.*, vol. 323, no. 6, pp. 567-569, Dec. 2002.

[14] S. H. Bauer, "Mass spectrometry in the mid-1930s: were chemists intrigued," *J. Am. Mass Spectrom.*, vol. 12, no. 11, pp. 975-988, Nov. 2001.

[15] S. Borman, H. Russell, G. Siuzdak, "A mass spec timeline," *Today's chemist at work*, vol. 12, no. 9, pp. 47-49, Sep. 2003.

[16] H. E. Duckworth, R. C. Barber, V. S. Venkatasubramanian, "*Modern spectroscopy (Cambridge monographs on physics)*," Cambridge: England: U.K.: Cambridge University Press, 1986.

[17] F. W. Aston, "The constitution of ordinary lead," *Nature*, vol. 120, pp. 224-224, 1927.

[18] S. K. Allison, "*Arthur Jeffrey Dempster 1886-1950 a biographical memoir by Samuel King Allison*," Washington, U.S.A., National Academy of Sciences, 1952.

[19] W. Paul, H. Steinwedel, Apparatus for Separating Charged Particles of Different Specific charges, *German Patent* 944,900, 1956.

[20] W. Paul, H. Steinwedel, Apparatus for Separating Charged Particles of Different Specific charges, *U.S. Patent* 2,939,952, 1960.

[21] W. Paul, M. Raether, "Das Elektrische Massenfilter als Massenspektrometer und Isotopentrenner, " *Z. f. Physik*, vol. 140, pp. 262-273, Jul. 1955.

[22] U. v Zahn, "Monopole Spectrometer, a New Electric Field Mass Spectrometer," *Rev. Sci. Instrum.*, vol. 34, no. 1, pp. 1-4, Jan. 1963.

[23] E. de Hoffman, V. Stroobant, "Mass analysers," in *Mass Spectrometry Principles and Applications*, Chichester: Great Britain: Wiley, pp. 63-132, 2003.

[24] W. M. Brubaker, "Study directed toward selection of apparatus for analysis of lunar crust and atmosphere," report prepared for George C. Marshall Space Flight Centre, NASA, Oct. 1963.

[25] W. M. Brubaker, "Astronaut Breath Analyser," report prepared for NASA Manned Spacecraft Centre, Jul. 1969.

[26] P. H. Dawson, "The quadrupole: system design and residual gas analyser performance," *J. Vac. Sci. Technol. A*, vol. 4, no. 3, pp. 1709-1714, May 1986.

[27] N. W. McLachlan, "Functions of integral order," in *Theory and application of Mathieu Functions*, reprinted Oxford University Press, pp. 10-27, 1951.

[28] W. M. Brubaker, J. Tuul, "Performance studies of a quadrupole mass filter," *Rev. Sci. Instrum.*, vol. 35, no. 8, pp. 1007-1010, Aug. 1964.

[29] W. M. Brubaker, *Advances in Mass Spectrometry*, vol. 4, Amsterdam: Holland: Elsevier, 1964.

[30] P. H. Dawson, N. R. Whetten, "Non-linear resonances in quadrupole mass spectrometers due to imperfect fields," *Int. J. Mass Spectrom.* I. Phys., vol. 3, no. 1-2, pp. 1-12, Sep. 1969.

[31] N. R. Whetten, P. H. Dawson, "Some causes of poor peak shape in quadrupole field mass analysers," *J. Vac. Sci. Technol.*, vol. 6, no. 1, pp. 100-103, Jan. 1969.

[32] P. H. Dawson, "Fringing fields in the quadrupole mass filter," *Int. J. Mass Spectrom. Ion Processes*, vol. 6, no. 1-2, pp. 33-44, Jan. 1971.

[33] P. H. Dawson, N. R. Whetten, "Quadrupole mass filter: Circular rods and peak shapes," *J. Vac. Sci. Technol.*, vol. 7, no. 3, pp. 440-441, May 1970.

[34] F. M. Ma, S. Taylor, "Simulation of ion trajectories through the mass filter of a quadrupole mass spectrometer," *IEE Proc. Sci. Meas. Technol.* vol. 143, no. 1, pp. 71-76, Jan. 1996.

[35] A.C.C. Voo, R. Ng, J. J. Tunstall, S. Taylor, "Transmission through the quadrupole mass spectrometer mass filter: The effect of aperture and harmonics," *J. Vac. Sci. Tech. A*, vol. 15, no. 4, pp. 2276-2281, Jul. 1997.

[36] J. J. Tunstall, A .C. C. Voo, S. Taylor, "Computer Simulation of the Mass Filter for a Finite Length Quadrupole," *Rapid Commun. Mass Spectrom.*, vol. 11, no. 2, pp. 184-188, Jan. 1997.

[37] P. H. Dawson, "The mass filter: Design and performance," in *Quadrupole Mass Spectrometry and its Applications*, Amsterdam: Holland: Elsevier, pp. 121-152, 1976.

[38] M. Szilagyi, "Determination of Electric and Magnetic Fields," in *Electron and Ion Optics*, I. Brodie and J. J Muray, Ed. New York, U.S.A., Plenum Press, pp. 51-150, 1988.

[39] I. E. Dayton, F. C. Shoemaker, R. F. Mozley, "The measurement of two-dimensional fields Part 2: Study of a quadrupole magnet," *Rev. Sci. Instrum.*, vol. 25, no. 5, May 1954.

[40] D. R. Denison, "Operating parameters of a quadrupole in a grounded cylindrical housing," *J. Vac. Sci. Tech.*, vol. 8, no. 1, pp. 485-489, May 1971.

[41] A. J. Reuban, G. B. Smith, P. Moses, A. V. Vagov, M. D. Woods, D. B. Gordon, R. W. Munn., "Ion trajectories in exactly determined quadrupole fields," *Int. J. Mass Spectrom.* Ion Processes, vol. 154, no. 1-2, pp. 43-59, May 1996.

[42] J. Schulte, P. V. Shevchenko, A. V. Radchik, "Nonlinear field effects in quadrupole mass filters," *Rev. Sci. Instrum.*, vol. 70, no. 9, pp. 3566-3571, Sep. 1999.

[43] J. R. Gibson, S. Taylor, "Numerical investigation of the effect of electrode size on the behaviour of quadrupole mass filters," *Rapid Commun. Mass Spectrom.*, vol. 15, no. 20, pp. 1960-1964, Oct. 2001.

[44] A. D. McNaught, A. Wilkinson, "Recommendations for nomenclature and symbolism for mass spectroscopy" in *Compendium of Chemical Terminology (the "Gold Book")*, Oxford, U.K.: Blackwell Scientific Publications, pp. 1554-1555, 1997.

[45] J. R. Gibson, S. Taylor, "Asymmetrical features of mass spectral peaks produced by quadrupole mass filters," *Rapid Commun. Mass Spectrom.*, vol. 17, no. 10, pp. 1051-1055, May 2003.

[46] M .S. Story, in Proc. Pacific Conf. on Chem. Spectrom., Oct. 6-9, 1969.

[47] P. H. Dawson, M. Meunier, "Some distortions in quadrupole fields and their relation to mass filter performance," *Int. J. M. Spectrom.* Ion Phys., vol. 29, no. 3, pp. 269-299, Mar. 1979.

[48] P. H. Dawson, "Quadrupole mass filters with bent or bowed rod sets," *Int. J. Mass Spectrom. Ion Processes*, vol. 84, no. 1-2, pp. 185-201, Jun. 1988.

[49] S. Taylor, J. R. Gibson, "Prediction of the effects of imperfect construction of a QMS filter," *J. Mass Spectrom.*, vol. 43, no. 5, pp. 609-616, May 2008.

[50] F. L. Krawczyk, J. H. Billen, R. D. Ryne, H. Takeda, L. M. Young, "The Los Alamos Accelerator Code Group," in Proc. IEEE Particle Accelerator Conf. vol. 4, pp. 2306-2308, 1995.

[51] Poisson/Superfish, LANL, obtainable online from http://laacg1.lanl.gov/laacg/services/download_sf.phtml, May 2011.

[52] D. M. Burns, S. Taylor, J. R. Gibson, "Quadrupole Mass Filter," *U.K. Patent* GB2390222, 2003.

[53] D. M. Burns, S. Taylor, J. R. Gibson, "Quadrupole Mass Filter," *U.S. Patent* 6940068, 2005.

[54] D. M. Burns, S. Taylor, J. R. Gibson, "Quadrupole Mass Filter," *European Patent* EP1649488, 2006.

[55] P. H. Dawson, "Higher zones of stability for the quadrupole mass filter," *J. Vac. Sci. Technol.*, vol. 11, no. 6, pp. 1151-1153, Nov. 1974.

[56] Z. Du, T. N. Olney, D. J. Douglas, "Inductively coupled plasma spectrometry with a quadrupole mass filter operated in the third stability region," *J. Am. Soc. Mass Spectrom.*, vol. 8, no. 12, pp. 1230-1236, Dec. 1997.

[57] S. Hiroki, T. Abe, Y. Murakami, "Separation of helium and deuterium peaks with a quadrupole mass spectrometer by using the second stability zone in the Mathieu diagram," *Rev. Sci. Instrum.* vol. 63, no. 8, pp. 3874-3876, Aug. 1992.

[58] S. Hiroki, T. Abe, Y. Murakami, K. Yanagishita, S. Nakamura, "Development of a high-resolution quadrupole mass spectrometer capable of detecting ^{3}He and ^{4}He in a hydrogen isotope atmosphere," *J. Vac. Sci. Technol.* A, vol. 12, no. 5, pp. 2711-2715, Sep. 1994.

[59] S. Hiroki, T. Abe, Y. Murakami, "Detection of a 10^{-4} helium peak in a deuterium atmosphere using a modified high-resolution quadrupole mass spectrometer," *Rev. Sci. Instrum.* vol. 65, no. 6, pp. 1912-1917, Jun. 1994.

[60] R. E. Pedder, R. A. Schaeffer, "Quadrupole mass spectrometry using the second Mathieu stability region," presented at the 43rd ASMS Conference on Mass Spectrometry and Allied Topics, May 25, 1995.

[61]R. E. Pedder, "Practical quadrupole theory: Quadrupole Emittance characteristics," presented at the 51st ASMS Conference on Mass Spectrometry and Allied Topics, Jun. 8th, 2003.

[62] Z. Du, D. J. Douglas, T. Glebova, N. V. Konenkov, "Peak structure with a quadrupole mass filter operated in the third stability region," *Int. J. Mass Spectrom.*, vol. 197, no. 1-3, pp. 113-121, Feb. 2000.

[63] K. L. Hunter, B. J. McIntosh, "An improved model of the fringing fields of a quadrupole mass filter," *Int. J. Mass Spectrom. Ion Processes*, vol. 87, no. 2, pp. 157-164, Jan. 1989.

[64] P. Marmet, "Quadrupole mass analysers," *J. Vac. Sci. Technol.*, vol. 8, no. 1, pp 262, Jan. 1971.

[65] W. L. Fite, "Spatial separation of fringe fields in quadrupole mass filters," *Rev. Sci. Instrum.*, vol. 47, no. 3, pp. 326-330, Mar. 1976.

[66] N. V. Konenkov, "Influence of fringing fields on the acceptance of a quadrupole mass filter in the separation mode of the intermediate stability region," *Int. J. Mass Spectrom. Ion Processes*, vol. 123, no. 2, pp. 101-105, Feb. 1993.

[67] S. Hiroki, Y. Murakami, "Influence of the fringing field length on the separated $^4He/D_2$ peak shape of a high-resolution quadrupole mass spectrometer," *Int. J. Mass Spectrom. Ion Processes*, vol. 136, no. 1, pp. 85-89, Sept. 1994.

[68] S. Hiroki, K. Sakata, N. Sugiyama, T. Abe, Y. Murakami, "Effect of a pre-filter on the sensitivity of a high-resolution quadrupole mass spectrometer," *Vacuum*, vol. 46, no. 7, pp. 681-683, Jul. 1995.

[69] T. Hayashi, N. Sakudo, "Quadrupole Field in Circular Concave Electrodes," *Rev. Sci. Instrum.*, vol. 38, no. 7, pp. 958-961, Jul. 1968.

[70] N. Sakudo, T. Hayashi, "Quadrupole electrodes with flat faces," *Rev. Sci. Instrum.*, vol. 46, no. 8, pp. 1060-1062, Aug. 1975.

[71] C. G. Pearce, D. Halsall, "A Quadrupole Mass Filter with Flat Electrodes," *J. Mass Spectrom.*, vol. 27, no. 1, pp. 31-41, May 1978.

[72] S. Hiroki, T. Abe, Y. Murakami, Y. Takano, M. Higuchi, M. Miyake, "Development of a QMS with a ceramic single-piece quadrupole," *Vacuum*, vol. 44, no. 2, pp. 71-74, Feb. 1993.

[73] C. Ding, N. V. Konenkov, D. J. Douglas, "Quadrupole mass filters with octopole fields," *Rapid Commun. Mass Spectrom.*, vol. 17, no. 22, pp. 2495-2502, Nov. 2003.

[74] C. M. Henry, "The incredible shrinking mass spectrometer," *Anal. Chem.*, vol. 71, no .4, pp. 264A–268A, Apr. 1999.

[75] A. H. W.Beck, H. Ahmed, "Gas discharges," in *An introduction to physical electronics* 1st. ed., London: Edward Arnold (Publishers) Ltd., 1968, pp. 18-36.

[76] R. R. A. Syms, T. J. Tate, M. M. Ahmed, S. Taylor, "Fabrication of a microengineered quadrupole electrostatic lens," *IEE Electronic Letters*, vol. 32, no. 22, pp. 2094-2095, Mar. 1996.

[77] S. Taylor, J. J. Tunstall, R. R. A. Syms, T. J Tate, M. M. Ahmed, "Initial results for a quadrupole mass spectrometer with a silicon micromachined mass filter," *IEE Electronic Letters*, vol. 34, no. 6, pp. 546-547, Mar. 1998.

[78] R. A. Syms, T. J. Tate, M. M. Ahmed, S. Taylor, "Design of a microengineered electrostatic quadrupole lens," *IEEE Trans. Electron Devices*, vol. 45, no. 11, pp. 2304-2311, Nov. 1998.

[79] S. Taylor, J. J. Tunstall, J. H. Leck, R. F. Tindall, J. P. Jullien, J. Batey, R. R. A. Syms, T. Tate, M. M. Ahmed, "Performance improvements for a miniature quadrupole with a micromachined mass filter," *Vacuum*, vol. 53, no. 1-2, pp. 203-206, May 1999.

[80] S. Taylor, B. Srigengan, J. R. Gibson, D. Tindall, R. Syms, T. Tate, M. Ahmed, "A miniature mass spectrometer for chemical and biological sensing," in Proc. SPIE-Int. Soc. Opt. Eng., vol. 4036, pp. 187-193, Jul. 2000.

[81] S. Taylor, R. F. Tindall, R. R. A. Syms, "Silicon based quadrupole mass spectrometry using microelectromechanical systems," *J. Vac. Sci. Technol. B*, vol. 19, no. 2, pp. 557-562, Mar. 2001.

[82] L. F. Velásquez-García, A. I. Akinwande, "An out-of-plane MEMS quadrupole for a portable mass spectrometer," presented at The 14th International Conference on Solid-State Sensors, Actuators, and Microsystems, Lyon, France, June, 2007.

[83] L. F. Velásquez-García, Kerry Cheung, A. I. Akinwande, "An Application of 3-D MEMS Packaging: Out-of-Plane Quadrupole Mass Filters," *J. Microelectromech. Syst.*, vol. 17, no. 6, pp. 1430-1438, Dec. 2008.

[84] M. Geear, R. R. A. Syms, S. Wright, A. S. Holmes, "Monolithic MEMS quadrupole mass spectrometers by deep silicon etching," *IEEE J. Microelectromech. Syst.*, vol. 14, no. 5, pp.1156-1166, Oct. 2005.

[85] O. J. Orient, A. Chutjian, V. Garkanian, "Miniature high-resolution, quadrupole mass-spectrometry array," *Rev. Sci. Instrum.*, vol. 63, no. 3, pp. 1393-1397, Mar. 1997.

[86] R. J. Ferran, S. Boumsellek, "High-pressure effects in miniature arrays of quadrupole analysers for residual gas analysis from 10^{-9} to 10^{-2} Torr," *J. Vac. Sci. Technol. A*, vol. 14, no. 3, pp. 1258-1265, May 1996.

[87] L. Ding, S. Kumashiro, "Ion motion in the rectangular wave quadrupole field and digital operation mode of a quadrupole ion trap mass spectrometer," *Rapid Commun. Mass Spectrom.*, vol. 20, no. 1, pp. 3-8, Jan. 2006.

[88] J. A. Richards, R. M. Huey, J. Hiller, "A new operating mode for the quadrupole mass filter," *Int. J. Mass Spectrom. Ion. Phys.*, vol. 12, no. 4, pp. 317-339, Nov. 1973.

[89] R. E. March and J. F. J. Todd, "Theory of Quadrupole Instruments," in *Quadrupole ion trap mass spectrometry* 2nd. ed., J. D. Winefordner Ed. New Jersey: Wiley–Interscience, John Wiley & Sons Inc., pp. 34-72, 2005.

[90] S. H. Qasim, *SI unit in engineering and technology*, 1st, ed., Oxford: England: Pergamon Press Ltd., pp. 18-28, 1977.

[91]R. E. Pedder, "Practical quadrupole theory: Quadrupole Emittance characteristics," presented at the 49th ASMS Conference on Mass Spectrometry and Allied Topics, May 28th, 2001.

[92] Z. Du, D. J. Douglas, N. V. Konenkov, "Elemental analysis with quadrupole mass filters operated in higher stability regions," *Int. J. Anal At. Spectrom.*, vol. 14, no. 8, pp. 1111-1119, Aug. 1999.

[93] V. V. Titov, "Detailed study of the quadrupole mass analyzer operating within the first, second, and third (intermediate) stability regions. II. transmission and resolution," *J. Am. Soc. Mass Spectrom.*, vol. 9, no. 1, pp. 70-87, 1998.

[94] R. E. March and J. F. J. Todd, "Dynamics of ion trapping," in *Quadrupole ion trap mass spectrometry* 2nd. ed., J. D. Winefordner Ed. New Jersey: Wiley–Interscience, John Wiley & Sons Inc., pp. 73-132, 2005.

[95] W. H. Hayt, Jr., J. A. Buck, "Poisson's and Laplace's Equations," in *Engineering electromagnetics*, 6th ed., S. W. Director, Ed., McGraw-Hill, New York, U.S.A., pp. 195-223, 2001.

[96] W. H. Hayt, Jr., J. A. Buck, "Experimental mapping methods," in *Engineering electromagnetics*, 6th ed., S. W. Director, Ed., McGraw-Hill, New York, U.S.A., pp. 169-194, 2001.

[97] W. Press, S. A. Teukolsky, W. T. Vetterling, B. P. Flannery, "Partial differential equations," in *Numerical recipes in C++ The art of scientific computing*, 2nd ed. Cambridge, England, Cambridge University Press, pp. 829-890, 2003.

[98] D. Cubric, B. Lencova, F. H. Read, J. Zlamal, "*Comparison of FDM, FEM and BEM for Electrostatic Charged Particle Optics*," Nucl. Instr. Meth. Phys. Res. A, vol. 427, no. 1-2, pp. 357-362, May 1999.

[99] J. R. Gibson, K. G. Evans, S. Taylor, "Modelling mass analysers performance with fields determined using the boundary element method," *J. Mass Spectrom.*, vol. 45, no. 4, pp. 364-371, 2010.

[100] A. M. Winslow, "Numerical solution of the quasilinear Poisson equation in a nonuniform triangle mesh," *J. Computational Phys.*, vol. 1, no. 2, pp. 149-172, Nov. 1966.

[101] J. H. Billen, "User manual for Superfish programs on PC compatibles," available online at http://laacg1.lanl.gov/laacg/services/download_sf.phtml, Apr. 2010.

[102] F. L. Krawczyk, J. H. Billen, R. D. Ryne, H. Takeda and L. M. Young., "The Los Alamos Accelerator Code Group," in Proc. IEEE Particle Accelerator Conf. vol. 4, pp. 2306-2308, 1995.

[103] J. R. Gibson, *Private communication,* Sep. 2005.

[104] W. Press, S. A. Teukolsky, W. T. Vetterling, B. P. Flannery, "Interpolation and extrapolation," in *Numerical recipes in C++ The art of scientific computing*, 2nd ed. Cambridge, England, Cambridge University Press, pp. 108-132, 2003.

[105] E. Kreyszig, "Ordinary differential equations of the first order," in *Advanced engineering mathematics*, 2nd ed. New York, U.S.A., J. Wiley and Sons, pp. 39-92, 1967.

[106] K. Maeda, A. Fukuda, M. Sakimura, "Tables relating to the Mathieu functions appearing in mass filter problems," *Mass Spectrom.* vol. 17, no. 1, pp. 530 - 574, Mar. 1970.

[107] R. G. Lyons, "The discrete Fourier transform," in *Understanding Digital Signal Processing*, Massachusetts: Addison Wesley Longman Inc., pp.49-128, 1996.

[108] P. H. Dawson, "Fringing fields and other imperfections," in *Quadrupole Mass Spectrometry and its Applications*, Amsterdam: Holland: Elsevier, pp. 95-119, 1976.

[109] M. Y. Sudakov, "Spectrum of Charged Particle Oscillations in an RF Quadrupole Field," *Tech. Phy.*, vol.45, no.3, pp. 322-329, Mar. 2000.

[110] M. Sudakov, D. J. Douglas, "Linear quadrupoles with added octopole fields," *Rapid Commun. Mass Spectrom.*, vol. 17, no. 20, pp. 2290-2294, Oct. 2003.

[111] N. V. Konenkov, F. Londry, C. Ding and D. J. Douglas, "Linear quadrupoles with added hexapole fields," *J. American Society Mass Spectrom.*, vol. 17, no. 8, pp. 1063-1073, Aug. 2006.

[112] D. Gentsch, T. Fugel, "Measurements by residual gas analysis (RGA) inside vacuum interrupters," *IEEE Trans. Plasma Science*, vol. 37, iss. 8, pp. 1484-1489 Aug. 2009.

[113] P. Turner, S. Taylor, E. Clarke, C. Harwood, K. Cooke and H. Frampton, "Calibration effects during natural gas analysis using a quadrupole mass spectrometer," *Trends Anal. Chem.*, vol. 23, no. 4, pp. 281-286, Apr. 2004.

[114] T. Winkel and J. L. Hemmerich, "Helium leak detection in JET in the presence of high deuterium partial pressure," *J. Vac. Sci. Technol. A*, vol. 5, no. 4, pp. 2637-2640, Jul. 1987.

[115] R. E. Ellefson, W. E. Moddeman, H. F. Dylia, "Hydrogen Isotope Analysis by Quadrupole Mass Spectrometry," *J. Vac. Sci. Technol.* vol. 18, no. 3, pp. 1062-1066, Apr. 1981.

[116] A. Frattolillo, A. De Ninno, "A powerful tool to quantitatively detect tiny amounts of ^{4}He in a deuterium rich background for fusion research," in *Proc 22nd IEEE Sym. Fusion Eng.*, Albuquerque, NM, U.S.A, pp. 1-4, Jun. 2007.

[117] S. Hiroki, T. Abe, Y. Murakami, "Sensitive helium leak detection in a deuterium atmosphere using a high-resolution quadrupole mass spectrometer," *Vacuum*, vol. 47, no. 6-8, pp. 767–769, Jun. 1996.

[118] W. L. Fite, "Spatial separation of fringe fields in quadrupole mass filters," *Rev. Sci. Instrum.*, vol. 47, no. 3, pp. 326-330, Mar. 1976.

[119] B. Garney, "Process gases and their atomic weight," *private communication*, Atomic Weapons Establishment, Aldermaston, U.K., Sept. 2008.

[120] Z. Du, N. Terry, D. J. Douglas, "Inductively coupled plasma mass spectrometry with a quadrupole mass filter operated in the third stability region," *J. Am. Soc. Mass Spectrom.*, vol. 8, no. 12, pp. 1230-1236, Dec. 1997.

[121] J. P. Bentley, "Signal processing elements," in *Principles of Measurement Systems*, London, U.K. : Longman, 1983, pp. 209-234.

[122] R. G. Lyons, "Periodic sampling," in *Understanding Digital Signal Processing*, Massachusetts, U.S.A.: Addison Wesley Longman, pp. 23-47, 1997.

[123] P. Turner, S. Taylor and J. R .Gibson, "The effect of ion entry acceptance conditions on the performance of a quadrupole mass spectrometer operated in the upper and lower stability regions," *J. Vac. Sci. Tech.* A, vol.23, no.3, pp. 480-487, May 2005.

[124] S. Wright, R. R. A. Syms, S. O' Prey, G. Hong and A. S. Holmes, "Comparison of ion coupling strategies for a microengineered quadrupole mass spectrometer," *J. Am. Soc. Mass Spectrom.,* vol. 20, iss. 1, pp. 146-156, Jan. 2009.

[125] L. F. Velásquez-García and A. I. Akinwande, "An out-of-plane MEMS quadrupole for a portable mass spectrometer," *The 14th International Conference on Solid-State Sensors, Actuators, and Microsystems,* Lyon, France, Jun. 2007.

[126] K.Cheung, L. F. Velásquez-García and A. I. Akinwande, "First principles optimization of mass producible microscaled linear quadrupoles for operation in higher stability regions," in *Proc 20th IEEE Int. Vac. Nanoelectronics Conf.*, pp. 214-5, Chicago, ILL, U.S.A., Jul. 2007.

[127] N. Sillon and R. Baptist, "Micromachined mass spectrometer," *Sensors and Actuators B: Chemical,* vol. 83, no. 1-3, pp. 129-137, Mar. 2002.

[128] R. Baptist, "Miniature device for generating a multi-polar field, in particular for filtering of deviating or focusing charged particles," *U.S. Patent* 6,465,792 *B*1, Oct. 15, 2002.

[129] K. Cheung, " Chip-scale quadrupole mass filters for a micro-gas analyser," Ph.D thesis, Dept. Elec. Eng. Comp. Sc., Mass. Inst. Tech., Cambridge, U.S.A., Jun. 2009.

[130] Extrel CMS L. L. C., Pittsburgh, U.S.A., http://www.extrel.com, Nov. 2011.

[131] Ardara Technologies L.P., Pennsylvania, U.S.A., http://www.ardaratech.com, Nov. 2011.

[132] K. Cheung, *Private communication,* Nov. 2008.

[133] Thermo Fisher Scientific Inc., Loughborough, U.K., www.fisher.co.uk, Nov. 2011.

[134] Extrel CMS LLC, Pittsburh, U.S.A., www.extrel.com, Nov. 2011.

[135]Stanford Research Systems, Sunnyvale, Calafornia, U.S.A., www.thinksrs.com, Nov. 2011.

[136] The Vacuum Science Group, ASTeC, Daresbury Laboratory, Daresbury, Warrington, U.K., www.stfc.ac.uk/ASTeC/17505.aspx, Nov. 2011.

[137] P. B. O'Connor, C. E. Costello, W. E. Earle, "A high voltage RF oscillator for driving multipole ion guides," *J. Am. Soc. Mass Spectrom.*, vol. 13, no. 12, pp. 1370-1375, Dec. 2002.

[138] I. Cermak, "Compact radio-frequency power supply for ion and particle guides and traps," *Rev. Sci. Instrum.*, vol.76, no. 6, pp. 063302/1-9, Jun., 2008.

[139] R. T. Schaefer, J. A. MacAskill, M. Mojarradi, A. Chutjian, M. R. Darrach, S. Madzunkov and B. J. Shortt, "Digitally synthesized high purity, high-voltage radio frequency drive electronics for mass spectrometry," *Rev. Sci. Instrum.*, vol. 79, no. 9, pp. 095107/1-6, Sep. 2008.

[140] M. D. Robbins, O. K. Yoon, I. Zuletta, G. Barbula and R. N. Zare, "Computer-controlled, variable frequency power supply for driving multipole ion guides," *Rev. Sci. Instrum.*, vol. 79, no. 3, pp. 034702/1-6, May 2008.

[141] Y. Jiang, X. Fang, Y. Rang, D. Tian, "Development and application of digital control technology of resonant excitation for quadrupole ion trap," *Chin. J. Anal. Chem.*, vol. 36, no. 5, pp. 715-718, May 2008.

[142] F. P. Clay, F. J. Brock, "Switching regulator emission control circuit for ion sources," *Rev. Sci. Instrum.*, vol. 46, no. 5, pp. 528-532, May 1975.

[143] S. Reynolds, "A high voltage, high frequency linear amplifier/driver for capacitive loads," *Meas. Sci. Technol.*, vol.3, pp. 283-288, Mar. 1992.

[144] J. W. Ting, W. –P, Peng, H. –C. Chang, "High voltage amplifier," in *Proc. IEEE Nuclear Science Symposium Conference*, pp. 1246-1249, 19th – 25th Oct. 2003, Portland, Oregon, U.S.A.

[145] H. Muller, "Fast high voltage amplifiers for driving electro-optic modulators," *Rev. Sci. Instrum.*, vol. 76, no. 8, pp. 1-7, Feb. 2005.

[146] S. S. Rajput, "An improved multigain range linear current electrometer," *Rev. Sci. Instrum.*, vol. 74, no. 6, pp. 3120-3126, Jun. 2003.

[147] Y. B. Acharya, "Analytical correction for temperature and diode characteristics for application in a wide dynamic range logarithmic electrometer," *Rev. Sci. Instrum.*, vol. 72, no. 8, pp. 3431-3434, Aug. 2001.

[148] Y. B. Acharya, P. D. Vyavahare, "Response time of light emitting diode-logarithmic electrometer," *Rev. Sci. Instrum.*, vol. 69, no. 2, pp. 595-598, Feb. 1998.

[149] Microchip Technology Inc., "PIC32 Reference manual DS61127C," 2008.

[150] Microchip Technology Inc., "PIC32MX3XX/4XX Family data sheet DS61143F," 2009.

[151] MIPS Technologies Inc., Sunnyvale, California, U.S.A., www.mips.com, Nov. 2011.

[152] MIPS Technologies Inc., "MIPS32 Architecture for programmers volume 1: Introduction for the MIPS32 architecture," MD00082, rev. 2.60, Jun. 2008.

[153] Microchip Technology Inc., "MPLAB® ICD 3 In-Circuit Debugger User's Guide," DS51766B, 2010.

[154] Altera Corporation, San Jose, California, U.S.A., www.altera.com, Nov. 2011.

[155] Altera Corporation, "USB-Blaster download cable user guide UG-USB81204-2.5," Apr. 2009.

[156] Microchip Technology Inc., "Section 23 serial peripheral interface (SPI)," in *PIC32 Reference manual DS61132B*, 2008.

[157] L. Di Jasio "Communication," in *Programming 32-bit microcontrollers in C exploring the PIC32*, Elsevier-Newnes, Oxford U.K., 2008.

[158] Microchip Technology Inc., "Section 27 USB on the go (OTG)," in *PIC32 Reference manual DS61132B*, 2008.

[159] USB Implementors Forum Inc. Beaverton, Oregon, U.S.A., www.usb.org, Nov. 2011.

[160] USB Implementers Forum Inc., "Universal serial bus specification Revision 2.0," Apr. 2000.

[161] Microchip Technology Inc., "USB device stack for PIC32 programmers guide DS0116A," 2008.

[162] J. Axelson, USB Complete, 3rd ed., Lakeview Research LLC, Wisconsin, U.S.A., 2005.

[163] Microchip Technology Inc., "USB HID on an embedded device DS01163A," 2008.

[164] Microchip Technology Inc., "25AA010A/25LC010A datasheet DS21832C," 2006.

[165] XP Power plc, Reading, Berkshire, U.K., www.xppower.com, Nov. 2011.

[166] J. G. Bollinger, Neil A. Duffie, Computer control of machines and processes, Addison-Wesley, Massachusetts, U.S.A., 1988.

[167] Microchip Technology Inc., "Implementing a PID controller using a PIC18 MCU AN937 DS00937A," 2004.

[168] F. W. McLafferty, F. Turecek, "Auxillary techniques," in *Interpretation of mass spectra*, University Science Books, Sausalito, U.S.A., pp. 103-115, 1993.

[169] D. Jarman, Intersil Corporation, "A brief introduction to sigma delta conversion," 1999.

[170] Analog Devices Inc., "Using sigma delta convertors-Part 1 AN-388," 1993.

[171] Analog Devices Inc., "Using sigma delta convertors-Part 2 AN-388," 1994.

[172] Analog Devices Inc, "A technical tutorial on digital signal synthesis," 1999.

[173] C. Kitchin, L. Counts, "RMS to DC conversion application guide," Analog Devices Inc., 1986.

[174] S. J. G. Gift, "Versatile Precision Full-Wave Rectifiers for Instrumentation and Measurements," *IEEE Trans. Insturm. Meas.*, vol. 56, no. 5, pp. Oct. 2007.

[175] C. D. Prestil, F. Carrara1, A. Scuderi2, and G. Palmisano1, "Fast Peak Detector with Improved Accuracy and Linearity for High-Frequency Waveform Processing," IEEE Int. Sym. Circuits Systems, New Orleans, LA, U.S.A., pp. 3884-3887, Jun., 2007.

[176] J. McLucas, "Wideband peak detector operates over wide input-frequency range," *EDN*, Nov. 2007.

[177] OrCad Capture Cadence Design Systems Inc., San Jose, CA, U.S.A., http://www.cadence.com, Nov. 2011.

[178] K. Mitzner, Complete PCB design using Orcad Capture and PCB editor, Newnes-Elsevier, Oxford, Oxfordshire, U.K., 2009.

[179] Vutrax Computamation Systems Ltd. Great Brickhill, Beds., U.K., http://www.vutrax.co.uk, Nov. 2011.

[180] A. Rushton, VHDL for logic synthesis, J. Wiley and Sons Ltd., Chichester, West Sussex, U.K., 1998.

[181] M. Zwoliński, Digital systems design with VHDL, Pearson Education Ltd., Harlow, Essex, U.K., 2000.

[182] Altera Corporation, Quartus II Handbook Version 11.0 Volume 1: Design and Synthesis (QII5V1-11.0.0), 2011.

[183] Microsoft Corporation, Reading, Berks., U.K., http://www.microsoft.com, Nov. 2011.

Appendices

Appendix A Automesh geometry definition file

Quadrupole consisting of 4 circular electrodes
with radius (r) = 1.127 * Radial Aperture (r_0)
Excitation voltage = ± 1 volt
;TEST FOR QMS2FIELD
;Multipole control added Harmonic analysis

```
&reg kprob=0,      ! Poisson or Pandira problem
xjfact=0.0,        ! Electrostatic problem
dx=0.0020,         ! Mesh interval
icylin=0,          ! Cartesian coordinates
ibound=-1,         ! Potential is specified on this region's boundary
voltage=0.0        ! Potential for this boundary
ktype=1,           ! No symmetry assumed in harmonic analysis
conv=100.00,       !use cm as scale use 0.1 for mm
nterm=14,          ! Number of terms in harmonic analysis
xorg=0.0           !Arc centre X coordinate for harmonic analysis
yorg=0.0           !Arc centre Y coordinate for harmonic analysis
nptc=10000         !Number of arc points for interpolating the potential
rint=1.0           ! Radius of arc for interpolated points
anglz=0,           ! Starting point on arc for interpolating potential
angle=360,         ! Extent of arc for interpolating potential
rnorm=1,           ! Normalization radius for harmonic analysis
xazero=0.0         !Physical X coordinate where A=0
yazero=0.0         !Physical Y coordinate where A=0
epsila=5.D-15      !Convergence parameter for air and interface points
&
&po x=3.6,y=0.0  &
&po nt=2,r=3.6,theta=180.,x0=0.,y0=0. &
&po nt=2,r=3.6,theta=360.,x0=0.,y0=0. &

&reg mat=0,ibound=-1,voltage=-1.0 &
&po y=3.254,x=0. &
&po nt=2,r=1.127,theta=270.,y0=2.127,x0=0. &
&po nt=2,r=1.127,theta=90.,y0=2.127,x0=0. &

&reg mat=0,ibound=-1,voltage=-1.0 &
&po y=-3.254,x=0. &
&po nt=2,r=1.127,theta=90.,y0=-2.127,x0=0. &
&po nt=2,r=1.127,theta=270.,y0=-2.127,x0=0. &

&reg mat=0,ibound=-1,voltage=+1.0 &
&po x=3.254,y=0. &
&po nt=2,r=1.127,theta=180.,x0=2.127,y0=0. &
```

```
&po nt=2,r=1.127,theta=360.,x0=2.127,y0=0. &

&reg mat=0,ibound=-1,voltage=+1.0 &
&po x=-1,y=0. &
&po nt=2,r=1.127,theta=180.,x0=-2.127,y0=0. &
&po nt=2,r=1.127,theta=360.,x0=-2.127,y0=0. &
```

Appendix B Code for calculating ion trajectories QMS2-Field

```
//Provides the control for the main trajectory calculation loop including parametric
control

int run_control(StringBuilder* outfile,StringBuilder* ionfile,StringBuilder*
par1,StringBuilder*par2)
{
     int error;

    String* trajfile;
    error = ERROR_NONE;

    Rnd_1 = Safe_C+20;
    Rnd_2 = Safe_C+20;
   while (run_flag == TRUE)
   {
        if (parametric_flag == false && results_file_flag == true && trajectory_flag
        ==          false)
         {
              Write_HdrRes_Information(outfile);
         }
         else if(parametric_flag == true && para_count <= para_steps)
         {
            parametric_control(outfile);
            histogram_clear();
            if(histogram_flag == true)
            {
                histogram_initialize();
            }
            if (results_file_flag == true)
            {
                Write_HdrRes_Information(outfile);
                Add_Header_Information(outfile);
            }
         }
         else if (trajectory_flag == true && results_file_flag == true)
         {
                            Write_HdrTrj_Information(outfile);
         }
        Idx_v = 0;
       do
       {
          Ttl_v[Idx_v] = 0;
       }while (++Idx_v < MaxMass);
       IonTy_v = 0;
      do
      {
         sqrt(mass_specs[IonTy_v][0])/Dbl_H_v;
         Step_Fac_v = qm_length_mtrs * sqrt(mass_specs[IonTy_v][0])/H_v;
```

```
    Rt_Fac_v = 2 /(rf_ohmega_freq * sqrt(mass_specs[IonTy_v][0
    B_Fac_v = 2 * active_q/mass_specs[IonTy_v][0];
   mass_charge = ElecChg_C/(AmuToKg_C*mass_specs[IonTy_v][0]);
   Idx_v = 0;
do
{
    csnT[Idx_v] = cos(Idx_v*rf_ohmega_freq*H_v);
    sinT[Idx_v] = sin(Idx_v*rf_ohmega_freq*H_v);
}while (++Idx_v<=MxStps_v);
Idx_v = 0;
do
{
  mas_v = mass_start+(Idx_v * scan_interval_amu
  V_volt = mas_v * scale_factor_v ;
  textBoxV->Text = Convert::ToString(V_volt);
  textBoxV->Update();
  U_volt = (uv_ratio * V_volt * scale_factor_u) - dc_offset;
  textBoxU->Text = Convert::ToString(U_volt);
  textBoxU->Update();
  B_v = mass_charge*V_volt;
   A_v = (U_volt * B_v)/V_volt;
   pass_update_flag = false;
  fail_update_flag = false;
  Ix2_v = 0;
  if ((Rnd_1 + mass_specs[IonTy_v][0]) > Safe_C)
  {
    if (ion_phase_mode == PHASE_FIXED_START) Rnd_1 = 0;
    else Rnd_1 = static_cast<int>(20000 * Ran2_Rnd(&du_v));
  }
  if ((Rnd_2 + mass_specs[IonTy_v][1]) > Safe_C)
  {
    if (ion_phase_mode == PHASE_FIXED_START) Rnd_2 = 0;
    else  Rnd_2 = static_cast<int>(20000 * Ran2_Rnd(&du_v));
  }
  IonCou_v = 0;
  do
  {
     float x =0;
     if (trajectory_flag == false)
     {
          Xp_v = x_p[Rnd_2] + ion_offset_x ;
          Yp_v = y_p[Rnd_2] + ion_offset_y;
          Yp_v_old = Yp_v;
          Wx_v = vx[Rnd_2]*Rt_Fac_v;
          Wy_v = vy[Rnd_2]*Rt_Fac_v;
          RunStps_v = int(Step_Fac_v/vz[Rnd_2]);
          vz_start = vz[Rnd_2];
```

```
            if(ion_phase_mode == PHASE_SET)
            {
               double tmpphase;
               tmpphase = Convert::ToDouble(textBoxIonPhase->Text);
               tmpphase = D_Pi* tmpphase/360;
               sn_p[Rnd_1] = sin(tmpphase);
               cs_p[Rnd_1] = cos(tmpphase);
            }
            else if (comboBoxSelectParameter->SelectedIndex == ION_PHASE)
            {
               double tmpphase;
               tmpphase = Convert::ToDouble(ion_phase);
               tmpphase = D_Pi* tmpphase/360;
               sn_p[Rnd_1] = sin(tmpphase);
               cs_p[Rnd_1] = cos(tmpphase);
            }
            sinphi_start = sn_p[Rnd_1];
            cosphi_start = cs_p[Rnd_1];
            xp_start = x_p[Rnd_2];
            yp_start = y_p[Rnd_2];
}
else
{
            Xp_v = Convert::ToDouble(textBoxPosx->Text);
            Yp_v = Convert::ToDouble(textBoxPosy->Text);
            Wx_v = traj_start_para[3]*Rt_Fac_v;
           Wy_v = traj_start_para[4]*Rt_Fac_v;
           vz_mass = traj_start_para[6]/(sqrt(mass_specs[IonTy_v][0]));
           RunStps_v = int(Step_Fac_v/traj_start_para[6]);
           Rnd_1 = 0;
          if(ion_phase_mode == PHASE_SET)
          {
              double tmpphase;
              tmpphase = Convert::ToDouble(textBoxIonPhase->Text);
              tmpphase = D_Pi* tmpphase/360;
             sn_p[Rnd_1] = sin(tmpphase);
             cs_p[Rnd_1] = cos(tmpphase);
          }
           else
           {
               sn_p[Rnd_1] = traj_start_phi[0];
              cs_p[Rnd_1] = traj_start_phi[1];
           }
      }
      StepIdx_v = 0;
      Detect_y = true;
      Detect_x = true;
      do
```

```
{

  cs_v = csnT[StepIdx_v]*cs_p[Rnd_1]-sinT[StepIdx_v]*sn_p[Rnd_1];
  sn_v = sinT[StepIdx_v]*cs_p[Rnd_1]+csnT[StepIdx_v]*sn_p[Rnd_1];
  cs_H_v = cs_v * cst - sn_v * snt;
  cs_2H_v = cs_v * csd - sn_v * snd;
    if((trajectory_flag == true && Detect_y == true) || trajectory_flag ==
    false)
    {
            quad_field =
            Get_Field_Y(Xp_v,Yp_v,radius_r0_mtrs,x_electrode_offset,y
            _electrode_offset);
            F1y_v = (A_v-(B_v*cs_v))*quad_field;
            quad_field =
            Get_Field_Y(Xp_v,Yp_v+(Hlf_H_v*Wy_v),radius_r0_mtrs,x
            _electrode_offset,y_electrode_offset);
             F2y_v = (A_v-(B_v*cs_H_v))*quad_field;
             quad_field =
            Get_Field_Y(Xp_v,Sqt_H_v*F1y_v,radius_r0_mtrs,x_electro
            de_offset,y_electrode_offset);
            F3y_v = F2y_v+(A_v-(B_v*cs_H_v))* quad_field;
             quad_field =
            Get_Field_Y(Xp_v,(Yp_v+(H_v*Wy_v))+(Shf_H_v*F2y_v),
            radius_r0_mtrs,x_electrode_offset,y_electrode_offset);
             F4y_v = (A_v-(B_v*cs_2H_v))* quad_field
              Yp_v = Yp_v + H_v*Wy_v +
                    Ssq_H_v*(F1y_v+F2y_v+F3y_v);
  }

            double ytemp;
            ytemp = Yp_v;
           if ((Yp_v < -radius_r0_mtrs) || (Yp_v > (radius_r0_mtrs*(1+
           y_electrode_offset))))
          {
            Detect_y = false;
             if(fail_trajectory_flag == true && results_file_flag == true)
             {
                    if(fail_update_flag == false)
                    {
                            trajfile =
                            Write_HdrIonSource_File(outfile,ionfile,par1,p
                            ar2);
                            fail_update_flag = true;
                    }
                    Write_IonSource_File(trajfile,MODE_FAIL);
             }
          }
```

```
        else
        {
          Wy_v = Wy_v +
          Sxt_H_v*(F1y_v+2*F2y_v+2*F3y_v+F4y_v);
        }
 if((trajectory_flag == true && Detect_x == true) || (trajectory_flag ==
 false && Detect_v == true))
{
          quad_field =
          Get_Field_X(Xp_v,Yp_v_old,radius_r0_mtrs,x_electrode_off
          set,y_electrode_offset);
           F1x_v = (A_v-(B_v*cs_v))*quad_field;
           quad_field =
          Get_Field_X(Xp_v+(Hlf_H_v*Wx_v),Yp_v_old,radius_r0_m
          trs,x_electrode_offset,y_electrode_offset);
          F2x_v = (A_v-(B_v*cs_H_v))*quad_field;
          quad_field =
          Get_Field_X(Sqt_H_v*F1x_v,Yp_v_old,radius_r0_mtrs,
          x_electrode_offset,y_electrode_offset);
           F3x_v = F2x_v+(A_v-(B_v*cs_H_v))*quad_field;
           quad_field =
          Get_Field_X((Xp_v+(H_v*Wx_v))+(Shf_H_v*F2x_v),
           Yp_v_old,radius_r0_mtrs,x_electrode_offset
           y_electrode_offset);
           F4x_v = (A_v-(B_v*cs_2H_v))* quad_field;
          Xp_v = Xp_v + H_v*Wx_v +
          Ssq_H_v*(F1x_v+F2x_v+F3x_v);
          if ((Xp_v < -radius_r0_mtrs) || (Xp_v > (radius_r0_mtrs *
          (1+ x_electrode_offset))))
          {
                Detect_v = false;
                 Detect_x = false;
                if(fail_trajectory_flag == true &&
                      results_file_flag == true)
                {
                      if(fail_update_flag == false)
                      {
                            trajfile =
                            Write_HdrIonSource_File(outfile,
                            ionfile,par1,par2);
                            fail_update_flag = true;
                      }

                       Write_IonSource_File(trajfile,MODE_FAIL);
                }
          }
```

```
                else
                {
                  Wx_v = Wx_v + Sxt_H_v*(F1x_v+2*F2x_v+2*F3x_v+F4x_v);
                  Yp_v_old = Yp_v;
                  if (trajectory_flag == true && results_file_flag == true)
                  {
                      Write_Trajectory_File(outfile);        //Write if ion still valid
                  }
                 }
                }
                 if(trajectory_flag == TRUE)
                 {
                     plot_update();
                 }
             } while ((++StepIdx_v < RunStps_v) && ((Detect_v &&
                trajectory_flag == false)|| (trajectory_flag == true && (Detect_x ||
                Detect_y))) );
            Xp_v = Xp_v - det_offset_x;
            Yp_v = Yp_v - det_offset_y;
        if ((Detect_v)  && (((Xp_v * Xp_v) + (Yp_v * Yp_v)) <
                exit_areaouter_mtr2) &&
                        (((Xp_v * Xp_v) + (Yp_v * Yp_v)) > exit_areainner_mtr2))
        {
             Ttl_v[Idx_v]++;   // ion reached detector
             if (pass_trajectory_flag == true && results_file_flag == true)
             {
                if(pass_update_flag == false)
                {
                     trajfile = Write_HdrIonSource_File(outfile,ionfile,par1,par2);
                     pass_update_flag = true;
                }
                 Write_IonSource_File(trajfile,MODE_PASS);
             }
             if (exit_file_flag == true && results_file_flag == true && Idx_v ==0)
{
Write_ExitValues_File(outfile,Xp_v,Yp_v,Wx_v,Wy_v,vz_start);
}
}

            Rnd_1++;  Rnd_2++;
            if(Rnd_1 > Num_C_Rnd)
            {
                Rnd_1 = 0;
            }

            } while (++IonCou_v < mass_specs[IonTy_v][1]);
             Application::DoEvents();

            int x = Ttl_v[Idx_v];
```

```
        if(histogram_flag == true && trajectory_flag == false)
        {
              histogram_update(Idx_v, x);
        }
        if ((Idx_v % 2) == 0)
        {
        }
        if (IonTy_v == (number_ion_types-1))
        {
             if (trajectory_flag == false && results_file_flag == true)
             {
                 Write_Results_File(outfile);
             }
         }
          if (mass_steps ==0)
          {
             ++Idx_v;
          }
      } while ((++Idx_v <= mass_steps));

        update_count++;
     } while ((++IonTy_v < number_ion_types));
    para_count++;
    if(parametric_flag == true && para_count > para_steps)
          {
            run_flag       = false;
          }
          else if (parametric_flag == false)
          {
                run_flag       = false;
          }
   }
  return (error);
}
```

Appendix C RGA specification as supplied by The Vacuum Science Group.

1. Minimum of 2 filaments
2. Low Outgassing Ion Source (XHV materials and preparation)
3. Minimum of 50amu although 100amu is more desirable and 200amu is our standard but thinking is that this could be relaxed.4.Degas function that allows user to input power settings and dwell time (as well as recommended settings)
5. Simple diagnostic feature that removes gas phase ions and only allows ESD ions thorough to the collector.
6. Analogue Scan with full control of mass range and pressure range
7. Leak chase mode
8. Multitrend/peak jump
9. Bakeable to at least 250C
10. Some level of operation while at temperature thus requirement for a bakeable cable
11. Minimum detectable partial pressure, noise free! (minimum of 1e-12mbar but ideally down to 1e-16mbar)
12. Uses a 2.3/4 inch connection flange
13. Ideal operation can be achieved without the need for an increased bore size on housing.
14. Software to be very simple to use at the top level while underneath more complex functions can be performed
15. VG Gas style calibration and tuning functions
16. MKS style feedthrough which is intrinsically safe against damage
17. A functional data storage facility, with straightforward recall and replay - preferably with a clock feature to enable timescales to be readily assessed.
18. Option for XHV preparation and assembly of all in vacuum components (vac fire, clean room, pre-bake sub assembly etc..)
19. When scanning peaks, the readout should plot peaks solidly, not trace an outline; otherwise it's really quite hard to read the plot.
20. Offer of provision of elbow for housing with optional fitted and self regulated heating system.
21. An automatic tuning system would be good if it was reliable!
22. Selected Icons chosen/designed to reflect what the button actually does - most are

random!

23. Spare filament set as part of a new package
24. Filaments to be easily replaced.
25. Choice of filament materials
26. Resolution to allow identification of CO from N_2 at 28amu.

Appendix D Additional ECU control functions to support research.

1. Operator control of instrument resolution.
2. Ability to change RF frequency easily
3. Operator control of the mass step increment size.
4. Provision for pole bias.
5. High speed gating circuit to support phase control of ion injection to QMF.
6. Support both faraday cup and electron multiplier detectors.
7. Facility to easily switch between Faraday cup and electron multiplier ion detectors.
8. Two channel RF drive to support investigation into phase errors between x and y electrode drive. This facility can also be used to support investigation of asymmetrical x and y electrode drive.
9. Auto-ranging electrometer amplifier(s).
10. Ability to support series tuned coupling or transformer coupling of QMF.

Appendix E QMS test equipment

Pressure sensor	Oerlikon Leybold Model ITR90 and Centre one display unit
Rotary vacuum pump	Edwards model E2M1.5
Turbomolecular pump	Pfeiffer Balzers TMH
Turbomolecular controllers	Pfeiffer Balzers DC100 turbo controller and DCU100 display
QMF	r_0 = 0.9 mm, length = 100mm custom manufactured.

Appendix F Vacuum flange connector signal pin allocation.

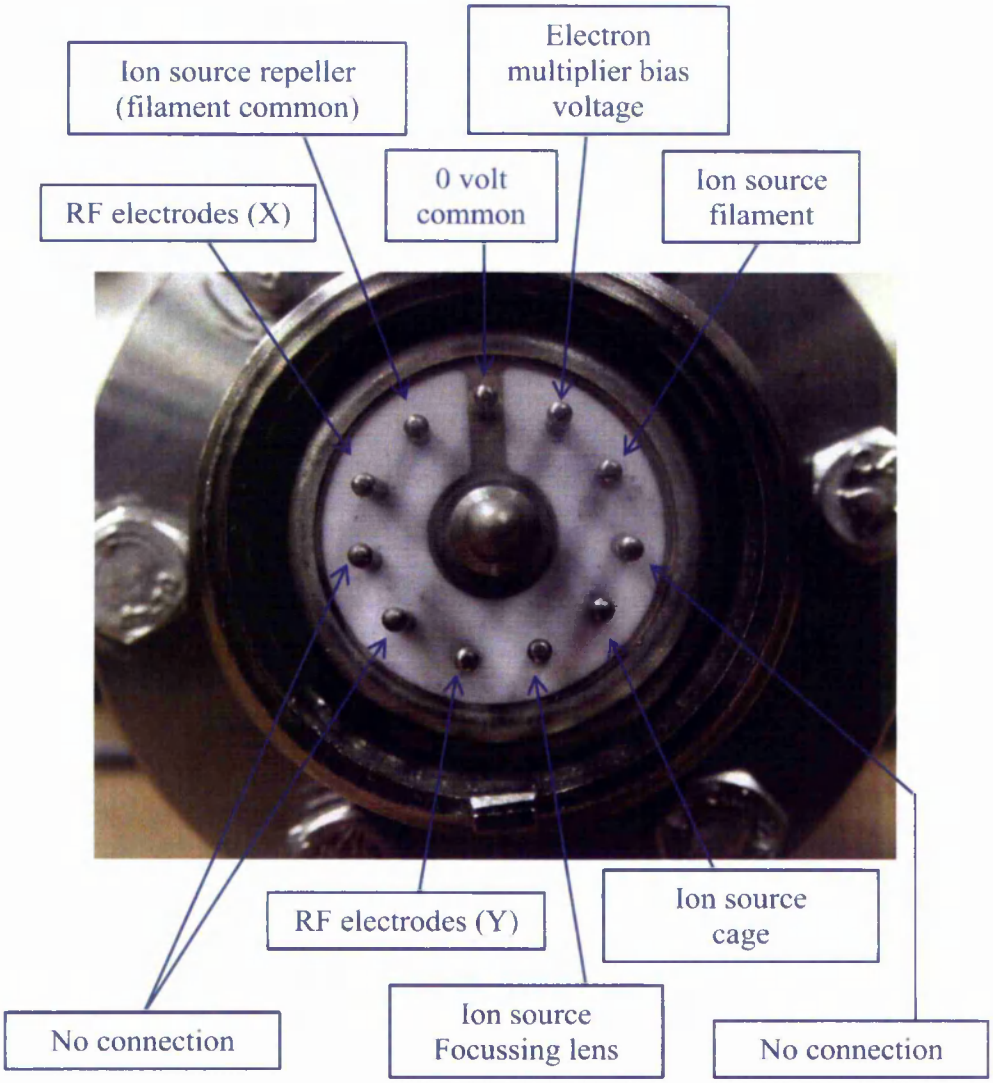

Appendix G List of publications

Journal papers

[1] Sarfaraz U. A. H. Syed, **Thomas J. Hogan**, John R. Gibson, and Stephen Taylor, "Factors influencing the QMS resolution for operation in stability Zones 1 and 3," *J. Amer. Soc. Mass Spectrometry*, vol. 23, no. 5, pp. 988-995, May 2012.

[2] Jeyan Sreekumar, **Thomas J. Hogan**, and Stephen Taylor, "Simulation of a QMS including the effects of pressure in an electron impact ion source," *IEEE Trans. Instrum. Meas.*, (accepted Mar. 2012).

[3] Jeyan Sreekumar, **Thomas J. Hogan**, Stephen Taylor, Phillip G. Turner and Christopher Knott, "A quadrupole mass spectrometer for resolution of low mass isotopes," *J. Amer. Soc. Mass Spectrom.*, vol. 21, no. 8, pp. 1364-1370, Aug. 2010.

[4] **Thomas J. Hogan**, Stephen Taylor, Kerry Cheung, Luis Velásquez-García, Akintunde Ibitayo Akinwande and Randall E. Pedder, "Performance characteristics of a MEMS quadrupole mass filter with square electrodes – experimental and simulated results," *IEEE Trans. Instrum. Meas.*, vol. 59, no. 9, pp. 2458-2467, Sep. 2010.

[5] **Thomas J. Hogan**, Stephen Taylor, "Effects of mechanical tolerances on QMF performance for operation in the third stability zone," *IEEE Trans. Instrum. Meas.*, vol. 59, no. 7, pp. 1933-1940, Jul. 2010.

[6] **Thomas J. Hogan**, Stephen Taylor, "Performance simulation of a quadrupole mass spectrometer operating in the first and third stability zones," *IEEE Trans. Instrum. Meas.*, vol. 57, no. 3, pp. 498-508, Mar. 2008.

Conference presentations

[1] Jeyan Sreekumar (Presenter), Boris Brkić, **Thomas J. Hogan** and Steve Taylor,"RGA modelling and simulation to include pressure dependence in the ion source," Presented at the 10th RGA User Group Meeting, Coventry, U.K., 18th Oct. 2011.

[2] **Thomas J. Hogan** (Presenter), Stephen Taylor, "RGA performance simulation in the first and third stability zones," presented at the 8th RGA User Group Meeting, UKAEA, Culham Laboratories, Abingdon, Oxfordshire, U.K., 13th Mar. 2008.

[3] Neil France (Presenter), **Thomas J. Hogan**, Boris Brkić and Stephen Taylor, "Ion Source for a miniature RGA: results and simulation for Zone 1 and Zone 3,"presented at the 7th RGA User Group Meeting, Cockcroft Institute, Daresbury, U.K., 20th Sep. 2006.

Conference presentations

[1] J. Sreekumar, B. Brkić, **T. J. Hogan** and S. Taylor, RGA modelling and simulation to include pressure dependence in the ion source, The 10th RGA Users Group Meeting, Coventry, U.K., 8th Oct. 2011.

[2] B. Brkić, J. Singh, N. France, **T. J. Hogan**, C. J. Sutcliffe and S. Taylor, "Development of a portable mass spectrometer using linear ion traps", The 32nd BMSS Annual Meeting, Cardiff, U.K., 11th-14th Sept. 2011.

[3] Jeyan Sreekumar, **Thomas J. Hogan**, and Stephen Taylor, "Modelling the effect of pressure in an electron impact ion source QMS for residual gas analysis", Mass Spectrometry @ Manchester Symposia, University of Manchester, Manchester, U.K., 14th Oct. 2010.

[4] Farnoush Salarzaei, Boris Brkić, Stephen Taylor, **Thomas J. Hogan**, Ryan Bell, Tim Short, "Development and mathematical modelling of a Membrane Inlet Mass Spectrometer for environmental monitoring," The 7th HEMS Workshop, Santa Barbara, California, U.S.A., 21st –24th Sep. 2009.

[5] **Thomas J. Hogan**, Jeyan Sreekumar, Stephen Taylor, Phillip G. Turner, Christopher Knott, Brian Garney and Antonio Provenzano, "Point of sample quadrupole mass spectrometer (QMS) for the identification of low mass isotopes," The 57th ASMS Conference, Philadelphia, Pennsylvania, U.S.A., 31st May–4th Jun. 2009.

[6] Stephen Taylor, Boris Brkić, **Thomas J. Hogan**, Adam Clare and Neil France, "Fundamentals of miniature quadrupole mass filters," Proceedings of the 57th ASMS Conference on Mass Spectrometry, Convention Centre. Philadelphia, Pennsylvania, U.S.A., 31st May–4th Jun. 2009.

[7] **Thomas J. Hogan**, Jeyan Sreekumar, Stephen Taylor, Phillip G. Turner, Christopher Knott, Antonio Provenzano and Brian Garney, "Feasibility study for a low cost high-resolution Quadrupole Mass Spectrometer," The 4th Annual Materials Science in Action, AWE, Aldermaston, U.K., 25th Nov. 2008.

[8] Jeyan Sreekumar, Boris Brkić , Neil France, **Thomas J. Hogan**, John R. Gibson and Stephen Taylor, "Simulation of a QMS with an Electron Impact Ion Source including pressure dependence," The 30th BMSS Annual Meeting, University of York, York, U.K., 7th – 10th Sep. 2008.

[9] **Thomas J. Hogan**, Stephen Taylor, Kerry Cheung, Luis Velasquez-Garcia and Akintunde I. Akinwande, "Simulation of a Square Electrode MEMS Quadrupole Mass Filter operating in stability Zones 1 and 3," The 56th ASMS Conference on Mass Spectrometry & Allied Topics, Denver, Colorado, U.S.A., 1st - 5th Jun. 2008.

[10] Boris Brkić, Neil France, **Thomas J. Hogan**, Stephen Taylor, "Advanced Modelling of a QMS to include Ion Source and Mass Filter," 56th ASMS Conference on Mass Spectrometry & Allied Topics, Denver, Colorado, U.S.A., 1st – 5th Jun. 2008.

[11] Boris Brkić, Neil France, **Thomas J. Hogan**, Stephen Taylor, 3D modelling of a miniature ion source for an RGA, The 8th RGA User Group Meeting, UKAEA, Culham Laboratories, Abingdon, Oxfordshire, U.K., 13th Mar. 2008.

[12] **Thomas J. Hogan**, Neil France, John R. Gibson and Stephen Taylor, "A design and simulation tool for miniature mass spectrometers," The 6th HEMS Workshop, Cocoa Beach, Florida, U.S.A., 17th – 20th Sep. 2007.

[13] Boris Brkić, **Thomas J. Hogan** and Stephen Taylor, "Advanced Modelling of Quadrupole Mass Filters and Ion Traps," The 28th BMSS Annual Meeting, University of York, York, U.K., 4th – 7th Sep. 2005.

External Reports

[1] **Thomas J. Hogan**, Stephen Taylor, "Feasibility study for a low cost high-resolution Quadrupole Mass Spectrometer - Interim report," Undertaken for AWE, University of Liverpool, 8th Dec. 2008.

[2] **Thomas J. Hogan**, Stephen Taylor, "AWE Feasibility study for a low cost high-resolution Quadrupole Mass Spectrometer - Final report," Undertaken for AWE, University of Liverpool, 24th Jul. 2009.

Awards

Highly commended for University of Liverpool postgraduate research day poster.